



Dipl.-Ing. Stefan Breuer, BSc

**Li⁺- und F⁻-Ionendynamik in nanokristallinen
Festkörperionenleitern für moderne
Energiespeichersysteme**

DISSERTATION
zur Erlangung des akademischen Grades
Doktor der technischen Wissenschaften (Dr.techn.)
eingereicht an der
Technischen Universität Graz

Betreuer
Univ.-Prof. Dr. Martin Wilkening
Institut für Chemische Technologie von Materialien

Graz, Juli 2018

EIDESSTATTLICHE ERKLÄRUNG

Ich erkläre an Eides statt, dass ich die vorliegende Arbeit selbstständig verfasst, andere als die angegebenen Quellen/Hilfsmittel nicht benutzt, und die den benutzten Quellen wörtlich und inhaltlich entnommenen Stellen als solche kenntlich gemacht habe. Das in TUGRAZonline hochgeladene Textdokument ist mit der vorliegenden Dissertation identisch.

Datum

Unterschrift

*Der größte Feind des Wissens
ist nicht Unwissenheit, sondern
die Illusion, wissend zu sein.*

Stephen Hawking

Kurzfassung

Die Suche nach leistungsfähigen und nachhaltigen elektrochemischen Energiespeichern ist in den letzten Jahren zu einem zentralen Thema in den Materialwissenschaften geworden. Gerade durch den immer größer werdenden Bedarf an tragbaren elektronischen Geräten wie Laptops oder Smartphones, das Aufkommen von Elektrofahrzeugen oder die stetig zunehmende Nachfrage nach Systemen zur Zwischenspeicherung erneuerbarer Energien, hat die Entwicklung von Energiespeichern mit hohen Energiedichten höchste Priorität erlangt. Für die Umsetzung neuer Technologien ist dabei die Materialklasse der Festkörper-Ionenleiter in den Fokus gerückt, die sowohl im Bereich der Grundlagenforschung, als auch der anwendungsorientierten Forschung auf großes Interesse stößt. Verwendet werden diese Verbindungen, die sich durch hohe Ionenleitfähigkeiten bzw. Selbstdiffusionsraten auszeichnen, für die Anwendung in Sensoren oder Sekundärbatterien und haben den großen Vorteil, den wichtigsten Anforderungen zu entsprechen. Diese wären höhere Energiedichten, eine längere Lebensdauer und vor allem ein höheres Maß an Sicherheit durch den Austausch des flüssigen, leicht brennbaren Elektrolyten mit einem Feststoff.

Entscheidend für Festkörper-Ionenleiter ist eine hohe ionische Leitfähigkeit, die von vielen Parametern, wie der atomaren Struktur (inkl. der Defektchemie), der makroskopischen Morphologie oder der chemischen Zusammensetzung der jeweiligen Verbindung abhängt. Bereits bei der Herstellung wird versucht, maßgeschneiderte Materialien mit verbesserten Transporteigenschaften zu präparieren. Eine geeignete Methode dafür ist die Mechanochemische Synthese, mit der Verbindungen hergestellt werden können, die durch konventionelle Festkörperrouten unzugänglich bleiben. Die Herstellung nanokristalliner Materialien durch Hochenergiekugelmahlen erzeugt auf der anderen Seite hoch defektreiche Verbindungen, die neue oder verbesserte Eigenschaften zeigen können. Hier spielen Grenzflächendiffusionsprozesse und der Einfluss von Raumladungszonen eine Rolle.

Im Rahmen dieser Dissertation wurden unterschiedliche Lithium- und Fluor-Ionenleiter mechanochemisch in einer Hochenergie-Kugelmühle hergestellt und strukturell über Röntgenkristallstrukturanalysen und hochauflösende *magic angle spinning* (MAS)-NMR-Messungen untersucht. Die Ionendynamik und Diffusionsparameter dieser Proben wurden anschließend in einem weiten Längen-, Zeit- und Temperaturbereich mittels Impedanzspektroskopie sowie Festkörper-NMR detailliert studiert. Bei den mechanisch behandelten, fluorhaltigen nano-Systemen, wie zum Beispiel $(\text{Ba},\text{Ca})\text{F}_2$, $\text{La}_{1-x}\text{Ba}_x\text{F}_{3-x}$ oder

$\text{LaF}_3:\text{SrF}_2$ konnte so eine zeitskalenabhängige, heterogene Dynamik nachgewiesen werden. Im Falle des LiBH_4 ist durch Linienformmessungen und Spin-Gitter-Relaxationsratenmessungen ein separates Studium der Ionendynamik in den Grenzflächen gelungen. Bei LATP wurde erstmals eine zuverlässige Trennung und Analyse der Ionenbewegung in bulk- und Korngrenzen-Regionen möglich.

Die Ergebnisse dieser Arbeit sind in Form von publizierten Artikeln, in Fachzeitschriften mit *peer-review* Prozess, und noch nicht veröffentlichten Manuskripten zusammengefasst. Für ein besseres Verständnis der Materie sind davor noch relevante theoretische Grundlagen beziehungsweise kurze Einführungen zu den verwendeten Methoden zu finden

Abstract

The search for powerful and sustainable electrochemical energy storage systems has turned into a central topic in materials science in the last couple of years. In particular, the development of energy storage systems featuring high energy densities has become a top priority, especially because of the permanently growing demand for portable electronic devices such as laptops or smartphones, the emergence of electronic vehicles or the continuously increasing need for intermediate storage systems for renewable energies. For the realization of such new technologies solid ion conductors have moved into focus; a material class, which is of great interest in the field of fundamental research as well as application-oriented research. These compounds, which are characterized by a high diffusivity, are utilized in sensors or secondary batteries and have the major benefit of meeting the most important requirements such as higher energy densities, a longer lifetime and particularly a higher level of safety via an exchange of the liquid, flammable electrolyte with a solid material.

A high ionic conductivity is crucial for all solid ion conductors. This parameter is influenced by many factors like the atomic structure (incl. the defect chemistry) as well as the macroscopic morphology or the chemical composition of the respective compound. It is therefore attempted to use a synthesis method, which allows the preparation of tailor-made materials featuring improved transport properties. Mechanochemical synthesis is an appropriate technique in this context as it enables on the one hand the tuning of known substances via structural modifications and on the other hand the fabrication of new, so far inaccessible products via new synthesis routes. In particular, nanocrystalline materials are available by high-energy ball milling whose properties may be considerably different to those of their coarse-grained counterparts. The differences can be explained by the influence of interfacial regions or space charge regions governing dynamic properties in materials with nm-sized crystallites.

In the framework of this thesis various lithium and fluorine ion conductors were mechanochemically prepared in a high-energy ball mill and structurally characterized via X-ray powder diffraction and magic angle spinning (MAS) NMR measurements. Subsequently the ion dynamics and the diffusion parameters of these samples were investigated in detail by impedance and NMR spectroscopy over a broad dynamic range. Thus it was possible to prove a timescale dependent, heterogeneous dynamics for the mechanically treated, fluorine containing systems, such as $(\text{Ba},\text{Ca})\text{F}_2$, $\text{La}_{1-x}\text{Ba}_x\text{F}_{3-x}$ or $\text{LaF}_3:\text{SrF}_2$. In the case of LiBH_4 we were

able to study the ion dynamics in the interface separated via line-shape-measurements and spin-lattice-relaxation rate experiments. In terms of LATP, for the first time a reliable separation and analysis of the ion movement in the bulk- and g.b.-regions was realized.

The results of this work are presented cumulatively in the way of published articles in different peer-review journals and prepared manuscripts. Prior to that relevant theoretical basics as well as short introductions regarding the employed methods are integrated for a better understanding of the subject.

Inhaltsverzeichnis

1. Einleitung	1
2. Theorie der Festkörperdiffusion und Methoden	4
2.1 Allgemeine Grundlagen zur Diffusion in Festkörpern	4
2.1.1 Makroskopische Diffusion – Die Kontinuum-Theorie	5
2.1.2 Mikroskopische Diffusion – Die „random walk“ Theorie	6
2.1.3 Die Temperaturabhängigkeit des Diffusionkoeffizienten	8
2.1.4 Defekte in Festkörpern	8
2.1.5 Diffusionsmechanismen	11
2.2 Mechanochemische Reaktionen und ihre Produkte	13
2.2.1 Mechanochemische Synthese	13
2.2.2 Hochenergie-Kugelmahlen in einer Planetenmühle	15
2.2.3 Nanostrukturierte Materialien	16
2.3 Röntgenkristallstrukturanalyse	18
2.3.1 Die Braggsche Gleichung	18
2.3.2 Das Debye-Scherrer-Verfahren	19
2.3.3 Kristallitgrößenbestimmung – Die Scherrer-Formel	21
2.4 Impedanzspektroskopie	22
2.4.1 Das Prinzip der Impedanzspektroskopie	23
2.4.2 Weitere grundlegende Funktionen	26
2.4.3 Leitfähigkeitsisothermen und Nyquist-Diagramme	28
2.4.4 Der Ladungsdiffusionskoeffizient	31
2.5 Festkörper Kernspinresonanzspektroskopie (NMR)	32
2.5.1 Theoretische Grundlagen der NMR Spektroskopie	32
2.5.2 Relaxationsmessungen	36
2.5.3 Interpretation der Relaxationsdaten	38
2.5.4 MAS NMR	41

3. Ergebnisse	43
<i>3.1 Lithium-basierte Festkörperelektrolyte</i>	44
3.1.1 Separating bulk from grain boundary Li ion conductivity in the sol-gel prepared solid electrolyte $\text{Li}_{1.5}\text{Al}_{0.5}\text{Ti}_{1.5}(\text{PO}_4)_3$	45
3.1.2 Rapid Li Ion Dynamics in the Interfacial Regions of Nanocrystalline Solids	55
<i>3.2 Nanokristalline Fluor-Ionenleiter</i>	62
3.2.1 Mismatch in cation size causes rapid anion dynamics in solid electrolytes: the role of the Arrhenius pre-factor	63
3.2.2 Fluorine Translational Anion Dynamics in Nanocrystalline Ceramics: $\text{SrF}_2\text{-YF}_3$ Solid Solutions	78
3.2.3 F anion dynamics in cation-mixed nanocrystalline $\text{LaF}_3\text{:SrF}_2$	90
3.2.4 Heterogeneous F anion transport, local dynamics and electrochemical stability of nanocrystalline $\text{La}_{1-x}\text{Ba}_x\text{F}_{3-x}$	105
<i>3.3 Nanokomposite mit zwei mobilen Ladungsträger-Spezies</i>	125
3.3.1 Interfacial Li ion dynamics in nanostructured LiF and LiF: Al_2O_3 composites	126
4. Zusammenfassung und Ausblick	139
A. Anhang	143
<i>A.1 Verwendete Geräte</i>	143
<i>A.2 Verwendete Software</i>	144
B. Literaturverzeichnis	146
C. Publikationen	150
<i>C.1 Artikel in referierten Fachzeitschriften</i>	150
<i>C.2 Manuskripte</i>	152
<i>C.3 Posterbeiträge auf internationalen Konferenzen</i>	152
<i>C.4 Vorträge</i>	153
D. Danksagung	154

1. Einleitung

Fossile Energieträger tragen durch die Emission von Treibhausgasen und die damit verbundene Erwärmung der Erdatmosphäre signifikant zum aktuellen Klimawandel bei. Diese Tatsache, zusammen mit der kontinuierlichen Verknappung fossiler Brennstoffe, macht eine Neuausrichtung der derzeitigen Energieversorgung unumgänglich. Ziel dabei ist eine deutliche Steigerung des Anteils an erneuerbaren Energiequellen, wie zum Beispiel aus Solaranlagen, Wind- oder Wasserkraftwerken, am gesamten Energiemix. Moderne Energiespeichersysteme können eine zeitliche Entkopplung von der Erzeugung solcher Energien hin zum Verbrauch ermöglichen und sind somit als Schlüsseltechnologien der Zukunft anzusehen. Zurzeit werden für die Speicherung Konzepte verwendet, die auf unterschiedlichen Technologien beruhen, wobei die im Rahmen dieser Arbeit wichtigste Methode die chemische Speicherung in so genannten Sekundärbatterien oder Akkumulatoren darstellt. Diese Systeme stellen nicht nur wichtige Kapazitäten für die zukünftige Zwischenspeicherung von erneuerbaren Energien dar, sondern sind durch den Einsatz in der Unterhaltungselektronik oder der Elektromobilität bereits jetzt nicht mehr aus dem Alltag wegzudenken. Für diesen breiten Anwendungsbereich ist es daher essentiell, dass sowohl die Sicherheit als auch die Leistungsfähigkeit und damit die Energie- beziehungsweise Leistungsdichte gesteigert wird. Die Materialwissenschaften beschäftigen sich aus diesem Grund intensiv mit der Verbesserung bestehender Systeme sowie der Erforschung neuer Batterietechnologien.

Das grundlegende Prinzip bei Sekundärbatterien ist der Erhalt des Ladungsausgleiches. Um für diesen zu sorgen, wandern mobilen Ionen zwischen zwei Elektroden, die durch einen Elektrolyten voneinander getrennt sind, hin und her. Die Analyse der dort stattfindenden Ionendiffusionsprozesse ist von größter Bedeutung für die Leistungsfähigkeit dieser

chemischen Speicher. Im Umfang dieser Dissertation sind Festkörperbatterien in den Fokus gerückt, welche einen keramischen Feststoff als Elektrolyten verwenden. Die großen Vorteile davon sind zum einen ein höheres Maß an Sicherheit durch Wegfallen des flüssigen, leicht brennbaren Elektrolyten, zum anderen eine höhere Zyklustabilität sowie eine höhere theoretische Energiedichte. Um Limitierungen und diverse noch auftretende Hürden dieser Systeme zu überwinden, wird viel in die Entwicklung neuer und die Verbesserung bereits bekannter Energiespeichermaterialien und Ionenleiter investiert. Entscheidend ist es in diesem Zusammenhang detaillierte Informationen über die Strukturen der Verbindungen sowie über wichtige Eigenschaften, wie etwa die ionischen und elektronischen Leitfähigkeiten, zu sammeln und dadurch die Proben bestmöglich zu charakterisieren. Grenzflächen und Durchtrittswiderstände spielen dabei eine immer größer werdende Rolle.

Bereits die gewählte Synthesemethode hat enormen Einfluss auf die Ionendiffusion in den hergestellten Produkten. So kann zum Beispiel die hier häufig verwendete Präparationsmethode des Hochenergie-Kugelmahlens, durch Verkleinerung der Kristallitgröße in den nanokristallinen Bereich und das gezielte Einbringen von strukturellen Unordnungen, zu Materialien mit maßgeschneiderten, stark verbesserten (Ladungsträger-) Transporteigenschaften führen. Ein besseres Verständnis der elementaren Diffusionsprozesse in Festkörpern, das nur durch ein Zusammenspiel der Analyse von Struktur und Dynamik erreicht werden kann, ist unverzichtbar für die Implementierung neuer Konzepte oder die Verbesserung der bereits bestehenden Speichersysteme. Im Rahmen dieser Arbeit wurden für die detaillierte Charakterisierung der Diffusionsparameter zwei komplementäre Spektroskopiemethoden verwendet: die Impedanzspektroskopie, welche hier Informationen über die langreichweite, makroskopische Ladungsträgerbewegung liefert, und die Kernspinresonanzspektroskopie, die elementare, mikroskopische Sprungprozesse genauer unter die Lupe nimmt. Erst die Kombination der Ergebnisse beider Techniken hilft bei Aufklärung der Bewegungsmechanismen und ermöglicht so ein besseres Verständnis des oftmals sehr komplexen Gesamtbildes der Ionendiffusion in Festkörpern.¹⁻⁷

Das Ziel der vorliegenden Dissertation war es, durch grundlagenorientierte Forschung, die Li⁺- und F⁻-Ionendynamik in verschiedenen (mikro- und) nanokristallinen Festkörperionenleitern für Energiespeichersysteme zu studieren. Die untersuchten Proben wurden teilweise selbst mechanochemisch hergestellt und anschließend strukturell beziehungsweise

spektroskopisch mit Leitfähigkeitsmessungen und NMR-Relaxometrie sowie hochauflösender MAS NMR charakterisiert.

Die Dissertationsschrift ist wie folgt gegliedert: zu Anfang wird in einem Theorieteil auf die relevanten Grundlagen sowie die verwendeten Methoden eingegangen. Dabei werden zuerst die Grundprinzipien der Ionendiffusion (Kap. 2.1) und der mechanochemischen Reaktionen (Kap. 2.2) erläutert. Anschließend folgt eine Einführung in die verwendeten Analysemethoden, *ergo* Röntgenkristallstrukturanalyse (Kap. 2.3), Impedanzspektroskopie (Kap. 2.4) und Festkörper-Kernspinresonanzspektroskopie (Kap. 2.5). In Kapitel 3 sind die Ergebnisse kumulativ, in Form von bereits publizierten Artikeln oder von zur Veröffentlichung vorbereiteten Manuskripten, zusammengefasst. Abgerundet wird diese Dissertation mit einer kurzen Zusammenfassung und einem Ausblick auf zukünftige Arbeiten (Kap. 4)

2. Theorie der Festkörperdiffusion und Methoden

Der Begriff ‚Diffusion‘ leitet sich vom lateinischen Wort *diffundere* ab und bedeutet ausbreiten oder sich zerstreuen. Er beschreibt eine Durchmischung von verschiedenen miteinander in Berührung befindlichen Stoffen, die sich im gasförmigen, flüssigen oder festen Zustand befinden können. Die Durchmischung beruht dabei auf der Brownschen Molekularbewegung der Ionen, Atome, Moleküle oder Kolloid-Teilchen und wird durch Konzentrationsunterschiede, Temperaturunterschiede, Druckunterschiede oder äußere Feldkräfte hervorgerufen. Diffusion, die von Konzentrationsunterschieden ausgelöst wurde, führt zu einem Abbau eines Konzentrationsgefälles, wohingegen die anderen Effekte den Aufbau einer Konzentrationsdifferenz zur Folge haben.^{8, 9}

2.1 Allgemeine Grundlagen zur Diffusion in Festkörpern

Die Diffusion in Festkörpern ist von enormer Bedeutung für die Materialwissenschaften sowie die Metallurgie, da die verschiedensten Diffusionsprozesse eine entscheidende Rolle im Hinblick auf die Kinetik der mikrostrukturellen Veränderungen spielen, die während der Verarbeitung der Metalle, Legierungen, Keramiken, Halbleiter oder Polymere auftreten. In kristallinen Materialien sind die atomaren Mechanismen der Diffusion eng mit den unterschiedlichsten Arten von Defekten verbunden, die die Bewegung von Teilchen überhaupt erst ermöglichen. Zentrale Punkte der Festkörperdiffusion sind die makroskopische sowie die mikroskopische (atomare) Diffusion, die im folgenden Abschnitt näher behandelt werden.^{9, 10}

2.1.1 Makroskopische Diffusion – Die Kontinuum-Theorie

Die makroskopische Bewegung eines Atoms oder Moleküls durch einen Festkörper kann mithilfe der Fickschen Gesetze beschrieben werden, welche den Zusammenhang zwischen einem Teilchenfluss J und einem Konzentrationsgradienten c darstellen. Unter Annahme einer eindimensionalen Teilchenbewegung in einem isotropen Medium ergibt sich folgende Beziehung:

$$J_x = -D \frac{\partial c}{\partial x} \quad (2.1)$$

die auch als erstes Ficksches Gesetz bekannt ist. Das negative Vorzeichen weist hierbei auf entgegengesetzte Richtungen des Teilchenflusses und des Konzentrationsgradienten hin, da sich die Partikel von Regionen höherer Konzentration zu Regionen niedrigerer Konzentration bewegen. Der Proportionalitätsfaktor D wird auch als Diffusionskoeffizient bezeichnet und besitzt die Dimension *Länge² pro Zeiteinheit*, beschreibt also, wie viele Teilchen pro Zeiteinheit durch eine definierte Fläche in x-Richtung durchtreten.

Eine Erweiterung des Teilchenstroms J auf eine dreidimensionale Ebene führt zu einer verallgemeinerten Modifikation von Gleichung (2.1) in Vektordarstellung:

$$\mathbf{J} = -D \nabla c \quad (2.2)$$

Hierbei repräsentiert \mathbf{J} den Teilchenfluss in x-, y- und z-Richtung. Das Nabla Symbol ∇ wird als vektorieller Differentialoperator eingeführt und entspricht der Vektoroperation $(\partial/\partial x, \partial/\partial y, \partial/\partial z)$ in allen drei Dimensionen. Bei anisotroper Diffusion stellt D einen Tensor dar und wird als makroskopischer Diffusionskoeffizient oder Tracerdiffusionskoeffizient D^{tr} bezeichnet. Wichtig zu beachten ist, dass Gleichung (2.2) nur gültig ist, wenn der Konzentrationsgradient ∇c konstant ist, beziehungsweise der Gradient für einen sehr langsamem Diffusionsprozess als quasi-konstant angesehen werden kann.

Zur Beschreibung nicht stationärer Vorgänge kann das durch Kombination der Kontinuitätsgleichung

$$\frac{\partial c}{\partial t} = -\nabla \cdot \mathbf{J} \quad (2.3)$$

mit Gleichung (2.2) erhaltene zweite Ficksche Gesetz verwendet werden, welches auch als Diffusionsgleichung bezeichnet wird:

$$\frac{\partial c}{\partial t} = \nabla \cdot (D^{\text{tr}} \nabla c) \quad (2.4)$$

Sollte die Diffusion unabhängig von der Konzentration sein, lässt sich Gleichung (2.4) zu

$$\frac{\partial c}{\partial t} = D^{\text{tr}} \Delta c \quad (2.5)$$

vereinfachen. Diese lineare partielle Differentialgleichung zweiter Ordnung, auch als lineare Diffusionsgleichung bekannt, kann bei Verwendung bestimmter Anfangs- und Grenzbedingungen mit Hilfe der Laplace Transformation gelöst werden, wobei Δ den Laplace Operator darstellt ($\Delta = \nabla^2 = \partial^2/\partial x^2, \partial^2/\partial y^2, \partial^2/\partial z^2$).^{9,11}

2.1.2 Mikroskopische Diffusion – Die „random walk“ Theorie

Makroskopische Diffusion in Festkörpern resultiert aus der Aneinanderreihung einzelner mikroskopischer Teilchensprünge. Bei diesen elementaren Sprungprozessen auf atomarer Ebene wandern die Atome oder Moleküle in kleinen, zufälligen Sprüngen („random walk“) durch den Feststoff (siehe Abbildung 1). Ermöglicht wird diese Bewegung zumeist durch Defekte im Gitter, wie zum Beispiel Lehrstellen oder Zwischengitterplätze, entlang derer sich die Teilchen bewegen (detailliertere Informationen sind in Kapitel 2.1.4 zu finden).⁹

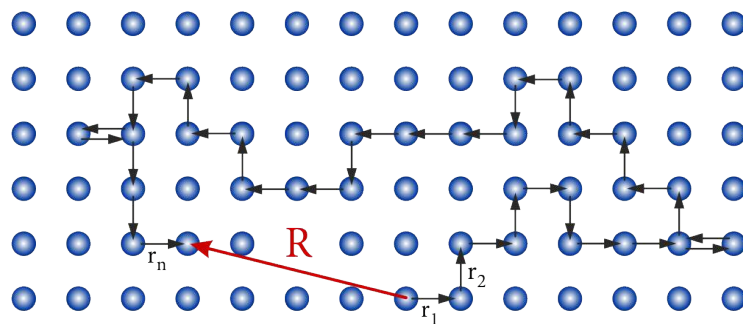


Abbildung 1: Schematische Darstellung der zufälligen Bewegung eines Teilchens durch einen Festkörper. Die individuellen Sprungprozesse r_i führen zu einer Gesamtverschiebung R . Die Abbildung wurde adaptiert von Referenz [10].

Die resultierende Gesamtverschiebung R setzt sich dabei aus der Summe der Einzelsprünge zusammen

$$R = \sum_{i=1}^n r_i \quad (2.6)$$

Physikalische Größen wie die Sprunglänge oder die Sprungrate werden benutzt, um die elementaren Sprünge zu beschreiben und tragen in weiterer Folge zu einem besseren Verständnis der Diffusion bei. Mit Hilfe dieser Größen kann eine Beziehung zwischen der Gesamtverschiebung R eines Teilchens und dem Diffusionskoeffizienten hergestellt werden. Unkorrelierte Diffusionsprozesse werden über die Einstein-Smoluchowski Gleichung

$$D^{sd} = \frac{\langle R^2 \rangle}{6\tau} \quad (2.7)$$

erläutert, bei der D^{sd} den mikroskopischen Selbstdiffusionskoeffizienten und τ die mittlere Verweilzeit eines Teilchens an einem Gitterplatz darstellt, die auch als Sprungrate τ^{-1} dargestellt werden kann. Für zufällige unkorrelierte Bewegungen zwischen benachbarten freien Gitterplätzen vereinfacht sich Gleichung (2.7) zu

$$D^{sd} = \frac{d^2}{6\tau} \quad (2.8)$$

wobei d die Sprunglänge zwischen zwei Gitterpositionen repräsentiert. Unkorreliert bedeutet in diesem Zusammenhang, dass die einzelnen Sprünge völlig unabhängig voneinander sind.¹⁰ Über einen so genannten Korrelationsfaktor f kann ein Zusammenhang zwischen dem mikroskopischen Selbstdiffusionskoeffizienten und dem in Kapitel 2.1.1 eingeführten makroskopischen Tracerdiffusionskoeffizienten wie folgt hergestellt werden:

$$D^{tr} = f \cdot D^{sd} \quad (2.9)$$

Der Korrelationsfaktor kann hierbei Werte zwischen 0 und 1 annehmen, wobei 1 einer komplett unkorrelierten Teilchenbewegung entspricht.⁹

2.1.3 Die Temperaturabhängigkeit des Diffusionkoeffizienten

Allgemein ist der makroskopische Diffusionskoeffizient von Festkörpern (stark) temperatur-abhängig. Diese Abhängigkeit wird daher empirisch oftmals mittels einer Arrhenius-Beziehung⁹ beschrieben:

$$D^{\text{tr}} = D_0^{\text{tr}} \exp\left(-\frac{\Delta H}{k_B T}\right) \quad (2.10)$$

bei der D_0^{tr} den prä-exponentiellen Faktor, ΔH die Aktivierungsenthalpie, k_B die Boltzmann-Konstante und T die absolute Temperatur repräsentiert. Bei konstantem Druck kann Gleichung (2.10) für feste Materialien zu

$$D^{\text{tr}} = D_0^{\text{tr}} \exp\left(-\frac{E_A}{k_B T}\right) \quad (2.11)$$

mit E_A als der Aktivierungsenergie für einen erfolgreichen Sprungprozess modifiziert werden.⁹

2.1.4 Defekte in Festkörpern

Das Vorhandensein von Leerstellen oder Defekten in Festkörpern ist die Grundvoraussetzung, ohne die eine Diffusion gar nicht erst möglich wäre. In idealen Kristallen sind alle Gitterplätze von Teilchen besetzt, die um ihren Gleichgewichtszustand oszillieren und diesen nicht verlassen können. Dieser Idealzustand kann allerdings nur am absoluten Nullpunkt existieren. Oberhalb der 0 K besitzt jeder Kristall Fehlordnungen, da aufgrund des zweiten Hauptsatzes der Thermodynamik immer ein gewisser Grad an Unordnung im thermischen Gleichgewicht vorherrschen muss. Betrachtet man die Gibbs-Helmholtz-Gleichung

$$\Delta G = \Delta H - T\Delta S \quad (2.12)$$

mit ΔG als der Gibbs freien Energie, wird deutlich, dass bei steigenden Temperaturen höhere Defektkonzentrationen auftreten. Ein realer Kristall besitzt damit ein höheres Maß an Entropie ΔS , was zu einem thermodynamisch bevorzugten (niedrigeren) Energiezustand ΔG im Vergleich zu seinem idealen Gegenstück führt.^{10, 11}

Allgemein lassen sich Fehlordnungen auf unterschiedliche Arten klassifizieren. Eine Möglichkeit der Unterscheidung ist die Einteilung in intrinsische Defekte, das heißt

Eigenfehler, die im „reinen Kristall“ auftreten, und extrinsische Defekte, also Fremdfehler, die durch den Einbau fremder Atome ins Gitter hervorgerufen werden.¹¹

Häufiger zu finden ist allerdings die Unterteilung der Defekte anhand ihrer Ausdehnung:

Punktdefekte: Punktdefekte sind nulldimensionale Baufehler, die sich auf einzelne Atome beziehen. Aufgrund der Tatsache, dass solche Defekte durch den Kristall wandern können, tragen sie erheblich zur Diffusion sowie zur Reaktivität eines Festkörpers bei. Zu ihnen zählen Fremdbausteine, Schottky- beziehungsweise Frenkel-Fehlordnungen und Mischkristalle. In Abbildung 2 sind diese Fehlordnungstypen schematisch dargestellt.

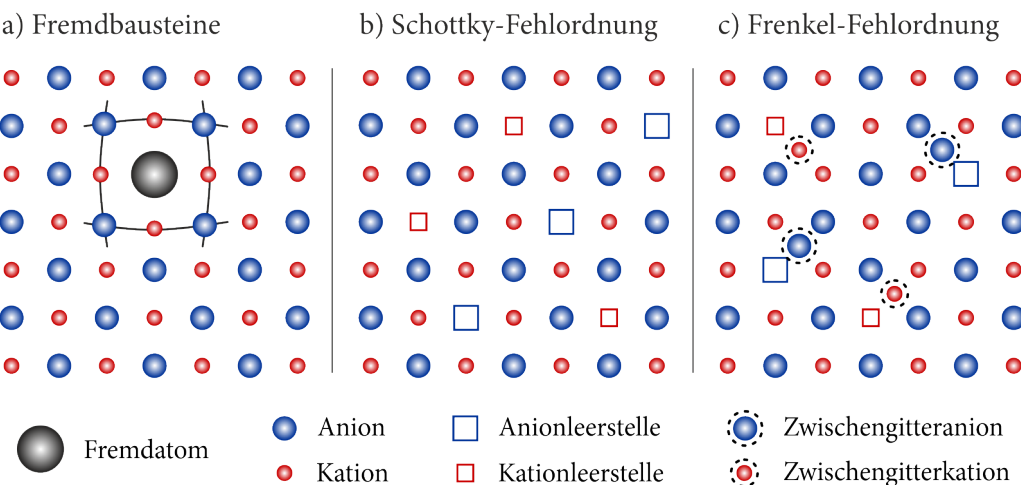


Abbildung 2: Schematische Darstellung der wichtigsten Punktdefekte in Kristallgittern.

- In diesem Fall führt die Substitution von Gitterbausteinen mit Fremdatomen zu einer Expansion oder Kompression des Kristallgitters.
 - Durch die Wanderung von Ionen an die Kristalloberfläche kommt es bei Schottky-Fehlordnungen zur Bildung von Leerstellen im Gitter
 - Bei der Frenkel-Fehlordnung bewegen sich Ionen auf Zwischengitterplätze und hinterlassen abermals Leerstellen im Kristall zurück.
- Die Abbildung wurde adaptiert von Referenz [12].

Fremdbausteine sind Substitutionsatome, die in der Regel kleiner oder größer sind als die Bausteine des Kristallgitters, deren Plätze sie einnehmen. Die Substitution kann dabei durch Dotierung oder Verunreinigung der Ausgangsmaterialien hervorgerufen werden. Die unterschiedliche Größe der Fremdatome führt entweder zu einer Expansion oder einer Kompression des Gitters und hat daher großen Einfluss auf die Eigenschaften des Kristalls. Werden Atome anderer Valenz eingebracht, können – unter Einhaltung der

Ladungsneutralität – zusätzliche Leerstellen generiert werden. Bei einer Schottky-Fehlordnung wandern Kationen oder Anionen an die Oberfläche eines Kristalls und hinterlassen dabei Leerstellen im Gitter. Die Frenkel-Fehlordnung kommt dadurch zustande, dass Ionen ihre regulären Gitterplätze verlassen und sich auf normalerweise nicht besetzten Zwischengitterplätzen positionieren. Es entstehen somit sowohl Leerstellen als auch Zwischengitteratome.^{11, 12}

Liniendefekte: Liniendefekte sind eindimensionale Baufehler, die entlang von Versetzungslinien verlaufen. Ihre wichtigsten Vertreter sind Stufen- oder Schraubenversetzungen (siehe Abbildung 3). Sie kennzeichnen sich durch Fehlausrichtungen der Gitterebene und können sich über das gesamte Kristallgitter erstrecken, weshalb sie großen Einfluss auf die innere Struktur und damit auf die mechanischen Eigenschaften sowie die Diffusivität des Kristalls haben.¹²

Flächendefekte: In polykristallinen Materialien treten zweidimensionale Flächendefekte an Stellen auf, wo zwei oder mehr Kristalle aufeinandertreffen. Hierzu gehören Korngrenzen, Stapelfehler oder Zwillingsgrenzen. Insbesondere Korngrenzen sind für die im Rahmen dieser Arbeit betrachteten Materialien von großer Bedeutung, da sie oftmals schnelle Diffusionspfade für mobile Atome oder Ionen bereitstellen. Sie trennen zwei Körner eines Kristalls mit unterschiedlicher räumlicher Orientierung. Die unterschiedlichen Bereiche sind dabei gegeneinander geneigt (siehe Abbildung 3). Speziell bei nanokristallinen Proben treten Korngrenzen, aufgrund des hohen Anteils an Grenzflächen, sehr häufig auf.¹²

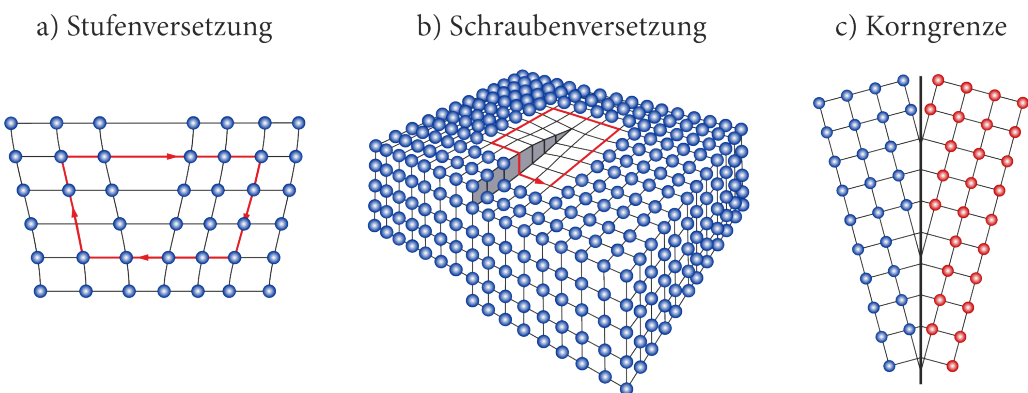


Abbildung 3: a) – c) Schematische Darstellung von ein- und zweidimensionalen Baufehlern in Kristallen, nach Referenz [12].

2.1.5 Diffusionsmechanismen

Wie bereits im vorigen Abschnitt erwähnt oszillieren Atome in einem Kristall um ihren Gleichgewichtszustand. Gelegentlich werden diese Oszillationen groß genug, sodass ein Teilchen seine Position ändern kann. Diese Positionsänderung wird als Sprung bezeichnet und ist die Grundlage für Diffusion in Festkörpern. Im folgenden Abschnitt werden die unterschiedlichen Diffusionsmechanismen genauer behandelt und sind in Abbildung 4 schematisch dargestellt.¹⁰

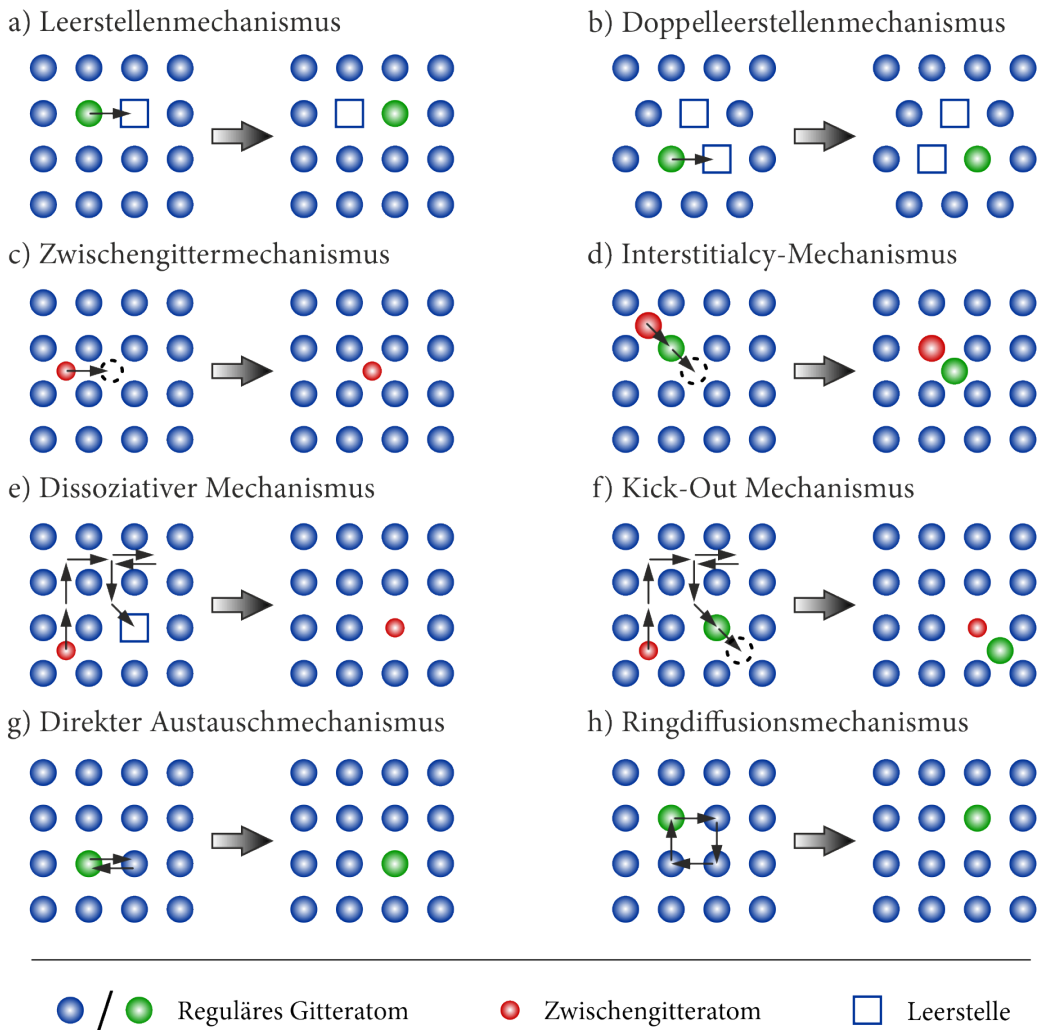


Abbildung 4: Schematische Darstellung der unterschiedlichen Diffusionsmechanismen adaptiert von den Referenzen [9], [10] und [13].

Leerstellenmechanismus: Der Leerstellenmechanismus (Abbildung 4 a)) ist der häufigste und wichtigste Diffusionsmechanismus und kommt bevorzugt in Metallen und Legierungen vor. Dabei springt ein Atom von seiner Position auf eine benachbarte Leerstelle und hinterlässt auf seinem ursprünglichen Platz wiederum eine Leerstelle. Es erfolgt also ein Austausch von Platz und Leerstelle, in die anschließend wieder ein benachbartes Teilchen springen kann. Diese Art der Diffusion hängt stark von der Leerstellenkonzentration sowie ihrer Mobilität ab.^{9, 13}

Doppelleerstellenmechanismus: Ein dem Leerstellenmechanismus sehr ähnlicher Diffusionsprozess ist der Doppelleerstellenmechanismus (Abbildung 4 b)), bei dem die Bewegung der Atome über gebundene Leerstellenpaare erfolgt. Doppelleerstellen können sich, sofern genügend Bindungsenergie vorhanden ist, aus so genannten Monoleerstellen bilden. Insgesamt steigt die Konzentration von beiden Arten von Leerstellen mit steigender Temperatur an. Allerdings erhöht sich die Doppelleerstellenkonzentration mit einer höheren Rate, weshalb den Leerstellenpaaren bei höheren Temperaturen eine größere Bedeutung zugeordnet wird.^{9, 10}

Zwischengittermechanismus: Atome, die deutlich kleiner sind als reguläre Gitteratome, sitzen hierbei auf Zwischengitterplätzen und besetzen in der Regel Tetraeder- oder Oktaederplätze. Die Diffusion erfolgt durch direkte Sprünge der Teilchen von einem Zwischengitterplatz zum nächsten, weshalb dieser Mechanismus auch als direkter Zwischengittermechanismus (Abbildung 4 c)) bezeichnet wird. Aufgrund der Unabhängigkeit von Defekten ist dieser Vorgang üblicherweise schneller als der Leerstellenmechanismus und führt zu größeren Diffusionskoeffizienten.^{9, 10, 13}

Interstitialcy-Mechanismus: Der Interstitialcy-Mechanismus (Abbildung 4 d)) oder auch indirekter Zwischengittermechanismus genannt, ist zu finden, wenn Zwischengitteratome im Kristall vorhanden sind, die fast die gleiche Größe wie reguläre Gitteratome aufweisen. Dabei wird ein Atom auf einem regulären Platz von einem großen Zwischengitterteilchen verdrängt und springt selbst auf einen Zwischengitterplatz. Da für diese Art der Diffusion hohe Bildungsenthalpien aufzuwenden sind, ist sie unter Gleichgewichtsbedingungen selten zu finden.^{9, 10, 13}

Zwischengitter-Austausch-Mechanismus: Wenn ein Atom sowohl Zwischengitterplätze als auch Austauschplätze einnehmen kann, ist es in der Lage via eines Zwischengitter-Austausch-Mechanismus zu diffundieren. Dieser zweistufige Prozess kann auf zwei unterschiedliche Arten erfolgen. In beiden Fällen wandert zuerst ein Teilchen über den

Zwischengittermechanismus durch das Kristallgitter. Wird anschließend eine Fehlstelle eingenommen, spricht man vom dissoziativen Mechanismus (Abbildung 4 e)). Verdrängt das Atom danach ein reguläres Gitteratom, wie es im Interstitialcy-Mechanismus der Fall ist, wird von einem Kick-Out Mechanismus gesprochen (Abbildung 4 f)).^{9, 10, 14}

Kollektive Mechanismen: Zuletzt seien an dieser Stelle noch für Atome ähnlicher Größe die kollektiven Diffusionsmechanismen genannt, in die keine Defekte involviert sind. Hierbei kann es entweder zu einem direkten Austausch (Abbildung 4 g)) benachbarter Teilchen kommen, oder zu einem Ringmechanismus (Abbildung 4 h)), also einer Rotation von drei oder mehreren Atomen um jeweils einen Platz. Beide Typen gelten aufgrund ihrer hohen Aktivierungsenergien als äußerst unwahrscheinlich in Kristallen, können allerdings in amorphen Systemen durchaus verbreitet sein.⁹

2.2 Mechanochemische Reaktionen und ihre Produkte

Jede chemische Reaktion benötigt zur Aktivierung eine Energie, die üblicherweise in Form von Wärme, Licht oder als elektrisches Potential eingebracht wird. Wird die Reaktion durch die Absorption von mechanischer Energie hervorgerufen, spricht man von mechanochemischen Reaktionen.¹⁵⁻¹⁷ Gerhard Heinicke hat im Jahr 1984 Mechanochemie wie folgt definiert: „Die Mechanochemie ist der Zweig der Chemie, der sich mit den chemischen und physikalischen Umwandlungen von Festkörpern beschäftigt, die durch das Einwirken mechanischer Einflüsse induziert werden“.¹⁸ Diese noch heute akzeptierte Definition beschreibt ein mittlerweile stark etabliertes Gebiet der Materialwissenschaften und der Festkörperchemie, das aufgrund der zahlreichen Vorteile dieses Wissenschaftszweiges eine Vielzahl an Anwendungsgebieten besitzt. Im Rahmen dieser Arbeit wurden nahezu alle untersuchten Materialien mechanochemisch durch Mahlen in einer Hochenergiiekugelmühle hergestellt, mit dem Ziel neue Materialien mit maßgeschneiderten Eigenschaften zu synthetisieren beziehungsweise bereits vorhandene zu modifizieren.^{15-17, 19}

2.2.1 Mechanochemische Synthese

Ein großer Pluspunkt der mechanochemischen Synthese ist die Möglichkeit, neue nanokristalline Materialien herzustellen, die über konventionelle Herstellungs Routen wie etwa

die nasschemische Synthese oder die Hochtemperatursynthese nicht zugänglich wären.^{15, 16} Zu diesen Verbindungen zählen zum Beispiel amorphe Phasen, die bei höheren Temperaturen kristallisieren würden²⁰, oder metastabile Nichtgleichgewichtsphasen, die eine andere Struktur aufweisen als ihre thermodynamisch stabilere Modifikation.^{21, 22} Mechanochemie stellt also eine einfache und sehr vielseitige Möglichkeit zur Probenpräparation dar, die schon bei geringen Temperaturen erfolgreich abläuft.¹⁵⁻¹⁷

Die mechanischen Belastungen, denen die Materialien während des Prozesses ausgesetzt sind, können mehrere Auswirkungen haben: (i) Zum einen ein Verringern der Partikelgröße in den nanokristallinen Bereich bei gleichzeitiger Veränderung der Defektstruktur ohne den Ablauf einer chemischen Reaktion. (ii) Zum anderen die Veränderung der kristallchemischen Struktur mit Hilfe einer chemischen Reaktion, also durch ausbilden oder aufbrechen von chemischen Bindungen. Der erste Aspekt beschreibt strukturelle Veränderungen in dem Material, die sowohl makroskopischer als auch mikroskopischer Natur sein können. Durch Scher-, Reibungs- oder Aufprallkräfte erfolgt eine Abreibung beziehungsweise ein Bruch der einzelnen Kristallite in kleinere Nanoteilchen (< 50 nm). Das führt einerseits zu einem größeren Volumenanteil an strukturell ungeordneten Grenzflächen, andererseits werden durch die mechanische Belastung auch bulk-Regionen in den Materialien verändert, indem unterschiedliche Arten von Defekten (siehe Abschnitt 2.1.4) im bulk-Anteil der Kristalle generiert werden. Der zweite wichtige Aspekt der Mechanochemie veranschaulicht die Möglichkeit der direkten Umwandlung von Edukten in die gewünschten Produkte, ohne dabei weitere Prozess- oder Reinigungsschritte zu benötigen. Wie bereits zuvor erwähnt ist es so möglich, Materialien herzustellen, die über konventionelle Synthesemethoden nicht zugänglich sind. Obwohl eine Vielzahl an Modellen zum Ablauf der mechanochemischen Reaktionen in der Literatur zu finden ist, ist der genaue Reaktionsmechanismus noch nicht eindeutig definiert. Die bekanntesten Theorien in diesem Zusammenhang sind die Hot-Spot Theorie und das Magma-Plasma Modell. Beide schlagen eine kurzzeitige, extreme Temperaturerhöhung am Punkt der mechanischen Belastung vor, die ausreichend hohe Energien für einen erfolgreichen Prozess zur Verfügung stellt. Durchgeführt werden mechanochemische Synthesen durch Mahlen in Hochenergie-Mühlen, wie zum Beispiel der Vibrationsmühle, der Planetenmühle oder der Mixer-Mühle. Da im Rahmen dieser Arbeit ausschließlich eine Planetenmühle verwendet wurde, wird im folgenden Abschnitt auf die Funktionsweise dieser Technik detaillierter eingegangen.^{15-17, 23, 24}

2.2.2 Hochenergie-Kugelmahlen in einer Planetenmühle

Bei dieser mechanochemischen Synthesemethode werden zwei Mahlbecher mit Mahlkugeln sowie den jeweiligen Materialien gefüllt und anschließend verschlossen. Die Mahlwerkzeuge bestehen dabei aus sehr beständigen, harten Verbindungen wie Zirkoniumdioxid oder Wolframcarbid, die für einen Einsatz unter dem Einfluss hoher mechanischer Kräfte geeignet sind. Die beiden Becher werden gegenüberliegend auf einer Trägerplatte fixiert, wie in Abbildung 5 dargestellt, und beginnen sich entgegen der Rotationsrichtung der Platte zu drehen. Durch die entgegengesetzte Drehbewegung von Trägerscheibe und Bechern entsteht eine planetenähnliche Bewegung, die für die Namensgebung dieser Technik verantwortlich ist. Die dabei entstehenden Zentrifugalkräfte wirken abwechselnd in gleiche oder entgegengesetzte Richtungen, was einerseits zu Reibungs- und Scherkräften bei der Rotation der Mahlkugeln entlang der Becherwände führt, andererseits werden dadurch die Mahlkugeln quer durch die Becher geschleudert und prallen auf der anderen Seite mit sehr hoher Energie gegen die Kristallite. Die hier durch mechanische Behandlung entstehende Energie ist groß genug, um die Materialien zu zerkleinern, Defekte einzubringen und chemische Reaktionen zu ermöglichen. Abhängig von dem jeweiligen Material und den gewünschten Endprodukten können verschiedenste Einstellungen für den Mahlvorgang getroffen werden. Wichtige Parameter, die hier modifiziert werden können, sind zum Beispiel die Umdrehungsgeschwindigkeit, die Anzahl der Mahlkugeln oder die Masse der verwendeten Materialien.^{15-17, 19, 25}

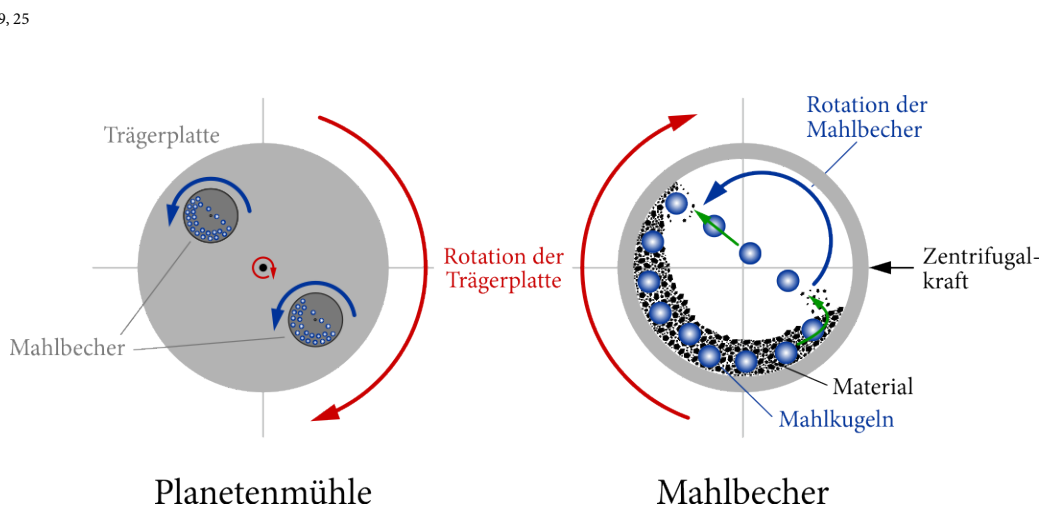


Abbildung 5: Aufbau einer Planetenmühle mit dazugehörigen Mahlbechern. Die roten und blauen Pfeile deuten die entgegengesetzte Drehrichtung von Trägerplatte und Bechern an. Die Abbildung wurde adaptiert von Referenz [17] und [26].

2.2.3 Nanostrukturierte Materialien

Die Eigenschaften eines jeden Festkörpers werden stark von der Modifikation seiner Teilchen beeinflusst. In fast allen Fällen führt eine mechanochemische Synthese in einer Planetenmühle zu Modifikationen mit sehr kleinen Partikelgrößen. Die für diese Arbeit wichtigsten Strukturen sind nanokristalline und amorphe Festkörper, welche im folgenden Abschnitt genauer beschrieben werden.

Nanokristalline Materialien: Aufgrund ihrer veränderten Struktur beziehungsweise Dimension weisen nanokristalline Materialien oftmals grundlegend verschiedene Eigenschaften auf als ihre mikrokristallinen Analoga. Die gezielte Modifikation der mikrokristallinen Festkörper hin zu maßgeschneiderten nanokristallinen Materialien mit neuen mechanischen, elektrischen, magnetischen, optischen oder thermodynamischen Eigenschaften ist daher aktuell von großer Bedeutung für Forschungen im Bereich der Materialwissenschaften und der Festkörperchemie. Allgemein sind nanokristalline Verbindungen polykristalline Festkörper, die aus Kristalliten bestehen, die in allen drei Dimensionen eine Längenausdehnung im Nanometerbereich aufweisen. Sie sind zum einen aus willkürlich orientierten Kristallen mit einer durchschnittlichen Korngröße von 5 – 50 nm aufgebaut, zum anderen enthalten sie einen sehr großen Volumenanteil (bis zu 50 %) an Korngrenzen und Grenzflächen.

In Abbildung 6 a) sind die Grenzflächenatome als unausgefüllte Kreise dargestellt, die Atome der geordneten Kristalle als schwarze Kugeln. Da sowohl Teilchen in strukturell geordneten Kristallen als auch ungeordnete Grenzflächen vorhanden sind, spricht man hierbei von heterogener Unordnung. Für die Synthese dieser Materialien gibt es zwei Vorgehensweisen: den *bottom-up* oder den *top-down* Prozess. Bei dem *bottom-up* Prinzip werden die nanokristallinen Verbindungen von Grund auf aus ihren Atomen oder Molekülen aufgebaut. Dazu gehören Methoden wie die kolloidale Dispersion, die Edelgaskondensation, Sol-Gel-Synthesen oder elektrochemische Abscheidungen. Bei *top-down* Verfahren wird von den grobkörnigen Ausgangsmaterialien ausgegangen, bei denen die Kristallitgröße durch Zerkleinerung verringert wird. Hierzu zählen die Lithographie oder das Kugelmahlen.²⁷⁻²⁹

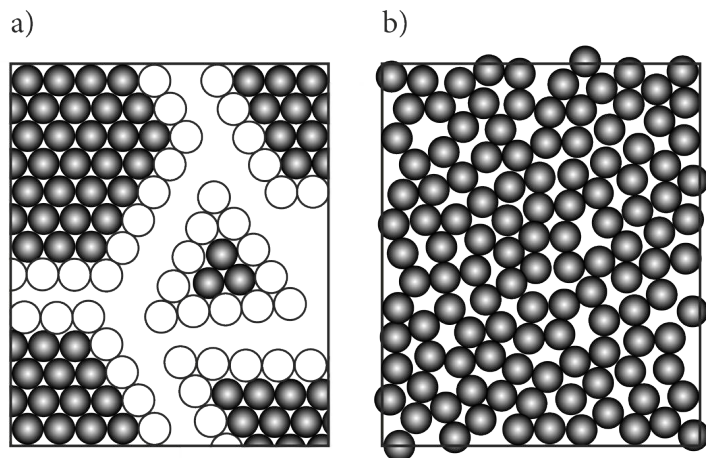


Abbildung 6: Grafische Darstellung nanostrukturierter Festkörper gemäß Referenz [27].
a) Nanokristallines Material b) Amorphes Material

Nanomaterialien besitzen aktuell ein sehr breites Anwendungsgebiet, im Speziellen in der Forschung an modernen Energiespeichersystemen spielen sie als Festkörperelektrolyte oder Elektrodenmaterialien eine wichtige Rolle. Zum Beispiel ist LiFePO₄, welches ein bekanntes Aktivmaterial in Kathoden von Lithium-Ionen-Batterien ist, in mikrokristalliner Form ein schlechter Ionenleiter mit langsamem Li⁺-Insertionsraten, weist allerdings in seiner defektreichen nanokristallinen Modifikation sehr gute Raten auf.³⁰ Weitere Beispiele wären Li₂O:Al₂O₃ oder LiBH₄:Al₂O₃ Komposite, die durch Nanostrukturierung schnelle Li⁺-Diffusionspfade entlang der Grenzflächen ausbilden.^{31,32} In Li₂O:Al₂O₃-Kompositen werden so genannte Raumladungszoneneffekte erwartet, wie von Maier³³ publiziert, die ebenfalls zur Erhöhung der Li-Diffusion beitragen.

Amorphe Materialien: Festkörper, die eine Nahordnung aber keine Fernordnung mehr aufweisen, werden als amorphe Materialien bezeichnet. Sie besitzen ein höheres Maß an Fehlordnungen im Vergleich zu nanokristallinen Verbindungen, wobei die interatomaren Abstände und die Koordinationszahlen für alle Atome gleich sind. Man spricht in diesem Fall von einer homogenen Unordnung. Häufig werden amorphe Phasen durch schnelles Abkühlen von Schmelzen erzeugt, wie zum Beispiel bei der Glasherstellung. Unter bestimmten Mahlbedingungen können sich aber auch bei mechanochemischen Synthesen in einer Hochenergie-Kugelmühle amorphe Phasen bilden, die durch Temperaturbehandlung wieder kristallisieren würden.^{27, 34} Beispiele für die Entstehung von amorphem Material bei

mechanochemische Reaktionen sind die BaMgF₄ Synthese, wie sie in der Arbeit von Preishuber-Pflügl und Wilkening³⁵ gezeigt wurde oder die Herstellung von LiAlO₂, wie sie von Wohlmuth *et al.*²⁰ erläutert wurde.

2.3 Röntgenkristallstrukturanalyse

Röntgenbeugungsuntersuchungen werden seit vielen Jahren eingesetzt, um strukturelle Eigenschaften von kristallinen oder amorphen Materialien im atomaren Maßstab zu untersuchen. Die Grundlage für alle röntgenographischen Analysen an Kristallen stellt der 1912 von Max von Laue postulierte Beugungseffekt dar. Dieser besagt, dass Röntgenstrahlen an einem Kristallgitter gebeugt werden können, da die Wellenlänge der Röntgenstrahlung und die Gitterkonstanten der Kristalle dieselbe Größenordnung aufweisen.

Trifft Röntgenstrahlung in einem bestimmten Winkel auf eine Materie auf, wird die Strahlung gestreut. Erfolgt diese Streuung unter Beibehaltung der Wellenlänge und sind die Streuzentren in nicht willkürlichen Abständen voneinander getrennt, kommt es zu Interferenzen und damit zu gebeugten Wellen mit – abhängig vom Winkel – höherer oder niedrigerer Intensität. Die Analyse des entstandenen Beugungsmusters ermöglicht anschließend eine Aussage über die Struktur des untersuchten Materials zu treffen.^{12, 36, 37}

2.3.1 Die Braggsche Gleichung

Die Braggsche Gleichung beschreibt das Auftreten von konstruktiver Interferenz bei der Streuung von Wellen an einem dreidimensionalen Gitter. Die Beugung an Materie kann dabei auch als Reflexion der Röntgenstrahlen an Netzebenenscharen betrachtet werden. Trifft ein paralleler monochromatischer Röntgenstrahl unter einem bestimmten Winkel θ auf eine Netzebenenschar, die aus parallelen im gleichen Abstand d_{hkl} angeordneten Ebenen besteht, kommt es zu einer Streuung und sofern die Strahlen in Phase sind, zu einer konstruktiven Interferenz. Ein Interferenzmaximum ist also nur dann zu erkennen, wenn die Ordnung der Interferenz n ein ganzzahliges Vielfaches der Wellenlänge λ ist. Aus diesen Einschränkungen lässt sich die Braggsche Gleichung

$$n \lambda = 2 d \sin \theta \quad (2.13)$$

definieren, die in Abbildung 7 grafisch dargestellt ist.^{12,38}

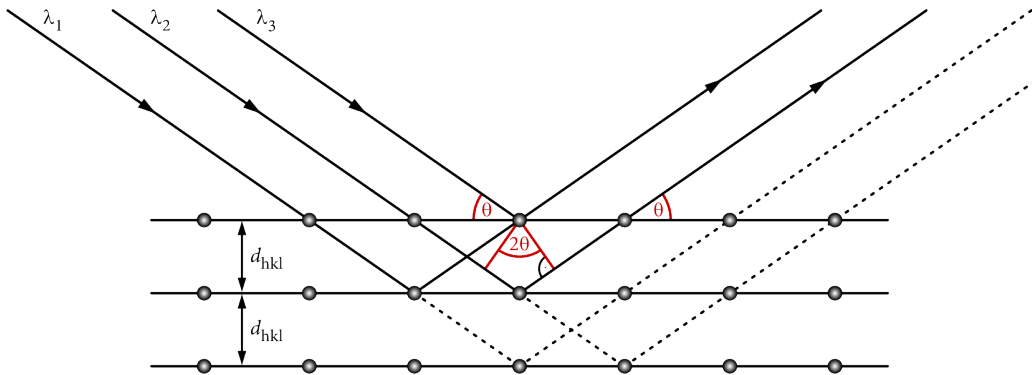


Abbildung 7: Streuung von monochromatischer Röntgenstrahlung an einer Netzebenenschar, die aus parallel angeordneten Ebenen besteht (Illustration nach Referenz [12] und [38]).

2.3.2 Das Debye-Scherrer-Verfahren

Für die strukturelle Analyse der im Rahmen dieser Arbeit hergestellten Proben wurden hauptsächlich Pulverdiffraktogramme nach dem Debye-Scherrer-Prinzip aufgenommen. Dafür werden die kristallinen Pulverproben mit monochromatischer Röntgenstrahlung beschossen. Aufgrund der statistischen Verteilung der Kristalle im Pulver befinden sich für jede Netzebenenschar zahlreiche Kristallite in Reflexionsstellung und sind somit in der Lage, die Strahlen zu reflektieren. Für die gebeugten Strahlen, die auf einem Kegelmantel liegen, ergibt sich ein Öffnungswinkel von 4θ . Eine Pulverprobe emittiert dementsprechend also Strahlung in Form von koaxialen Reflexionskegeln. Zur Aufzeichnung der Beugungslinien wird bei diesem Diffraktionsverfahren eine Kamera verwendet, die aus einem metallischen Kreiszylinder mit einem fotografischen Film an seiner Innenseite besteht. Der Röntgenstrahl steht dabei senkrecht zur Zylinderachse. Die entstehenden Reflexionskegeln schneiden den fotografischen Film in so genannte Debye-Scherrer-Linien und führen zu einem charakteristischen Pulverdiagramm, bei dem die durch konstruktive Interferenz bei bestimmten Winkeln auftretenden Intensitäten gegen 2θ aufgetragen werden. Der Winkel zwischen zwei vom selben Beugungskegel stammenden Linien beträgt $4\theta r$, wobei r den Radius der Kamera darstellt. Mit Hilfe der Braggschen Gleichung ist es in der Folge möglich, den Netzebenenabstand d_{hkl} über die Wellenlänge λ und den Winkel θ zu bestimmen. Für eine

vollständige Aufklärung der unbekannten Struktur ist zusätzlich noch die Ermittlung der einzelnen Gitterparameter a_0 , b_0 , und c_0 sowie der Millerschen Indizes (hkl) essentiell.^{12, 38}

An dieser Stelle sei für ein besseres Verständnis noch ein kurzer Exkurs zur Beziehung zwischen dem Netzebenenabstand und den Millerschen Indizes vonnöten:

Millersche Indizes sind als kleinste ganzzahlige Vielfache der reziproken Achsenabschnitte definiert und beschreiben die dem Ursprung am nächsten gelegene Gitterebene. Die Lage einer Ebene, welche die Achsen x, y und z schneidet, wird durch die Punkte (m00), (0n0) und (00p) eindeutig festgelegt. Angegeben werden diese Achsenabschnitte in Form von reziproken Werten entweder in der Form

$$h = \frac{1}{m} \quad (2.14)$$

$$k = \frac{1}{n} \quad (2.15)$$

$$l = \frac{1}{p} \quad (2.16)$$

oder zusammengefasst als Tripel (hkl). Wichtig zu beachten ist dabei, dass die Indizes nicht nur eine einzige Ebene beschreiben, sondern die Position einer unendlichen Anzahl von parallelen Gitterebenen mit jeweils demselben Abstand d voneinander angeben.¹²

Aus dem ermittelten Netzebenenabstand kann für ein orthorhombrisches System über

$$d_{hkl} = \frac{1}{\sqrt{\frac{h^2}{a_0^2} + \frac{k^2}{b_0^2} + \frac{l^2}{c_0^2}}} \quad (2.17)$$

ein Bezug zu den Gitterparametern und den Millerschen Indizes hergestellt werden. Diese Gleichung vereinfacht sich im kubischen Kristallsystem zu

$$d_{hkl} = \frac{a_0}{\sqrt{h^2 + k^2 + l^2}} \quad (2.18)$$

Integriert man anschließend die Netzebenenabstandsgleichung (2.18) in das Braggsche Gesetz (2.13), wird für das kubische System

$$\sin^2 \theta = \frac{\lambda^2}{4a_0^2} (h^2 + k^2 + l^2) \quad (2.19)$$

erhalten, mit $\lambda^2 / 4a_0^2$ als konstantem Faktor und $(h^2 + k^2 + l^2)$ als positivem ganzzahligen Wert. Insgesamt ist dieses Strukturanalyseverfahren von großer Bedeutung für die Identifizierung von kristallinen Festkörpern. Jede Probe besitzt ein nur für sie charakteristisches Pulverdiffraktogramm mit einer spezifischen Abfolge an Linien, die bei verschiedenen Winkeln und mit unterschiedlichen Intensitäten auftreten. Zur Identifizierung wird das Muster der unbekannten Struktur mit bekannten Daten, die in verschiedensten Datenbanken gesammelt vorliegen, verglichen.^{12, 38}

2.3.3 Kristallitgrößenbestimmung – Die Scherrer-Formel

Einen wichtigen Parameter zur Charakterisierung kristalliner Festkörper stellt die Kristallitgröße dar, die mit Hilfe der Scherrer-Formel (2.20) aus den Daten der Röntgenstrukturanalyse bestimmt werden kann. Entscheidend hierfür ist die Reflexverbreiterung im Diffraktogramm für Proben mit geringeren Partikelgrößen, die dadurch zustande kommt, dass weniger parallele Netzebenen in Reflexionsstellung zur Verfügung stehen. Zur Berechnung der mittleren Kristallitgröße $\langle d \rangle$ ist es wichtig, zuerst die vom Messgerät stammenden Verbreiterungseffekte zu eliminieren. Dazu wird die Halbwertsbreite des Reflexes eines meist mikrokristallinen Referenzmaterials $\beta_{g(\theta)}$ ermittelt und von dem Wert des betreffenden Materials $\beta_{f(\theta)}$ subtrahiert, was zu einer nur von der Probe selbst verursachten Halbwertsbreite $\beta_{f(\theta)}$ führt. Unter Berücksichtigung dieser Information kann anschließend die Scherrer-Formel³⁹

$$\langle \langle d \rangle \rangle = \frac{K \lambda_{XRD} 360^\circ}{2\pi \beta_{f(\theta, hkl)} [\circ 2\theta] \cos \theta} \quad (2.20)$$

angewendet werden. K stellt dabei einen geometrischen Faktor dar (0.89 bei Annahme von sphärischen Kristalliten), λ_{XRD} die Wellenlänge und θ den Einfallswinkel der Röntgenstrahlung.⁴⁰⁻⁴²

Eine weitere wichtige Quelle der Reflexverbreiterung sind Verzerrungen und Deformationen in Materialien. Mechanische Belastungen, wie sie etwa durch Mahlen in einer Hochenergie-Kugelmühle eingebracht werden können, führen zu plastischen Verformungen

und damit zu Verspannungen in den Proben. Die Gitterverspannung ε , die über folgende Gleichung berechnet werden kann:

$$\varepsilon = \frac{d_{\text{hkl}} - d_{\text{hkl},0}}{d_{\text{hkl},0}} \quad (2.21)$$

beschreibt eine lokale Veränderung des Netzebenenabstandes, die sich durch strukturelle Unordnungen ergibt. Bei den beiden Größen d_{hkl} und $d_{\text{hkl},0}$ handelt es sich um die Netzebenenabstände in dem verspannten und dem nicht verspannten System.^{41, 43}

Zuletzt stellt die Methode nach Williamson und Hall⁴⁴ (Formel (2.22)) eine Möglichkeit dar, die Beziehung zwischen der mittleren Kristallitgröße und der Gitterverspannung in einem Zusammenhang darzustellen:

$$\frac{\beta_{f(\theta, \text{hkl})} \cos \theta}{\lambda_{\text{XRD}}} = 4\varepsilon \frac{\sin \theta}{\lambda} + \frac{1}{\langle d \rangle} \quad (2.22)$$

2.4 Impedanzspektroskopie

Impedanz- oder Leitfähigkeitsspektroskopie ist eine relativ neue und sehr weit verbreitete analytische Methode im Bereich der Materialwissenschaften. Sie liefert Informationen über die Dynamik von mobilen Ladungsträgern in Festkörpern und ermöglicht die Bestimmung der Diffusionsparameter. Grundlage ist dabei die Interaktion von elektromagnetischen Wellen mit Materie in einem Frequenzbereich von 10^{-6} bis 10^{12} Hz. Der Begriff Impedanz steht in diesem Zusammenhang für einen komplexen Widerstand, der aus dem Verhältnis einer komplexen Wechselspannung, die an eine Probe angelegt wird, und eines resultierenden komplexen Wechselstromes, welcher gemessen werden kann, ermittelt wird. Aus den sich ergebenden frequenzabhängigen Daten können anschließend verschiedenste Informationen und Kenngrößen in Bezug auf die Festkörperdiffusion abgeleitet werden. Im folgenden Kapitel wird detailliert auf diese Analysenmethode eingegangen, die eine essentielle Rolle für die Charakterisierung der im Rahmen dieser Arbeit betrachteten Proben gespielt hat.⁴⁵⁻⁴⁷ Weiterführende Literatur zu diesem Thema ist zusätzlich noch in den Referenzen [45], [46] und [48] zu finden.

2.4.1 Das Prinzip der Impedanzspektroskopie

Die Impedanzspektroskopie basiert grundsätzlich auf zwei Konzepten. Zum einen dem Ohmschen Gesetz, das den Widerstand eines elektrischen Schaltelements wie folgt beschreibt:

$$R = \frac{U}{I} \quad (2.23)$$

R ist dabei der Widerstand, also ein Maß für die Fähigkeit eines Systems sich dem Fluss von elektrischem Strom zu widersetzen. U repräsentiert die Spannung und I den Strom. Anzuwenden ist das Ohmsche Gesetz allerdings nur für ideale Widerstände, für die das Gesetz bei allen Stromstärken, Spannungen und Wechselstromfrequenzen gültig ist. Spannungs- und Stromsignal sind hierbei gleichphasig. Nimmt man ein ideal homogenes Material an, das das Volumen zwischen zwei Elektroden komplett ausfüllt und eine definierte Grundfläche A sowie einen definierten Elektrodenabstand d besitzt, wird der Widerstand als

$$R = \rho \frac{d}{A} \quad (2.24)$$

definiert, mit ρ als charakteristischem Widerstand des Materials. Der inverse Widerstand $1/R$ wird auch als Leitfähigkeit σ mit der Einheit S/cm bezeichnet und spiegelt die Fähigkeit eines Materials wider, elektrischen Strom zwischen zwei Elektroden zu leiten.^{46, 48}

Ein idealer Kondensator ist im Gegensatz dazu ein Schaltelement, das keinen elektrischen Strom leitet allerdings Energie in Form von Ladungsträgern an den Elektroden speichern kann, wenn zwischen ihnen ein dielektrisches Material platziert ist. Hierbei sind Spannungs- und Stromsignal phasenverschoben, wobei der Strom der Spannung nachfolgt. Eine wichtige Kenngröße für die Fähigkeit eines Kondensators, Energie zu speichern, ist die Kapazität, die über die Beziehung

$$C = \frac{\epsilon_0 \epsilon A}{d} \quad (2.25)$$

ausgedrückt werden kann. C ist dabei die Kapazität in der Einheit Farad, die abhängig ist von der relativen Permittivität ϵ , der Fläche der Elektroden A , dem Abstand der Elektroden d und einer Konstanten, der Permittivität des Vakuums ϵ_0 .⁴⁶

Die komplexe Impedanz Z^* , die aus einem Realteil Z' und einem Imaginärteil Z'' besteht, vereint die beiden Konzepte von Widerstand und Kondensator. Der Realteil der Impedanz

reflektiert dabei den Widerstand eines Systems gegen den Fluss von elektrischem Strom, der Imaginärteil die Fähigkeit eines Systems elektrische Energie zu speichern. Bei der Messung (siehe Abbildung 8 a)) wird ein monochromatisches, sinusförmiges Spannungssignal der Form

$$U(t) = U_0 \sin(\omega t) \quad (2.26)$$

angelegt, mit U_0 als der Amplitude und einer Frequenz von $\nu = \omega / 2\pi$. Der resultierende Strom, der aufgezeichnet wird, ist ebenfalls wieder sinusförmig und besitzt dieselbe Frequenz, weist jedoch eine Phasenverschiebung φ und eine andere Amplitude I_0 auf (siehe Abbildung 8 b)):

$$I(t) = I_0 \sin(\omega t + \varphi) \quad (2.27)$$

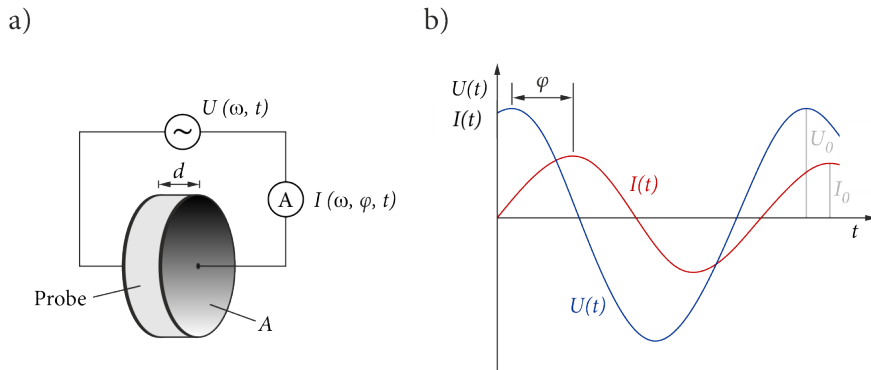


Abbildung 8: a) Vereinfachte schematische Darstellung eines Impedanzexperiments. Mit Hilfe eines Generators (\sim), der mit den Elektroden der Probe verbunden ist, wird ein Wechselstrom angelegt und der resultierende, phasenverschobene Strom mittels eines Amperemeters (A) aufgezeichnet. Das zu untersuchende Material ist dabei zwischen zwei Elektroden mit der Grundfläche A und einem Abstand von d positioniert. b) Illustration der sinusförmigen Wechselspannung $U(t)$ und des nachlaufenden, phasenverschobenen (φ) Wechselstromes $I(t)$. U_0 und I_0 geben die Amplitude der jeweiligen Funktion an. Die Abbildung wurde adaptiert von Referenz [46] und [48].

Wenn keine Phasenverschiebung auftritt, handelt es sich um einen idealen Widerstand und das Ohmsche Gesetz (2.23) kann angewendet werden. Da bei dielektrischen Materialien allerdings immer eine Phasenverschiebung zu finden ist, muss hierbei die Formel für einen

komplexen Widerstand, sprich die Impedanz, verwendet werden, die analog zum Ohmschen Gesetz wie folgt berechnet werden kann:

$$Z^* = \frac{U(t)}{I(t)} = \frac{U_0 \sin(\omega t)}{I_0 \sin(\omega t + \varphi)} = |Z| \frac{\sin(\omega t)}{\sin(\omega t + \varphi)} \quad (2.28)$$

Die Impedanz setzt sich also aus einem Betrag $|Z|$ und der Phasenverschiebung φ zusammen. Für eine einfachere Behandlung der zeitabhängigen Größen ist es von Vorteil für die weitere mathematische Beschreibung des komplexen Widerstandes in die komplexe Zahlenebene zu wechseln. Über die Eulersche Formel

$$\exp(i\varphi) = \cos(\varphi) + i \sin(\varphi) \quad (2.29)$$

mit $i = \sqrt{-1}$ kann ein Zusammenhang zwischen Real- und Imaginärteil hergestellt werden, wodurch sich Gleichungen (2.26) und (2.27) zu

$$U^*(t) = U_0 \exp(i\omega t) \quad (2.30)$$

beziehungsweise

$$I^*(t) = I_0 \exp(i(\omega t - \varphi)) \quad (2.31)$$

verändern, mit $U^*(t)$ und $I^*(t)$ als komplexen Zahlen. Die Impedanz formt sich dann angelehnt an Gleichung (2.28) zu

$$Z^* = \frac{U^*(t)}{I^*(t)} = \frac{U_0 \exp(i\omega t)}{I_0 \exp(i(\omega t - \varphi))} = |Z^*| \exp(i\varphi) = |Z^*| (\cos \varphi + i \sin \varphi) = Z' + iZ'' \quad (2.32)$$

um. Sie kann als Vektor in einer komplexen Zahlenebene angesehen werden, mit Z' und Z'' als den kartesischen Koordinaten und $|Z^*|$ beziehungsweise φ als den Polarkoordinaten (siehe Abbildung 9)^{45, 46, 48}.

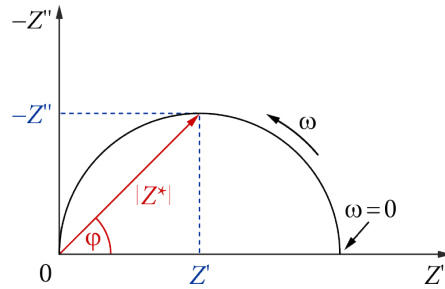


Abbildung 9: Nyquist-Auftragung der Impedanzdaten in einer komplexen Zahlebene, bei der der Realteil der Impedanz gegen den negativen Imaginärteil aufgetragen wird. Die Darstellung von Z^* kann sowohl in kartesischen (Z', Z'') als auch in polaren Koordinaten ($|Z^*|, \varphi$) erfolgen. ω stellt die radiale Frequenz dar, die in Richtung des Ursprungs ansteigt. Abbildung gemäß Referenz [45] und [46].

Wie anhand von Gleichung (2.32) und Abbildung 9 deutlich wird, gilt daher⁴⁵:

$$|Z^*| = \sqrt{(Z')^2 + (Z'')^2} \quad (2.33)$$

$$\varphi = \arctan(Z''/Z') \quad (2.34)$$

2.4.2 Weitere grundlegende Funktionen

Neben der Impedanzfunktion sind für dieses Spektroskopieverfahren noch viele weitere verwandte Basisfunktionen von Bedeutung, die alle unter den Überbegriff „Immitanzen“ fallen. Die wichtigsten sind im folgenden Abschnitt zusammengefasst.

Der Kehrwert der Impedanz wird als Admittanz Y^* bezeichnet,

$$Y^* = Z^{*-1} = |Z^*|^{-1} \exp(-i\varphi) = Y' + iY'' \quad (2.35)$$

und kann ebenfalls in Real- und Imaginärteil aufgetrennt werden.⁴⁵

Dielektrische Analysen liefern zwei wichtige Größen, die Permittivität ϵ und die Leitfähigkeit σ , jeweils als Funktion der Zeit, Temperatur und der radialem Frequenz. Die dielektrische Permittivität kann dabei analog zu (2.32) und (2.35) notiert werden:

$$\epsilon^* = \epsilon' - i\epsilon'' = \frac{Y^*}{i\omega C_0} \quad (2.36)$$

C_0 entspricht hierbei der Kapazität einer leeren Messzelle, die über

$$C_0 = \frac{\epsilon_0 A}{d} \quad (2.37)$$

berechnet werden kann, wiederum mit der Elektrodenfläche A , dem Elektrodenabstand d und der Permittivität des Vakuums ϵ_0 . Wie auch die Impedanz besteht die komplexe Permittivität aus einem Real- und einem Imaginärteil. Der Realteil ϵ' repräsentiert die Energiespeicher-Komponente und ist daher äquivalent zu $1 / Z'$. Der Imaginärteil ϵ'' , auch als Verlustfaktor bezeichnet, stellt den Term der Ionenleitung dar und ist dementsprechend äquivalent zu $1 / Z''$. ϵ' kann mittels einer umgeformten Version von Gleichung (2.25) -

$$\epsilon' = \frac{C d}{\epsilon_0 A} \quad (2.38)$$

- berechnet werden, ϵ'' mit Hilfe von Formel (2.39):

$$\epsilon'' = \frac{d}{RA\omega\epsilon_0} = \frac{1}{\rho\omega\epsilon_0} = \frac{\sigma}{\omega\epsilon_0} \quad (2.39)$$

Der Imaginärteil kann also über verschiedene Größen wie den Widerstand R , den spezifischen Widerstand ρ oder die Leitfähigkeit σ gewonnen werden.^{45, 46}

Sowohl der spezifische Widerstand als auch die Leitfähigkeit sind materialabhängige Größen, die stark von der Probengeometrie beeinflusst sind, wie in den folgenden Beziehungen deutlich wird:

$$\rho^* = Z^* \frac{A}{l} \quad (2.40)$$

$$\sigma^* = \sigma' + i\sigma'' = \frac{1}{\rho^*} = \frac{1}{Z^*} \frac{l}{A} = Y^* \frac{l}{A} \quad (2.41)$$

A und l repräsentieren dabei die Grundfläche und Dicke der Probe, stellen also den Term der Probengeometrie.

Die für diese Dissertation wohl wichtigste Größe, die aus impedanzspektroskopischen Messungen gewonnen werden kann, ist die dc-Leitfähigkeit σ_{DC} , die, sofern sie nur durch Ionenbewegung zustande kommt, vom Realteil der komplexen Leitfähigkeit abgeleitet werden kann^{9, 45, 48}.

Eine weitere Möglichkeit, die dielektrischen Eigenschaften einer vermessenen Probe darzustellen, bietet der komplexe Modulus M^* . Dieser ergibt sich aus dem Kehrwert der komplexen Permittivität, kann aber auch von der komplexen Impedanz abgeleitet werden⁴⁵:

$$M^* = M' - iM'' = i\omega C_0 Z^* = \frac{1}{\epsilon^*} \quad (2.42)$$

2.4.3 Leitfähigkeitsisothermen und Nyquist-Diagramme

Die mittels Impedanzspektroskopie erhaltenen Daten können auf unterschiedlichste Arten illustriert werden, wobei die – auch im Rahmen dieser Arbeit – gebräuchlichsten Methoden die Darstellungen der Leitfähigkeitsisothermen beziehungsweise der so genannten Nyquist-Diagramme sind.

Leitfähigkeitsspektren: Abbildung 10 zeigt eine Leitfähigkeitsisotherme mit ihren charakteristischen Bereichen in einem Spektrum, bei dem der Realteil der Leitfähigkeit σ' gegen die Frequenz ν in einer doppelt logarithmischen Form aufgetragen ist.

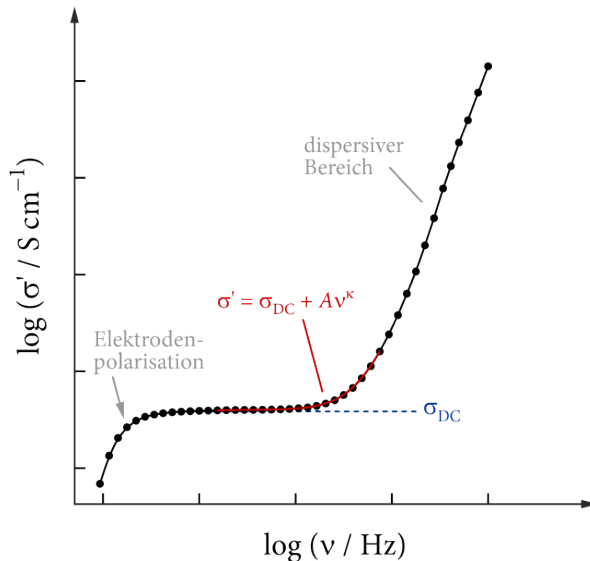


Abbildung 10: Darstellung einer Leitfähigkeitsisotherme mit ihren charakteristischen Regionen in einem standardmäßigen Frequenzbereich von wenigen Hertz bis zu einigen Megahertz. Genauere Informationen zu dieser Abbildung (gemäß Referenz [49]) sind im Text auf der nächsten Seite zu finden.

Die erste interessante Region, bei der eine Elektrodenpolarisation auftritt, ist bei niedrigen Frequenzen und ausreichend hohen Temperaturen zu finden. Hierbei kommt es durch die Verwendung von blockierenden Metallelektroden zur Akkumulation von Ionen an der Grenzfläche von Material und Elektrode, was zur Ausbildung von Raumladungszonen führt. Dadurch wird der weitere Ionentransport gehemmt und resultiert in einem deutlichen Abfall der Leitfähigkeit.⁴⁹

Betrachtet man die Isotherme bei etwas erhöhten Frequenzen, taucht ein frequenzunabhängiges Plateau σ_{DC} auf, das den langreichweiten Ionentransport durch das Material repräsentiert und sich bei steigenden Temperaturen zu höheren Frequenzen verschiebt. In Feststoffen zeigt das Produkt $\sigma_{DC}T$ meist Arrhenius-Verhalten und ermöglicht so die Berechnung einer Aktivierungsenergie E_A^{DC} für die langreichweite Ionendiffusion über die Beziehung $\sigma_{DC} T \propto \exp(-E_A^{DC} / k_B T)$, analog zu Gleichung (2.11).^{9, 50}

Werden die Frequenzen weiter erhöht, beginnt die Leitfähigkeit σ' erneut anzusteigen und wird wieder frequenzabhängig. Der Übergang von σ_{DC} in diesen Bereich kann mit einem Potenzgesetz nach Jonscher

$$\sigma' = \sigma_{DC} + A\nu^\kappa \quad (2.43)$$

detailliert beschrieben werden. A ist dabei der Dispersionsparameter, ν die Frequenz und κ die Steigung der Isotherme in diesem Abschnitt.⁵⁰⁻⁵²

Die Region bei den höchsten Frequenzen in der Isotherme von Abbildung 10 zeigt eine lineare Frequenzabhängigkeit der Leitfähigkeit und wird als dispersiver Bereich bezeichnet. Da mit steigenden Temperaturen die Temperaturabhängigkeit von σ' immer geringer wird, ergibt sich hier eine Proportionalität von $\sigma' \propto \nu$. Dieses bis heute noch nicht vollständig verstandene, beziehungsweise aufgeklärte lineare Verhalten, ist auch als NCL („*nearly constant loss*“) bekannt und lässt sich möglicherweise lokalen Bewegungen oder Relaxationen von nicht erfolgreichen Vorwärts- oder Rückwärtssprüngen zuordnen.^{49, 50, 52}

Bei extrem hohen Frequenzen im Gigahertz-Bereich, der allerdings in Abbildung 10 nicht mehr zu sehen ist, entsteht ein weiteres Plateau bei dem jeder Sprung zur Leitfähigkeit beiträgt. In Festkörpern ist dieses Hochfrequenzplateau jedoch größtenteils von Gitterschwingungen überlagert und daher sehr schwierig zu detektieren.^{49, 53}

Nyquist-Diagramme: Eine weit verbreitete Methode für die Darstellung der komplexen Impedanz ist die Visualisierung in einem Nyquist-Diagramm, bei dem der Realteil der Impedanz Z' gegen den negativen Imaginärteil $-Z''$ aufgetragen wird. Der resultierende Graph besteht aus einem oder mehreren Halbkreisen (vgl. Abbildung 9), wobei jeder davon zu einem elektrischen Phänomen im Material korrespondiert. Tragen in der Probe also mehrere unterschiedliche Prozesse zur Impedanz bei, wie etwa Elektrodenpolarisationseffekte oder verschiedene Diffusionsbeiträge (z.B. Bulk- beziehungsweise Korngrenzenleitfähigkeiten), entsteht ein Nyquist-Diagramm wie es in Abbildung 11 schematisch dargestellt ist.

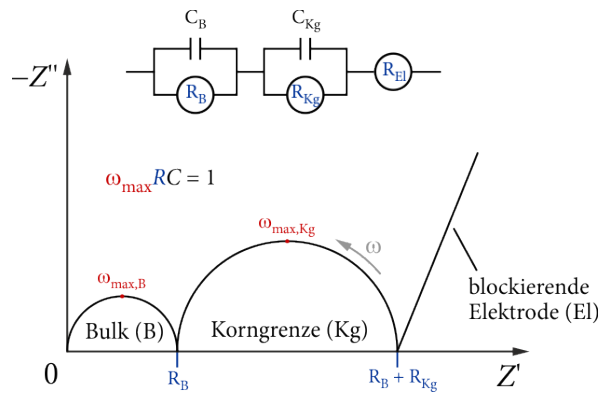


Abbildung 11: Schematische Darstellung der komplexen Impedanz einer keramischen Probe inklusive ihrem Ersatzschaltbild zur Interpretation der Daten. Die Abbildung wurde adaptiert von Referenz [54].

Bei sehr niedrigen Frequenzen, hier auf der rechten Seite zu sehen, wird eine stark ansteigende Gerade sichtbar, die von den blockierenden Metallelektroden stammt. In einem Ersatzschaltbild, wie in Abbildung 11 oben gezeigt, gleicht dieser Effekt einem Widerstand R_{El} . Geht man zu höheren Frequenzen, werden die unterschiedlichen Diffusionsphänomene sichtbar. Da die komplexe Impedanz sowohl Widerstands- als auch Kondensatorbeiträge aufweist, kann jeder Prozess mit einem Widerstand R und einer Kapazität C beschrieben werden. In einem Ersatzschaltbild entspricht jeder Diffusionsbeitrag einem parallel geschalteten RC -Element, das mit Hilfe der Gleichungen

$$\tau = RC \quad (2.44)$$

und

$$\omega_{\max} RC = 1 \quad (2.45)$$

charakterisiert werden kann. τ repräsentiert dabei die Relaxationszeit und ω_{\max} die radiale Frequenz bei maximalem Verlust des jeweiligen Phänomens, markiert durch die roten Punkte in Abbildung 11. Der Widerstand R kann aus den Schnittpunkten der Halbkreise mit der Abszisse extrahiert werden, respektive aus dem Realteil der Impedanz. Es ist somit also möglich, die Kapazitäten zu berechnen, verschiedene RC -Glieder zu identifizieren und diese anschließend den entsprechenden Regionen in der Probe zuzuordnen. Die Größenordnung der Kapazität gibt dabei Aufschluss über den jeweiligen Prozess, wie von Irvine *et al.*⁵⁴ im Jahr 1990 detailliert beschrieben wurde. Üblicherweise werden an den Elektroden oder bei Korngrenzen größere Kapazitäten erhalten als im Bulk.^{26, 54}

2.4.4 Der Ladungsdiffusionskoeffizient

Der Ladungsdiffusionskoeffizient D^σ ist eng verknüpft mit der aus der Impedanzspektroskopie gewonnenen DC-Leitfähigkeit und wird daher auch als Leitfähigkeitskoeffizient bezeichnet. Er kann über die Nernst-Einstein Beziehung

$$D^\sigma = \frac{\sigma_{DC} k_B T}{N q^2} \quad (2.46)$$

berechnet werden, bei der N die Ladungsträgerdichte und q die Ladung der Ionen darstellt. Wichtig zu beachten ist hierbei, dass D^σ , obwohl er die Dimension eines Diffusionskoeffizienten besitzt, formal nicht gleich wie die Koeffizienten der Fick'schen Gesetze interpretiert werden kann. Trotzdem ist es üblich, den Ladungsdiffusionskoeffizienten mit dem Tracerdiffusionskoeffizienten D^{tr} durch Einführung des Haven-Verhältnisses H_R in Verbindung zu setzen:

$$H_R = \frac{D^{tr}}{D^\sigma} \quad (2.47)$$

Das Haven-Verhältnis ist ein Maß für Korrelationseffekte und gibt Aufschluss, ob die Leitfähigkeit auf einer Ladungsträgerspezies beruht oder auf einer Überlagerung mehrerer verschiedener Beiträge. Für den Idealfall von willkürlichen Sprüngen einer einzigen Spezies

von Ionen ergibt sich $H_R = f = 1$, was wiederum zu $D^{\text{tr}} = D^\sigma = D^{\text{sd}}$ führt. Wird für H_R ein Wert kleiner als 1 erhalten, deutet das auf Korrelationen in der Bewegung der Ladungsträger oder auf das Vorhandensein von elektronischer Leitfähigkeit hin. Sind Leerstellenpaare, die mittels Leitfähigkeitsmessungen nicht erfasst werden können, am Diffusionsprozess beteiligt, werden für das Haven-Verhältnis Werte bestimmt, die größer als 1 sind.^{9, 10, 13}

2.5 Festkörper Kernspinresonanzspektroskopie (NMR)

Kernspinresonanz ist ein Phänomen, das in der heutigen Zeit einen integralen Bestandteil in verschiedensten Wissenschaftsrichtungen wie zum Beispiel der Physik, Chemie, Medizin oder der Materialwissenschaften darstellt. Die Messung beruht auf einer magnetischen Kernresonanz, also einer resonanten Wechselwirkung zwischen dem magnetischen Moment des Atomkerns einer Probe, die sich in einem starken Magnetfeld befindet, mit einem magnetischen Wechselfeld. Die NMR-Spektroskopie kann sowohl zur Strukturaufklärung also auch zur Untersuchung von Reaktionsmechanismen oder dynamischen Prozessen in Festkörpern verwendet werden. Im Rahmen dieser Arbeit wurde diese Methode gemeinsam mit der Impedanzspektroskopie genutzt, um zwischen langreichweitigem beziehungsweise kurzreichweitigem Ionentransport zu unterscheiden und so eine Beziehung zwischen den lokalen Strukturen und der Ionendynamik in den synthetisierten Proben herzustellen. Im folgenden Kapitel wird ein kurzer Überblick über die wichtigsten theoretischen Grundlagen der Festkörper Kernspinresonanzspektroskopie gegeben.⁵⁵⁻⁵⁸ Detailliertere Informationen zu diesem Thema können zusätzlich noch in den Referenzen [55], [56] und [57] nachgeschlagen werden.

2.5.1 Theoretische Grundlagen der NMR Spektroskopie

Ein für NMR Messungen geeignetes Material muss Atome mit bestimmten Eigenschaften enthalten, die vom Aufbau des Atomkerns abhängig sind. Jeder Kern besitzt einen so genannten Kernspin, der mit Hilfe einer Kernspinquantenzahl l beschrieben werden kann und über einen Drehimpuls \mathbf{I} verfügt (alle fett gedruckten Buchstaben im folgenden Kapitel repräsentieren Vektoren). Der Betrag des Drehimpulses kann anhand von Gleichung (2.48):

$$| I | = \sqrt{I(I+1)) \hbar} \quad (2.48)$$

quantifiziert werden, wobei \hbar die Planck-Konstante dividiert durch 2π darstellt. I kann dabei laut Definition nur diskrete Werte annehmen ($I = 0, 1/2, 1, 3/2, \dots$). Weist ein Kern einen Spin ungleich Null ($I \neq 0$) auf, so kann zusätzlich noch ein magnetisches Moment μ bestimmt werden, das parallel zu I ist:

$$\mu = \gamma I \quad (2.49)$$

Der Proportionalitätsfaktor γ entspricht einer kernspezifischen Konstante, die als gyromagnetisches Verhältnis bezeichnet wird. Alle Atomkerne, die ein magnetisches Moment $\mu \neq 0$ besitzen, können mittels NMR Spektroskopie detektiert werden und gelten somit als NMR aktiv.^{56, 58}

Wird das magnetische Moment einem externen Magnetfeld B_0 mit Ausrichtung entlang der z-Achse ausgesetzt, beginnt μ eine zeitabhängige Kreiselbewegung um diese Achse, die über

$$\mu \times B_0 = \frac{dI}{dt} \quad (2.50)$$

beschrieben werden kann. Durch Einsetzen von Gleichung (2.49) kann diese Beziehung zu

$$\mu \times B_0 = \frac{1}{\gamma} \frac{d\mu}{dt} \quad (2.51)$$

modifiziert werden. Die Kreisfrequenz ω_0 , mit der μ um die z-Achse rotiert, ist auch als Larmor-Frequenz bekannt:

$$\omega_0 = -\gamma B_0 \quad (2.52)$$

Sie liefert für jeden Kern, abhängig von der Größe des angelegten Magnetfeldes, charakteristische Werte. Durch die Ausrichtung der einzelnen Spins im externen Magnetfeld entsteht eine makroskopische Gesamtmagnetisierung M_0 , die sich aus der Summe der magnetischen Momente der einzelnen Atomkerne zusammensetzt und im thermodynamischen Gleichgewicht nur von der z-Komponente abhängig ist. In Abbildung 12 sind die eben erwähnten Größen in einem kartesischen Koordinatensystem dargestellt.^{9, 55, 57}

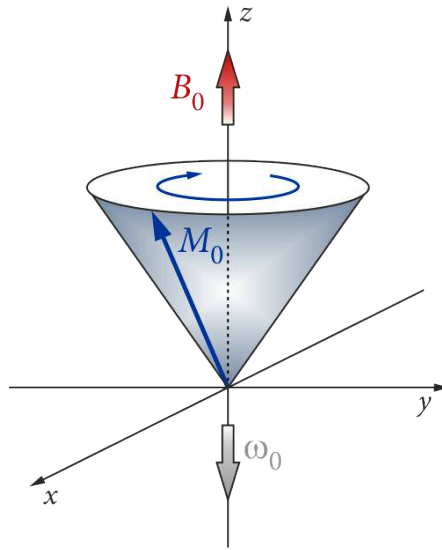


Abbildung 12: Schematische Darstellung der kreisförmigen Bewegungen des Gesamtmagnetisierungsvektors M_0 in einem externen Magnetfeld B_0 im thermodynamischen Gleichgewicht. ω_0 entspricht der Larmor-Frequenz. Die Abbildung wurde von Referenz [56] und [57] adaptiert.

Zusätzlich ist es möglich, jedem Kern in einem externen Magnetfeld eine magnetische Kernspinquantenzahl m_I zuzuordnen. Der Drehimpuls bekommt in dem Feld $B_0 = (0, 0, B_0)$ eine Orientierung, deren Komponente I_z via

$$I_z = m_I \hbar \quad \text{mit} \quad m_I = I, I-1, \dots, -I \quad (2.53)$$

quantifiziert werden kann. Gleichung (2.49) wird analog dazu zu

$$\mu_z = m_I \gamma \hbar \quad (2.54)$$

Ohne das Vorhandensein eines äußeren Magnetfeldes sind die Zustände m_I energetisch entartet. Im Gegensatz dazu sind in einem Magnetfeld für m_I und in weiterer Folge für I_z , $(2I + 1)$ unterschiedliche diskrete Orientierungen möglich, die analog zum Drehimpuls in $(2I + 1)$ unterschiedliche Zeeman-Energieniveaus aufgespalten werden können. Die Berechnung der entsprechende Energielevels der magnetische Dipole erfolgt über

$$E_m = -\mu_z B_0 = -m_I \gamma \hbar B_0 \quad (2.55)$$

Bei den beiden für diese Dissertation wichtigsten Atomkernen, ^7Li und ^{19}F , kommt es zu einer Aufspaltung in vier beziehungsweise zwei energetisch unterschiedliche Niveaus, wie in Abbildung 13 gezeigt ist.^{9,56}

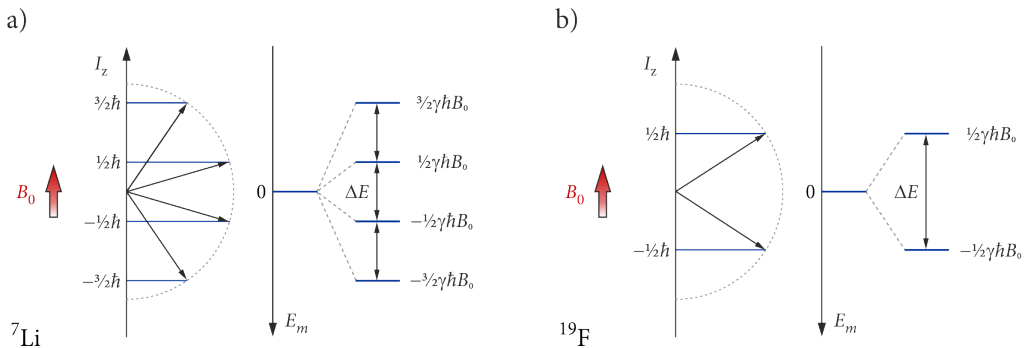


Abbildung 13: Illustration der Zeeman-Aufspaltung unterschiedlicher Kerne in einem externen Magnetfeld B_0 . I_z kann hier verschiedene Orientierungen annehmen, was zu unterschiedlichen abstandsgleichen Energieniveaus E_m führt. a) Darstellung für einen ^7Li Kern mit einem Spin von $I = 3/2$. b) Aufspaltung eines ^{19}F Kerns mit einem Spin von $I = 1/2$. Illustration gemäß Referenz [56].

Spinübergänge zwischen den einzelnen Zeeman-Niveaus sind, sofern die Bedingung $\Delta m_I = \pm 1$ erfüllt ist, erlaubt und erfolgen durch Anregung mit elektromagnetischen Wellen geeigneter Energie. Die dafür benötigte Energie ist abhängig von dem gyromagnetischen Verhältnis, dem externen Magnetfeld und der Frequenz:

$$\Delta E = \gamma \hbar B_0 = h \nu = \hbar \omega_0 \quad (2.56)$$

ν entspricht hierbei der Frequenz und ω_0 der Kreisfrequenz.

Die Verteilung auf die einzelnen Energieniveaus findet im thermodynamischen Gleichgewicht gemäß einer Boltzmann-Verteilung statt und ist temperaturabhängig. Für Kerne mit einem Spin von $I = 1/2$ würde die Besetzung eines niedrigeren Zeeman-Energieniveaus N_β und eines höheren N_α folgendermaßen aussehen:

$$\frac{N_\beta}{N_\alpha} = \exp\left(-\frac{\Delta E}{k_B T}\right) = \exp\left(-\frac{\gamma \hbar B_0}{k_B T}\right) \quad (2.57)$$

Die bereits weiter oben erwähnte makroskopische Gesamtmagnetisierung setzt sich aus der Summe N aller magnetischen Momente μ_i in einem definierten Probenvolumen V zusammen. Gleichung (2.51) kann dadurch zu

$$\frac{dM}{dt} = \gamma (M \times B_0) \quad (2.58)$$

verändert werden. Im thermodynamischen Gleichgewicht setzt sich M nur aus der Summe der z-Komponente zusammen, daher gilt: $M = M_0 = M_z$ und $M_x = M_y = 0$.

Ein letzter wichtiger Punkt ist an dieser Stelle noch die Einführung des rotierenden Koordinatensystems. Während einer NMR-Messung wird ein Radiofrequenzpuls (RF-Puls) angelegt, um die Spins aus ihrem relaxierten Zustand in einen angeregten Nicht-Gleichgewichtszustand zu bringen und so Spinübergänge herbeizuführen. Um die Zeitabhängigkeit dieses Radiofrequenzfeldes zu eliminieren, kann ein rotierendes Koordinatensystem um B_0 verwendet werden. In diesem führt der RF-Puls zu zwei entgegengesetzt rotierenden Feldern: einem, das sich in die entgegengesetzte Richtung der Magnetisierung M_0 bewegt und daher ignoriert werden kann, und einem, das stationär entlang der rotierenden x-Achse erscheint, hier als B_1 bezeichnet. Die beiden Felder führen zu einem effektiven Magnetfeld B_{eff} , das mit Hilfe von

$$B_{\text{eff}} = \frac{\omega}{\gamma} + B_1 \quad (2.59)$$

beschrieben werden kann und entlang dem sich die Magnetisierung im rotierenden Koordinatensystem bewegt.^{9,55-57}

2.5.2 Relaxationsmessungen

In einem externen Magnetfeld B_0 befinden sich alle Spins im thermodynamischen Gleichgewicht und sind entsprechend der Boltzmann-Verteilung in den verschiedenen Energieniveaus besetzt (siehe Abbildung 14). Wechseln bei einem NMR-Experiment die Spins durch Anlegen eines RF-Pulses in einen Nicht-Gleichgewichtszustand, startet umgehend danach die Relaxation zurück in den Gleichgewichtszustand.

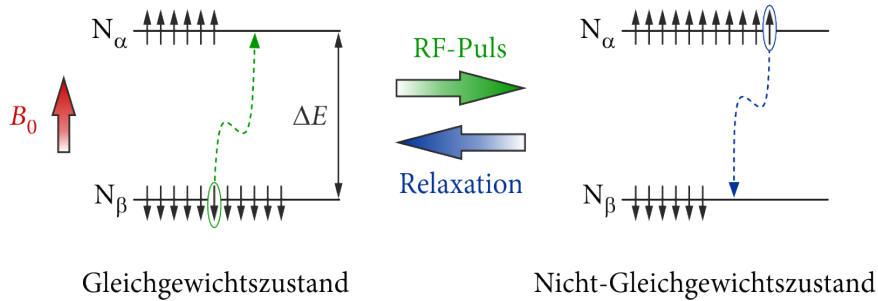


Abbildung 14: Schematische Darstellung der Zustände der Kernspins während einer Spin-Gitter-Relaxationsmessung. Durch Anregung mittels eines RF-Pulses kommt es zu Energieübergängen der Spins, die anschließend wieder während einer bestimmten Zeit T_1 , in ihren Ausgangszustand zurückkehren. Abbildung 14 wurde adaptiert von Referenz [56].

Diese Relaxationsprozesse und die dazugehörigen Raten liefern detaillierte Informationen über die Dynamik der jeweiligen Ladungsträgerdiffusion in den zu untersuchenden Materialen. Im folgenden Abschnitt werden diese Prozesse genauer behandelt.^{9, 56, 58}

Der RF-Puls lenkt die Magnetisierung in Richtung der x,y-Ebene aus. Bei der anschließenden Rückkehr in den Ausgangszustand kann zwischen zwei unterschiedlichen Phänomenen unterschieden werden: die Relaxation in Richtung des externen Magnetfeldes, charakterisiert durch die Spin-Gitter oder longitudinale Relaxationszeit T_1 und die Relaxation senkrecht zur Richtung des angelegten Magnetfeldes, die zur Spin-Spin oder transversalen Relaxationszeit T_2 führt.

Mathematisch beschrieben werden diese Vorgänge entsprechend der Gleichung von F. Bloch:

$$\frac{d\mathbf{M}}{dt} = \gamma (\mathbf{M} \times \mathbf{B}_0) - \frac{\mathbf{M}_{x,y}}{T_2} - \frac{\mathbf{M}_z - \mathbf{M}_0}{T_1} + \nabla [D \nabla (\mathbf{M} - \mathbf{M}_{eq})] \quad (2.60)$$

Der letzte Term erläutert hierbei die Zeithängigkeit der Magnetisierung, wenn die Probe einem Magnetfeldgradienten ausgesetzt ist, wobei \mathbf{M}_{eq} den Wert des magnetischen Moments im Gleichgewicht und D den Diffusionskoeffizienten darstellt.

Im Fall der longitudinalen Relaxationszeit wird Energie zwischen den Spins und dem Gitter ausgetauscht, man spricht daher auch von Spin-Gitter Relaxationen. Die Rate $1/T_1$ dieses Prozesses kann über

$$\frac{dM_z}{dt} = -\frac{M_z - M_0}{T_1} \quad (2.61)$$

bestimmt werden.

Der Wiederaufbau der Magnetisierung – nach Auslenkung – erfolgt entlang der z-Richtung gemäß

$$M_z(t) = M_0 - M_0 \exp\left(-\frac{t}{T_1}\right) \quad (2.62)$$

Dabei induziert die zeitabhängige Rückkehr in den Gleichgewichtszustand ein Wechselspannungssignal, das exponentiell abklingt und als FID („*free induction decay*“) bezeichnet wird. Mit Hilfe einer Fourier-Transformation kann dieses zeitabhängige Signal in ein frequenzabhängiges umgewandelt werden, was letztlich zum typischen NMR Spektrum führt.

Eine alternative Methode zu T_1 ist die Messung von $T_{1\rho}$ in einem rotierenden Koordinatensystem, bei der ein schwacher RF-Puls verwendet wird, um die Magnetisierung in der transversalen Ebene zu fixieren. Die Relaxation führt dann wiederum zu einer zeitabhängigen Rate $1/T_{1\rho}$. $T_{1\rho}$ liefert kürzere Zeiten als T_1 und ermöglicht somit die Detektion langamerer atomarer Bewegungen.

Die Spin-Spin Relaxationszeit T_2 beschreibt die Transversalmagnetisierung in der x', y'-Ebene im rotierenden Koordinatensystem. Die Rate $1/T_2$ kann in diesem Fall mit Hilfe von den Gleichungen (2.63) beziehungsweise (2.64) bestimmt werden:

$$\frac{dM_{x'}}{dt} = -\frac{M_{x'}}{T_2} \quad (2.63)$$

$$\frac{dM_{y'}}{dt} = -\frac{M_{y'}}{T_2} \quad (2.64)$$

Die Energie bleibt in diesem System konstant.^{9, 55, 56}

2.5.3 Interpretation der Relaxationsdaten

Die Interpretation der bei Relaxationsmessungen erhaltenen NMR-Daten stellt sich in den meisten Fällen als sehr komplex heraus. Daher werden zumeist geeignete Modellsysteme zur Unterstützung und Vereinfachung genutzt.

Am häufigsten erfolgt die Analyse der Raten mit Hilfe eines Arrhenius-Diagramms, bei der der Logarithmus von $1/T_1$ beziehungsweise $1/T_{1\rho}$ gegen die inverse Temperatur aufgetragen wird, wie in Abbildung 15 dargestellt.

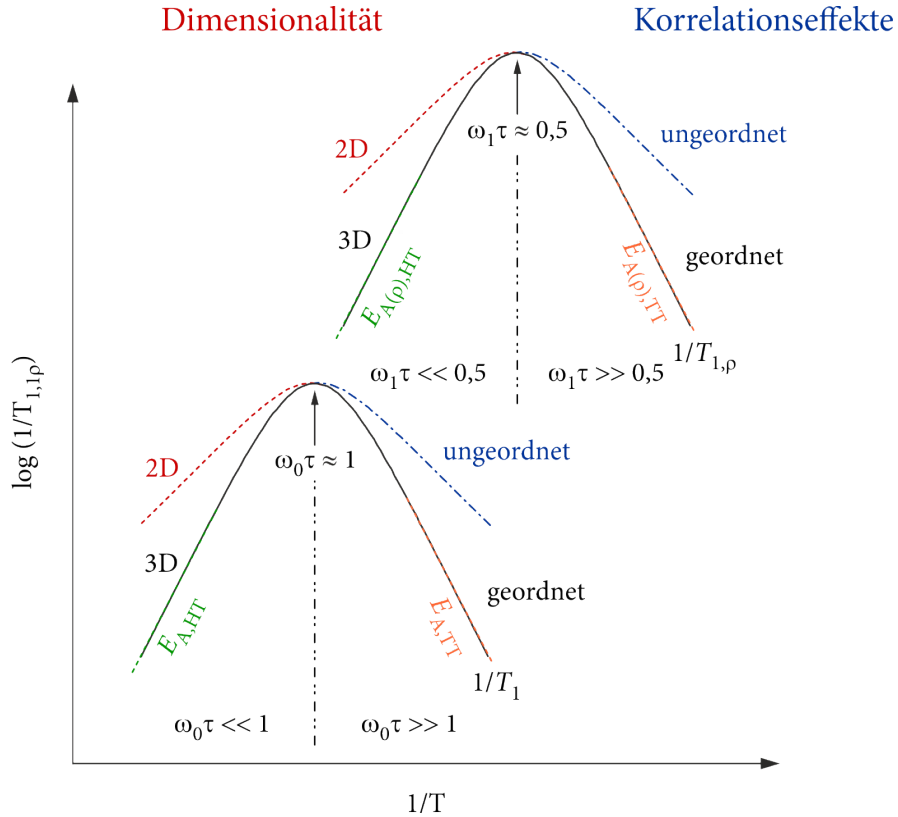


Abbildung 15: Arrhenius-Auftragung der Spin-Gitter-Relaxationsraten $1/T_1$ und $1/T_{1\rho}$. Genauere Informationen können dem Text entnommen werden. Die Abbildung wurde adaptiert von den Referenzen [15] und [59].

Die schwarzen durchgezogenen Kurven in Abbildung 15 repräsentieren einen dreidimensionalen, geordneten Diffusionsprozess, der mit Hilfe des häufig verwendete BBP-Modells nach Bloembergen, Purcell und Pound⁶⁰ charakterisiert wurde. Dieses Modell beschreibt eine Korrelationsfunktion, die einen einfachen exponentiellen Abfall zeigt:

$$G(t) = G(0) \exp\left(-\frac{|t|}{\tau}\right) \quad (2.65)$$

τ entspricht der Korrelationszeit, die direkt in Verbindung steht zur mittleren Verweilzeit eines Ions zwischen zwei erfolgreichen Sprüngen. Die Fourier-Transformation von $G(t)$ führt zu einer Lorentz-förmigen, spektralen Dichtefunktion $J(\omega)$, die direkt proportional zur Relaxationsrate $1/T_1$ ist:

$$\frac{1}{T_1} \propto J(\omega_0) = G(0) \frac{2\tau}{1 + (\omega_0\tau)^2} \quad (2.66)$$

Über einen Arrhenius-Zusammenhang

$$\tau = \tau_0 \exp\left(\frac{E_A}{k_B T}\right) \quad (2.67)$$

kann die Temperaturabhängigkeit von τ dargestellt werden. τ_0 ist hierbei der präexponentielle Faktor, E_A die Aktivierungsenergie für einen erfolgreichen Ionensprung zwischen zwei Gitterplätzen, k_B die Boltzmann-Konstante und T wiederum die Temperatur.

Für jede bestimmte Larmor-Frequenz wird daher bei einer Arrhenius-Auftragung, wie in Abbildung 15 illustriert, ein Maximum in den Ratenpeaks erhalten, an dem $\omega_0\tau \approx 1$ gilt. Jedes Maximum entspricht, analog zum Leitfähigkeitsplateau in den Impedanzanalysen, einem dynamischen Prozess in der Probe, für den eine Sprungrate $1/\tau$ berechnet werden kann, die an diesem Punkt äquivalent zur Larmor-Frequenz ist. Allgemein kann gesagt werden, je niedriger die Temperatur ist, bei der sich das Maximum des diffusionsinduzierten Ratenpeaks befindet, desto höher ist die Diffusivität des Prozesses.

Ein klassischer Ratenpeak von Relaxationsmessungen besitzt neben dem Maximum noch eine Hoch- und eine Tieftemperaturflanke. Die Tieftemperaturflanke auf der rechten Seite ist sensitiv für kurzreichweitige Dynamik, d.h. lokale Sprungprozesse. Hier gilt $\omega_0\tau \gg 1$, $1/\tau$ ist somit um einiges kleiner als ω_0 . Die Flanke auf der linken Seite, bei hohen Temperaturen reflektiert langreichweitige Ionendynamik. In diesem Bereich gilt $\omega_0\tau \ll 1$, τ ist viel größer als ω_0 und daher frequenzunabhängig.

Zusätzlich ist es noch möglich aus der Steigung jeder Flanke eine Aktivierungsenergie zu berechnen, $E_{A,HT}$ für hohe Temperaturen und $E_{A,TT}$ für tiefe Temperaturen. Das BBP-Modell geht von symmetrischen Ratenpeaks aus, bei denen die beiden Aktivierungsenergien identisch sind $E_{A,HT} = E_{A,TT}$. In den meisten realen Proben, wie auch in den im Rahmen dieser Arbeit untersuchten Materialen, werden allerdings asymmetrische Ratenpeaks erhalten. Korrelationseffekte wie strukturelle Unordnung und/oder Coulomb-Interaktionen

beeinflussen die Tieftemperaturregion auf der rechten Seite und führen zu niedrigeren Aktivierungsenergien.⁶¹ Dimensionalitäten haben Auswirkung auf E_A im Hochtemperaturbereich auf der linken Seite. Ist die Bewegung der Teilchen auf einen zweidimensionalen (2D) Raum beschränkt, wie es zum Beispiel bei schichtstrukturierten Materialen der Fall ist, verläuft die Steigung flacher als bei dreidimensionalem (3D) Verhalten.¹⁰

Alternativ kann die Messung von Spin-Gitter-Relaxationsraten, wie bereits im vorigen Abschnitt erwähnt, auch im rotierenden Koordinatensystem erfolgen und damit bei viel geringeren Frequenzen ω_1 . Entsprechend der Beziehung $\omega_1\tau \approx 1$ verschiebt sich dadurch das Maximum und damit der gesamte Ratenpeak zu niedrigeren Temperaturen (siehe Abbildung 15). Auf diese Weise können oftmals Maxima und Aktivierungsenergien von Proben zugänglich gemacht werden, die ansonsten bei zu hohen Temperaturen auftreten und experimentell nicht mehr messbar wären.^{15, 59, 62}

NMR Diffusionskoeffizient: Aus den Ratenpeaks der Relaxationsmessungen ist es ebenso möglich einen mikroskopischen Diffusionskoeffizienten zu bestimmen. Dafür wird zuerst über die Maximum Bedingung $\omega_1\tau \approx 1$ (oder $\omega_1\tau \approx 0,5$ im rotierenden Koordinatensystem) eine Sprungrate berechnet und diese anschließend in Gleichung (2.8) integriert. Sofern die mittlere Sprungdistanz zwischen zwei Gitterplätzen bekannt ist, kann so der mikroskopische NMR Selbstdiffusionskoeffizient D_{NMR} ermittelt werden.⁶³

2.5.4 MAS NMR

Festkörper NMR Messungen dienen nicht nur der Untersuchung von Ladungsträgerdynamiken sondern ermöglichen auch die strukturelle Aufklärung von Proben. Magic-Angle-Spinning (MAS) NMR ist eine wichtige Methode, um hochauflöste Daten zur Strukturaufklärung von Festkörperproben zu erhalten. In Flüssigkeiten werden anisotrope Interaktionen, wie dipolare Kopplungen und chemische Verschiebungen durch die schnelle Bewegung der Moleküle herausgemittelt, was zu scharfen und damit gut aufgelösten Signalen führt. In Feststoffen dagegen haben diese Interaktionen breite NMR Linien zur Folge, die eine genaue Analyse beziehungsweise Interpretation der Daten verhindern. Um hierbei einen ähnlichen Effekt für eine hohe Auflösung zu erzielen, ist es möglich, die Probe sehr schnell in einem Winkel von 54,74° (magischer Winkel) gegen das externe Magnetfeld B_0 zu rotieren. Dadurch wird die Signalverbreiterung durch anisotrope Interaktionen gehemmt und ein schmales, gut aufgelöstes isotropes NMR Signal entsteht.

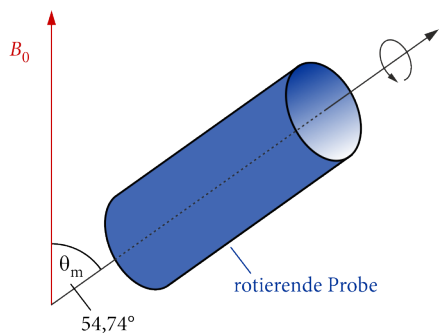


Abbildung 16: Schematische Darstellung der MAS NMR Technik. Die Probe rotiert dabei in einem magischen Winkel von $54,74^\circ$ gegen das externe Magnetfeld B_0 . Die Abbildung wurde adaptiert von den Referenzen [64] und [65].

Die anisotropen Anteile führen zu Seitenbanden, die symmetrisch links und rechts der isotropen Linie angeordnet sind. Da ihre Position von der Rotationsgeschwindigkeit abhängig ist, können sie allerdings relativ einfach identifiziert werden.^{56, 64, 65}

3. Ergebnisse

Im Rahmen dieser Arbeit wurden unterschiedliche Li⁺- und F⁻-Festkörperionenleiter untersucht. Für die Synthese aller verwendeten Proben wurden fast ausschließlich mechanochemische Reaktionen genutzt, die in einer Hochenergie-Kugelmühle durchgeführt wurden. Die anschließende strukturelle Charakterisierung der Produkte erfolgte mittels Röntgenkristallstrukturanalyse. Der Fokus dieser Arbeit lag aber vor allem auf der Untersuchung der mikroskopischen und makroskopischen Ionenbewegung und dem Einfluss der jeweiligen Struktur auf die Ladungsträgerdynamik. Dafür standen zum einen impedanzspektroskopische Leitfähigkeitsmessungen im Vordergrund, zum anderen komplementäre NMR Experimente (Spin-Gitter Relaxometrie), um so dynamische Parameter auf unterschiedlichen Längenskalen studieren zu können.

Im folgenden Kapitel sind die Ergebnisse der experimentell durchgeführten Arbeiten zusammengefasst. Die Darstellung erfolgt dabei in kumulativer Form und setzt sich aus publizierten Artikeln in Fachzeitschriften mit *peer-review* Prozess sowie aus zwei noch nicht veröffentlichten Manuskripten zusammen. Jeder Beitrag wird mit einer kurzen Einleitung und etwaigen zusätzlichen Informationen präsentiert. Grundsätzlich ist es möglich, die Artikel und Manuskripte in drei Untergruppen zu gliedern:

3.1 Lithium-basierte Festkörperelektrolyte

- 3.1.1 “Separating bulk from grain boundary Li ion conductivity in the sol-gel prepared solid electrolyte $\text{Li}_{1.5}\text{Al}_{0.5}\text{Ti}_{1.5}(\text{PO}_4)_3$ ”

- 3.1.2 "Rapid Li Ion Dynamics in the Interfacial Regions of Nanocrystalline Solids"

3.2 Nanokristalline Fluor-Ionenleiter

- 3.2.1 "Mismatch in cation size causes rapid anion dynamics in solid electrolytes: the role of the Arrhenius pre-factor"
- 3.2.2 "Fluorine Translational Anion Dynamics in Nanocrystalline Ceramics: $\text{SrF}_2\text{-YF}_3$ Solid Solutions"
- 3.2.3 "F anion dynamics in cation-mixed nanocrystalline $\text{LaF}_3\text{:SrF}_2$ "
- 3.2.4 "Heterogeneous F anion transport, local dynamics and electrochemical stability of nanocrystalline $\text{La}_{1-x}\text{Ba}_x\text{F}_{3-x}$ "

3.3 Nanokomposite mit zwei mobilen Ladungsträger-Spezies

- 3.3.1 "Interfacial Li ion dynamics in nanostructured LiF and LiF: Al_2O_3 composites"

3.1 Lithium-basierte Festkörperelektrolyte

Das Interesse an modernen, elektrochemischen Energiespeichersystemen ist in den letzten Jahren und Jahrzehnten enorm angestiegen. Im Speziellen die Entwicklung einer Festkörperbatterie, die einen Feststoff als Elektrolyt enthält, und dadurch eine Reihe Vorteilen zur Folge hat, ist von großer Bedeutung. Solche Systeme können einerseits bei höheren Temperaturen betrieben werden, andererseits erhöht die mögliche direkte Verwendung von Lithium Metall als Anode die Energiedichte. Der Einsatz von Festkörperelektrolyten führt zudem zu einer verbesserten Zyklustabilität, Lebensdauer und Sicherheit im Vergleich zu flüssigen, brennbaren Elektrolyten. Die beiden folgenden veröffentlichten Artikel beschäftigen sich mit der Entwicklung und Weiterentwicklung potentieller Festkörperelektrolyte für Lithium Ionen Festkörperbatterien.^{5, 66-68}

3.1.1 Separating bulk from grain boundary Li ion conductivity in the sol-gel prepared solid electrolyte $\text{Li}_{1.5}\text{Al}_{0.5}\text{Ti}_{1.5}(\text{PO}_4)_3$

Die erste Veröffentlichung hatte zum Ziel, die unterschiedlichen Beiträge der Gesamtleitfähigkeit eines schnellen Ionenleiters ($\text{Li}_{1.5}\text{Al}_{0.5}\text{Ti}_{1.5}(\text{PO}_4)_3$ – LATP) zu separieren und zu analysieren. LATP ist ein Material das aufgrund seiner guten ionischen und vernachlässigbaren elektronischen Leitfähigkeit einen geeigneten Festkörperionenleiter darstellt. Es kristallisiert mit NASICON-Struktur (*sodium superionic conductor*), einer Struktur bei der sich die Ladungsträger entlang der Zwischengitterplätze bewegen und die bekannt für ihre hohen Ionenleitfähigkeiten ist.⁶⁹

In diesem Fall wurde die Verbindung über ein Sol-Gel-Verfahren in der Arbeitsgruppe von Frank Tietz am FZ Jülich hergestellt. Die anschließende Charakterisierung der Proben erfolgte mittels Röntgendiffraktometrie sowie Rasterelektronenmikroskopie. Zur Unterscheidung zwischen den Bulk- und Korngrenzenanteilen des Ionentransportes wurde die Methode der Leitfähigkeitsspektroskopie verwendet. Es ist dabei gelungen, die beiden Prozesse durch Messungen bei sehr tiefen Temperaturen zu identifizieren und zu separieren. Des Weiteren konnte gezeigt werden, dass das Sintern der Proben deutlichen Einfluss auf die Leitfähigkeiten, sogar die des Bulkprozesses, hat. Da bei Impedanzmessungen, was Messungen im sogenannten DC-Plateau betrifft, langreichweitige Transportphänomene analysiert werden, konnten erwartungsgemäß deutlich höhere Aktivierungsenergien gefunden werden als in der Literatur. Diese stammen meist von NMR-Messungen und sind daher sensitiv auf atomare Sprungprozesse, was zu niedrigeren Sprungbarrieren führt.

Separating bulk from grain boundary Li ion conductivity in the sol-gel prepared solid electrolyte $\text{Li}_{1.5}\text{Al}_{0.5}\text{Ti}_{1.5}(\text{PO}_4)_3$

S. Breuer, D. Prutsch, Q. Ma, V. Epp, F. Preishuber-Pflügl, F. Tietz, and M. Wilkening, *J. Mater. Chem. A*, 2015, **3**, 21343-21350.



Cite this: *J. Mater. Chem. A*, 2015, **3**,
21343

Separating bulk from grain boundary Li ion conductivity in the sol–gel prepared solid electrolyte $\text{Li}_{1.5}\text{Al}_{0.5}\text{Ti}_{1.5}(\text{PO}_4)_3$

Stefan Breuer,^{*a} Denise Prutsch,^a Qianli Ma,^b Viktor Epp,^a Florian Preishuber-Pflügl,^a Frank Tietz^{bc} and Martin Wilkening^{*a}

Lithium aluminium titanium phosphate (LATP) belongs to one of the most promising solid electrolytes. Besides sufficiently high electrochemical stability, its use in lithium-based all-solid-state batteries crucially depends on the ionic transport properties. While many impedance studies can be found in literature that report on overall ion conductivities, a discrimination of bulk and grain boundary electrical responses *via* conductivity spectroscopy has rarely been reported so far. Here, we took advantage of impedance measurements that were carried out at low temperatures to separate bulk contributions from the grain boundary responses. It turned out that bulk ion conductivity is by at least three orders of magnitude higher than ion transport across the grain boundary regions. At temperatures well below ambient long-range Li ion dynamics is governed by activation energies ranging from 0.26 to 0.29 eV depending on the sintering conditions. As an example, at temperatures as low as 173 K, the bulk ion conductivity, measured in N_2 inert gas atmosphere, is in the order of 8.1×10^{-6} S cm⁻¹. Extrapolating this value to room temperature yields *ca.* 3.4×10^{-3} S cm⁻¹ at 293 K. Interestingly, exposing the dense pellets to air atmosphere over a long period of time causes a significant decrease of bulk ion transport. This process can be reversed if the phosphate is calcined at elevated temperatures again.

Received 14th August 2015
Accepted 19th September 2015

DOI: 10.1039/c5ta06379e
www.rsc.org/MaterialsA

1 Introduction

The interest in powerful electrochemical energy storage systems has tremendously increased over the last couple of years. In particular, the development of all-solid-state batteries taking advantage of solid electrolytes with high ion conductivity^{1–9} represents one of the growing fields in energy science. Such systems would allow higher operation temperatures as well as the use of Li metal anodes directly increasing the energy density. Moreover, in contrast to systems using flammable liquid electrolytes, solid-state batteries should benefit from increased cycling stability and lifetime due to less ageing processes; as a consequence thereof, a significant increase in safety is expected.

A suitable solid electrolyte should guarantee electrochemical stability coupled with fast ion dynamics and negligible electronic conductivity. In recent years, garnet-type oxides^{10–13} and argyrodite-type sulfides^{14–16} entered the limelight; in addition,

there is renewed interest in lithium aluminium titanium phosphates¹⁷ $\text{Li}_{1+x}\text{Al}_x\text{Ti}_{2-x}(\text{PO}_4)_3$ ($0 < x < 0.5$; LATP) crystallising with NASICON-type (Na superionic conductor) structure^{18–23} that is based on $\text{Na}_{1+x}\text{Zr}_2\text{Si}_x\text{P}_{3-x}\text{O}_{12}$, $0 < x < 3$. LATP crystallises with rhombohedral structure (space group $R\bar{3}c$, see Fig. 1) and offers various Li sites, such as M1, M2 and M3. The site occupancy is controlled by the amount of substituted Al^{3+} cations which replace the Ti^{4+} ions.^{17,21,24} The extra Li ions, which are needed for charge compensation, are anticipated to occupy the M3 sites.

Although a quite large number of studies^{1,10} have been published that present new synthesis routes for oxides and deal with the characterisation of the overall ion transport properties by means of impedance spectroscopy, investigations focusing on the separation of the bulk and grain boundary electrical responses are less frequent.²⁵ To design, however, electrolytes with high ionic conductivity we need to know the key processes that govern both (i) bulk ion dynamics and (ii) ion transport across the grain boundaries or near the interfacial regions. Here, we took advantage of low-temperature impedance and conductivity spectroscopy to elucidate long-range ion dynamics inside the crystal lattice of LATP.²⁵ For this purpose a sol–gel prepared sample with the composition $\text{Li}_{1.5}\text{Al}_{0.5}\text{Ti}_{1.5}(\text{PO}_4)_3$ was used to perform impedance measurements from the mHz to the MHz range. In general, compared to solid-state preparation techniques the use of solution-based synthesis methods, as it is

^aChristian Doppler Laboratory for Lithium Batteries and Institute for Chemistry and Technology of Materials, Graz University of Technology (NAWI Graz), Stremayrgasse 9, 8010 Graz, Austria

^bForschungszentrum Jülich GmbH, Institute of Energy and Climate Research, Materials Synthesis and Processing (IEK-1), 52425 Jülich, Germany

^cHelmholtz Institute Münster, c/o Forschungszentrum Jülich GmbH, 52425 Jülich, Germany

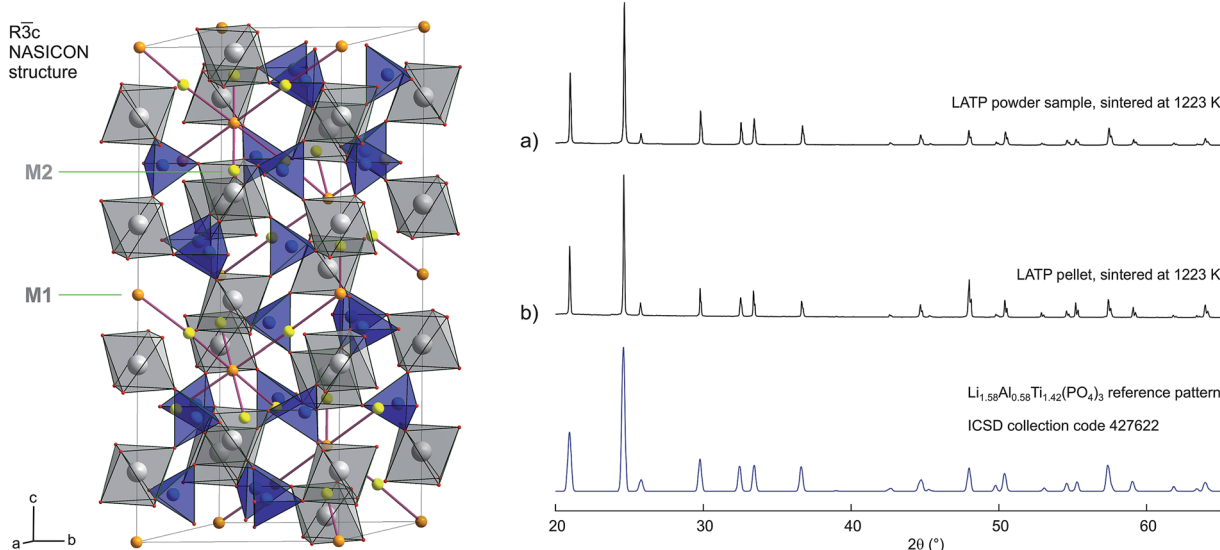


Fig. 1 Left: Crystal structure of LATP that is based on the NASICON type. As an example, orange and yellow spheres represent possible Li sites the ions may use to diffuse through the crystal lattice. Right: X-ray powder diffraction patterns of the powder sample investigated (a) and the pellet (b); both patterns were recorded after a sintering step at 1273 K. At the bottom a reference pattern (ICSD 427622) is given. The pattern were recorded after the conductivity measurements.

performed here, offers the possibility to better control composition, homogeneity and morphology of the final product.

Remarkably, it turned out that at a temperature of 173 K the ionic bulk conductivity of the sol-gel prepared phosphate $\text{Li}_{1.5}\text{Al}_{0.5}\text{Ti}_{1.5}(\text{PO}_4)_3$ is in the order of $8.1 \times 10^{-6} \text{ S cm}^{-1}$. This translates, after extrapolation to room temperature, into a value of *ca.* $3.4 \times 10^{-3} \text{ S cm}^{-1}$ at 293 K, which is among the highest conductivities reported for LATP-based ion conductors.^{17,20,26} It is even comparable with conductivities known for sulphides⁴ such as $\text{Li}_{10}\text{SnP}_2\text{S}_{12}$ ($4 \times 10^{-3} \text{ S cm}^{-1}$) and the glass ceramic $\text{Li}_3\text{P}_3\text{S}_{11}$ ($3.2 \times 10^{-3} \text{ S cm}^{-1}$).^{27,28} The corresponding activation energy E_a turns out to be approximately 0.26 eV. This value is between that of, *e.g.*, Al-stabilised garnet-based electrolytes (0.34 eV)¹¹ and argyrodite-type sulfides (0.20 eV).¹⁶ Together with the fast ion conductor $\text{Li}_{10}\text{GeP}_2\text{S}_{12}$, which has been introduced by Kamaya *et al.*,⁴ the latter belong to the best ion conductors presented over the last years.

2 Experimental

The $\text{Li}_{1.5}\text{Al}_{0.5}\text{Ti}_{1.5}(\text{PO}_4)_3$ sample was synthesized *via* a new sol-gel process. Stoichiometric amounts of LiNO_3 (99%, Alfa Aesar), $\text{Al}(\text{NO}_3)_3 \cdot 9\text{H}_2\text{O}$ (99%, Alfa Aesar), titanium(IV) isopropoxide (97%, Aldrich) and $\text{NH}_4\text{H}_2\text{PO}_4$ (99%, Merck) were used. At first, titanium(IV) isopropoxide (97%, Aldrich) was added into deionized water immediately forming a precipitate of titanium hydroxide. The fresh precipitate was filtered, washed and dissolved in nitric acid (65%, Aldrich). After a clear TiO^{2+} nitrate solution had been formed, a twofold molar amount of citric acid monohydrate (99%, Merck) was added into the solution to stabilise it. LiNO_3 and $\text{Al}(\text{NO}_3)_3 \cdot 9\text{H}_2\text{O}$ were then added into the TiO^{2+} nitrate solution while stirring. After the salts were dissolved, $\text{NH}_4\text{H}_2\text{PO}_4$ was added to the solution; this led to the

formation of a sol. Stirring was maintained for another 0.5 h. After about 1 h, a stiff gel was spontaneously obtained. The gel was dried, calcined and milled in ethanol with zirconia balls on a milling bench. The ball-milled powder was put into a cylindrical pressing mold (10 mm in diameter, 4 mm in thickness) and pressed at a uniaxial pressure of 100 MPa. The pressed pellets were then sintered at 1123 K. Pure white samples with rhombohedral phase (Fig. 1) were obtained after sintering. The density of the pellets was over 95% of the theoretical density.

Immediately before the conductivity and impedance measurements, the pellet annealed at 1123 K was once again dried at 873 K for 16 hours to remove any moisture on its surface. Au electrodes of *ca.* 100 nm in thickness were applied using a sputter coater (Leica). The impedance measurements were carried out on a Novocontrol Concept 80 broadband dielectric spectrometer at frequencies ranging from 0.1 Hz to 10 MHz. The temperature was varied from 123 K to 423 K using either a stream of heated nitrogen gas or a constant flow of cold nitrogen in the cryostat. Any contamination with water or carbon dioxide was avoided as best as possible.

In order to use the same pellet for further impedance investigations, the Au layer was sanded down and the surface polished afterwards. Then, the specimen was annealed at 1223 K for 16 hours again; the density remained almost the same. Subsequently, impedances measurements were carried out under the same conditions in order to test the impact of sintering conditions on conductivity properties.

For comparison, also a powder sample of $\text{Li}_{1.5}\text{Al}_{0.5}\text{Ti}_{1.5}(\text{PO}_4)_3$ was investigated by impedance spectroscopy. A cylindrical pellet with a diameter of 5 mm and a thickness of *ca.* 1.2 mm was produced by pressing the pristine powder at a uniaxial pressure of approximately 0.5 GPa; the powder sample is a green body pellet with a density of reaching almost 90%. After

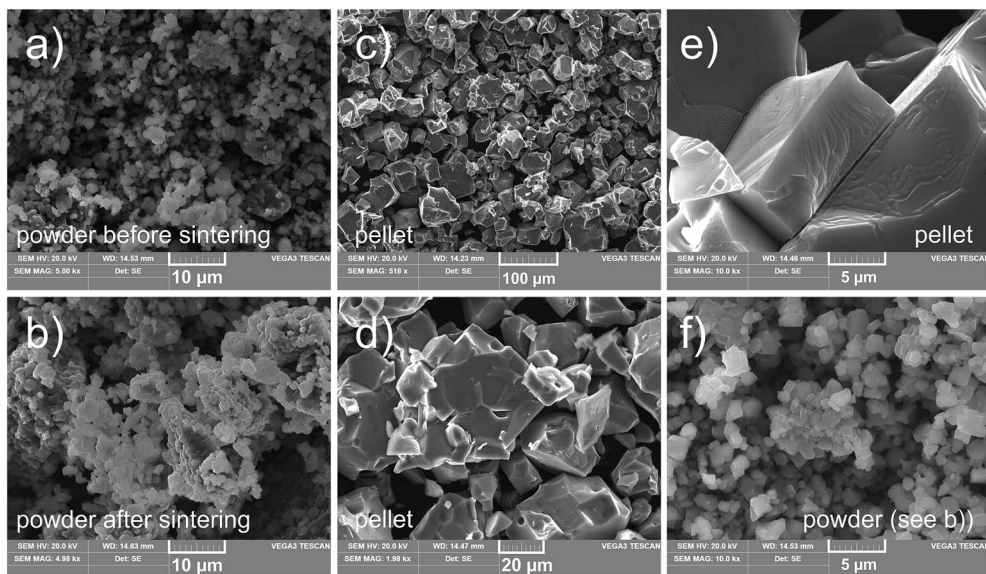


Fig. 2 SEM images of the powder sample ((a), (b) and (f)) as well as the pellet investigated ((c)–(e), just differing by the magnification). Except the one shown in (a) all images were taken after the sintering step at 1223 K and the conductivity measurements. (b) and (f) refer to the same sample; the images differ in magnification.

the drying process (873 K for 16 hours, see above), Li ion blocking electrodes with a thickness of *ca.* 100 nm were again applied at each side by Au sputtering. For comparison, the powder was also used to prepare a pellet that was sintered at 1223 K for 16 h.

The pellet as well as the samples prepared from the LATP powder were investigated by scanning electron microscopy (SEM) using a VEGA3 (Tescan) before and after the sintering steps (see Fig. 2). X-ray powder diffraction (D8 Advance, Bruker) using Cu-K α radiation was employed to check the phase purity of the samples prepared.

3 Results and discussion

The phase purity of the samples investigated was examined by X-ray powder diffraction (XRD) carried out before and after the

conductivity measurements. Apart from an ‘order-disorder’ transition, LATP shows no phase transformation down to 100 K.²⁹ The samples investigated in the present study reveal the diffraction pattern expected for $\text{Li}_{1.5}\text{Al}_{0.5}\text{Ti}_{1.5}(\text{PO}_4)_3$. In Fig. 1 (right) the pattern of $\text{Li}_{1.58}\text{Al}_{0.58}\text{Ti}_{1.42}(\text{PO}_4)_3$ (ICSD 427662) crystallising with the NASICON structure serves as a reference to check the purity of the samples with respect to additional crystalline phases. Since no other than the reflections of LATP were observed, such impurity phases are absent within the detection limit of X-ray diffraction. Because a flat background signal is seen with no humps that indicates amorphous material, we deal with highly crystalline samples. The narrow reflections of the XRD powder pattern indicate crystallites with diameters in the μm range. This observation is corroborated by our SEM investigations (see Fig. 2) revealing large crystallites in the case of the sintered pellet, in particular.

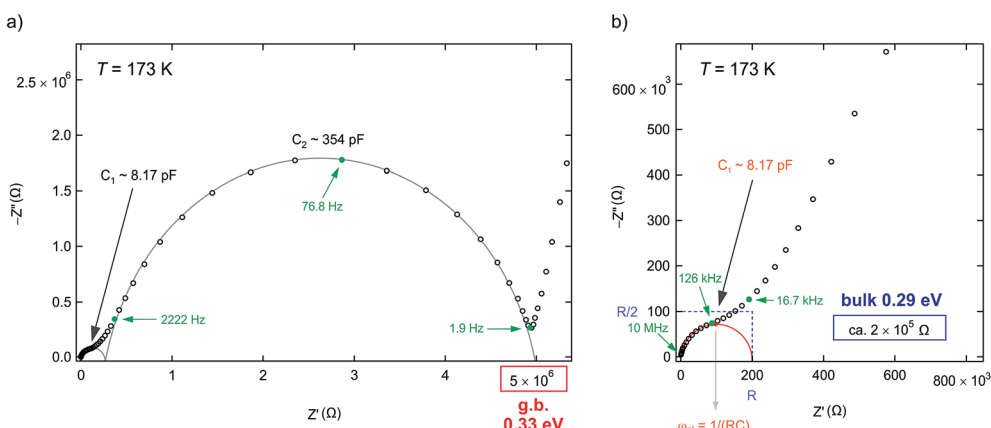


Fig. 3 (a) Complex plane plot, *i.e.*, AC-impedance diagram, of the $\text{Li}_{1.5}\text{Al}_{0.5}\text{Ti}_{1.5}(\text{PO}_4)_3$ pellet sintered at 1123 K. In (b) a magnification of the high-frequency region is shown. The highest frequency used to measure the data was 10 MHz. The solid line shows a fit using individual resistances and CPEs connected in parallel; see text for further discussion.

In Fig. 3(a) and (b) a typical complex plane plot, *i.e.*, the imaginary part $-Z''$ of the impedance is shown *vs.* its real part, Z' , is displayed for the $\text{Li}_{1.5}\text{Al}_{0.5}\text{Ti}_{1.5}(\text{PO}_4)_3$ pellet, which was sintered at 1123 K. By using a relatively thick sample, 4 mm in the present case, the Nyquist plot is definitely composed of two semi-circles that can be satisfactorily separated on the frequency scale if the data are recorded at temperatures as low as 173 K. In Fig. 3(b) the high-frequency region of the plot is enlarged. The solid line in (a) and (b) represents a fit (ZView software) using an equivalent circuit that consists of a resistor R and a constant phase element CPE connected in parallel for each circle: $(R_1\text{CPE}_1)(R_2\text{CPE}_2)$. The resulting capacities are $C_1 = 8.2 \text{ pF}$ and $C_2 = 354 \text{ pF}$ for the arc at high and low frequencies, respectively (see Fig. 3). They are in agreement with those that can be directly derived *via* the maximum condition $\omega_{\text{el}} = 1/(RC)$, see Fig. 2(b), where the relaxation frequency is given by $\omega_{\text{el}} = 2\pi\nu$. A value of 8.2 pF clearly points to bulk ion dynamics, whereas a value larger than 300 pF can be attributed to the grain boundary (g.b.) response.³⁰

The spike seen at the lowest frequencies represents electrode polarisation that needs not to be taken into account in the analysis of the impedance curve. At temperatures higher than ambient, only the g.b. arc and the near-vertical line associated to electrode polarisation is visible.

Interestingly, the two resistances R_1 and R_2 differ by more than one order of magnitude. Thus, Li motion across the grain boundaries in our LATP sample is significantly reduced as compared to intragranular ion hopping. At 173 K the bulk resistance R_1 is in the order of 200 k Ω while R_2 is in the M Ω range. Such differences between ion transport in the grain interior and overall conductivity were also reported by Arbi *et al.* earlier.³¹ This suggests that manipulation of the microstructure could be used to improve the total conductivity, *e.g.*, by increasing the grain size and minimizing the number of grain boundaries. As has been shown for highly conducting sulphides, see, *e.g.*, the study of Hayashi on Na_3PS_4 ,³² in the case of a glass ceramic pellet, the g.b. regions are largely reduced and seem to have a much less blocking effect on overall ion transport. Quite recently, Ma *et al.* used transmission electron microscopy to visualize the structural and chemical characteristics of ion blocking g.b. in $(\text{Li}_{3x}\text{La}_{2/3-x})\text{TiO}_3$.³³

The features of (i) electrode polarisation, (ii) electrical bulk response and (iii) g.b. response also appear in the corresponding conductivity spectra, which we used to analyse the data as a function of temperature. In Fig. 4 collections of conductivity spectra, that is, the real part, σ' , of the complex conductivity plotted *vs.* frequency ν , is shown for the pellet sintered at 1123 K (a) and 1223 K (b). Whereas at elevated temperatures both the g.b. response and electrode polarisation govern the spectra, at lower T the bulk response comes to light. Considerable polarisation effects are seen because of sufficiently fast Li ion transport causing a piling up of ions in front of the surface of the ion blocking electrode applied. While the low-frequency g.b. response yields distinct and almost flat DC plateaus, characterised by $\sigma_{\text{P}1}$ (see Fig. 4(a)), those of the bulk response, $\sigma_{\text{P}2}$, are more difficult to analyse. Fortunately, at sufficiently low temperatures, see, *e.g.*, the isotherms at 153 K

and 173 K, it is possible to read off reliable conductivities representing long-range Li ion transport through the crystal lattice of LATP. This analysis was also performed for the pellet that was sintered at 1273 K, see Fig. 4(b), although the determination of the inflection point of the isotherms turns out to be even more difficult. It is worth noting that the inverse of the values of $\sigma_{\text{P}1}$ and $\sigma_{\text{P}2}$ agree well with those deduced from the Nyquist plots, *viz.* R_1 and R_2 .

The characteristics of both bulk and g.b. responses are also visible when the imaginary part $-Z''$ of the complex impedance is plotted *vs.* frequency, see Fig. 5. While the maximum at low frequencies is assigned to ion dynamics governed by grain boundaries, the local maximum at higher frequencies represents lattice ion dynamics. Since the electric modulus M'' is inversely proportional to the capacitance C , in a $\log_{10}(M''(\nu))$ plot bulk contributions are pronounced while the responses

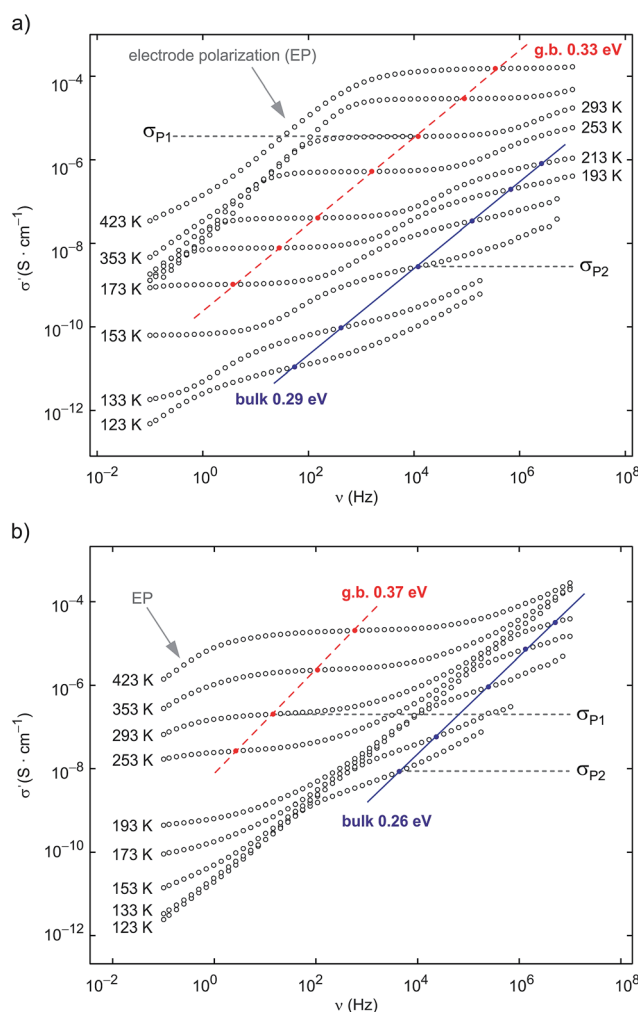


Fig. 4 (a) Conductivity isotherms of a sintered LATP pellet ($\text{Li}_{1.5}\text{Al}_{0.5}\text{Ti}_{1.5}(\text{PO}_4)_3$) with a thickness of 4 mm. The pellet was sintered at 1123 K. In (b) the corresponding isotherms of the same sample are shown after sintering at 1223 K. The conductivity spectra exhibit two separate plateaus reflecting grain boundary (g.b.) and bulk ion conductivities: $\sigma_{\text{P}1}$ and $\sigma_{\text{P}2}$. EP denotes electrode polarisation because of the ion blocking electrodes used to record the data.

due to grain boundaries decrease in intensity.³⁰ The ratio of $C_2/C_1 = 43$ (see above) agrees well with $1/(M''_{\max,1}/M''_{\max,2})$. As expected, increasing the temperature from 153 K to 173 K shifts the maxima in M'' and $-Z''$ towards higher frequencies.

To analyse the underlying temperature dependence of the electrical relaxation processes we evaluated the conductivity isotherms shown in Fig. 4. Plotting the DC conductivities inferred from the isotherms as a function of the inverse temperature in an Arrhenius diagram, the activation energy of the bulk response can be obtained (see Fig. 6). Starting with 0.29 eV for the pellet sintered at 1123 K, E_a slightly decreases to 0.26 eV after the same sample was sintered again at 1223 K. Simultaneously, the value for the g.b. response increases from 0.33 eV to 0.37 eV.

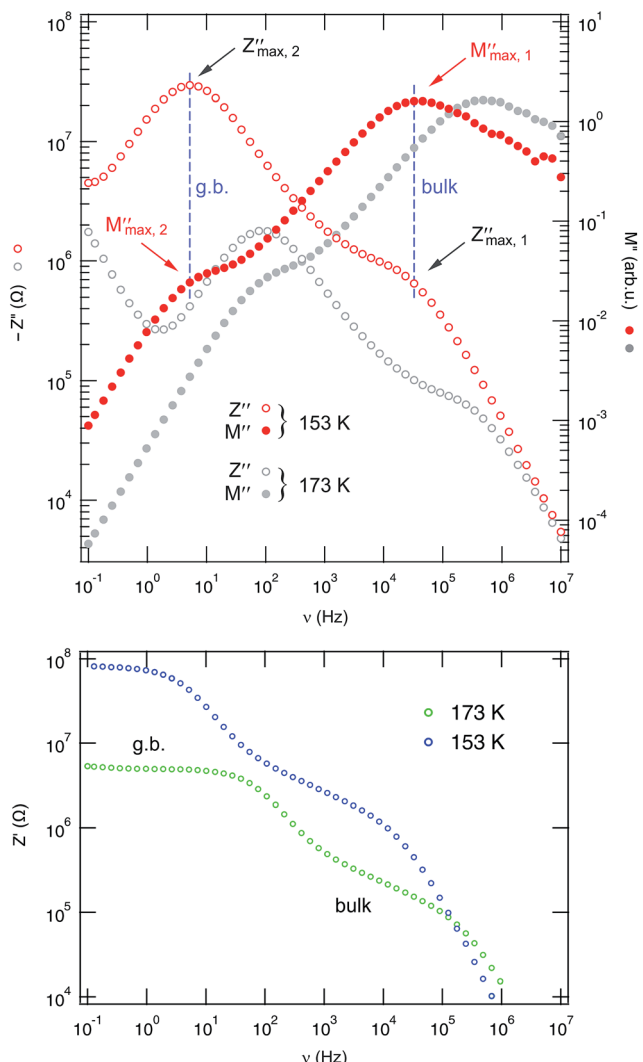


Fig. 5 Top: Change of the imaginary part of the complex impedance of $\text{Li}_{1.5}\text{Al}_{0.5}\text{Ti}_{1.5}(\text{PO}_4)_3$ with frequency. The curves exhibit two maxima that are ascribed to bulk and g.b. response. The maximum associated with lattice ion dynamics is more pronounced in the modulus representation, see right axis. Besides the data recorded at 153 K, the two spectra acquired at 173 K are also shown. Bottom: Variation of the real part of the complex impedance with frequency. As in the case of $\sigma'(\nu)$ the bulk regions appear at higher frequencies.

If we extrapolate the bulk data towards higher temperatures, the bulk ion conductivity would be in the order of 3.4 mS cm^{-1} at room temperature (see Fig. 6). This value, exceeding that reported by Fu for a glass ceramic (1.3 mS cm^{-1}),²⁶ is in good agreement with the results reported by several groups studying LATP-based solid electrolytes (see Table 1). In particular, it agrees well with the data measured by Arbi *et al.* quite recently.^{31,34} This makes crystalline LATP indeed an extremely fast ion conductor with superior conductivity properties. Its exact bulk ion conductivity, however, depends on the sintering conditions chosen and can be somewhat tuned by post-annealing. The origins of this conductivity increase are, however, still unknown. Since the activation energy does not depend much on the sintering conditions, one might suppose a small change in the number of charge carriers that are allowed to move over long distances. Further work is needed to clarify the microstructural changes and alterations of the defect chemistry taking place during the high- T sintering steps. Of course, Li loss might change local Li^+ environments as well as Li and Al site occupancies in LATP.

Interestingly, if the pellet sample is exposed to ambient air for several days, a decrease of the bulk ion conductivity is observed by about two orders of magnitude, see the dashed-dotted line in Fig. 6. The feature is completely reversible: drying the sample at 873 K for 16 h resets the initially found high conductivity values. We attribute this effect to the influence of moisture on ion dynamics; further studies are in progress to elucidate the change in conductivity. Irrespective of the conductivity drop observed here, recent studies have been published that demonstrate the usability of water-stable LATP as electrolyte in aqueous battery systems such as Li-air batteries.³⁵ Moreover, LATP turned out to be relatively resistant to static corrosion in a hot, aqueous LiOH solution.³⁶

Comparing our activation energies with those recently presented in literature, there is good agreement with recent studies.^{34,37} Values slightly below 0.3 eV seem to accurately describe bulk long-range ion transport. Considering the work by Bucharsky *et al.*,³⁸ the authors found the same influence of sintering on ionic conductivity. Their activation energies are, however, higher than our values and range from 0.42 eV to 0.37 eV depending on the sintering temperature (850 °C to 1100 °C). Worth noting, we have re-calculated the activation energies using the data of Bucharsky *et al.*³⁸ because there is an error in their publication, which leads to much smaller values for E_a : the authors calculated activation energies from a \log_{10} plot but forgot to take into account the conversion factor of $\log(e) \approx 2.3$ originating from the \log_{10} to $\ln = \log_e$ (*logarithmus naturalis*) transformation. Hence, the activation energies announced by Bucharsky *et al.*³⁸ are by a factor of 0.43 too small. Although their absolute ion conductivities are quite high, *viz.* in the mS cm^{-1} range at ambient temperature, the activation energies resemble those we found for the grain boundary response.

For comparison, hopping barriers of *ca.* $E_a = 0.16 \text{ eV}$ were reported by Kosova *et al.*⁴⁸ Worth noting, such small activation energies were extracted from preliminary NMR relaxometry instead of conductivity spectroscopy. In contrast to conductivity measurements, NMR spin-lattice relaxation (SLR), when

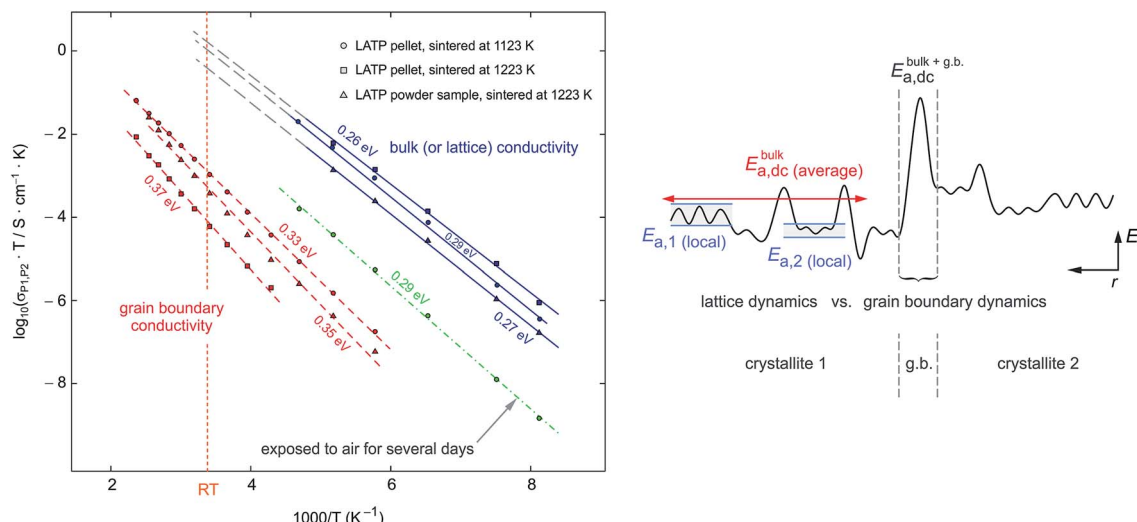


Fig. 6 Left: Arrhenius plot of the g.b. and bulk ion conductivities of the $\text{Li}_{1.5}\text{Al}_{0.5}\text{Ti}_{1.5}(\text{PO}_4)_3$ samples studied. The data were deduced from the conductivity isotherms partly shown in Fig. 3(a) and (b). The dashed and solid lines represent fits according to an Arrhenius law: $\sigma T \propto \exp(-E_a/(k_B T))$, k_B denotes Boltzmann's constant. The activation energies obtained are indicated. At ambient temperature, see vertical line, a DC bulk conductivity of ca. 3.4 mS cm^{-1} is obtained after extrapolation. Right: Schematic illustration of a heterogeneous potential landscape. Depending on the length scale, the method chosen to study ion dynamics is either sensitive to long-range ion dynamics or to local ionic jump processes. While atomic-scale methods, such as Li NMR, are also sensitive to individual ion hopping with low energy barriers, dc conductivity measurements probe an average value that characterises long-range, i.e., through-going, ion dynamics.

Table 1 Overview of recent impedance measurements presented for LATP-based inorganic compounds in the literature

Composition	Synthesis method, reference	Conductivity (300 K)	Activation energy	Notes
$\text{Li}_{1+x}\text{Al}_x\text{Ti}_{2-x}(\text{PO}_4)_3$				
$x = 0, 0.2, 0.4$	Solid state reaction, Arbi <i>et al.</i> ³⁴	$3.4 \times 10^{-3} \text{ S cm}^{-1}$ (bulk)	0.24–0.28 eV ($x = 0.2, 0.4$)	Up to 3 GHz, 100–500 K
$x = 0.45$	Mechanochemical synthesis, Morimoto <i>et al.</i> ³⁹	$2.9 \times 10^{-4} \text{ S cm}^{-1}$	0.31 eV	Annealing of amorphous powder
$x = 0.3$	Mechanochemical synthesis, Morimoto <i>et al.</i> ⁴⁰	ca. $10^{-4} \text{ S cm}^{-1}$	0.36 eV	Sintered at 1173 K
$x = 0.3$	Citrate sol-gel process, Kunshina <i>et al.</i> ⁴¹	$3\text{--}4 \times 10^{-4} \text{ S cm}^{-1}$	0.21 eV	Sintered at 1273 K, 293–473 K, up to 1 MHz; 86–90% density
$x = 0.3$	Wet chemical synthesis, Duluard <i>et al.</i> ⁴²	$1.6 \times 10^{-4} \text{ S cm}^{-1}$	—	Densified, 97%
$x = 0.3$	Samples obtained from Ceramatec Inc., Jackman <i>et al.</i> ⁴³	$6.7 \times 10^{-4} \text{ S cm}^{-1}$	0.31–0.36 eV	Effect of micro-cracking
$x = 0.3$	Citric acid-assisted sol-gel process, Yoon <i>et al.</i> ⁴⁴	$7.8 \times 10^{-5} \text{ S cm}^{-1}$ (g.b.) $9.4 \times 10^{-4} \text{ S cm}^{-1}$ (bulk)	0.395 eV (total); 0.13 eV (bulk)	
Composition unknown, glass ceramic	Samples obtained from Ohara Inc., Mariappan <i>et al.</i> ⁴⁵	10^{-5} to $10^{-6} \text{ S cm}^{-1}$ (190 K)	0.37 eV (total); 0.33 eV (bulk)	Total and bulk conductivity differ by one order of magnitude; 0.1–10 MHz
$x = 0.5$	Co-precipitation method, Kotobuki <i>et al.</i> ⁴⁶	$1.4 \times 10^{-3} \text{ S cm}^{-1}$ (bulk) $1.5 \times 10^{-4} \text{ S cm}^{-1}$ (total)	0.31 eV	Sintered at 1323 K
$x = 0.5$	Co-precipitation method, Kotobuki <i>et al.</i> ⁴⁷	$1.2\text{--}3.1 \times 10^{-3} \text{ S cm}^{-1}$ (bulk) 7.1×10^{-7} to $4.5 \times 10^{-4} \text{ S cm}^{-1}$ (total)	0.13–0.19 eV (bulk) 0.28–0.35 eV (total)	Bulk and overall conductivity depends on the Al source used: $\text{Al}(\text{NO}_3)_3$, $\text{Al}(\text{C}_3\text{H}_7\text{O})_3$
$x = 0.5$	Crystallisation of a glass, Narváez-Semanate and Rodrigues ³⁷	$1.3 \times 10^{-3} \text{ S cm}^{-1}$	0.27 eV	Glass ceramic, several samples, sintered at 973 K to 1273 K, see also references therein

performed in the laboratory frame of reference, in particular, is sensitive to both long-range and local Li jump processes depending on the conditions used to collect the data. While values in the order of 0.3 eV refer to through-going (that is, long-range) ion transport in the bulk, activation energies from SLR NMR, on the other hand, have to be carefully analysed. In many cases they reflect the elementary steps of ion jumping, *i.e.*, diffusion processes on a shorter length scale than usually accessible by conductivity spectroscopy or AC impedance measurements, respectively.

Our own NMR relaxometry measurements, which were carried out in both the rotating and laboratory frame of reference point to very similar activation energies ranging from 0.16 to 0.18 eV only.⁴⁹ Most importantly, the barriers seen *via* NMR have to be attributed to two different diffusion processes the ions are subject to almost simultaneously. At higher temperatures NMR was able to sense a third diffusion process with a higher energy barrier. Thus, NMR activation energies as low as 0.16 eV indeed characterise individual hopping processes rather than the averaged, long-range ion transport seen *via* Li ion conductivity measurements. Quite recently, Lang *et al.*⁵⁰ studied Li ion hopping using first-principle methods based on density functional theory. The authors report an interstitial diffusion mechanism that is characterised by an activation energy of 0.19 eV.⁵⁰

4 Conclusions

$\text{Li}_{1+x}\text{Al}_x\text{Ti}_{2-x}(\text{PO}_4)_3$ belongs to the group of solid electrolytes which are expected to largely influence the development of all-solid-state batteries. A sufficiently high ion conductivity, being in the same order of magnitude as that of a liquid electrolyte, is one of the basic requirements needed. So far, the separate study of bulk and grain boundary conductivity has only rarely been documented. Here, we took advantage of low temperature conductivity measurements and impedance spectroscopy to study bulk ion dynamics at temperatures lower than 215 K. In this temperature range Li ion transport through the lattice is governed by an average activation $E_{\text{a},\sigma}$ of only 0.26 eV when a pellet sample is considered that was annealed at 950 °C. The grain boundary response is determined by notably larger activation energies ranging from 0.33 eV to 0.37 eV; the exact value depends on the sintering temperature applied.

We could further show that even bulk ionic conductivity seems to depend on the sintering conditions. Exposing the samples to ambient air for a long period of time slows down ion transport. The effect is reversible: after annealing the same pellet at elevated temperature, the original high ion conductivity is observed again. We attribute this finding to the influence of moisture on Li ion dynamics.

When compared with results from NMR spectroscopy and DFT calculations presented in the literature so far, we have to keep in mind that DC conductivity measurements probe long-range ion transport while NMR is sensitive to the local barriers between next neighbouring Li ions. Moreover, whereas $E_{\text{a},\sigma}$ represents an average over the whole potential landscape, Li NMR is able to characterise individual diffusion processes

whose superposition results in overall ion transport measured by conductivity spectroscopy in the so-called low-frequency range, *i.e.*, the DC limit.

Acknowledgements

We thank our colleagues at the TU Graz for valuable discussions. Financial support by the Deutsche Forschungsgemeinschaft (DFG Research Unit 1277, grant no. WI3600/2-2 and 4-1) as well as by the Austrian Federal Ministry of Science, Research and Economy, and the Austrian National Foundation for Research, Technology and Development (CD-Laboratory of Lithium Batteries: Ageing Effects, Technology and New Materials) is greatly appreciated.

References

- 1 J. Sakamoto, in *Handbook of Solid State Batteries*, World Scientific, 2015, pp. 391–414.
- 2 K. Takada, *Acta Mater.*, 2013, **61**, 759–770.
- 3 P. Knauth, *Solid State Ionics*, 2009, **180**, 911–916.
- 4 N. Kamaya, K. Homma, Y. Yamakawa, M. Hirayama, R. Kanno, M. Yonemura, T. Kamiyama, Y. Kato, S. Hama, K. Kawamoto and A. Mitsui, *Nat. Mater.*, 2011, **10**, 682–686.
- 5 A. Hayashi and M. Tatsumisago, *Electron. Mater. Lett.*, 2012, **8**, 199–207.
- 6 M. Tatsumisago and A. Hayashi, *Int. J. Appl. Glass Sci.*, 2014, **5**, 226–235.
- 7 V. Epp and M. Wilkening, in *Handbook of Solid State Batteries*, World Scientific, 2015, pp. 133–190.
- 8 K. Minami, F. Mizuno, A. Hayashi and M. Tatsumisago, *Solid State Ionics*, 2007, **178**, 837–841.
- 9 M. Park, X. Zhang, M. Chung, G. B. Less and A. M. Sastry, *J. Power Sources*, 2010, **195**, 7904–7929.
- 10 V. Thangadurai, S. Narayanan and D. Pinzaru, *Chem. Soc. Rev.*, 2014, **43**, 4714–4727.
- 11 H. Buschmann, J. Dölle, S. Berendts, A. Kuhn, P. Bottke, M. Wilkening, P. Heitjans, A. Senyshyn, H. Ehrenberg, A. Lotnyk, V. Duppel, L. Kienle and J. Janek, *Phys. Chem. Chem. Phys.*, 2011, **13**, 19378–19392.
- 12 A. Kuhn, S. Narayanan, L. Spencer, G. Goward, V. Thangadurai and M. Wilkening, *Phys. Rev. B: Condens. Matter Mater. Phys.*, 2011, **83**, 094302.
- 13 S. Narayanan, V. Epp, M. Wilkening and V. Thangadurai, *RSC Adv.*, 2012, **2**, 2553–2561.
- 14 H. Deisereth, S. Kong, H. Eckert, J. Vannahme, C. Reiner, T. Zaif and M. Schlosser, *Angew. Chem.*, 2008, **120**, 767–770.
- 15 O. Pecher, S. T. Kong, T. Goebel, V. Nickel, K. Weichert, C. Reiner, H. J. Deisereth, J. Maier, F. Haarmann and D. Zahn, *Chem.-Eur. J.*, 2010, **16**, 8349–8354.
- 16 V. Epp, Ö. Gün, H.-J. Deisereth and M. Wilkening, *J. Phys. Chem. Lett.*, 2013, **4**, 2118–2123.
- 17 H. Aono, E. Sugimoto, Y. Sadaoka, N. Imanaka and G. Adachi, *J. Electrochem. Soc.*, 1990, **137**, 1023–1027.
- 18 H. Aono, E. Sugimoto, Y. Sadaoka, N. Imanaka and G. Adachi, *J. Electrochem. Soc.*, 1989, **136**, 590–591.
- 19 J. Fu, *J. Am. Ceram. Soc.*, 1997, **80**, 1901–1903.

- 20 K. Takahashi, J. Ohmura, D. Im, D. J. Lee, T. Zhang, N. Imanishi, A. Hirano, M. B. Phillipps, Y. Takeda and O. Yamamoto, *J. Electrochem. Soc.*, 2012, **159**, A342–A348.
- 21 P. Maldonado-Manso, E. R. Losilla, M. Martínez-Lara, M. A. G. Aranda, S. Bruque, F. E. Mouahid and M. Zahir, *Chem. Mater.*, 2003, **15**, 1879–1885.
- 22 F. E. Mouahid, M. Zahir, P. Maldonado-Manso, S. Bruque, E. R. Losilla, D. Chimie, C. Doukkali and E. Jadida, *J. Mater. Chem.*, 2001, **3**, 3258–3263.
- 23 K. Takada, M. Tansho, I. Yanase, T. Inada, A. Kajiyama, M. Kouuchi, S. Kondo and M. Watanabe, *Solid State Ionics*, 2001, **139**, 241–247.
- 24 J. Fu, *J. Mater. Sci.*, 1998, **33**, 1549–1553.
- 25 W. E. Tenhaeff, E. Rangasamy, Y. Wang, A. P. Sokolov, J. Wolfenstine, J. Sakamoto and N. J. Dudney, *ChemElectroChem*, 2014, **1**, 375–378.
- 26 J. Fu, *Solid State Ionics*, 1997, **96**, 195–200.
- 27 P. Bron, S. Johansson, K. Zick, J. Schmedt auf der Günne, S. Dehnen and B. Roling, *J. Am. Chem. Soc.*, 2013, **135**, 15694–15697.
- 28 F. Mizuno, A. Hayashi, K. Tadanaga and M. Tatsumisago, *Adv. Mater.*, 2005, **17**, 918–921.
- 29 I. Y. Pinus, A. V. Khoroshilov, K. S. Gavrichev, V. P. Tarasov and A. B. Yaroslavtsev, *Solid State Ionics*, 2012, **212**, 112–116.
- 30 J. T. S. Irvine, D. C. Sinclair and A. R. West, *Adv. Mater.*, 1990, **2**, 132–138.
- 31 K. Arbi, S. Mandal, J. M. Rojo and J. Sanz, *Chem. Mater.*, 2002, **14**, 1091–1097.
- 32 A. Hayashi, K. Noi, A. Sakuda and M. Tatsumisago, *Nat. Commun.*, 2012, **3**, 856–860.
- 33 C. Ma, K. Chen, C. Liang, C.-W. Nan, R. Ishikawa, K. More and M. Chi, *Energy Environ. Sci.*, 2014, **7**, 1638–1642.
- 34 K. Arbi, W. Bucheli, R. Jiménez and J. Sanz, *J. Eur. Ceram. Soc.*, 2015, **35**, 1477–1484.
- 35 S. Hasegawa, N. Imanishi, T. Zhang, J. Xie, A. Hirano, Y. Takeda and O. Yamamoto, *J. Power Sources*, 2009, **189**, 371–377.
- 36 S. D. Jackman and R. A. Cutler, *J. Power Sources*, 2013, **230**, 251–260.
- 37 J. L. Narváez-Semanate and A. C. M. Rodrigues, *Solid State Ionics*, 2010, **181**, 1197–1204.
- 38 E. C. Bucharsky, K. G. Schell, A. Hintennach and M. J. Hoffmann, *Solid State Ionics*, 2015, **274**, 77–82.
- 39 H. Morimoto, M. Hirukawa, A. Matsumoto, T. Kurabayashi, N. Ito and S. Tobishima, *Electrochemistry*, 2014, **82**, 870–874.
- 40 H. Morimoto, H. Awano, J. Terashima, Y. Shindo, S. Nakanishi, N. Ito, K. Ishikawa and S. I. Tobishima, *J. Power Sources*, 2013, **240**, 636–643.
- 41 G. B. Kunshina, O. G. Gromov, E. P. Lokshin and V. T. Kalinnikov, *Russ. J. Inorg. Chem.*, 2014, **59**, 424–430.
- 42 S. Duluard, A. Paillassa, L. Puech, P. Vinatier, V. Turq, P. Rozier, P. Lenormand, P. L. Taberna, P. Simon and F. Ansart, *J. Eur. Ceram. Soc.*, 2013, **33**, 1145–1153.
- 43 S. D. Jackman and R. A. Cutler, *J. Power Sources*, 2012, **218**, 65–72.
- 44 Y. Yoon, J. Kim, C. Park and D. Shin, *J. Ceram. Process. Res.*, 2013, **14**, 563–566.
- 45 C. R. Mariappan, *Appl. Phys. A: Mater. Sci. Process.*, 2014, **117**, 847–852.
- 46 M. Kotobuki, M. Koishi and Y. Kato, *Ionics*, 2013, **19**, 1945–1948.
- 47 M. Kotobuki and M. Koishi, *Ceram. Int.*, 2012, **39**, 4645–4649.
- 48 N. V. Kosova, E. T. Devyatkina, A. P. Stepanov and A. L. Buzlukov, *Ionics*, 2008, **14**, 303–311.
- 49 V. Epp, Q. Ma, E.-M. Hammer, F. Tietz and M. Wilkening, 2015, unpublished results.
- 50 B. Lang, B. Ziebarth and C. Elsässer, *Chem. Mater.*, 2015, **27**, 5040–5048.

3.1.2 Rapid Li Ion Dynamics in the Interfacial Regions of Nanocrystalline Solids

Dieser Artikel beschäftigt sich mit nanokristallinem Lithiumborhydrid, einem Material das bei erhöhten Temperaturen als Elektrolyt für Festkörperbatterien eingesetzt werden kann und zudem noch als Modellsubstanz dient, um Li-Bewegungsprozesse im hohen Volumenanteil der Grenzflächenregionen separat zu erfassen. Grenzflächenvolumina werden durch Hochenergiekugelmahlen in das Material eingetragen; es wird erwartet, dass diese Regionen hoch defektreich sind.

Um den Einfluss unterschiedlicher Kristallitgrößen und den Unordnungsgrad auf das Diffusionsverhalten zu untersuchen, wurde sowohl mikrokristallines LiBH_4 als auch nanokristallines LiBH_4 vermessen. Die Nanostrukturierung des Feststoffes führte zu einem vergrößerten Volumenanteil ungeordneter Grenzflächen, die oftmals schnelle Diffusionspfade für Ladungsträger bereitstellen und somit die makroskopische Ionenleitfähigkeit erhöhen. Mit Hilfe von zeitabhängigen ^7Li NMR Messungen ist es gelungen, die mobilen Li Ionen, die sich entlang der Grenzflächen bewegen, von den langsameren Ionen im Bulk zu unterscheiden und selektiv nur die Ionendynamik dieser Ladungsträger zu untersuchen. Diese beiden unterschiedlichen Prozesse konnten zudem noch über ^7Li -NMR-Spin-Gitter-Relaxationsmessungen sichtbar gemacht werden, wodurch es ebenfalls möglich war Aktivierungsenergien zu bestimmen. Für die schnellen Austauschprozesse in den Grenzflächen wurden mit $E_A = 0,18 \text{ eV}$ äußerst geringe Werte erhalten und deutlich niedrigere als für die Diffusion in den inneren Regionen der Kristallite selbst.

Rapid Li Ion Dynamics in the Interfacial Regions of Nanocrystalline Solids

S. Breuer, M. Uitz, and H. M. R. Wilkering, *J. Phys. Chem. Lett.*, 2018, **9**, 2093-2097.

Rapid Li Ion Dynamics in the Interfacial Regions of Nanocrystalline Solids

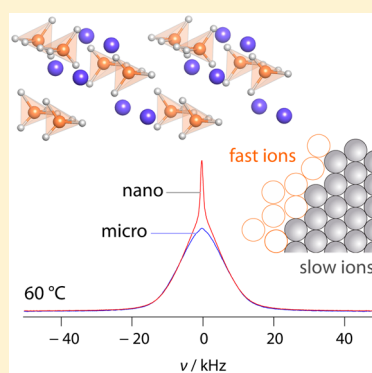
S. Breuer,[†] M. Uitz,[†] and H. M. R. Wilkering^{*,†,‡,ID}

[†]Christian Doppler Laboratory for Lithium Batteries, and Institute for Chemistry and Technology of Materials, Graz University of Technology, Stremayrgasse 9, 8010 Graz, Austria

[‡]Alistore-ERI European Research Institute, 33 rue Saint Leu, 80039 Amiens, France

Supporting Information

ABSTRACT: Diffusive processes are ubiquitous in nature. In solid state physics, metallurgy and materials science the diffusivity of ions govern the functionality of many devices such as sensors or batteries. Motional processes on surfaces, across interfaces or through membranes can be quite different to that in the bulk. A direct, quantitative description of such local diffusion processes is, however, rare. Here, we took advantage of ⁷Li longitudinal nuclear magnetic relaxation to study, on the atomic length scale, the diffusive motion of lithium spins in the interfacial regions of nanocrystalline, orthorhombic LiBH₄. Magnetization transients and free induction decays revealed a fast subset of Li ions having access to surface pathways that offer activation barriers (0.18 eV) much lower than those in the crystalline bulk regions (0.55 eV). These observations make orthorhombic borohydride a new nanostructured model system to study disorder-induced enhancements in interfacial diffusion processes.



Nanostructured ceramics contain crystallites with at least one dimension in the nanometre regime. Many experiments into such compounds reveal enhanced ion dynamics as compared to the situation in the coarse-grained counterparts.^{1–3} Also other properties, such as electrical and optical features, may benefit from shrinking the crystallite size. It is, however, not easy to identify the true origin of the changes or enhancements seen. The structurally disordered interfacial regions of nanocrystalline ceramics are considered to be responsible for these effects.^{3–5} In the case of ion dynamics, these areas may act as hosts for highly mobile charge carriers that govern overall transport properties. Interfacially controlled fast diffusion pathways are assumed to form a through-going network that boosts macroscopic, ionic transport. Thinking about applications, fast ion transport^{6,7} is needed to realize new energy storage systems or advanced sensors.^{8–11}

In general, increased ion dynamics is often explained with the help of space charge regions¹² or local disorder.³ Disorder in the interfacial regions is the general description for, e.g., an unfavorable arrangement of the ions, which are expected to be subjected to stress or local metastable states. To study exclusively the diffusivity of the ions in the interfacial regions of a nanoceramic is the motivation of this work. Here, we chose nuclear magnetic resonance (NMR) to directly measure the dynamic behavior from an angstrom point of view. While Schirmes et al. used nanoscopic electrostatic force spectroscopy to shed light on ion dynamics in interfacial regions of a nanostructured glass ceramic,⁴ NMR is able to probe the change in dynamics at atomic scale. For our purpose, nanocrystalline lithium borohydride (LiBH₄, see also ref 13) served as a very rewarding test substance (see Figure 1, which

illustrates the crystal structure of the poorly ion conducting orthorhombic phase).

Fortunately, since the volume fraction of interfacial regions in nanomaterials is large, a sufficiently high number of ions reside in or near these interfacial areas. From the point of view of NMR, this number density of spin-carrying species has been shown to be adequate to discriminate the ions in the interfaces from those located in the bulk.^{5,14} For those residing in the interfacial regions, higher diffusivities and lower hopping barriers are expected. Although in the very few NMR studies presented so far increased NMR SLR rates have been attributed to these ions,^{5,14} a significant difference in activation energies has not yet be found. While increased NMR relaxation rates may have different origins, a prominently lower, mean activation energy in combination with fast relaxation would be a clear-cut argument for enhanced diffusivity. In the quest for an appropriate inorganic material to test our assumption, the orthorhombic form of LiBH₄ caught our interest. Indeed, LiBH₄ turned out to be the so far missing model system to test our hypothesis.

In the present case, we recorded ⁷Li NMR spin-lattice relaxation magnetization transients. While those of microcrystalline LiBH₄ only revealed a single component, the transients of nanocrystalline LiBH₄ showed two-components. We attributed the fast relaxing component to the highly mobile Li ions in the interfacial regions. The corresponding activation energy, deduced from variable-temperature experiments, turned

Received: February 8, 2018

Accepted: April 9, 2018

Published: April 9, 2018



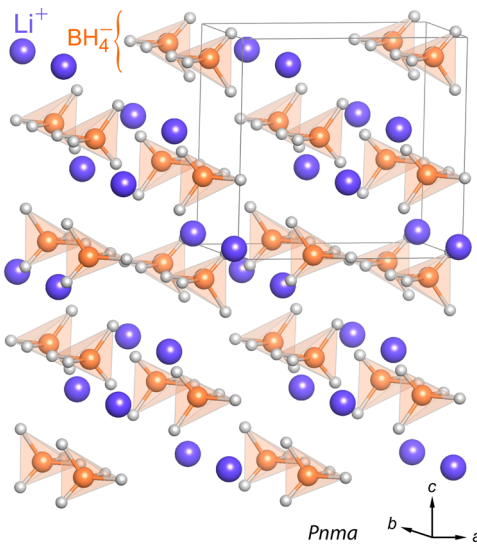


Figure 1. Crystal structure of orthorhombic LiBH_4 (space group *Pnma*). The blue spheres represent the Li ions; tetrahedra in orange illustrate the arrangement of the BH_4 units. In spite of the fast rotational motions of the latter, the Li ions remain unimpressed by these fast dynamics. Instead, they are only subject to extremely slow translational processes in coarse-grained, well-crystalline lithium borohydride. This situation dramatically changes in nanocrystalline LiBH_4 .

out to be much lower for this fast spin-ensemble (0.18 eV) than that of the Li ions in nontreated, that is, coarse-grained LiBH_4 (≈ 0.55 eV).^{15,16} The two spin-ensembles, greatly differing in diffusivity and, thus, spin relaxation behavior, are also clearly seen in ^7Li NMR spectra and free induction decays (FIDs). Such an analysis might also help explain the interfacial effects recently seen for nanoconfined LiBH_4 .^{17,18}

Nanocrystalline LiBH_4 was prepared from the coarse-grained source material, characterized by crystallites with a mean diameter in the micrometer range, through high-energy ball milling. We used a P7 planetary mill (Fritsch) to prepare LiBH_4 with an average crystallite diameter of 20 nm, as verified by X-ray powder diffraction (XRD). XRD confirmed the absence of any phase transformations or impurity phases; milling and characterization of the sample was strictly carried out under protective, water-free Ar atmosphere ($\text{O}_2 < 0.1$ ppm, $\text{H}_2\text{O} < 0.1$ ppm). The nanocrystalline powder was carefully fire-sealed in Duran glass ampules (4 mm in diameter, 3 cm in length) to protect it permanently from any reaction with moisture. It was analyzed via ^7Li (spin-quantum number $I = 3/2$) NMR spectroscopy using an Avance III solid-state spectrometer. The Avance III was connected to a shimmed cryomagnet with a nominal field of 7 T. We applied a saturation recovery pulse sequence to record the longitudinal recovery of the macroscopic magnetization $M_z(t_w)$ from a defined nonequilibrium state toward thermal equilibrium. At the beginning of each experiment, the spins populate the four energetically distinct NMR Zeeman levels according to Boltzmann's spin distribution. We used a train of $\pi/2$ radiofrequency pulses to destroy any longitudinal magnetization; the recovery of the spin-system, i.e., spin transitions between the Zeeman levels, is in our case solely induced by self-diffusion processes of the Li ions. LiBH_4 is a so-called SLR background free model substance. After a variable waiting time, t_w , we detected $M_z(t_w)$ via a $\pi/2$ detection pulse. We analyzed either directly the FIDs or the complete

curve $M_z(t_w)$, which is obtained by plotting the area under the FID as a function of t_w . NMR spectra were obtained by Fourier transformation of the FIDs. The pulse lengths varied from 2.6 to $3.2 \mu\text{s}$ depending on temperature. We used a broadband probe designed for solid-state NMR; the temperature in the sample chamber was controlled and stabilized with heated air (± 1 K) and NiCr-Ni thermocouples in the direct vicinity of the sample.

In Figure 2a variable-temperature ^7Li NMR spectra of nanocrystalline LiBH_4 are shown; the corresponding ^7Li NMR

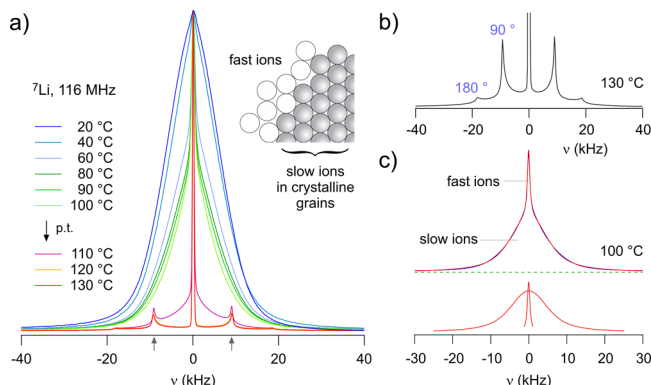


Figure 2. (a) ^7Li NMR spectra of nanocrystalline LiBH_4 . Well below the phase transition, orthorhombic LiBH_4 has to be described with a two-component (central) line. Above 120 °C, the electric quadrupole powder pattern known for highly conducting hexagonal LiBH_4 shows up¹⁹ (see the sharp pattern in panel b) with the 90° and 180° singularities indicated. (c) While the broad central line of orthorhombic LiBH_4 reflects the Li ions inside the crystalline grains, the mobile ones in the disordered interfacial regions (see inset in a) produce the translational motion-induced NMR line on top of the broad Gaussian shaped signal. The latter is completely absent for coarse-grained LiBH_4 (see Figure S1, Supporting Information) and, thus, is a characteristic feature of the nanocrystalline sample.

^1H NMR spectra of coarse-grained LiBH_4 are presented in Figures S1 and S2. Below $T_{\text{trans}} = 381$ K, the hydride crystallizes with orthorhombic structure. At low temperatures, the NMR central transition is dominated by a broad Gaussian line. Strong dipole–dipole interactions are responsible for this line broadening. The quadrupole intensities are suppressed with the one-pulse excitation applied; they, however, can be made visible by echo techniques (see Figure S3). Only sufficiently fast Li ion diffusion processes, with rates much larger than the line width, would be able to motionally narrow the line. With increasing temperature, we clearly see that such heterogeneous narrowing sets in, which results in a so-called two-component line shape. The motionally narrowed component on top of the broad Gaussian (see Figure 2c) reflects those ions already having access to fast diffusion pathways. It is, therefore, ascribed to the ions residing in the structurally disordered interfacial regions. The more pronounced motional narrowing caused by this subset of ions, the better the separation from the broad Gaussian line reflecting the less mobile ions. Worth noting, for chemically identical but coarse-grained LiBH_4 , the narrowed component is missing (see Figure S1, Supporting Information).

The majority of the Li ions belong to the immobile group represented by the broad line. As this line does not change significantly with T , and since its line width is much larger than that of the narrow component, precise deconvolution of the spectra is possible to determine the individual area fractions. As

an example, at 100 °C, the number of highly mobile Li ions reached almost 18% (Figure 2a). This value may be regarded as the upper limit of ions enjoying a high mobility in or near the interfacial regions. Similar two-component ¹H and ⁷Li NMR line shapes, as well their evolution with temperature, have been observed by Conradi's group for nanostructured, ball milled MgH₂,²⁰ other LiBH₄-based compounds,^{21,22} and the dispersed ionic conductors Li₂X₂O₃ (X = Al, B),^{5,14} for example. Also, in our case, the corresponding ¹H NMR spectra of nanocrystalline LiBH₄ reveal a pronounced two-component line shape (see Figure S2 for further details and the corresponding discussion). The narrow ¹H NMR component represents hydrogen spins of rapid BH₄⁻ units near the interfacial regions as already discussed in the literature.^{13,21,22} Of course, defects introduced into the interior of the nanometer-sized LiBH₄ grains might also be responsible for enhanced dynamics. In our opinion, an area fraction of 18% of mobile lithium ions is in good agreement with the number of spins residing in a 1–2 nm thick interfacial region covering the crystalline cores.²³ This assignment perfectly agrees with interpretations of NMR lines from related compounds (see, e.g., the study by Conradi and co-workers,²¹ in particular).

At temperatures higher than T_{trans} , LiBH₄ undergoes a reversible first-order phase transition (p.t.). Layer-structured, hexagonal LiBH₄, being stable until the melting point of LiBH₄, is a very fast 2D ion conductor.¹⁹ The corresponding NMR signal then consists of a sharp (first order) spin-3/2 quadrupolar powder pattern with a narrow central line completely free of any residual dipolar interactions (Figure 2c). Below T_{trans} , XRD confirmed that no hexagonal LiBH₄ has formed yet.

The two spectral components seen in the ⁷Li NMR Fourier transforms of orthorhombic LiBH₄ are also distinguishable in the time domain, i.e., the corresponding FIDs of the central line(s) are composed of two signals decaying with different ⁷Li NMR spin–spin relaxation rates (Figure 3a). The fast decaying contribution refers to the slow Li ions in the crystalline grains,

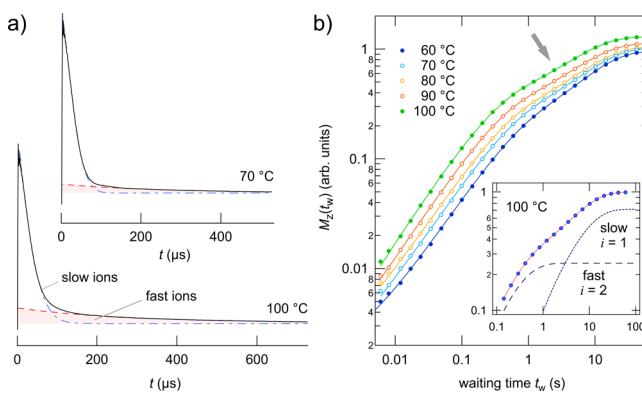


Figure 3. (a) FIDs of nanocrystalline orthorhombic LiBH₄, which are composed of a fast and slowly decaying part, reflecting the dynamically different spin reservoirs. Dashed lines show fits with exponential functions. (b) ⁷Li NMR recovery of longitudinal magnetization in nanocrystalline LiBH₄. The overall transients M_z show biexponential behavior. Those of coarse-grained LiBH₄ just reveal a single component, which is identical with the one governing the recovery at long waiting times. Solid lines in panel b show fits with a sum of two stretched exponentials (the individual functions are shown in the inset; stretching exponents γ_i turned out to be 0.91 (fast spins) and 0.81 (slow spins), respectively).

whereas Fourier transformation of the slowly decaying part yields the narrow NMR line representing the rapid Li ions. To analyze the buildup of the two components with increasing waiting time t_w , we parametrized the complete FIDs with a sum of two exponentials and calculated the areas A_i ($i = \text{fast, slow}$) under the curves as a function of t_w . The resulting two transients $M_{z,i}(t_w)$ were analyzed with stretched exponentials $M'_{z,i} \propto 1 - \exp(-(t_w/T_{1,i})^{\gamma_i})$ to extract the individual ⁷Li NMR rates of the two spin ensembles. The temperature dependence of $1/T_{1,i}$ is shown in Figure 4. The rates unequivocally show a marked difference in spin relaxation behavior.

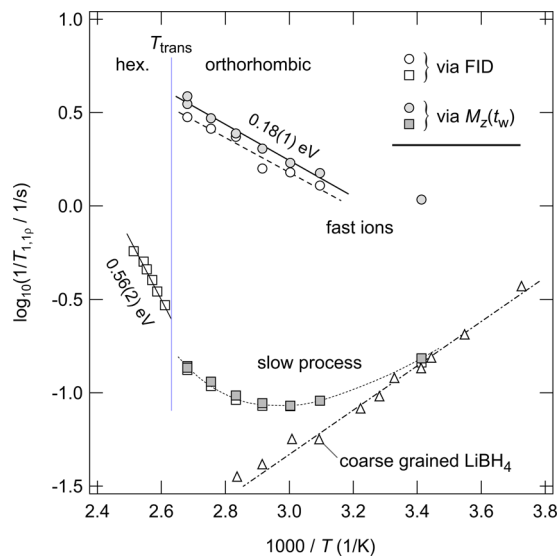


Figure 4. Temperature dependence of the ⁷Li NMR diffusion-induced relaxation rates of nanocrystalline LiBH₄ recorded at 116 MHz. In orthorhombic LiBH₄, fast and slow SLR processes can be clearly identified, which were either discriminated via the evaluation of FIDs or overall magnetization transients of a saturation recovery experiment. The fast spins are attributed to those in the structurally disordered interfacial regions of nano-LiBH₄. For comparison, the rates of coarse-grained, unmilled LiBH₄ are also shown (Δ) (see ref 16). These, as well as those characterizing the slow dynamic processes of nano-LiBH₄, are governed by rotational dynamics rather than by translational Li ion hopping. See text for further explanation.

Alternatively, we also plotted the area under the complete FIDs as a function of t_w . The resulting transient (see Figure 3b) can only be parametrized with a sum of two stretched exponentials $M_z = \sum_i(M'_{z,i})$. Note that transient solely refers to the central transition of the ⁷Li NMR spectrum of LiBH₄. In Figure 3b, several of these transients M_z are shown, which were roughly normalized for a better comparison of their shapes. It is evident that overall spin recovery does not follow a single exponential function (see the dent marked with an arrow in Figure 3b) and the deconvolution of the overall magnetization transient in the inset. The spins attributed to the interfacial regions recover thermal equilibrium much faster than those in the interior of the grains. Already, after a waiting time of 3 s, longitudinal magnetization $M_{z,\text{fast}}$ has reached its saturation value. The ensemble of fast relaxing spins has access to fast diffusion barriers and to low (local) activation barriers, and they are subjected to significantly faster Li⁺ translational diffusion than those residing in the bulk regions. Spin–lattice relaxation of the latter ions, as indicated by the broad ⁷Li NMR line width, is driven by rotational motions of the BH₄⁻ units rather than by

ion hopping processes¹⁹ (see also the recent NMR study on KAlH_4 ²⁴). These motions have, however, no influence on the ^7Li NMR line shape, as they do not average homonuclear Li–Li dipolar interactions giving rise to line broadening. Motion-induced narrowing of the NMR line is only possible by effective translational Li^+ ion dynamics.¹⁹

In Figure 4 the temperature dependence of the two rates $1/T_{1,i}$ is shown. $1/T_{1,i}$ rates were either obtained by analyzing the FIDs or by evaluating the overall transients M_z . Straight lines in Figure 4 represent fits using Arrhenius laws, $1/T_1 \propto \exp -E_a/(k_B T)$, to determine the underlying activation energy E_a . Here, for the fast spin ensemble, $E_{a,\text{fast}}$ turned out to be $0.18(1)$ eV, almost independent of the way to extract the rates $1/T_{1,\text{fast}}$. For hexagonal, nanocrystalline LiBH_4 , that is, at temperatures higher than T_{trans} , ion dynamics in the bulk is rapid as well and has to be characterized by an activation energy of $0.52(1)$ eV. This value is in line with earlier studies^{15,19} and agrees with the activation energy from direct current (d.c.) conductivity measurements.

Ion transport in coarse-grained orthorhombic LiBH_4 is expected to be governed by a much larger activation energy than 0.18 eV. Indeed, long-range ion transport, as seen by d.c. conductivity spectroscopy, yields $E_a = 0.56$ eV. For comparison, the ^7SLR NMR rates of coarse-grained LiBH_4 are also included in Figure 4; they describe the high- T flank of the corresponding $1/T_1(1/T)$ peak,¹⁹ which is caused by rapid BH_4^- rotations. Li^+ translational hopping is too slow to influence these rates; instead, SLR is almost exclusively driven by rotational dynamics (see above). The ^7Li spins sense these rotational motions as an immobile spectator; they do not take part themselves. In nanocrystalline LiBH_4 , on the other hand, and if prepared by ball milling, the rates $1/T_{1,\text{slow}}$ follow a curved, non-Arrhenius type temperature behavior, indicating an additional source of spin–lattice relaxation in orthorhombic LiBH_4 . Although mechanical treatment in planetary mills mainly generates fast ions in the interfacial regions, defects may also be introduced in the crystalline nanograins as briefly mentioned above. These point defects may facilitate, to a lesser extent, also ion hopping in the bulk (see also ref 16). In addition, the curved behavior of $1/T_{1,\text{slow}}$ presumably indicates a smooth transition from orthorhombic to hexagonal LiBH_4 , which is sharp for coarse-grained LiBH_4 but proceeds on a much broader temperature range for the ball-milled sample.¹⁶

In summary, through time-domain ^7Li NMR, we selectively studied fast Li ion dynamics in a nanocrystalline model compound such as LiBH_4 . A fast spin ensemble was identified that has to be described with both enhanced NMR SLR rates and a very low activation energy of only $0.18(1)$ eV. We attribute this fast ensemble to those ions that have access to rapid translational exchange processes in the disordered interfacial regions of nano-LiBH₄. Such processes are completely absent for coarse-grained LiBH_4 . Our results highlight, from an atomic point of view, how nanostructuring directly affects (local) Li ion diffusion parameters in an otherwise poorly conducting ceramic.

ASSOCIATED CONTENT

Supporting Information

The Supporting Information is available free of charge on the ACS Publications website at DOI: [10.1021/acs.jpclett.8b00418](https://doi.org/10.1021/acs.jpclett.8b00418).

Further ^7Li and ^1H NMR spectra of both microcrystalline and nanocrystalline LiBH_4 ([PDF](#))

AUTHOR INFORMATION

Corresponding Author

*E-mail: wilkening@tugraz.at.

ORCID

H. M. R. Wilkening: 0000-0001-9706-4892

Notes

The authors declare no competing financial interest.

ACKNOWLEDGMENTS

Financial support by the Deutsche Forschungsgemeinschaft (DFG) (Research Unit 1277, WI3600/2-2 and 4-1) is greatly appreciated. Further support by the Austrian Federal Ministry of Science, Research and Economy, as well as the Austrian National Foundation for Research, Technology and Development is highly appreciated.

REFERENCES

- (1) Prutsch, D.; Breuer, S.; Uitz, M.; Bottke, P.; Langer, J.; Lunghammer, S.; Philipp, M.; Posch, P.; Pregartner, V.; Stanje, B.; Dunst, A.; Wohlmuth, D.; Brandstätter, H.; Schmidt, W.; Epp, V.; Chadwick, A.; Hanzu, I.; Wilkening, M. Nanostructured Ceramics: Ionic Transport and Electrochemical Activity - A Short Journey Across Various Families of Materials. *Z. Phys. Chem.* **2017**, *231*, 1361.
- (2) Indris, S.; Heitjans, P.; Roman, H. E.; Bunde, A. Nanocrystalline versus Microcrystalline $\text{Li}_2\text{O}:\text{B}_2\text{O}_3$ Composites: Anomalous Ionic Conductivities and Percolation Theory. *Phys. Rev. Lett.* **2000**, *84*, 2889.
- (3) Heitjans, P.; Indris, S. Diffusion and Ionic Conduction in Nanocrystalline Ceramics. *J. Phys.: Condens. Matter* **2003**, *15*, R1257.
- (4) Schirmeisen, A.; Taskiran, A.; Fuchs, H.; Bracht, H.; Murugavel, S.; Roling, B. Fast Interfacial Ionic Conduction in Nanostructured Glass Ceramics. *Phys. Rev. Lett.* **2007**, *98*, 225901.
- (5) Heitjans, P.; Wilkening, M. Ion Dynamics at Interfaces: Nuclear Magnetic Resonance Studies. *MRS Bull.* **2009**, *34*, 915.
- (6) Knauth, P. Inorganic Solid Li Ion Conductors: An Overview. *Solid State Ionics* **2009**, *180*, 911.
- (7) Uitz, M.; Epp, V.; Bottke, P.; Wilkening, M. Ion Dynamics in Solid Electrolytes for Lithium Batteries. *J. Electroceram.* **2017**, *38*, 142.
- (8) Whittingham, M. S. Lithium Batteries and Cathode Materials. *Chem. Rev.* **2004**, *104*, 4271.
- (9) Aricó, A. S.; Bruce, P.; Scrosati, B.; Tarascon, J.-M.; van Schalkwijk, W. Nanostructured Materials for Advanced Energy Conversion and Storage Devices. *Nat. Mater.* **2005**, *4*, 366.
- (10) Bruce, P. G.; Scrosati, B.; Tarascon, J.-M. Nanomaterials for Rechargeable Lithium Batteries. *Angew. Chem., Int. Ed.* **2008**, *47*, 2930.
- (11) Goodenough, J. B.; Kim, Y. Challenges for Rechargeable Li Batteries. *Chem. Mater.* **2010**, *22*, 587.
- (12) Maier, J. Ionic Conduction in Space Charge Regions. *Prog. Solid State Chem.* **1995**, *23*, 171.
- (13) Corey, R. L.; Shane, D. T.; Bowman, R. C.; Conradi, M. S. Atomic Motions in LiBH_4 by NMR. *J. Phys. Chem. C* **2008**, *112*, 18706–18710.
- (14) Wilkening, M.; Indris, S.; Heitjans, P. Heterogeneous Lithium Diffusion in Nanocrystalline $\text{Li}_2\text{O}:\text{Al}_2\text{O}_3$ Composites. *Phys. Chem. Chem. Phys.* **2003**, *5*, 2225.
- (15) Matsuo, M.; Nakamori, Y.; Orimo, S.; Maekawa, H.; Takamura, H. Lithium Superionic Conduction in Lithium Borohydride Accompanied by Structural Transition. *Appl. Phys. Lett.* **2007**, *91*, 224103.
- (16) Epp, V.; Wilkening, M. Motion of Li^+ in Nano-Engineered LiBH_4 and $\text{LiBH}_4:\text{Al}_2\text{O}_3$ - Comparison with the Microcrystalline Form. *ChemPhysChem* **2013**, *14*, 3706.
- (17) Blanchard, D.; Nale, A.; Sveinbjörnsson, D.; Eggenhuisen, T. M.; Verkuijen, M. H. W.; Suwarno, S.; Vegge, T.; Kentgens, A. P. M.; de Jongh, P. E. Nanoconfined LiBH_4 as a Fast Lithium Ion Conductor. *Adv. Funct. Mater.* **2015**, *25*, 184.

- (18) Verkuijlen, M. H. W.; Ngene, P.; de Kort, D. W.; Barré, C.; Nale, A.; van Eck, E. R. H.; van Bentum, P. J. M.; de Jongh, P. E.; Kentgens, A. P. M. Nanoconfined LiBH₄ and Enhanced Mobility of Li⁺ and BH₄⁻ Studied by Solid-State NMR. *J. Phys. Chem. C* **2012**, *116*, 22169–22178.
- (19) Epp, V.; Wilkening, M. Fast Li Diffusion in Crystalline LiBH₄ due to Reduced Dimensionality: Frequency-Dependent NMR Spectroscopy. *Phys. Rev. B: Condens. Matter Mater. Phys.* **2010**, *82*, 020301.
- (20) Corey, R. L.; Ivancic, T. M.; Shane, D. T.; Carl, E. A.; Bowman, R. C.; Bellostas von Colbe, J. M.; Dornheim, M.; Bormann, R.; Huot, J.; Zidan, R.; Stowe, A. C.; Conradi, M. S. Hydrogen Motion in Magnesium Hydride by NMR. *J. Phys. Chem. C* **2008**, *112*, 19784–19790.
- (21) Zou, H.; Gradišek, A.; Emery, S. B.; Vajo, J. J.; Conradi, M. S. LiBH₄ in Aerogel: Ionic Motions by NMR. *J. Phys. Chem. C* **2017**, *121*, 15114–15119.
- (22) Shane, D. T.; Corey, R. L.; Rayhel, L. H.; Wellons, M.; Teprovich, J. A.; Zidan, R.; Hwang, S.-J.; Bowman, R. C.; Conradi, M. S. NMR Study of LiBH₄ with C₆₀. *J. Phys. Chem. C* **2010**, *114*, 19862–19866.
- (23) Vollath, D. *Nanomaterials - An Introduction to Synthesis, Properties and Applications*; Wiley-VCH, 2008; pp 21–22.
- (24) Sorte, E. G.; Emery, S. B.; Majzoub, E. H.; Ellis-Caleo, T.; Ma, Z. L.; Hammann, B. A.; Hayes, S. E.; Bowman, R. C.; Conradi, M. S. NMR Study of Anion Dynamics in Solid KAlH₄. *J. Phys. Chem. C* **2014**, *118*, 5725–5732.

3.2 Nanokristalline Fluor-Ionenleiter

Neben den aktuell am besten erforschten und leistungsfähigsten elektrochemischen Speichern, den Lithium-Ionen-Batterien, ist die Suche nach alternativen Methoden ein essentielles Thema der Materialwissenschaften. Bereits bekannt sind in diesem Zusammenhang Systeme mit H^+ , Na^+ oder Mg^{2+} als mobilen Ionen, die allerdings allesamt einige Limitierungen aufweisen. Eine vielversprechende neue Technologie stellt die Fluorid-Ionen-Batterie dar, die nur aus Feststoffen besteht und die F^- -Anionen als mobile Ladungsträger nutzt. Fluorid-Ionen sind aufgrund ihrer extrem hohen Elektronegativitäten stabil. Ob auch die zur Zeit anvisierten F^- -Anionenleiter ein ausreichendes elektrochemisches Stabilitätsfenster aufweisen, müssen zukünftige Studien noch zeigen. Die folgenden Beiträge befassen sich mit der Herstellung und Charakterisierung von neuen nanokristallinen Fluor-Ionenleitern, die für einen Einsatz als Elektroden oder Elektrolytmaterialien in Fluorid-Ionen-Batterien in Frage kommen könnten.⁶.

70

3.2.1 Mismatch in cation size causes rapid anion dynamics in solid electrolytes: the role of the Arrhenius pre-factor

Der erste Beitrag widmet sich dem Verständnis der Ionendynamik in metastabilem, nanokristallinen $(\text{Ba},\text{Ca})\text{F}_2$. Dabei stand das Herausarbeiten der Korrelation von lokalen Sprungprozessen mit langreichweitigen Diffusions- und Leitfähigkeitsprozessen im Vordergrund.

Die Proben für die Studie wurden durch gemeinsames Kugelmahlen der binären Fluoride hergestellt und mittels Röntgendiffraktometrie beziehungsweise ^{19}F -NMR Magic-Angle-Spinning strukturell charakterisiert. Zur Analyse der Ionendynamik sind sowohl NMR-Spin-Gitter-Relaxationsexperimente als auch Impedanzmessungen durchgeführt worden. Die zentralen Aussagen, die aus dieser Arbeit gewonnen werden konnten, sind zum einen, dass die erhöhte lokale Ladungsträgerbewegung bei den Proben mit den höchsten Gesamtleitfähigkeiten vor allem durch höhere absolute NMR-Relaxationsraten und weniger durch verringerte Aktivierungsenergien beeinflusst wird. Somit konnte hier der präexponentielle Faktor der zugrundeliegenden Arrhenius-Beziehung, der von der Anzahl der mobilen Spins, dem Frequenzfaktor und Entropieeffekten beeinflusst ist, als jener Parameter identifiziert werden, der direkten Einfluss auf die kurzreichweite Diffusion in strukturell ungeordnetem $(\text{Ba},\text{Ca})\text{F}_2$ hat. Zum anderen wurde deutlich, dass die makroskopischen Eigenschaften, wie etwa die ionische Leitfähigkeit σ_{DC} , im Gegensatz zu Nahordnungen oder lokaler, korrelierter Bewegung, ab einer gewissen Mahldauer kaum noch von der Dauer des Mahlvorganges abhängig sind. Offensichtlich bildet sich bereits bei kurzen Mahldauern ein metastabiles Mischsystem $(\text{Ba},\text{Ca})\text{F}_2$ aus, das genügend Perkolationspfade bietet, um die ionische, makroskopische Leitfähigkeit entscheidend zu prägen.

**Mismatch in cation size causes rapid anion dynamics in solid electrolytes:
the role of the Arrhenius pre-factor**

S. Breuer and M. Wilkening, *Dalton Trans.*, 2018, **47**, 4105-4117.



Cite this: *Dalton Trans.*, 2018, **47**, 4105

Mismatch in cation size causes rapid anion dynamics in solid electrolytes: the role of the Arrhenius pre-factor†

Stefan Breuer *^a and Martin Wilkening ^{a,b}

Crystalline ion conductors exhibiting fast ion dynamics are of utmost importance for the development of, e.g., sensors or rechargeable batteries. In some layer-structured or nanostructured compounds fluorine ions participate in remarkably fast self-diffusion processes. As has been shown earlier, F ion dynamics in nanocrystalline, defect-rich BaF₂ is much higher than that in the coarse-grained counterpart BaF₂. The thermally metastable fluoride (Ba,Ca)F₂, which can be prepared by joint high-energy ball milling of the binary fluorides, exhibits even better ion transport properties. While long-range ion dynamics has been studied recently, less information is known about local ion hopping processes to which ¹⁹F nuclear magnetic resonance (NMR) spin–lattice relaxation is sensitive. The present paper aims at understanding ion dynamics in metastable, nanocrystalline (Ba,Ca)F₂ by correlating short-range ion hopping with long-range transport properties. Variable-temperature NMR line shapes clearly indicate fast and slow F spin reservoirs. Surprisingly, from an atomic-scale point of view increased ion dynamics at intermediate values of composition is reflected by increased absolute spin–lattice relaxation rates rather than by a distinct minimum in activation energy. Hence, the pre-factor of the underlying Arrhenius relation, which is determined by the number of mobile spins, the attempt frequency and entropy effects, is identified as the parameter that directly enhances short-range ion dynamics in metastable (Ba,Ca)F₂. Concerted ion migration could also play an important role to explain the anomalies seen in NMR spin–lattice relaxation.

Received 28th November 2017,
Accepted 10th February 2018

DOI: 10.1039/c7dt04487a

rsc.li/dalton

Introduction

The irregular movement of small anions and cations in crystalline and amorphous solids is a natural phenomenon that plays a key role in many devices as well as technological and geological processes. Extracting general rules from the existing amount of experimental data that control ionic transport and ionic diffusivity is, thus, of importance if we want to optimize devices, such as batteries,^{1–4} relying on dynamic processes of ions. Nanostructured materials play a prominent role in these fields.^{1,5,6}

Although ion dynamics in a huge number of various nano-materials have been studied over the last decades with a wide range of techniques,^{7–11} our picture about ionic diffusivity is far from being completely understood. The introduction of defects, that is, in a more general sense describable with struc-

tural disorder, represents a powerful instrument with which we can control the chemical and physical properties of a material.^{12–17} Ion dynamics sensitively depend on local arrangements. The present work is aimed at describing the interrelations between local disorder and short-range ion dynamics using a suitable model substance that may also be of interest as a fast ion conducting solid electrolyte.^{4,18–23}

The metastable (quasi) solid-solution (Ba,Ca)F₂ served as such model substance.^{24,25} Recently, it has also attracted groups from theory to model ion conductivities.^{26,27} Nanocrystalline Ba_{1-x}Ca_xF₂ ($0 < x < 1$) can easily be prepared by mechanochemical reaction at low temperatures from the binary fluorides BaF₂ and CaF₂.^{24,25} Joint milling the two fluorides forces the cations to mix at atomic scale while the symmetry of the educts remains the same; both BaF₂ and CaF₂ crystallize with antifluorite structure. Thus, over the entire compositional range the original crystal symmetry is preserved whereas local atomic arrangements do, however, differ.²⁸ At $x = 0.5$, and after sufficiently long mechanical treatment, the majority of the F anions are directly surrounded by both Ba and Ca ions without any heavy clustering of Ba- and Ca-rich regions.²⁸ These features, as well as the possibility to prepare incompletely mixed samples, render Ba_{1-x}Ca_xF₂ a complex

^aChristian Doppler Laboratory for Lithium Batteries and Institute for Chemistry and Technology of Materials, Graz University of Technology (NAWI Graz), Stremayrgasse 9, 8010 Graz, Austria

^bALISTORE-ERI European Research Institute, 33 rue Saint Leu, 80039 Amiens, France

† Electronic supplementary information (ESI) available: XRPD patterns, crystallite sizes, deconvoluted ¹⁹F MAS NMR spectra. See DOI: 10.1039/c7dt04487a

model system to study the influence of structural disorder on local ion dynamics.

Although the mixing effect on (i) atomic structure and (ii) long-range ion transport in $\text{Ba}_{1-x}\text{Ca}_x\text{F}_2$ has recently been studied *via* DC conductivity measurements in detail,²⁸ less is known about the change of local hopping processes. Starting from $x = 0$ the ionic conductivity increases and passes through a maximum at approximately $x = 0.5$ before it decreases and reaches the value of pure CaF_2 ($x = 1$).²⁸ In turn, the associated activation energy runs through a minimum at $x = 0.5$ being the composition with maximum structural disorder with regard to intimate cation mixing. The specific conductivity of the solid solution $\text{Ba}_{0.5}\text{Ca}_{0.5}\text{F}_2$ prepared by ball milling exceeds even that of epitaxially grown $\text{BaF}_2\text{-CaF}_2\text{-BaF}_2$ layers.^{28,29} This layered system²⁹ is one of the most famous examples of an artificial ion conductor whose transport properties are explained by non-trivial size effects, *i.e.*, by overlapping space charge zones.^{9,10,30,31} Such effects might also influence ion transport in mechanosynthesized $(\text{Ba},\text{Ca})\text{F}_2$.²⁸

While local strain, *i.e.*, a strongly heterogeneous potential landscape, has been made responsible for the increase in conductivity of $\text{Ba}_{0.5}\text{Ca}_{0.5}\text{F}_2$,²⁸ short-range ion dynamics have so far not been probed. Shedding light on these hopping processes is expected to help identify the driving forces that control the increase in ionic diffusivity seen. Here, we took advantage of ¹⁹F NMR (spin-lock) relaxometry to extract mean activation barriers the ions are subjected to in $\text{Ba}_{1-x}\text{Ca}_x\text{F}_2$. For heterogeneous nanocrystalline materials with disordered interfacial regions and crystalline grains NMR can, in ideal cases, differentiate the mobile ions in or near the (percolating) interfaces from those in the defect-rich interior of the nm-sized grains.^{32–34} For Li_2O and the dispersed, nanocrystalline ion conductors $\text{Li}_2\text{O}:\text{X}_2\text{O}_3$ ($\text{X} = \text{Al}, \text{B}$) it was possible to draw conclusions about the location of the mobile ions responsible for fast macroscopic ion transport.^{32,33}

Experimental

Mechanochemical preparation and characterization of the samples

A series of nanocrystalline samples $\text{Ba}_{1-x}\text{Ca}_x\text{F}_2$ with the compositions of $x = 0, 0.1, 0.2, 0.5, 0.8, 1.0$ were prepared by high-energy ball milling. Pure, microcrystalline BaF_2 (99.99%, Sigma-Aldrich) and CaF_2 (99.9%, ABCR) served as starting materials. We used of a Fritsch Pulverisette 7 (premium line) planetary mill. Two 45 mL grinding beakers, filled with the reactants (the total mass was 4 g) and 180 ZrO_2 milling balls (5 mm in diameter) in each case, were employed. The mixtures were mechanically treated for 10 h at a rotational speed of 600 rpm. To exclude contamination with moisture or oxygen during milling, the beakers were filled and emptied in a glovebox with dry argon atmosphere. The powders obtained were characterized by X-ray powder diffraction (XRPD) using a Bruker D8 Advance diffractometer that operates with Bragg Brentano geometry and Cu K_α radiation.

Conductivity measurements

For our conductivity measurements cylindrical pellets with 5 mm in diameter and *ca.* 1.5 mm in thickness were used. The pellets were uniaxially cold-pressed at a pressure of approximately 0.5 GPa. Blocking electrodes with a layer thickness of 100 nm were applied with a Leica EM SCD 050 evaporator. Impedance measurements were carried out with a Novocontrol Concept 80 broadband dielectric spectrometer. Our measurements covered a frequency range from 0.01 Hz to 10 MHz; temperatures (173 K–473 K) were adjusted with a QUATRO controller (Novocontrol). To avoid any contamination with water or oxygen during the measurements, the pellets were dried inside the impedance cell, which was permanently flushed with dry nitrogen gas.

NMR measurements

To assess the fluorine self-diffusion parameters ¹⁹F NMR spectroscopy and relaxometry were used to estimate jump rates and activation energies. Here, we took advantage of the saturation recovery and the spin-lock technique to record longitudinal ($1/T_1$) as well as transversal ($1/T_{1\rho}$) NMR spin-lattice relaxation (SLR) rates. For the NMR measurements the dry powders were fire-sealed in Duran glass tubes (*ca.* 4 cm in length and 3 mm in diameter) under vacuum to protect them from any impact of humidity. All measurements were carried out on a Bruker Avance III spectrometer that was connected to a shimmed cryomagnet with a nominal magnetic field of 7 T. This field corresponds to a ¹⁹F NMR Larmor frequency of $\omega_0/2\pi = 282.0$ MHz. A home-built NMR probe, which is suitable to record NMR signals under static conditions in a temperature range from 193 K to 533 K, was used to record the SLR rates and the ¹⁹F NMR spectra. At 200 W the $\pi/2$ pulse length was approximately 1 μs . A Eurotherm temperature controller in combination with a type-T thermocouple was utilized for both temperature controlling and monitoring. The saturation recovery pulse sequence consisted of ten succeeding pulses that destroy any longitudinal magnetization M_z , after a delay time t_d the reading pulse was sent to detect the recovery of M_z as a free induction decay (FID): $10 \times \pi/2 \cdot t_d - \pi/2$ -acquisition (acq.). To construct the magnetization transients $M_z(t_d)$ we plotted the area under the FIDs *vs.* t_d . Additionally, rotating-frame ¹⁹F NMR SLR ρ rates $1/T_{1\rho}$ were measured by means of the spin-lock technique, $\pi/2 p(t_{\text{lock}})$ -acq., using a locking frequency $\omega_1/2\pi$ of approximately 100 kHz.^{18,35} We varied the locking pulse length from $t_{\text{lock}} = 46 \mu\text{s}$ to $t_{\text{lock}} = 460 \text{ ms}$. To guarantee full longitudinal relaxation between each scan the recycle delay was set to at least $5 \times T_1$. Both the $1/T_1$ and $1/T_{1\rho}$ rates were obtained by parameterizing the resulting transients $M_z(t_d)$ and $M_\rho(t_{\text{lock}})$ with stretched exponentials of the form $M_z(t_d) \propto 1 - \exp(-(t_w/T_1)^\gamma)$ and $M_\rho(t_{\text{lock}}) \propto \exp(-(t_{\text{lock}}/T_{1\rho})^\kappa)$, respectively. While the stretching exponents γ varied from 1 to 0.8, the parameter κ ranged from 0.4 to 1.0 depending on temperature.

Static ¹⁹F NMR spectra were obtained with a single 90° pulse experiment *via* Fourier transformation of the FID. We employed a 500 MHz Avance spectrometer (Bruker) to record

the spectra; the ^{19}F Larmor frequency was 470.4 MHz. The NMR lines shown represent Fourier transforms recorded under static, *i.e.*, non-rotating, conditions. ^{19}F NMR spectra under magic angle spinning (MAS) were measured at a rotation speed of 60 kHz using 1.3 mm rotors. Spectra were referenced to crystalline CaF_2 , which shows, as a secondary reference, an isotropic chemical shift δ_{iso} of 58 ppm; C_6F_6 served as primary reference.

Results and discussion

Characterization *via* X-ray powder diffraction and ^{19}F MAS NMR

The phase purity of the samples and the formation of a mixed $(\text{Ba}, \text{Ca})\text{F}_2$ phase with retained cubic symmetry (see Fig. 1) was verified with the help of XRPD. We collected diffraction patterns at room temperature and in air atmosphere. Exemplarily, Fig. 1(a) shows the pattern of the mixture with the composition $\text{Ba}_{0.2}\text{Ca}_{0.8}\text{F}_2$ which was milled for 10 h in the P7 planetary mill (see Fig. S1 in the ESI† for the characterization of the other samples studied). For comparison, in Fig. 1 the patterns of nanocrystalline BaF_2 and CaF_2 prepared under the same milling conditions are presented. The pure nanocrystalline samples feature reflections at exactly the same positions as their coarse-grained samples. A marked difference is, however,

that the reflections of the powders ball-milled for 10 h show noticeable broadening. This broadening is attributed to the formation of nm-sized crystallites and the generation of strain upon mechanical treatment. As has been shown by earlier studies on nanocrystalline $(\text{Ba}, \text{Ca})\text{F}_2$ as well as other fluorides and oxides prepared by high-energy ball milling the final average crystallite size reached after many hours of mechanical treatment is in the order of 10 to 17 nm for the mixed samples.³⁶ This result was obtained by evaluating the width of the reflections with the equation introduced by Scherrer³⁷ (see ESI (Table S1†) for the exact crystallite sizes calculated). These values are supported by high-resolution transmission electron microscopy carried out in early studies.^{24,25} It is worth noting that abrasion of ZrO_2 on ion conductivities turned out to be negligible in our case; such effects have been discussed by some of us in earlier studies.^{24,25,28}

A close look at the pattern of the $\text{Ba}_{0.2}\text{Ca}_{0.8}\text{F}_2$ mixture reveals that the reflections shifted to smaller diffraction angles if compared with those of pure (nanocrystalline) CaF_2 . The incorporation of the larger Ba^{2+} ions (ionic radius of 1.42) into the F-sublattice of CaF_2 , the ionic radius of Ca^{2+} is 1.12, causes the original lattice to expand. According to Bragg's law this mismatch in size results in lower diffraction angles. The reverse process is observed when some Ca^{2+} ions are introduced into BaF_2 . For $\text{Ba}_{1-x}\text{Ca}_x\text{F}_2$ with $x = 0.5$ the final reflections are characterized by almost the arithmetic average.²⁸ The

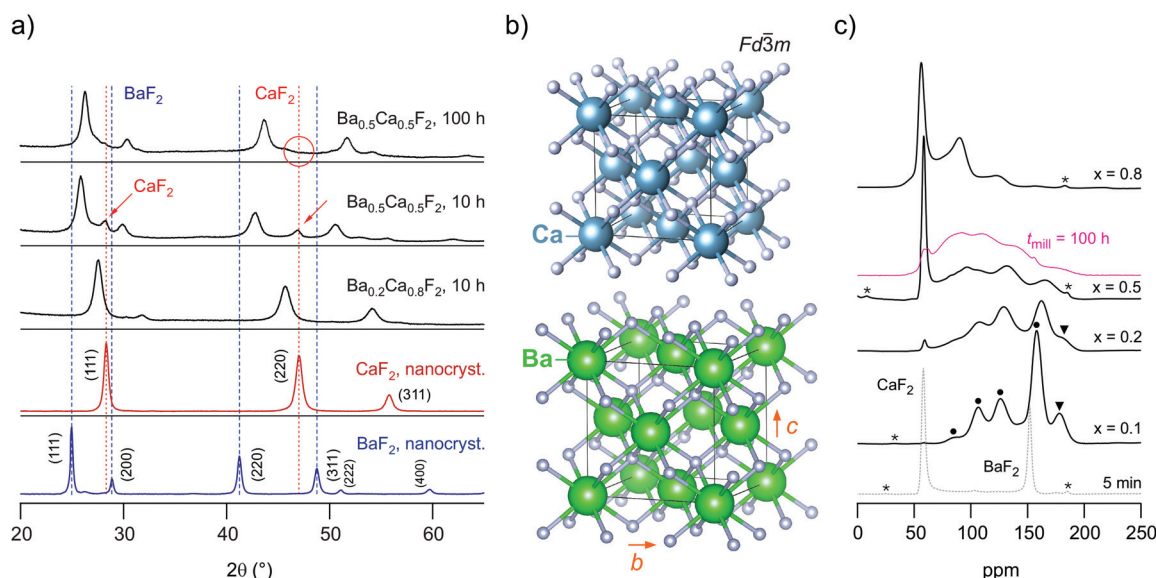


Fig. 1 (a) X-ray powder patterns of high-energy ball milled CaF_2 , BaF_2 and a mixtures $\text{Ba}_{1-x}\text{Ca}_x\text{F}_2$ with the compositions $\text{Ba}_{0.2}\text{Ca}_{0.8}\text{F}_2$ and $\text{Ba}_{0.5}\text{Ca}_{0.5}\text{F}_2$. From the point of view of XRPD, the pattern of the mixed phase with $x = 0.8$ reveals the formation of a nanocrystalline solid solution as all reflections refer to a cubic phase with shifts to lower diffraction angles. The same holds for $x = 0.2$. The samples were prepared in a planetary mill using a ZrO_2 vial set; the rotational speed was 600 rpm, the milling time was set to 10 h. To prepare $\text{Ba}_{0.5}\text{Ca}_{0.5}\text{F}_2$ free of any residuals of nanocrystalline $\text{Ca}(\text{Ba})\text{F}_2$ longer milling times are needed. The conductivity response of the two samples is the same. (b) Crystal structure of cubic CaF_2 and BaF_2 ; the two materials only differ by the lattice constant a . (c) ^{19}F MAS NMR spectra of $\text{Ba}_{1-x}\text{Ca}_x\text{F}_2$ recorded at 470.4 MHz and a spinning frequency of 60 kHz. The asterisks mark spinning sidebands, the black dots ($x = 0.1$) indicate the different F environments. Note that signals arising from orthorhombic BaF_2 , as also seen in X-ray diffraction (see Fig. 1(a)), are marked by red dots; these partly overlap with those from the mixed phases. If not stated otherwise, the milling time was 10 h. The spectrum, referring to a milling time of 5 min, shows a stoichiometric mixture of BaF_2 and CaF_2 to highlight the initial δ_{iso} values of the starting materials, 58 ppm (CaF_2) and 152 ppm (BaF_2), respectively.

formation of mixed $(\text{Ba}, \text{Ca})\text{F}_2$ and the discussion of the corresponding XRPD patterns is already well documented in literature.^{24,25,28} Most important for us is the following aspect: after milling the educts for 10 h, the reflections originating from the non-mixed starting materials BaF_2 are no longer visible for most compositions. As an example, for $\text{Ba}_{0.2}\text{Ca}_{0.8}\text{F}_2$ the formation of a mixed phase with no significant amounts of crystalline educts is seen by XRPD.

Besides decreasing the crystallite size and introducing structural disorder, it cannot be ruled out that mechanical treatment also lead to the formation of some amorphous material. Although recent EXAFS studies by Chadwick and co-workers³⁸ did not point to large fractions of amorphous regions in mechanosynthesized $\text{Ba}_{1-x}\text{Ca}_x\text{F}_2$, the XRPD pattern of $\text{Ba}_{0.2}\text{Ca}_{0.8}\text{F}_2$ revealed a shallow hump at low diffraction angles. This feature is frequently assigned to amorphous material.³⁹

For samples with x being close to 0.5, *i.e.*, considering equimolar mixtures, longer milling times than 10 h are needed to ensure intimate mixing of the earth alkaline cations. As an example, in Fig. 1 the XRPD pattern of two samples of $\text{Ba}_{0.5}\text{Ca}_{0.5}\text{F}_2$ are shown that were obtained after milling for $t_{\text{mill}} = 10$ h and 100 h, respectively. After 10 h residual CaF_2 is still present and not all Ca^{2+} ions have been fully incorporated into the BaF_2 lattice, as can be seen by the small CaF_2 reflections visible (see the red arrows in Fig. 1(a)). After milling the mixture for 100 h these reflections disappear. Additionally, the more Ca^{2+} ions are introduced into the BaF_2 lattice the larger the lattice contraction of BaF_2 which in turn causes a shift of the reflections toward larger diffraction angles. Hence, only very long milling times ensured the absence of any (nanocrystalline) starting materials.

The positions of the final reflections of the sample obtained after 100 h suggest the formation of an almost fully mixed sample. Of course, the existence of both Ba-rich and Ca-rich regions cannot be excluded on the basis of XRPD. As seen by (high-resolution) ^{19}F MAS NMR, which is sensitive to the local, atomic environments of the F nuclei, heavy clustering, however, seems to be negligible for $x = 0.5$. This conclusion is at least valid for mixtures obtained after sufficiently long periods of milling with $t_{\text{mill}} = 100$ h (see Fig. 1c). The ^{19}F MAS NMR spectra of the fully mixed samples are composed of several overlapping lines revealing partly the magnetically inequivalent F anions in $\text{Ba}_{0.5}\text{Ca}_{0.5}\text{F}_2$. In general, since each F anion is directly surrounded by 4 cations, in an ideal solid solution the environments are $[\text{Ba}]_3[\text{Ca}]$, $[\text{Ba}]_2[\text{Ca}]_2$, $[\text{Ba}][\text{Ca}]_3$ as well as $[\text{Ba}]_4$ and $[\text{Ca}]_4$ (see Fig. S2 in the ESI† for the assignment of the different atomic F environments in Ba-rich $\text{Ba}_{1-x}\text{Ca}_x\text{F}_2$ including a deconvolution of the spectra).²⁸

The signals of $[\text{Ba}]_4$ and $[\text{Ca}]_4$ are the weakest in intensity for $x = 0.5$ and $t_{\text{mill}} = 100$ h. Keeping in mind that the NMR chemical shift for $[\text{Ba}]_4$ in completely mixed $\text{Ba}_{0.5}\text{Ca}_{0.5}\text{F}_2$ (182 ppm) is different compared to that in pure nanocrystalline BaF_2 (152 ppm), the NMR spectra point to mixing of the earth alkaline ions on atomic scale. For the sample milled only for 10 h ($x = 0.5$) we see that the sharp signal around

52 ppm points to Ca-rich regions that only vanish if t_{mill} is increased to 100 h. The reason for the disappearance of the $[\text{Ca}]_4$ signal is, that more and more CaF_2 gets incorporated into BaF_2 the longer the milling time is chosen. After 100 h of milling, the equimolar mixture forms a disordered phase with a large amount of mixed F environments: $[\text{Ba}]_3[\text{Ca}]$, $[\text{Ba}]_2[\text{Ca}]_2$, $[\text{Ba}][\text{Ca}]_3$. The more effective the mixing process is, the less the probability to find Ba- and Ca-rich species $[\text{Ba}]_4$ and $[\text{Ca}]_4$ originating from the educts (see also the corresponding XRPD pattern in Fig. 1(a)).

When comparing the samples with $x = 0.8$ and $x = 0.1$ it is, however, evident that after a milling period of 10 h Ca-rich and Ba-rich regions are clearly present. The Ca-rich sample ($x = 0.8$) reveals the fastest ^{19}F SLR rates, see below. ^{19}F MAS NMR reveals further that mixing of the earth-alkaline ions seems to be easier for compositions $x < 0.5$, *i.e.*, for Ba-rich samples. Mechanical treatment of cubic- BaF_2 always leads to the formation of some orthorhombic material (up to 20 wt% depending on the milling conditions). The orthorhombic form is a high-pressure phase of BaF_2 ; it is also seen in ^{19}F MAS NMR. With increasing x the amount of orthorhombic BaF_2 decreases.

As outlined above, after the formation of the mixed phase, either completely or partially, the F anion conductivity σ_{DC} sharply increases when compared to the pure nanocrystalline starting materials. σ_{DC} passes through a maximum at intermediate compositions. Correspondingly, the activation energy takes a minimum at $x = 0.5$. While σ_{DC} refers to long-range ion transport, that is affected by grain boundaries, interfacial regions and porosity, NMR relaxometry, on the other hand, is primarily sensitive to bulk properties and, most importantly, to local F^- hopping processes. In ideal cases, NMR was able to differentiate between ions in the interfacial regions and those in the bulk. This separation was possible for some single- and two-phase nanocrystalline oxides as well as binary fluorides with a large number fraction of ions residing in the structurally disordered interfacial regions.

^{19}F NMR relaxometry to evaluate short-range F anion hopping

In Fig. 2 an overview of all variable-temperature ^{19}F spin-lattice and spin-lock NMR relaxation rates is presented. To identify the thermally activated regions, from which hopping activation energies can be extracted, the rates were plotted in an Arrhenius representation. Stretched exponential functions served to parameterize the magnetization transients $M_z(t_{\text{d}})$ and $M_p(t_{\text{lock}})$, see Fig. 3(a) and (b) and section 2. The corresponding stretching exponents γ are illustrated in Fig. 3(c).

The stretching factors of the $M_z(t_{\text{d}})$ transients, which contain the rate T_1 , are almost exponential, except for few compositions deviations from $\gamma = 1$ show up at temperatures above 393 K. The κ values of the spin-lock transients reveal a more complex behavior and pass through minima at temperatures higher than 333 K; this feature is especially seen for the mixed sample $\text{Ba}_{0.5}\text{Ca}_{0.5}\text{F}_2$. The educts, which are characterized by lower ionic conductivities (see below), do not show such behav-

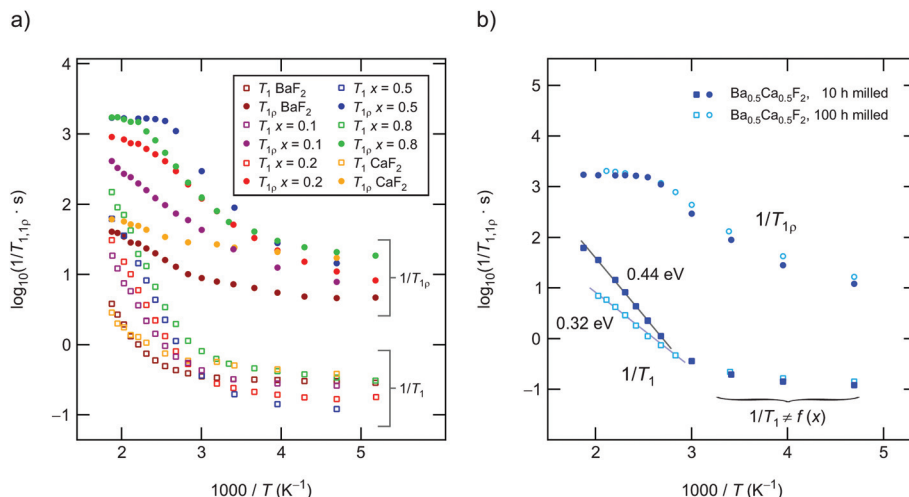


Fig. 2 (a) Temperature dependence of the ^{19}F NMR SLR rates $1/T_1$ (282.0 MHz) and $1/T_{1p}$ (100 kHz) for all nanocrystalline samples $\text{Ba}_{1-x}\text{Ca}_x\text{F}_2$ prepared via high-energy ball milling. (b) ^{19}F NMR SLR behavior of nanocrystalline $\text{Ba}_{0.5}\text{Ca}_{0.5}\text{F}_2$ obtained after $t_{\text{mill}} = 10$ h and $t_{\text{mill}} = 100$ h. While measurements in the kHz range ($1/T_{1p}$) are unaffected by t_{mill} , local jump processes, as seen by T_1 NMR, depend on the degree of cation mixing. The activation energies indicated refer to non-corrected rates; background correction to calculate $1/T_{1\text{diff}}$ changes E_a from 0.32 eV to 0.35 eV (100 h) and from 0.44 eV to 0.49 eV with no effect on the ratio of the two activation energies.

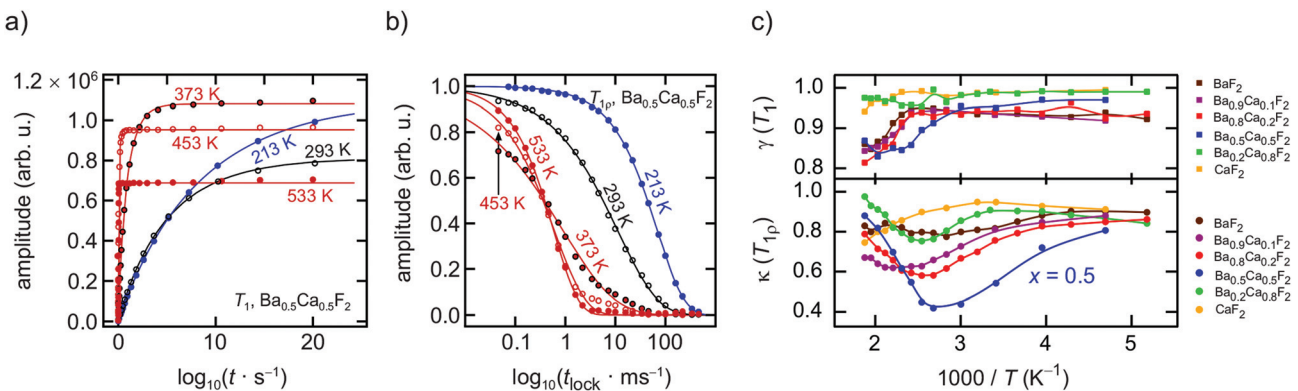


Fig. 3 (a) Selected variable-temperature ^{19}F NMR T_1 transients of nanocrystalline $\text{Ba}_{0.5}\text{Ca}_{0.5}\text{F}_2$. The solid lines represent fits according to stretched exponentials: $M_z(t_d) \propto 1 - \exp(-(t/T_1)^\beta)$. (b) Spin-lock ^{19}F NMR T_{1p} magnetization transients of the same sample shown in (a); the amplitude was scaled such that it ranges from 0 to 1. The solid lines represent fits according to $M_p(t_{\text{lock}}) \propto \exp(-t_{\text{lock}}/T_{1p})^\alpha$. (c) Change of γ and κ as a function of the inverse temperature $1/T$.

ior. The $\text{Ba}_{0.5}\text{Ca}_{0.5}\text{F}_2$ sample features the lowest minimum with values of approximately $\kappa = 0.4$ at $T = 360$ K.

For all samples the ^{19}F NMR SLR rates, measured in the laboratory frame of reference ($1/T_1$), show a non-diffusion induced regime below 330 K. In this T range the rates only marginally depend on temperature, see also Fig. 4(a). Background relaxation is in many cases driven by lattice vibrations or coupling of the spins to paramagnetic impurities.⁴⁰

Above 330 K the rates start to increase because of F jumps on the time scale of the NMR experiment. We approximated the background rates with a power law, $1/T_{1,\text{bgr}} \propto T^\beta$, and extrapolated the rates to higher T to calculate background-free, diffusion-induced rates: $1/T_{1\text{diff}} = 1/T_1 - 1/T_{1,\text{bgr}}$.⁴¹ β values ranged from 0.3 ($x = 0$) to 1.5 ($x = 0.5$). For intermediate values

of x we obtained $\beta \approx 1$. In Fig. 4(a) this procedure is exemplarily shown for nanocrystalline BaF_2 , see unfilled symbols. The rates $1/T_{1\text{diff}}$ follow Arrhenius behavior characterized by an activation energy of 0.4 eV.

As x in $\text{Ba}_{x-1}\text{Ca}_x\text{F}_2$ is increased, the beginning of the diffusion-induced flank is shifted toward lower T . This clearly indicates increased F self-diffusion in the partially or completely mixed phases. As can be already seen in Fig. 4(a), the slope of the different flanks do not vary much but run in parallel to each other. The diffusion induced rates, see Fig. 4(b), reveal measurable but by far not great differences in activation energies which range, disregarding the results of CaF_2 , from 0.41 eV to 0.50 eV. These values are in good agreement with results from recently performed molecular dynamics studies.²⁷ For nanocrystalline CaF_2 background effects are predominant

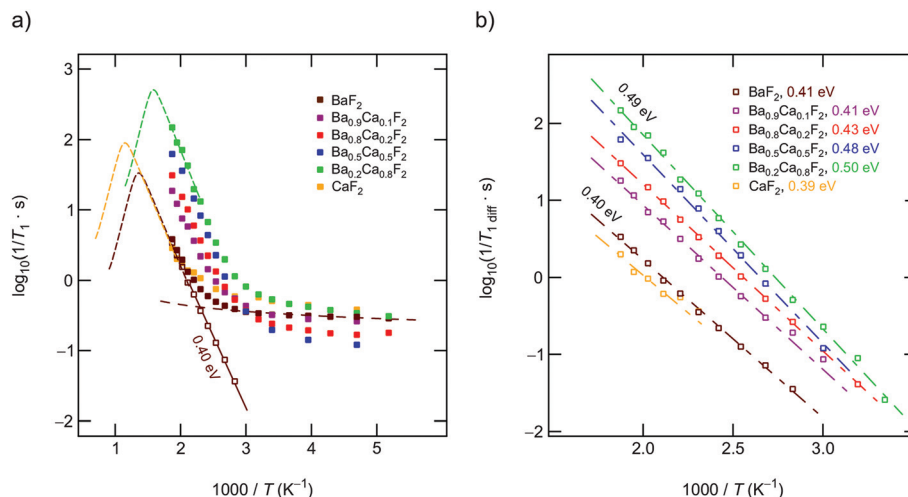


Fig. 4 (a) Temperature dependence of the ^{19}F NMR SLR rates $1/T_1$ (282.0 MHz). A power law is used to extrapolate the background rates to higher T to obtain purely diffusion-induced relaxation rates $1/T_{1\text{diff}}$. The dashed lines indicate possible positions of the peak maxima. (b) Diffusion induced ^{19}F NMR rates after the correction procedure. The lines show linear fits to extract NMR activation energies, which range from 0.40 to 0.49 eV.

in the T range investigated; these effects do not allow the proper determination of an activation energy in the T range covered. Here, we estimated E_a after background correction to be approximately 0.39 eV. The better the flank is accessible the more precise the activation energy can be determined.

Fig. 4(b) entails two important information. First, the absolute rates $1/T_{1\text{diff}}$ increase with increasing x and sharply decrease if x exceeds 0.8. As a function of x , the diffusion-induced rates pass through a maximum that is similar, but not exactly the same, to that seen *via* DC conductivity spectroscopy. T_1 is most effective for Ca-rich samples, see the rates for $x = 0.8$. Apart from this small but important distinctions, the rates support the mixed earthy-alkaline effect observed in our earlier study.²⁸ Second, the activation energies from NMR

turn out to be smaller than those seen by DC conductivity spectroscopy (see Table 1). Furthermore, their overall change with composition is less pronounced as seen for long-range ion transport.²⁸ In contrast to conductivity measurements, E_a from NMR pass through a very shallow maximum (*ca.* 0.5 eV at $x = 0.5$) rather than a minimum.

To further support the activation energies obtained according the correction procedure sketched above, we also analyzed our T_1 data with an Arrhenius fit that directly takes into account the deviation at low temperatures with the help of a power law ansatz: $1/T_1 = c \cdot \exp(-E_a/(k_B T)) + a \cdot (1/T)^n$. c and a denote fitting parameters. The exponent n ($0.4 < n < 1.2$) should agree with β . It characterizes the type of relaxation, *e.g.*, driven by coupling of the spins to electrons or phonons, being

Table 1 Activation energies and ionic conductivities as derived from conductivity and NMR spectroscopy for the samples milled for 10 h in a high-energy planetary mill. Note that E_a from NMR, as well as E'_a , steadily increases from $x = 0$ to $x = 0.8$ although σ_{DC} and $E_a(\sigma_{\text{DC}})$ pass through a maximum and a minimum, respectively

x	Conductivity spectroscopy		NMR relaxation				
	E_a	$\sigma_{\text{DC}}(298 \text{ K}) (\text{S cm}^{-1})$	$\log(\sigma_0/\text{S cm}^{-1} \text{ K})$	$E_a(T_1)^a$ (eV)	$E'_a(T_1)^f$ (eV)	$E_a(T_{1\rho})$ (eV)	α^g
0	0.78	1.6×10^{-11}	5.17	0.41	0.43	0.19	1.51
0.1	—	—	—	0.41	0.45	0.17	Low- T flank not completely reached
0.2	0.64 ^b	4.6×10^{-9}	5.06	0.43	0.43	0.22	1.66
0.5	0.61 ^c	1.6×10^{-8}	5.23 ^e	0.49	0.46	0.29	1.80
0.8	0.71 ^d	8.7×10^{-10}	5.52	0.50	0.51	0.32	1.70
1.0	0.80	7.2×10^{-14}	3.41	0.39	0.35	0.09	1.39

^a Corrected values that take into account a non-diffusive background; the error for all values is ± 0.01 eV. ^b Activation energy read off at 1 MHz: 0.50 eV. ^c 0.58 eV (1 MHz). ^d 0.55 eV (1 MHz). ^e After 100 h of milling a value of 5.44 is obtained; the largest increase for the pre-factor is seen when comparing nanocrystalline CaF_2 with nanocrystalline BaF_2 . ^f E'_a denotes values corrected using a joint fit of both diffusion and non-diffusive effects. ^g Values refer to $E_a(T_1)$; $\alpha = 2$ would result for 3D (isotropic) uncorrelated motion. ^h For $x = 0.5$ and $t_{\text{mill}} = 100$ h we obtained $E'_a = E_a = 0.35$ eV. After 100 h of milling we obtain $\alpha = 1.54$.

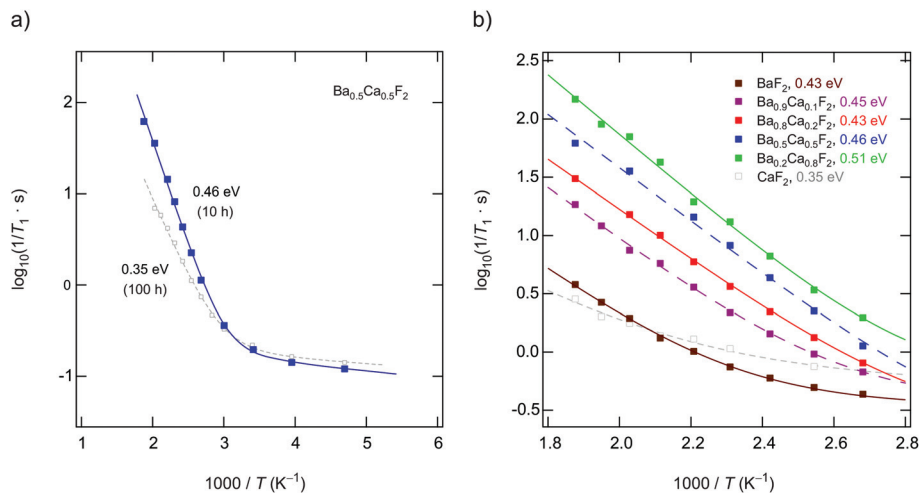


Fig. 5 (a) Temperature dependence of the ^{19}F NMR SLR rates $1/T_1$ (282.0 MHz) for nanocrystalline $\text{Ba}_{0.5}\text{Ca}_{0.5}\text{F}_2$ obtained after $t_{\text{mill}} = 10 \text{ h}$ and $t_{\text{mill}} = 100 \text{ h}$. A joint fit of both diffusion and non-diffusive effects is used to obtain the activation energies. (b) Change of the low- T ^{19}F NMR $1/T_1$ rates of $\text{Ba}_{1-x}\text{Ca}_x\text{F}_2$ as a function of x . Solid and dashed lines show fits with the joint fit mentioned. The extracted NMR activation energies range from 0.35 to 0.51 eV .

responsible for the change in $1/T_1$ at low T . The fitting results are shown in Fig. 5; the activation energies E'_a are listed also in Table 1. E'_a is, for all samples, closely comparable with E_a .

Comparison with results from conductivity spectroscopy and ^{19}F NMR line shapes

To characterize long-range F ion transport through impedance spectroscopy, in Fig. 6(a) the conductivity isotherms of $\text{Ba}_{0.5}\text{Ca}_{0.5}\text{F}_2$ are shown. While at low frequencies and sufficiently high T electrode polarization effects show up, the main parts of the spectra are dominated by the so-called DC

plateau ($\nu \rightarrow 0$) from which σ_{DC} can be read off. Pronounced dispersion regions are only visible at sufficiently low T . The DC plateau transforms into a semi-circle when the Nyquist representation is used to analyze the impedance data. The semi-circle shown in Fig. 6(b) is characterized by a capacity C of 3 pF which unequivocally points to a bulk electrical relaxation process. Blocking grain boundary resistances seem to be negligible. A value of 3 pF is also in perfect agreement with permittivities well below 10^2 , see Fig. 6(c). The modulus representation, $M''(\nu)$, reveals single peaks with a width (full width at half maximum) larger than that expected for a Debye process,

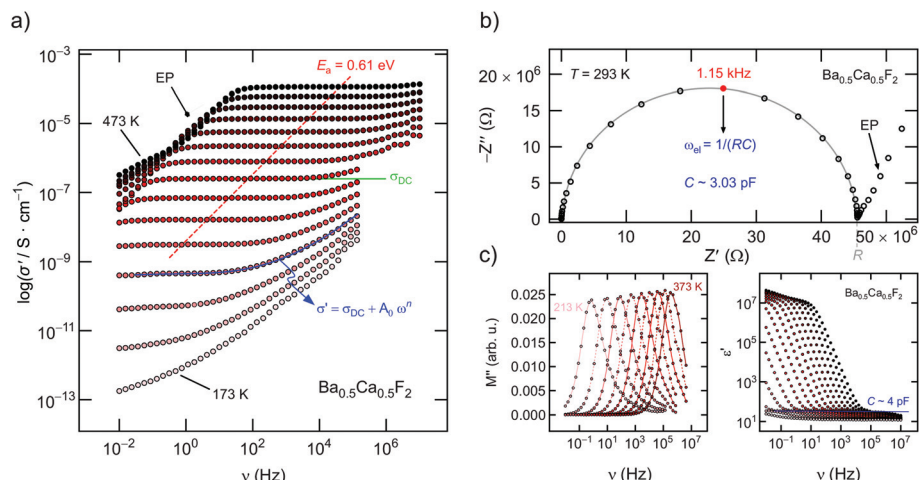


Fig. 6 (a) Conductivity isotherms of nanocrystalline $\text{Ba}_{0.5}\text{Ca}_{0.5}\text{F}_2$. A Jonscher-type power law is used to parameterize the dependency on frequency. While electrode polarization (EP) shows up at high T and low frequencies, at low T dispersive regions dominate the spectra. DC conductivities were read off from the frequency independent plateau regions. (b) Complex plane plot of the conductivity isotherm recorded at 293 K. Only one depressed semicircle is seen which corresponds to a relaxation process characterized by a capacity expected for a bulk response. The electrical relaxation frequency ω_{el} at 293 K is 1.15 kHz . (c) Modulus spectra and change of the real part of the complex permittivity with frequency in a temperature range between 173 K and 473 K (spectra recorded in steps of 20 K).

cf. Fig. 6(c). Hence, the F ions are subjected to correlated motion in $\text{Ba}_{0.5}\text{Ca}_{0.5}\text{F}_2$ sensing a distribution of diffusion pathways in an irregularly shaped potential landscape. Such dynamics are usually described with non-exponential motional correlation functions.⁴²

Evaluating $\sigma_{\text{DC}} T$, see Fig. 7(a), illustrates that, depending on x , the activation energy for long-range ion transport varies from 0.80 eV (CaF_2 , ball milled for 10 h) to 0.61 eV ($\text{Ba}_{0.5}\text{Ca}_{0.5}\text{F}_2$). Pure nanocrystalline BaF_2 (10 h) has to be characterized by 0.78 eV. These values perfectly agree with those published earlier.²⁸ In Fig. 7(b) we show the increase of $\sigma_{\text{DC}} T$ for $\text{Ba}_{0.5}\text{Ca}_{0.5}\text{F}_2$ with increasing milling time. While for a mixture of BaF_2 and CaF_2 milled for only 5 min σ_{DC} is still affected by the low-conducting CaF_2 , milling for 1 h already results in a significant increase of the DC ionic conductivity exceeding that of nanocrystalline BaF_2 (10 h) by one order of magnitude. After 10 h of mechanical treatment the upper limit of σ_{DC} is reached. Further increase of t_{mill} does not change σ_{DC} significantly.

While for σ_{DC} the activation energy and the σ_0 in $\sigma_{\text{DC}} T = \sigma_0 \exp(-E_{\text{a}, \text{DC}}/k_B T)$ may vary with x , in ^{19}F NMR relaxometry the change of the NMR pre-factor $1/\tau_{0, \text{NMR}}$ (see below) seems to play a more significant role. This idea is illustrated in Fig. 4(a). The higher F anion conductivity in mixed samples is a proven fact. Indeed, ^{19}F NMR line shape measurements also show enhanced F anion hopping in the mixed samples as compared to the pure end members. In contrast to BaF_2 and CaF_2 the corresponding NMR lines of the samples with $0.2 < x < 0.8$ are composed of a clearly visible motionally narrowed contribution that is attributed to F anions being fast enough to average (homonuclear) dipole–dipole couplings (Fig. 8). As the rigid lattice ^{19}F NMR line width of BaF_2 (and CaF_2) is at least 30 kHz, full narrowing, which is already seen slightly above

400 K, corresponds to F jump rates $1/\tau_{\text{NMR}}$ in the order of 10^6 s^{-1} , see also the estimation below via spin-lock NMR. Such a value will definitely affect the low- T regime of SLR NMR. The peak maximum of the $1/T_1$ rate would be expected to show up if $1/\tau_{\text{NMR}}$ reaches values in the order of $1.8 \times 10^9 \text{ s}^{-1}$.

As the rates of $\text{Ba}_{0.5}\text{Ca}_{0.5}\text{F}_2$ reveal the onset of the diffusion-induced low- T flank at lower temperatures we expect the corresponding rate peak, see dashed lines in Fig. 4(a), to show up at lower T as compared to BaF_2 and CaF_2 , respectively. With the low- T activation energies being rather similar, especially if we consider the flanks of the samples with $x = 0.2$, $x = 0.5$ and $x = 0.8$, the only parameter that can further increase $1/\tau_{\text{NMR}}$ is the pre-factor in $1/\tau_{\text{NMR}} = 1/\tau_0, \text{NMR} \exp(-E_{\text{a}, \text{high-}T}/k_B T)$. Here, $E_{\text{a}, \text{high-}T}$ denotes the activation energy of the high- T flank of the peaks indicated in Fig. 5(a). The flank is inaccessible as the nanocrystalline samples are sensitive to grain growth and decomposition if NMR experiments were performed at too high temperatures. $E_{\text{a}, \text{high-}T}$ can be identified with $E_{\text{a}, \text{DC}}$. Although $E_{\text{a}, \text{DC}}$ change from 0.61 eV to 0.71 eV for x ranging from 0.2 to 0.8 (cf. Table 1), the variation in $E_{\text{a}, \text{DC}}$ alone could not explain the significant shift of the low- T flank. As for σ_0 , also $1/\tau_0$ is, besides other factors, affected mainly by the attempt frequency v_0 , the activation entropy ΔS as well as the number of spins effectively taking part in ^{19}F NMR spin–lattice relaxation. The latter number is strongly associated to the concentration of available sites where the mobile ions can jump to. As has been shown recently, the softness of a lattice may influence v_0 .⁴³ In the present case, besides such an influence, effects of migration entropy, affected by both vibrational or configurational contributions, is expected to control the pre-factor mostly. Frenkel defects show a considerable high migration entropy that may especially affect the samples with $x = 0.5$ and $x = 0.8$.

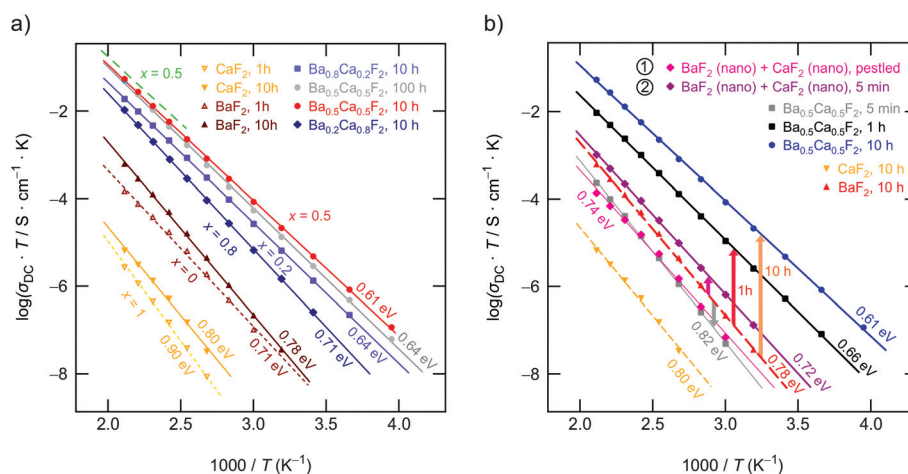


Fig. 7 (a) Change of the DC conductivity of $\text{Ba}_{1-x}\text{Ca}_x\text{F}_2$ as a function of inverse temperature. The highest conductivities are found for $x = 0.5$. While the solid lines show linear fits to extract activation energies for samples prepared by milling for $t_{\text{mill}} = 10 \text{ h}$, dashed lines refer to samples milled for 1 h only. (b) Conductivity of $\text{Ba}_{0.5}\text{Ca}_{0.5}\text{F}_2$ samples prepared by high-energy ball milling and comparison to $\text{BaF}_2 : \text{CaF}_2$ mixtures, see text for further details. Samples 1 and 2 refer to compounds which have been prepared by mixing nanocrystalline BaF_2 ($t_{\text{mill}} = 10 \text{ h}$) and CaF_2 ($t_{\text{mill}} = 10 \text{ h}$) either by hand with mortar and pestle or by high-energy ball milling the two components for only 5 min. For the ball-milled sample even the 5 min milling procedure results in a measurable increase of $\sigma_{\text{DC}} T$.

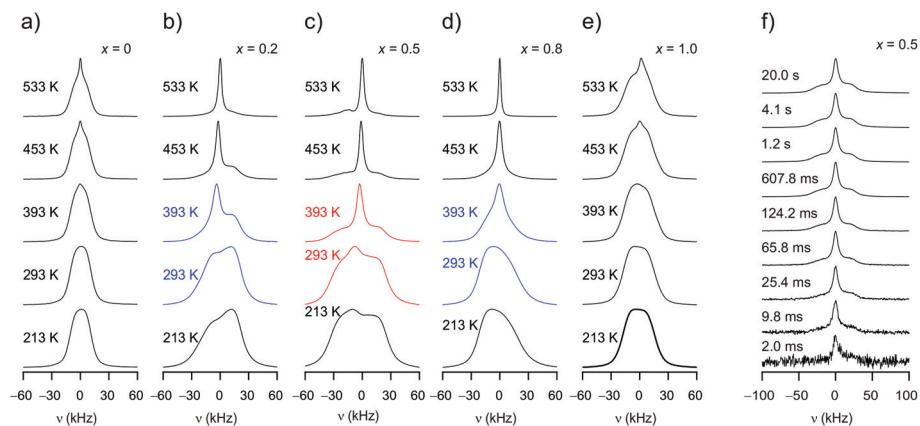


Fig. 8 (a) to (e) Variable-temperature ^{19}F NMR spectra of $\text{Ba}_{1-x}\text{Ca}_x\text{F}_2$ (282.0 MHz, static conditions). At low T broad NMR lines are seen. Broadening is due to dipole–dipole couplings and the existence of a (partially) mixed F environments with distinct chemical shifts. Spectra are shown such that the centre of the NMR signal is located at 0 kHz. As T increases heterogeneous motional narrowing sets in. The narrowed line, which emerges with increasing temperature at the centre of the NMR signal, reflects the number fraction of mobile F anions with respect to the NMR time scale. For $x = 0.5$ and $T = 393$ K the area fraction of this NMR line is larger for $x = 0.5$ than for $x = 0.2$ and $x = 0.8$. (f) Evolution of the ^{19}F NMR Fourier transforms in the frame of a T_1 saturation recovery experiment, that is, spectra obtained at different waiting times t . Strong spin-diffusion effects account for a single spin temperature with no differences in T_1 relaxation for both the narrow and the broad NMR spectral components.

As can be clearly inferred from the ^{19}F NMR spectra (Fig. 8(a)–(e)), the number fraction of mobile F anions, which are represented by the motionally narrowed lines for each sample, passes through a maximum at $x = 0.5$. This is best seen at $T = 393$ K. For the sake of clarity we deconvoluted the spectra with appropriate Voigt functions to estimate the area fraction A_f of the motionally narrowed NMR component (see Fig. 9).¹² The larger the number of mobile ions, performing net displacements as well as local jumps, the more effective spin fluctuations. Of course, the x -dependent number of effective charge carriers will, to some extent, also affect σ_0 , which is related to long-range ion transport. It turned out, however, that its influence on localized jump processes is much larger.

Although F anion dynamics is clearly heterogeneous in $\text{Ba}_{x-1}\text{Ca}_x\text{F}_2$, effective spin-diffusion, *i.e.*, flip-flop processes without any mass transfer, ensures homogeneous relaxation of

the spin system. Accordingly, the ^{19}F NMR transients do not feature a two-step decay of fast and slowly relaxing components as it has been seen for other nanocrystalline core–shell model systems.^{32–34} In the frame of a saturation recovery experiment ^{19}F NMR spectra uniformly buildup with increasing waiting time (see Fig. 8(f)). Thus, there is fast communication between all ^{19}F spins in mixed $\text{Ba}_{0.5}\text{Ca}_{0.5}\text{F}_2$.

Influence of correlated motion on activation energies

Understanding the slight increase in $E_{\text{a, low-}T}$ when going from $x = 0.2$ (0.43 eV) to $x = 0.5$ (0.48 eV) and further to $x = 0.8$ (0.50 eV) also needs our attention. Although perhaps not applicable to our disordered system with relatively low barriers, the trend of both pre-factor and E_{a} from NMR resembles that of the Meyer–Neldel rule after which a higher activation energy is associated with a higher pre-factor.⁴⁴ In our case, however, we have to consider the following. In contrast to $E_{\text{a, high-}T}$, $E_{\text{a, low-}T}$

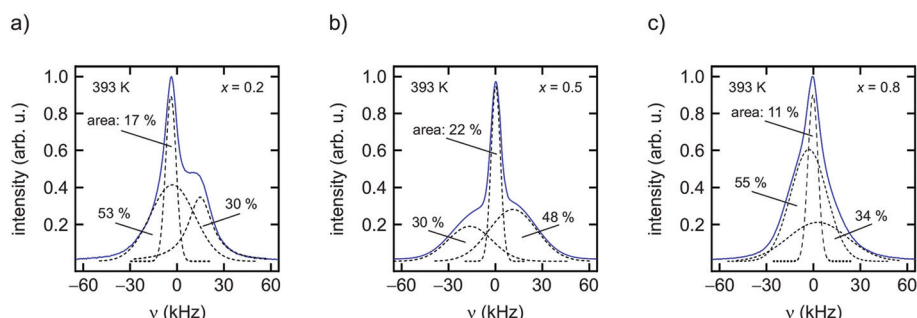


Fig. 9 (a) to (c) ^{19}F NMR spectra of $\text{Ba}_{1-x}\text{Ca}_x\text{F}_2$ ($x = 0.2$, $x = 0.5$ and $x = 0.8$) recorded at 393 K (282.0 MHz). In order to estimate the area fraction of the narrow component several Gaussian curves were used to deconvolute the spectra. The narrowed lines at the centre of the NMR signals reflect the number fraction A_f of mobile F anions. For $x = 0.5$ approximately 20% participate in fast ion dynamics. Although the Ca-rich sample with $x = 0.8$, see also the corresponding XRD pattern, is characterised by A_f of only 11%, ^{19}F relaxation is most effective for this sample. The mixed but Ca-rich regions seem to facilitate nuclear spin relaxation.

is a so-called apparent activation energy that is additionally affected by correlation effects.⁴⁵ It is comparable to AC conductivity activation energies read off in the dispersive regions of the conductivity isotherms (see also Table 1).¹⁶ The larger the impact of correlation effects, such as structural disorder and Coulomb interactions of F⁻ interstitials and vacancies, the larger the difference between $E_{a,\text{high-}T}$ and $E_{a,\text{low-}T}$. The two activation energies are linked according to the following relation $E_{a,\text{low-}T} = (\alpha - 1)E_{a,\text{high-}T}$.⁴⁶ For 3D uncorrelated motion the parameter α equals 2. Correlated motion results in $\alpha < 2$ and, thus, yields asymmetric NMR rate peaks.⁴⁵ Here it turned out that α pass through a maximum located near $x = 0.5$ (see Table 1). This result means less correlated motion for the samples with the highest diffusion-induced relaxation rates. To be clear, in all samples correlated motion is sensed by NMR; its extent, however, seems to be less for local ion dynamics in samples milled just for 10 h and $x = 0.5$ or $x = 0.8$. It is evident from XRPD and ¹⁹F MAS NMR that under these conditions mixing at atomic scale is incomplete; ¹⁹F MAS NMR revealed that the same is true for the sample with $x = 0.8$. Therefore, fast F anion diffusion might occur along or near Ca- and Ba-rich regions as mentioned above. Precisely speaking, diffusion induced T_1 relaxation is more effective for $x = 0.8$, i.e., for mixed but Ca-rich environments.

Recently, we probed a very similar trend of α for Li ion diffusivity in layer-structured 2H-Li_yNbS₂.⁴⁷ Although in 2H-Li_yNbS₂ Li diffusivity decreases when y approaches $y = 1$, which is the maximum Li load, the low- T activation energy deduced from $T_1(T)$ measurements steadily decreases when going from $y = 0.3$ to $y = 1.0$. This effect has been ascribed to an increasing effect of correlated ion motion which is maximal when the van-der-Waals gap in NbS₂ is completely filled with Li ions. At the same time, also dipolar magnetic and electric quadrupolar interactions increase the larger the Li concentration.

Here, the origin of correlated motion in mixed Ba_{x-1}Ca_xF₂ is, however, definitely different from that seen for 2H-Li_yNbS₂. An increasing number fraction of mobile F spins, activation entropy contributions and lower long-range activation energies cause a sharp increase in Li diffusivity and ionic conductivity when mixed phases are formed. For all samples correlated motion is expected because the ions are subjected to a highly irregular potential landscape, including also metastable states. The extent and origins of correlation effects seem, however, to change with composition. According to the NMR factor α the Ba-rich phases ($x = 0.1$, $x = 0.2$) provide an additional source of correlated motion leading to lower apparent activation energies than expected. Zahn *et al.* pointed out differences in the concentration of mobile charge carriers when Ca or Ba ions are introduced in BaF₂ and CaF₂, respectively. At very low levels of doping, the incorporation of Ca²⁺ ions resulted in trapped F interstitial sites and mobile F vacancies as the opponent defect.²⁶ The formation of such interstitial site next to a Ca²⁺ dopant in BaF₂ was promoted by 0.08 eV. On the other hand, the generation of Frenkel defects in Ba-doped CaF₂ is energetically disfavored by 0.14 eV.²⁶

In our case substitutional disorder is much larger than dopant concentrations and a direct comparison with results for extremely low levels of doping turns out to be difficult. At least we can say the following. Even if we consider complete and uniform mixing at atomic scale, we deal with samples that naturally have larger regions being rich in Ba²⁺. Segregation effects in interfacial regions or clustering on the nm scale will lead to even larger non-uniform areas. As has been shown recently for several types of ion conductors, concerted ion movements always cause the mean activation barrier to decrease.⁴⁸ Thus, concerted and, thus, highly correlated ion movements in the vicinity of Ca-doped Ba-rich regions or at the interface of Ba-rich and Ca-rich regions in non-intimately mixed samples could serve as an explanation for the unusual ¹⁹F NMR SLR behavior and the origin of additional correlation effects seen for the Ba-rich samples.

Obviously, on the angstrom length scale, to which ¹⁹F SLR NMR is sensitive, this effect levels off when the region $0.5 \leq x \leq 0.8$ is reached. Note that also the activation energy of Ba_{0.5}Ca_{0.5}F₂ (0.58 eV, see Table 1), when determined from AC impedance spectroscopy at 1 MHz, is higher than that of Ba_{0.2}Ca_{0.8}F₂ (0.55 eV) and Ba_{0.8}Ca_{0.2}F₂ (0.50 eV). In this compositional range, the increase in mobile spins near non-uniformly mixed interfaces is more significant and leads to a further increase in diffusivity. Simultaneously, the impact of correlation effects on the low- T ¹⁹F NMR T_1 measurements decreases, at least for samples milled for 10 h.

¹⁹F NMR spin-lock NMR and the effect of long-term milling

If we consider the corresponding rates measured in the kHz range through spin-lock NMR, see Fig. 10(a) and (b), the activation energies seem to reflect the same behavior. Regarding the absolute values for E_a suggests, however, that the temperature dependence of the ¹⁹F NMR SLR rates, see data for $x = 0.1$ and $x = 0.2$, are additionally influenced by other effects. Besides changes in the diffusion mechanisms, non-diffusive effects, such as spin-diffusion, presumably play the most important role. The characteristic spin-diffusion correlation times are expected to take values in the s to ms range, which fall into the time window of spin-lock NMR. Dipolarly coupled ¹⁹F spins with short distances to each other are prone to be affected by flip-flop effects. Hence, $1/T_{1\rho}$ NMR rates are expected to be much larger influenced by spin-diffusion as laboratory-frame SLR measurements performed in the MHz to GHz range. Apart from such interfering effects, spin-lock NMR relaxation is most effective for the sample with $x = 0.5$. This finding mirrors the change of long-range ion dynamics as seen by DC conductivity measurements.

Up to here, we discussed results from samples prepared by milling the starting materials for 10 h. Except for Ba_{0.5}Ca_{0.5}F₂ our results from XRPD do not reveal any substantial amounts of the nanocrystalline binary parents. Increasing t_{mill} up to 100 h forces the earth alkaline ions to mix almost completely, as is also verified by ¹⁹F MAS NMR. Importantly, the $1/T_{1\rho}$ rates, as well as the DC conductivity values, do not change when t_{mill} is increased from 10 to 100 h. Hence, bulk long-

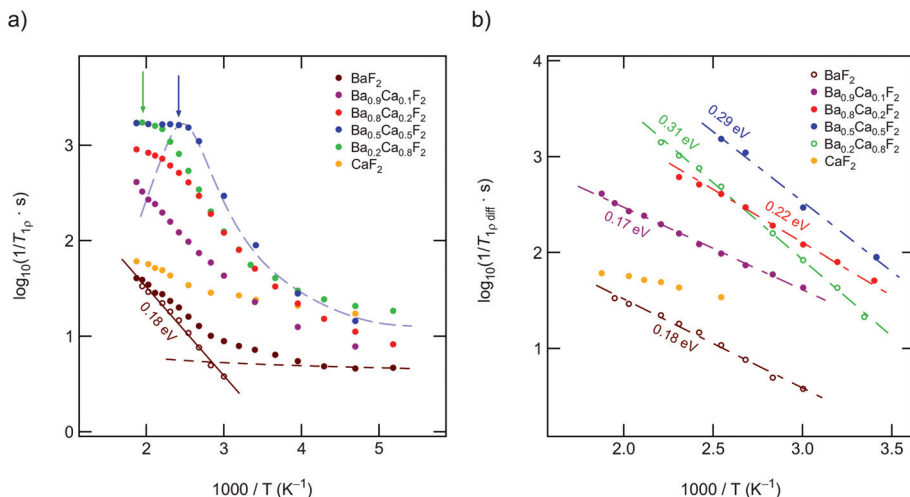


Fig. 10 (a) Arrhenius representation of the spin-lock ^{19}F MAS NMR rates $1/T_{1p}$ (100 kHz, 282.0 MHz) for $\text{Ba}_{1-x}\text{Ca}_x\text{F}_2$. As for T_1 , we used a power law ansatz to correct the measured rates for any non-diffusive background relaxation, as indicated for the data referring to nanocrystalline BaF_2 . The dashed line drawn through the data points of the $\text{Ba}_{0.5}\text{Ca}_{0.5}\text{F}_2$ sample is to guide the eye. The peak is located at the lowest possible temperature. For $x = 0.2$ and $x = 0.8$ we see that the peaks shift toward higher T (see vertical arrows). These shifts fully agree with a lower F anion diffusivity and, consequently, a lower F ion conductivity as seen through conductivity spectroscopy. (b) Diffusion induced ^{19}F NMR SLR rates $1/T_{1p,\text{diff}}$ after background correction.

range ion transport and spin-diffusion effects are already fully developed at shorter periods of mechanical treatment. In contrast, ^{19}F NMR spectra and $1/T_1$ do depend on t_{mill} . Although static line shapes reveal an increase of the number of mobile spins on the NMR time scale, this change does not cause an increase of σ_{DC} , see above (Table 1 and Fig. 7(a)). While the onset of the low- T ^{19}F NMR $1/T_1$ flank remains unchanged (see Fig. 4(b)), the corresponding activation energy decreases from $E_a = 0.49$ eV to only 0.35 eV. We attribute this unusual change in $E_a(T_1)$ to enhanced localized ion jump processes. Localized or caged jumps, including unsuccessful highly correlated forward-backward processes, will definitely affect the low- T $1/T_{1\text{diff}}$ rates but do not contribute to net charge transport, which is sensed by σ' in the limit of low frequencies. This is the classical way to interpret differences between diffusion parameters derived from NMR and those from conductivity spectroscopy. In general, the two methods are sensitive to quite different kinds of motional (auto-)correlation functions, see above. The relationship between parameters from NMR and conductivity spectroscopy in disordered media, such as glasses, has been discussed in detail by Ngai and co-workers.^{49–54}

Careful inspection of Fig. 7(a) shows that the sample milled for 100 h shows even lower conductivities as compared to that milled for 10 h. We also see a slight increase of the corresponding activation energy E_a (0.64 eV vs. 0.61 eV). This finding supports our idea that long-time milling, *i.e.*, the formation of solid-solution like environments, mainly lead to an increase of localized correlated motional processes. The corresponding factor α turned out to be 1.54. This value is lower than $\alpha \approx 1.8$ found for $\text{Ba}_{0.5}\text{Ca}_{0.5}\text{F}_2$, which was prepared using $t_{\text{mill}} = 10$ h. On the other hand, it resembles the behavior of nanocrystal-

line BaF_2 . Obviously, the most favorable configurations for long-range ion transport are internal, heterogeneously intermixed interfaces between Ca-rich and Ba-rich regions, as discussed above. Complete mixing, or the formation of clusters with, *e.g.*, diameters of 1 nm, as suggested recently,²⁶ seems to be not needed to ensure effective long-range ion transport. Here, we assume that these heterogeneous regions act as non-stopping or percolating pathways similar to those in dispersed ion conductors.^{32,33,55–58} Interestingly, these regions, acting as hosts for fast F anion diffusivity, have partly been formed already at shorter milling times of $t_{\text{mill}} = 1$ h (see Fig. 7(b)). As compared to nanocrystalline BaF_2 we see a considerable increase in σ_{DC} for such a sample. Even if we mix nanocrystalline BaF_2 and CaF_2 , each separately milled for 10 h, for just 5 min in a planetary mill, we found a measurable increase in ionic conductivity. For these samples ^{19}F MAS NMR also points to a very low, but detectable fraction of F anions residing in or near the earth-alkaline mixed environments.

Self-diffusion coefficient

In contrast to the T_1 measurements, the spin-lock data (see Fig. 10(a)) reveal the beginning of a peak maximum from which we can finally deduce an upper limit of a diffusion coefficient. Interestingly, at the temperature where $1/T_{1p}$ passes through a maximum, in many cases the corresponding stretching factor, κ , takes its minimal value (see Fig. 3(c)). At the $1/T_{1p}$ peak maximum the F anion jump rate τ_{NMR} should be in the order of the (effective) locking frequency. Using $\omega_1/2\pi = 100$ kHz as a lower limit, *via* $\omega_1\tau = 0.5$ we estimate $1/\tau_{\text{NMR}}$ to be in the order of $1.3 \times 10^6 \text{ s}^{-1}$ at 410 K ($x = 0.5$). This value translates into a self-diffusion coefficient of $D_{410 \text{ K}} = a^2/(6\tau_{\text{NMR}})$ of $1.8 \times 10^{-14} \text{ m}^2 \text{ s}^{-1}$. Here, a denotes the average jump distance;

for $\text{Ba}_{0.5}\text{Ca}_{0.5}\text{F}_2$ we used $a = 2.92 \text{ \AA}$ as a good approximation of the mean F–F distance in $\text{Ba}_{0.5}\text{Ca}_{0.5}\text{F}_2$ (10 h). $D_{410 \text{ K}}$ is a typical value for a moderate ionic conductor. The diffusion coefficient determined at the rate maximum of a spin-lock experiment carried out at 100 kHz should be comparable to that which we obtain when DC conductivities are analyzed that probe successful ion displacements. With the ionic conductivity at 410 K we estimated a solid-state diffusion coefficient *via* the Nernst–Einstein relation, $D_\sigma = \sigma_{\text{DC}} k_B T / (q^2 N)$ with q being the charge of the F anions and N the number density of charge carriers. From ^{19}F NMR we know that approximately 20% of the ions take part in ionic conduction. In this case $D_{\sigma, 410 \text{ K}}$ amounts to $1.7 \times 10^{-14} \text{ m}^2 \text{ s}^{-1}$, which is very close to the Einstein–Smoluchowski diffusion coefficient. For $x = 0.8$ the corresponding $1/T_{1\rho}$ peak is shifted toward higher T , directly reflecting the decrease in σ_{DC} as seen in Fig. 7(a). For $x = 0.2$, *i.e.*, Ba-rich samples, strongly correlated motions (see above) and spin-diffusion effects govern the low- T ^{19}F NMR spin-lock rates.

Summary and conclusions

Mechanical treatment of CaF_2 and BaF_2 in high-energy ball mills leads to the formation of metastable $\text{Ba}_{x-1}\text{Ca}_x\text{F}_2$. Long-range ion transport is maximized for equimolar compositions and E_a , determined from DC conductivity measurements, passes through a minimum value (0.61 eV) at this composition. Through ^{19}F NMR relaxometry measurements, being in our case sensitive to short-range F anion dynamics, we tried to sharpen this picture. Here, we showed that ion dynamics on the angstrom length scale is characterized by very similar activation energies if x varies from 0.2 (0.43 eV) to 0.5 (0.50 eV). The increase of the absolute ^{19}F SLR NMR rates can be explained by an increase of the pre-factor of the underlying Arrhenius equation, which is, besides other factors, governed by the activation entropy. For all samples we observed highly correlated ionic motion. While macroscopic properties, such as σ_{DC} , do not depend much on milling time; short-range order and motional correlation effects do. By comparing the various samples prepared we conclude that F anion diffusivity in earth-alkaline mixed interfacial regions, either rich in Ba or Ca, mainly boost long-range ion transport. Extensive mixing of the cations during long milling periods, on the other hand, primarily influences short-range ion dynamics.

Conflicts of interest

There are no conflicts to declare.

Acknowledgements

We thank Veronika Pregartner for her help with sample preparation and characterization. Financial support by the Deutsche Forschungsgemeinschaft (DFG Research Unit 1277, grant no.

WI3600/2-1(4-1) and WI3600/5-2 (SPP 1415)) as well as by the Austrian Federal Ministry of Science, Research and Economy, and the Austrian National Foundation for Research, Technology and Development (Christian Doppler Laboratory of Lithium Batteries: Ageing Effects, Technology and New Materials) is greatly appreciated.

References

- P. G. Bruce, B. Scrosati and J. M. Tarascon, *Angew. Chem., Int. Ed.*, 2008, **47**, 2930–2946.
- B. Dunn, H. Kamath and J. M. Tarascon, *Science*, 2011, **334**, 928–935.
- J. B. Goodenough and K. S. S. Park, *J. Am. Chem. Soc.*, 2013, **135**, 1167–1176.
- J. C. Bachman, S. Muy, A. Grimaud, H. H. Chang, N. Pour, S. F. Lux, O. Paschos, F. Maglia, S. Lupart, P. Lamp, L. Giordano and Y. Shao-Horn, *Chem. Rev.*, 2016, **116**, 140–162.
- A. S. Arico, P. Bruce, B. Scrosati, J. M. Tarascon and W. Van Schalkwijk, *Nat. Mater.*, 2005, **4**, 366–377.
- M. Anji Reddy and M. Fichtner, *J. Mater. Chem.*, 2011, **21**, 17059–17062.
- P. Heitjans and S. Indris, *J. Phys.: Condens. Matter*, 2003, **15**, R1257–R1289.
- A. Chadwick and S. Savin, *Solid State Ionics*, 2006, **177**, 3001–3008.
- J. Maier, *Chem. Mater.*, 2014, **26**, 348–360.
- J. Maier, *Phys. Chem. Chem. Phys.*, 2009, **11**, 3011–3022.
- J. Maier, *Z. Phys. Chem.*, 2003, **217**, 415–436.
- P. Heitjans, M. Masoud, A. Feldhoff and M. Wilkening, *Faraday Discuss.*, 2007, **134**, 67–82.
- F. Preishuber-Pflügl, V. Epp, S. Nakhal, M. Lerch and M. Wilkening, *Phys. Status Solidi C*, 2015, **12**, 10–14.
- D. Wohlmuth, V. Epp, P. Bottke, I. Hanzu, B. Bitschnau, I. Letofsky-Papst, M. Kriechbaum, H. Amenitsch, F. Hofer and M. Wilkening, *J. Mater. Chem. A*, 2014, **2**, 20295–20306.
- V. Epp and M. Wilkening, *ChemPhysChem*, 2013, **14**, 3706–3713.
- M. Wilkening, V. Epp, A. Feldhoff and P. Heitjans, *J. Phys. Chem. C*, 2008, **112**, 9291–9300.
- F. Preishuber-Pflügl, P. Bottke, V. Pregartner, B. Bitschnau and M. Wilkening, *Phys. Chem. Chem. Phys.*, 2014, **16**, 9580–9590.
- V. Epp and M. Wilkening, in *Handbook of Solid State Batteries*, World Scientific, Singapore, 2015, ch. Li dynamics in solids as seen via NMR relaxometry.
- M. Heise, G. Scholz, A. Düvel, P. Heitjans and E. Kemnitz, *Solid State Sci.*, 2016, **60**, 65–74.
- G. Scholz, S. Breitfeld, T. Krahl, A. Düvel, P. Heitjans and E. Kemnitz, *Solid State Sci.*, 2015, **50**, 32–41.
- H. Bhatia, D. T. Thieu, A. H. Pohl, V. S. K. Chakravadhanula, M. H. Fawey, C. Kubel and M. Fichtner, *ACS Appl. Mater. Interfaces*, 2017, **9**, 23707–23715.

- 22 C. Ronge, M. A. Reddy, R. Witter and M. Fichtner, *ACS Appl. Mater. Interfaces*, 2014, **6**, 2103–2110.
- 23 C. Ronge, M. A. Reddy, R. Witter and M. Fichtner, *J. Phys. Chem. C*, 2013, **117**, 4943–4950.
- 24 B. Ruprecht, M. Wilkening, A. Feldhoff, S. Steuernagel and P. Heitjans, *Phys. Chem. Chem. Phys.*, 2009, **11**, 3071–3081.
- 25 B. Ruprecht, M. Wilkening, S. Steuernagel and P. Heitjans, *J. Mater. Chem.*, 2008, **18**, 5412–5416.
- 26 D. Zahn, P. Heitjans and J. Maier, *Chem. – Eur. J.*, 2012, **18**, 6225–6229.
- 27 A. Düvel, P. Heitjans, P. Fedorov, G. Scholz, G. Cibin, A. V. Chadwick, D. M. Pickup, S. Ramos, L. W. L. Sayle, E. K. L. Sayle, T. X. T. Sayle and D. C. Sayle, *J. Am. Chem. Soc.*, 2017, **139**, 5842–5848.
- 28 A. Düvel, B. Ruprecht, P. Heitjans and M. Wilkening, *J. Phys. Chem. C*, 2011, **115**, 23784–23789.
- 29 N. Sata, K. Eberman, K. Eberl and J. Maier, *Nature*, 2000, **408**, 946–949.
- 30 J. Maier, *Prog. Solid State Chem.*, 1995, **23**, 171–263.
- 31 J. Maier, *J. Phys. Chem. Solids*, 1985, **46**, 309–320.
- 32 M. Wilkening, S. Indris and P. Heitjans, *Phys. Chem. Chem. Phys.*, 2003, **5**, 2225–2231.
- 33 S. Indris and P. Heitjans, *J. Non-Cryst. Solids*, 2002, **307**, 555–564.
- 34 P. Heitjans and M. Wilkening, *Mater. Res. Bull.*, 2009, **34**, 915–922.
- 35 D. C. Look and I. J. Lowe, *J. Chem. Phys.*, 1966, **44**, 2995–3000.
- 36 S. Indris, D. Bork and P. Heitjans, *J. Mater. Synth. Process.*, 2000, **8**, 245–250.
- 37 A. L. Patterson, *Phys. Rev.*, 1939, **56**, 978–982.
- 38 A. V. Chadwick, A. Düvel, P. Heitjans, D. M. Pickup, S. Ramos, D. C. Sayle and T. X. T. Sayle, *IOP Conf. Ser.: Mater. Sci. Eng.*, 2015, **80**, 012005.
- 39 D. Wohlmuth, V. Epp, B. Stanje, A. M. Welsch, H. Behrens and M. Wilkening, *J. Am. Ceram. Soc.*, 2016, **99**, 1687–1693.
- 40 M. Wilkening and P. Heitjans, *Phys. Rev. B: Condens. Matter Mater. Phys.*, 2008, **77**, 024311.
- 41 M. Wilkening, D. Bork, S. Indris and P. Heitjans, *Phys. Chem. Chem. Phys.*, 2002, **4**, 3246–3251.
- 42 B. Ruprecht, H. Billetter, U. Ruschewitz and M. Wilkening, *J. Phys.: Condens. Matter*, 2010, **22**, 245901.
- 43 M. A. Kraft, S. P. Culver, M. Calderon, F. Bocher, T. Krauskopf, A. Senyshyn, C. Dietrich, A. Zevalkink, J. Janek and W. G. Zeier, *J. Am. Chem. Soc.*, 2017, **139**, 10909–10918.
- 44 W. Meyer and H. Neldel, *Phys. Z.*, 1937, **38**, 1014–1019.
- 45 P. Heitjans, A. Schirmer and S. Indris, in *Diffusion in Condensed Matter – Methods, Materials, Models*, ed. P. Heitjans and J. Kärger, Springer, Berlin, 2005, pp. 367–415.
- 46 M. Uitz, V. Epp, P. Bottke and M. Wilkening, *J. Electroceram.*, 2017, **38**, 142.
- 47 B. Stanje, V. Epp, S. Nakhal, M. Lerch and M. Wilkening, *ACS Appl. Mater. Interfaces*, 2015, **7**, 4089–4099.
- 48 X. F. He, Y. Z. Zhu and Y. F. Mo, *Nat. Commun.*, 2017, **8**, 15893.
- 49 K. L. Ngai, *Solid State Ionics*, 1998, **105**, 225–230.
- 50 K. L. Ngai, *Phys. Rev. B: Condens. Matter Mater. Phys.*, 1993, **48**, 13481–13485.
- 51 V. Blache, J. Forster, H. Jain, O. Kanert, R. Kuchler and K. L. Ngai, *Solid State Ionics*, 1998, **113**, 723–731.
- 52 O. Kanert, R. Kuchler, K. L. Ngai and H. Jain, *Phys. Rev. B: Condens. Matter Mater. Phys.*, 1994, **49**, 76–82.
- 53 K. L. Ngai and O. Kanert, *Solid State Ionics*, 1992, **53**, 936–946.
- 54 O. Kanert, J. Steinert, H. Jain and K. L. Ngai, *J. Non-Cryst. Solids*, 1991, **131**, 1001–1010.
- 55 C. C. Liang, *J. Electrochem. Soc.*, 1973, **120**, 1289–1292.
- 56 S. Indris, P. Heitjans, M. Ulrich and A. Bunde, *Z. Phys. Chem.*, 2005, **219**, 89–103.
- 57 M. Ulrich, A. Bunde, S. Indris and P. Heitjans, *Phys. Chem. Chem. Phys.*, 2004, **6**, 3680–3683.
- 58 S. Indris, P. Heitjans, H. E. Roman and A. Bunde, *Phys. Rev. Lett.*, 2000, **84**, 2889–2892.

3.2.2 Fluorine Translational Anion Dynamics in Nanocrystalline Ceramics: $\text{SrF}_2\text{-YF}_3$ Solid Solutions

Nanokristalline Keramiken weisen aufgrund ihrer heterogenen Struktur, die aus defektreichen Kristalliten und ungeordneten Grenzflächen besteht, oftmals verbesserte Diffusionseigenschaften auf. Eine Methode, um ihre Ionendynamik noch weiter zu steigern, stellt die aliovalente Substitution dar, mit der sowohl die Anzahl der Defekte als auch die Ladungsträgerdichte beeinflusst werden kann. Hier wurde versucht SrF_2 , unter Erhaltung der kubischen Struktur, mit YF_3 zu substituieren und so die Teilchendichte von mobilen F Anionen zu erhöhen.

Im folgenden Artikel wird über die dynamischen Parameter von $\text{Sr}_{1-x}\text{Y}_x\text{F}_{2+x}$ Systemen berichtet, die durch den Einbau von YF_3 in SrF_2 mittels Hochenergie-Kugelmahlen synthetisiert wurden. Die strukturellen Eigenschaften wurden wiederum mit Hilfe von XRD Messungen und hochauflösenden MAS-NMR-Experimenten analysiert. Zur detaillierten Untersuchung des Ionentransportes wurden mittels Impedanzspektroskopie die Gesamtleitfähigkeiten sowie die Aktivierungsenergien bestimmt. Dadurch konnte gezeigt werden, dass sich die Leitfähigkeiten der Proben durch gemeinsames Mahlen von SrF_2 mit YF_3 um mehrere Größenordnungen erhöhten. Gleichzeitig sind die Aktivierungsenergien und damit die Barrieren für die Wanderung der Ladungsträger gesunken. Die Spektroskopieergebnisse machen zudem noch deutlich, dass keine Korngrenzenregionen in den Materialien vorhanden sind, die eine Ionenbewegung über längere Distanzen stark behindern. Die hergestellten Verbindungen sind daher bei erhöhten Temperaturen potentiell einsetzbare Ionenleiter in Fluorid-Ionen-Batterien.

**Fluorine Translational Anion Dynamics in Nanocrystalline Ceramics:
 $\text{SrF}_2\text{-YF}_3$ Solid Solutions**

S. Breuer, B. Stanje, V. Pregartner, S. Lunghammer, I. Hanzu, and M. Wilkening, *Crystals*, 2018, **8**, 122.

Article

Fluorine Translational Anion Dynamics in Nanocrystalline Ceramics: $\text{SrF}_2\text{-YF}_3$ Solid Solutions

Stefan Breuer ^{1*} , Bernhard Stanje ¹, Veronika Pregartner ¹, Sarah Lunghammer ¹, Ilie Hanzu ^{1,2}  and Martin Wilkening ^{1,2,*} 

¹ Christian Doppler Laboratory for Lithium Batteries, and Institute for Chemistry and Technology of Materials, Graz University of Technology (NAWI Graz), Stremayrgasse 9, 8010 Graz, Austria; bernhard.stanje@gmx.at (B.S.); veronika.pregartner@tugraz.at (V.P.); sarah.lunghammer@tugraz.at (S.L.); hanzu@tugraz.at (I.H.)

² Alistore-ERI European Research Institute, 33 rue Saint Leu, 80039 Amiens, France

* Correspondence: breuer@tugraz.at (S.B.); wilkening@tugraz.at (M.W.); Tel.: +43-316-873-32330 (M.W.)

Received: 24 January 2018; Accepted: 2 March 2018; Published: 5 March 2018

Abstract: Nanostructured materials have already become an integral part of our daily life. In many applications, ion mobility decisively affects the performance of, e.g., batteries and sensors. Nanocrystalline ceramics often exhibit enhanced transport properties due to their heterogeneous structure showing crystalline (defect-rich) grains and disordered interfacial regions. In particular, anion conductivity in nonstructural binary fluorides easily exceeds that of their coarse-grained counterparts. To further increase ion dynamics, aliovalent substitution is a practical method to influence the number of (i) defect sites and (ii) the charge carrier density. Here, we used high energy-ball milling to incorporate Y^{3+} ions into the cubic structure of SrF_2 . As compared to pure nanocrystalline SrF_2 the ionic conductivity of $\text{Sr}_{1-x}\text{Y}_x\text{F}_{2+x}$ with $x = 0.3$ increased by 4 orders of magnitude reaching $0.8 \times 10^{-5} \text{ S cm}^{-1}$ at 450 K. We discuss the effect of YF_3 incorporation on conductivities isotherms determined by both activation energies and Arrhenius pre-factors. The enhancement seen is explained by size mismatch of the cations involved, which are forced to form a cubic crystal structure with extra F anions if x is kept smaller than 0.5.

Keywords: nanocrystalline ceramics; binary fluorides, ionic conductivity; ball milling; cation mixing; aliovalent substitution

1. Introduction

Nanostructured materials assume a variety of functions in quite different applications and devices of our daily life [1]. Considering nanocrystalline ionic conductors [2–5], a range of studies report on enhanced anion and cation dynamics [6,7]. Structural disorder and defects [8–10], lattice mismatch [11–13] as well as size effects [14–19], which results in extended space charge regions, are used to explain the properties of nanocrystalline compounds. Especially for nano-engineered systems, which were prepared by bottom-up procedures, such as gas condensation or epitaxial methods [20,21], space charge regions lead to non-trivial effects that may enhance ion transport. This effect has not only been shown for the pioneering prototype system $\text{BaF}_2\text{-CaF}_3$ [20] but also, quite recently, for nanoscopic, grain-boundary engineered $\text{SrF}_2\text{-LaF}_3$ heterolayers [22].

If prepared via a top-down approach such as ball milling [8,23–25], the nanocrystalline material obtained is anticipated to consist of nm-sized crystals surrounded by structurally disordered regions [6,26]. In particular, this structural model helped rationalize ion dynamics in oxides [8]. For fluorides instead, amorphous regions are present to a much lesser extent [27,28]. High-energy ball milling also increases the density of defects in the interior of the nanograins [10,28]. Starting with binary fluorides, such as nanocrystalline BaF_2 , whose F anion conductivity exceeds that of BaF_2 monocrystals

by some orders of magnitude [12], iso- and aliovalent substitution of the metal cations drastically improves ion transport [11,29]. As an example, in the nanocrystalline solid solutions $\text{Me}_{1-x}\text{Sr}_x\text{F}_2$ ($\text{Me} = \text{Ca}, \text{Ba}$) the ionic conductivity passes through a maximum at intermediate values of x while the corresponding activation energy shows a minimum, the same holds for $\text{Ba}_{1-x}\text{Ca}_x\text{F}_2$ [11]. Although the original cubic crystal structure remains untouched for the mixed systems, strain and defects resulting from mixing sensitively affects F anion dynamics [11,12,30]. Metastable $\text{Ba}_{1-x}\text{Ca}_x\text{F}_2$, however, cannot be prepared via solid state synthesis; instead, it is only accessible by high-energy ball milling that forces the cations ions, substantially differing in size, to form a solid solution at atomic scale [12].

Provided the cubic crystal system is retained, aliovalent substitution, e.g., with LaF_3 or YF_3 , increases the number density of mobile F anions. This effect has been shown for $\text{Ba}_{1-x}\text{La}_x\text{F}_{2+x}$ [29,31]. Starting with SrF_2 and YF_3 (see Figure 1) a similar behavior is expected. So far, $\text{Sr}_{1-x}\text{Y}_x\text{F}_{2+x}$ solid solutions have been prepared by ceramic synthesis and wet chemical approaches. Here, we report the dynamic parameters of nanocrystalline $\text{Sr}_{1-x}\text{Y}_x\text{F}_{2+x}$ obtained through high-energy ball milling. By using high impact planetary mills we managed to incorporate YF_3 into SrF_2 until the composition $\text{Sr}_{0.7}\text{Y}_{0.3}\text{F}_{2.3}$. Ionic conductivity greatly differs from that of Y-free nanocrystalline SrF_2 . Ionic conductivities at elevated temperature might be high enough to realize high-temperature all-solid-state fluorine batteries [32–35]. In addition, as pointed out by Ritter et al. nanoscopic compounds based on SrF_2 as host for rare elements might act as new luminescent materials [36].

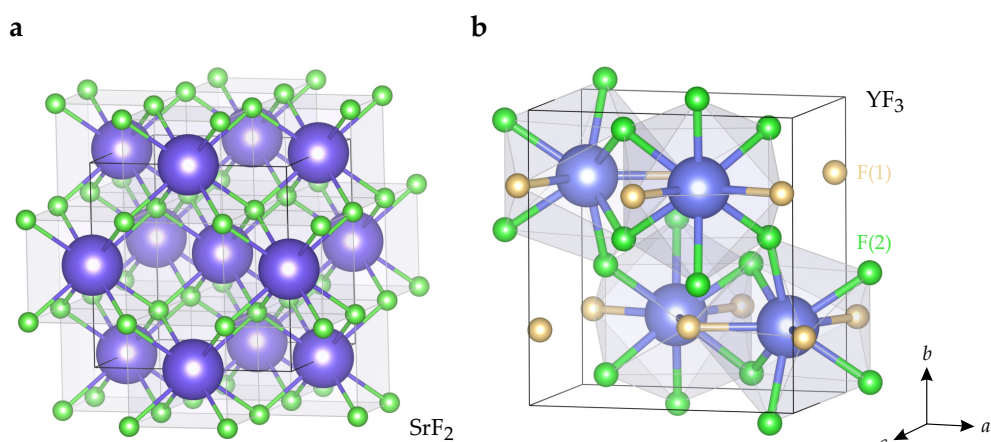


Figure 1. (a) Crystal structure ($Fd\bar{3}m$) of cubic SrF_2 with the Sr^{2+} ions (spheres in light blue, ionic radius 0.99 Å) occupying the $4b$ positions coordinated by eight fluorine anions residing on $8c$; In (b) the crystal structure orthorhombic of YF_3 ($Pnma$) is shown; the trivalent Y^{3+} ions (light blue spheres, ionic radius 0.90 Å) occupy the $4c$ sites, two further crystallographically inequivalent F sites exist which are filled by the F anions F(1) and F(2).

2. Materials and Methods

Nanocrystalline $\text{Sr}_{1-x}\text{Y}_x\text{F}_{2+x}$ samples were prepared in a planetary high-energy ball mill (Fritsch P7, Premium line, Fritsch, Idar-Oberstein, Germany) by mixing SrF_2 and YF_3 in the desired molar ratio. We used a 45 mL ZrO_2 cub with 140 zirconium oxide milling balls (5 mm in diameter). To guarantee complete transformation the mixtures were milled for 10 h at a rotation speed of 600 rpm under dry conditions, i.e., without the addition of any solvents.

The phase purity and crystal system was checked via X-ray diffraction (Bruker D8 Advance, Bragg Brentano geometry, 40 kV, Bruker AXS, Rheinstetten, Germany). With the help of the Scherrer equation [37] we roughly estimated the crystallite size of the samples, see ref. [10,38] for further details on this procedure. Usually, after sufficiently long milling periods the mean crystallite size reaches 10 to 20 nm [39]. ^{19}F magic angle spinning nuclear (MAS) magnetic resonance (NMR) was used to characterize SrF_2 and YF_3 as well as the mixed fluorides at atomic level. We recorded rotor-synchronized Hahn echoes by employing a Bruker 2.5-mm MAS probe placed in a 11.4 T

cryomagnet. Spectra were measured with a Bruker Avance 500 spectrometer (Bruker BioSpin, Rheinstetten, Germany). Spinning was carried out with ambient bearing gas pressure. The $\pi/2$ pulse length was 2.1 μ s at 50 W power level; the recycle delay was 20 s and 64 transients were accumulated for each spectrum. We took advantage of LiF powder as a secondary reference (-204.3 ppm) [40] to determine chemical shifts δ_{iso} ; CFCl_3 (0 ppm) served as the primary reference.

To analyze ionic conductivities, the powders were uniaxially cold-pressed to pellets (8 mm in diameter, 0.5 to 1 mm in thickness). After applying electrically conducting Au electrodes (100 to 200 nm) via sputtering, a Novocontrol Concept 80 broadband analyzer (Novocontrol Technologies, Montabaur, Germany) was employed to record conductivity isotherms and complex impedances as a function of temperature. The broadband dielectric analyzer was connected to a QUATRO cryo system (Novocontrol Technologies, Montabaur, Germany) that allows precise settings of temperature and an automatic execution of the measurements. The QUATRO is operated with a stream of freshly evaporated nitrogen gas that passes a heater and enters the sample chamber where the temperature is measured using Pt-100 thermocouples. We used a voltage amplitude of 100 mV and varied the frequency ν from 0.1 Hz to 10 MHz. The isotherms revealed distinct frequency-independent plateaus from which *direct current* DC conductivities σ_{DC} (see above) were read off for each temperature T .

3. Results and Discussion

Structure: X-ray Diffraction and ^{19}F High-Resolution MAS NMR Spectroscopy

Long-range and local structures of $\text{Sr}_{1-x}\text{Y}_x\text{F}_{2+x}$ ($0 \leq x \leq 1$) were studied by X-ray diffraction and ^{19}F MAS NMR, see Figures 2 and 3.

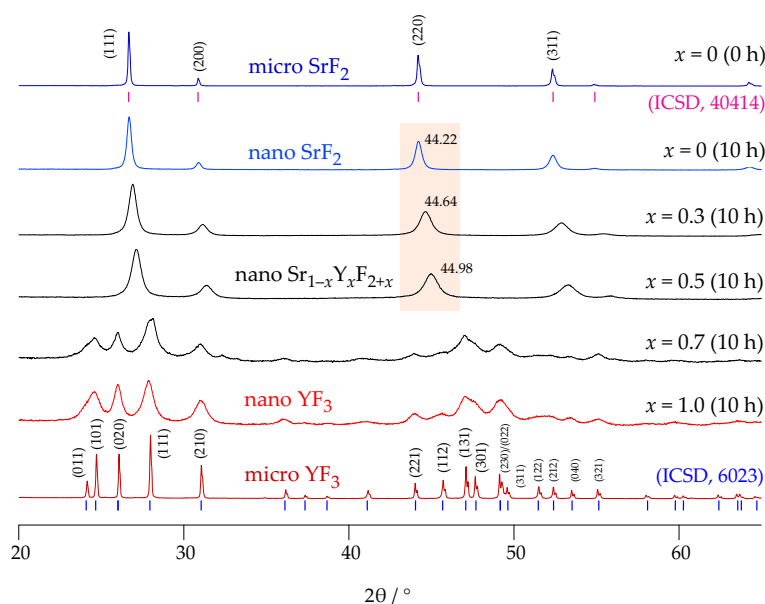


Figure 2. X-ray powder diffractograms recorded ($\text{CuK}_{\alpha 1}$, 1.54059 Å) to characterize the phase purity of the starting materials as well as that of the mixed phases formed. The periods indicated in brackets show the milling times. The patterns of microcrystalline SrF_2 and YF_3 perfectly match with those in literature; vertical bars show the average positions of the $\text{CuK}_{\alpha 1}$ and $\text{CuK}_{\alpha 2}$ reflections. The broadening of the reflections, which is evident for the milled samples, indicates nm-sized crystallites; lattice strain and a distribution of lattice constants due to cation mixing may contribute to the broadening effect seen as well. Mixing of the cations is anticipated to have a much larger effect on ionic conductivity than the decrease in crystallite size seen when going from $x = 0$ to $x = 0.3$. See text for further explanation.

SrF_2 crystallizes in the cubic crystal system and YF_3 adopts an orthorhombic structure (see Figure 1). In Figure 2 the X-ray powder patterns of the starting materials as well as those of the milled samples, with the composition $\text{Sr}_{1-x}\text{Y}_x\text{F}_{2+x}$, are shown.

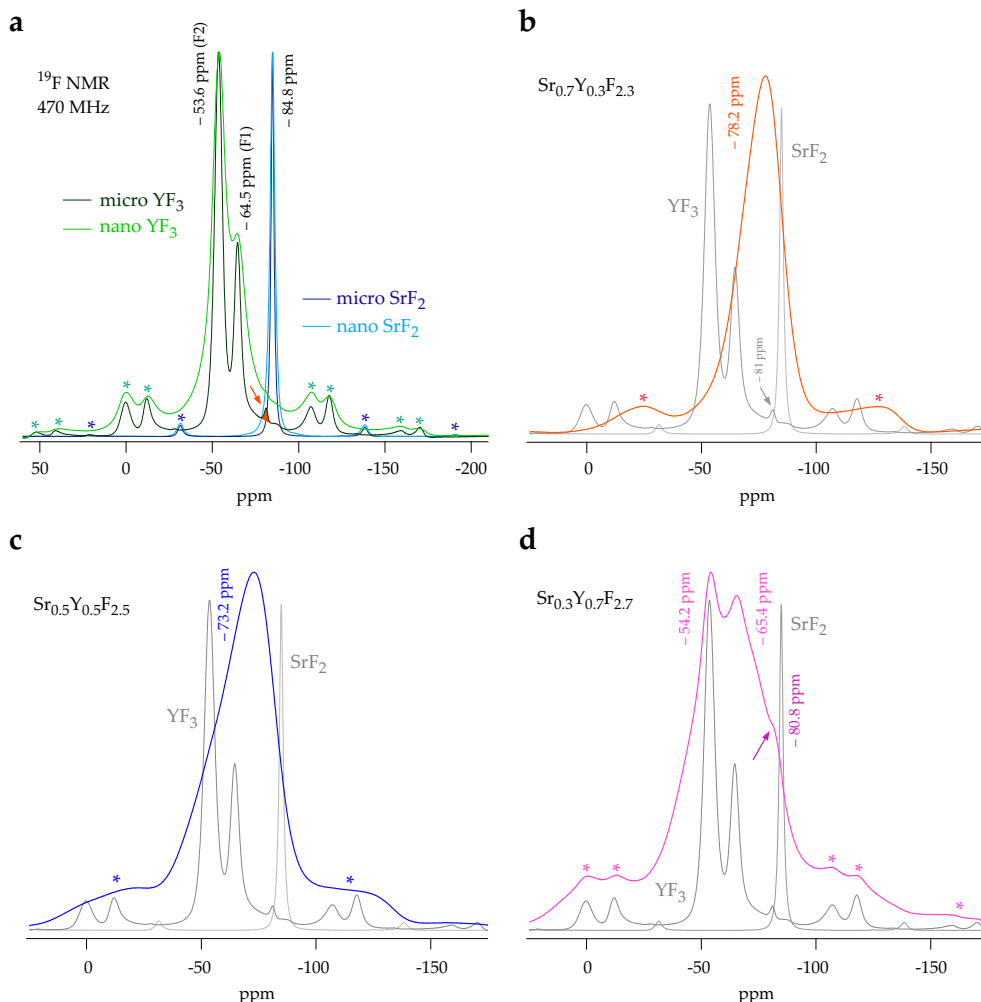


Figure 3. (a–d) ^{19}F magic angle spinning nuclear magnetic resonance (MAS NMR) spectra of $\text{Sr}_{1-x}\text{Y}_x\text{F}_{2+x}$ prepared by ball milling. We used a rotor-synchronized Hahn echo pulse sequence to record the spectra at a spinning speed of 25 kHz; asterisks (*) denote spinning sidebands. The spectra are referenced to CFCl_3 (0 ppm). In (a) the spectra of microcrystalline, i.e., unmilled, and nanocrystalline SrF_2 and YF_3 are shown. The nanocrystalline samples were obtained after milling the starting materials for 10 h under dry conditions. Mechanical treatment leads to broadening of the NMR lines because of the defects and polyhedra distortions introduced. The spectra of YF_3 reveal the two magnetically equivalent sites of YF_3 ; their isotropic chemical shifts δ_{iso} are -53.6 ppm and -84.8 ppm . For the Sr-rich and Y-rich samples; see (b,d), $\text{Sr}_{1-x}\text{Y}_x\text{F}_{2+x}$ with $x = 0.3$ and $x = 0.7$ the center of the broad MAS NMR lines shift toward that of SrF_2 and YF_3 , respectively. These isotropic shifts, together with the broadening of the lines, owing to a distribution of chemical shifts caused by atomic disorder, reveals the formation of mixed (Sr,Y) environments the F anions are subjected to. For $x = 0.5$ the extent of mixing is, of course, most effective; see (c).

As a result of heavy ball-milling in a planetary mill, the two fluorides form a product with cubic symmetry up to $x = 0.5$. Broadening of the reflections is caused by both lattice strain (ϵ) and nm-sized crystallites. The equation introduced by Scherrer yields 36(2) nm ($\epsilon = 0.0031(5)$), 13(2) nm ($\epsilon = 0.0083(5)$) and 10(2) nm ($\epsilon = 0.0123(10)$) as average crystallite size for the samples with $x = 0$,

$x = 0.3$ and $x = 0.5$, respectively. The values in brackets denote microstrain as estimated using the method proposed by Williamson and Hall [41], see also [42] for details. With increasing extent of cation mixing lattice strain enhances.

Furthermore, we clearly observe a shift of the reflections toward larger diffraction angles, see the positions of the (220) reflections as indicated in Figure 2. The lattice constant a gradually changes from 5.8040 Å (SrF_2) to 5.7442 Å ($\text{Sr}_{0.7}\text{Y}_{0.3}\text{F}_{2.3}$). The linear decrease of a , as a result of incorporation of the smaller Y cations, indicates Vegard behaviour. At the same time, F interstitials are generated that are expected to boost F^- ionic conductivity, vide infra (Figure 4).

When coming from pure YF_3 , Sr ions are incorporated into the trifluoride. Once again, small crystallites significantly broaden the X-ray reflections; the orthorhombic structure of YF_3 is, however, still conserved (see Figure 2). The patterns do not show large amounts of X-ray amorphous material as featureless, broad humps are missing. Hence, we deal with nanocrystalline samples with local disorder.

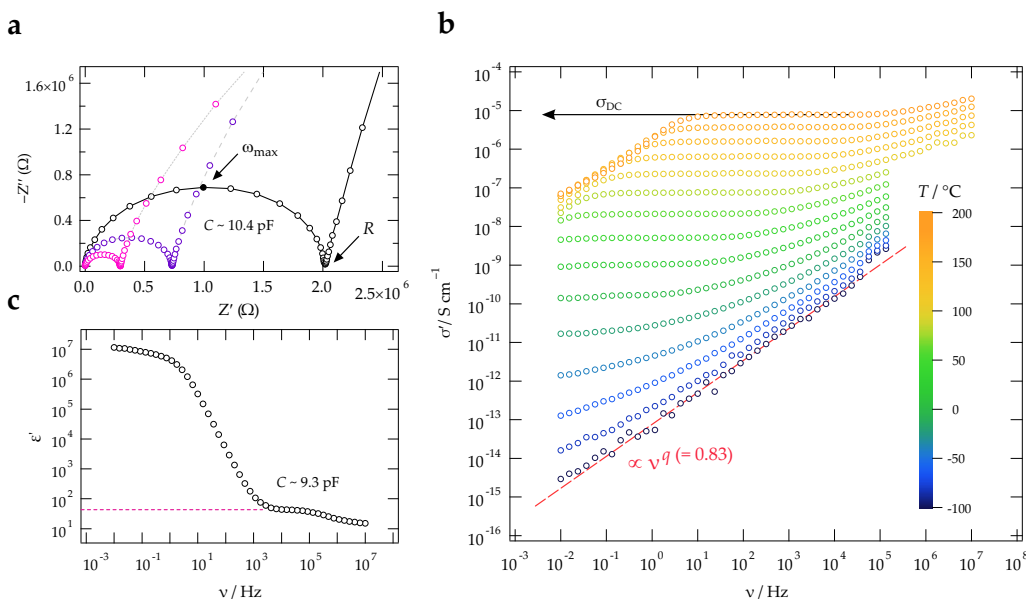


Figure 4. (a) Nyquist plots of the complex impedance of $\text{Sr}_{1-x}\text{Y}_x\text{F}_{2+x}$ with $x = 0.3$ recorded at the temperatures indicated. The solid lines are to guide the eye. The depressed semicircles indicate correlated ion movements in the ternary fluoride; from $\omega_{\max} (= \nu_{\max} 2\pi)$ and R electrical capacities, $C = 1/(\omega_{\max} R)$, in the order of 10 pF were estimated indicating that the overall electrical response is mainly given by bulk properties rather than by ion-blocking grain boundary contributions; (b) Conductivity isotherms of $\text{Sr}_{0.7}\text{Y}_{0.3}\text{F}_{2.3}$ recorded from -100 °C to $+180$ °C in steps of 20 °C. The pronounced plateaus at intermediate frequencies contain the DC conductivity σ_{DC} , as indicated; (c) Real part, ϵ' , of the complex primitivity as a function of frequency. Above 10^3 Hz the bulk response is seen; the capacity associated with that response is in the order of 10 pF.

Local disorder is also sensed by ^{19}F MAS NMR spectroscopy. In Figure 3a the spectra of the non-substituted binary fluorides are shown. As expected, coarse grained SrF_2 only shows a single resonance at -84.8 ppm and the spectrum of YF_3 reveals the two crystallographically inequivalent F positions F(1) and F(2). The samples with μm -sized crystallites are composed of sharp lines that perfectly agree with those presented and analyzed in literature [36,40]. Broadening, but no change in isotropic chemical shift, is observed for the samples treated mechanically. YF_3 shows a negligible amount of an impurity phase, see the NMR signal at $\delta_{\text{iso}} = -81$ ppm. Upon incorporation of YF_3 , the ^{19}F MAS NMR lines drastically broaden because of the introduction of structural disorder, see also [36]. The various Sr-F environments formed as well as the various defects present, including F vacancies and interstitials, result in a broad distribution of ^{19}F NMR chemical shifts. Depending on which cation is the major component in $\text{Sr}_{1-x}\text{Y}_x\text{F}_{2+x}$ the center of the broad lines is either located

near the original chemical shifts δ_{iso} of SrF_2 (Figure 3b) or those of YF_3 (Figure 3d). For the equimolar solid-solution with $x = 0.5$, the center of the line is in between that of SrF_2 and YF_3 . The shoulder near -50 ppm might indicate Y-rich regions or clusters. For a detailed analysis of ^{19}F MAS spectra we refer to [36]. Indeed, ^{89}Y MAS NMR measurements by Ritter et al. [36] suggested F clustering taking place in samples with more than 10 mol % of Y^{3+} .

In contrast to other solid-solutions, such as $\text{Me}_{1-z}\text{Sr}_z\text{F}_2$ ($\text{Me} = \text{Ca}, \text{Ba}; 0 \leq z \leq 1$) and $\text{Ba}_{1-z}\text{Ca}_z\text{F}_2$ [11], line broadening, i.e., the distribution of chemical shifts, is much larger for $\text{Sr}_{1-x}\text{Y}_x\text{F}_{2+x}$. Because of this effect, even under the MAS conditions applied here, we cannot resolve the (Sr,Y) environments as it was possible for the (Ca,Sr) species in cubic $\text{Ca}_{1-z}\text{Sr}_z\text{F}_2$ with a similar range of chemical shifts, see the MAS NMR spectra presented in [11].

In Figure 4a,b Nyquist plots and conductivity isotherms of $\text{Sr}_{1-x}\text{Y}_x\text{F}_{2+x}$ with $x = 0.3$ are displayed; Figure 5 gives an overview of the temperature dependence of the ionic conductivities.

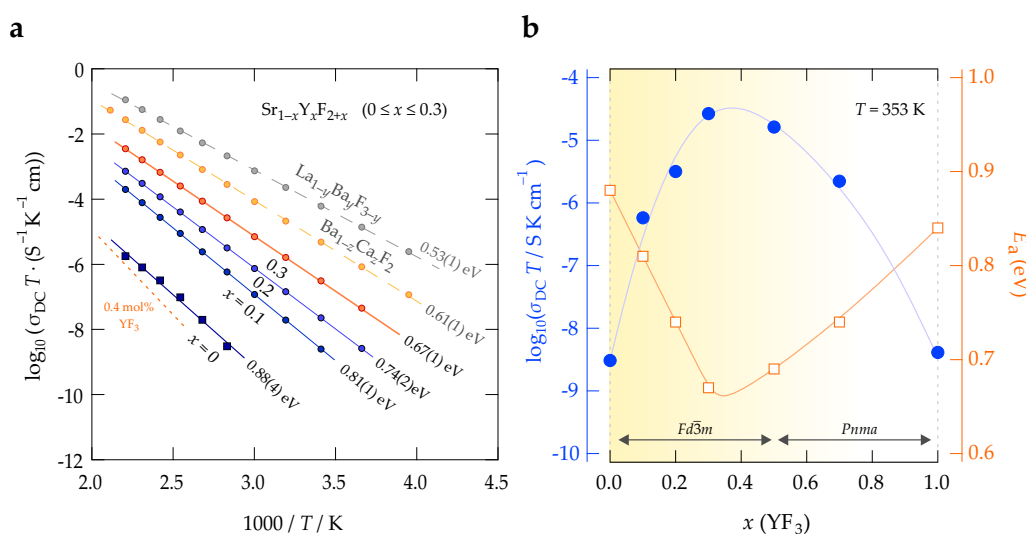


Figure 5. (a) Arrhenius plot of $\sigma_{\text{DC}} T$ vs. the $1/T$ of mechanochemically prepared $\text{Sr}_{1-x}\text{Y}_x\text{F}_{2+x}$ with $x \leq 0.3$. Solid and dashed lines represent fits according to an Arrhenius equation, $\sigma_{\text{DC}} T \propto \exp(-E_a/(k_B T))$; k_B denotes Boltzmanns constant. The activation energies obtained are indicated; (b) Change of E_a (see right axis) and $\sigma_{\text{DC}} T$ of nanocrystalline $\text{Sr}_{1-x}\text{Y}_x\text{F}_{2+x}$ as a function of x . See text for further explanation.

Plotting the real part σ' of the complex conductivity $\hat{\sigma}$ results in curves with (i) distinct DC plateaus at sufficiently low frequencies and (ii) a dispersive part at low T and high frequencies. The collapse of σ' at the lowest frequencies and highest temperature is because of F anion charge accumulation in front of the ion-blocking electrode. We used the frequency-independent plateau to determine specific ionic conductivities as a function of temperature. These values refer to long-range ion transport and characterize successful charge displacements in the fluoride. The same values for σ' can be inferred from analyzing Nyquist plots (see Figure 3a) that show the imaginary part ($-Z''$) of the complex impedance \hat{Z} as a function of its real part Z' . From the intercept of the semicircle the variable-temperature resistance R can be extracted and converted into σ' . The electrical relaxation process seen in conductivity (or impedance) spectroscopy mainly refers to a bulk process as the corresponding electrical capacity takes values in the pF range, see Figure 4a. Most likely, the broad semicircle also contains contributions from grain boundaries and interfacial regions. These regions do not seem to block ion transport as is known for other fast ion conductors [43].

The shape of the isotherms $\sigma'(\nu)$, cf. Figure 4b, does not change much with temperature indicating that the same relaxation process is probed at elevated T . At sufficiently high T , the data fulfill the so-called time-temperature superposition principle [44,45]. At low T , however, the dispersive part,

which is sensitive to ion dynamics on shorter length scales than those seen in the DC regime, dominates the spectra. This regime can be approximated with Jonscher's power law ansatz [46], $\sigma'(\nu) \propto \nu^q$ [44]. The exponent q increases with temperature, most likely reaching $q = 1$ at cryogenic temperatures. At such low temperatures localized ion movements might play a rôle that do not contribute to long-range charge transport any longer [47]. The isotherm of $\text{Sr}_{0.7}\text{Y}_{0.3}\text{F}_{2.3}$ recorded at $T = 100\text{ }^\circ\text{C}$ is characterized by $q = 0.83(2)$. q values of approximately 0.8 are frequently seen for disordered ion conductors in this T range [29].

In Figure 5a the product $\sigma_{\text{DC}} T$ is plotted vs. the inverse temperature $1/T$ to determine activation energies E_a of the samples prepared and to illustrate the change in ionic conductivity upon Y^{3+} incorporation. For comparison, we included the Arrhenius lines of two other mechanochemically prepared F^- anion conductors *viz.* $\text{Ba}_{0.5}\text{Ca}_{0.5}\text{F}_2$ and $\text{La}_{0.9}\text{Ba}_{0.1}\text{F}_{2.9}$. In addition, ionic conductivities of YF_3 -doped SrF_2 crystals is also shown [48]. While pure (nanocrystalline) SrF_2 is a poor ionic conductor with an activation energy as high as 0.88 eV; E_a is significantly decreased to 0.67 eV for $\text{Sr}_{0.7}\text{Y}_{0.3}\text{F}_{2.3}$. The ionic conductivity, as well as the activation energy (0.84 eV) of nanocrystalline YF_3 turned out to be very similar to that of nano- SrF_2 . In Figure 5b the change in $\sigma_{\text{DC}} T$ and E_a is shown as a function of x . From $x = 0$ to $x = 0.3$ the activation energy almost linearly decrease; $\sigma_{\text{DC}} T$ passes through a maximum at ca. $x = 0.3$. Further incorporation of YF_3 causes $\sigma_{\text{DC}} T$ to decrease again. Note that the $\text{Sr}_{1-x}\text{Y}_x\text{F}_{2+x}$ system adopts cubic structure up to approximately $x = 0.5$, while the Y-rich samples crystallize with orthorhombic structure. Ultimately, at $80\text{ }^\circ\text{C}$ (see Figure 5b) we notice an enhancement in ionic conductivity by 4 orders of magnitude when going from SrF_2 to $\text{Sr}_{0.7}\text{Y}_{0.3}\text{F}_{2.3}$. This opens the way to systematically vary the ionic conductivity of the ternary fluoride over a broad dynamic range.

Interestingly, already at low Y^{3+} contents, that is, at 10 mol%, we see an increase in ionic conductivity by one order of magnitude. For comparison, the ionic conductivity of the YF_3 -doped SrF_2 crystals studied by Bollmann et al. [48] in 1970 is still lower than that of nanocrystalline SrF_2 highlighting the importance of size effects on ionic transport even in the cation-mixed system. For single crystals based on the LaF_3 tysonite structure also quite high ion conductivities have, however, been reported [49].

The change in E_a from 0.88 eV to 0.81 eV is accompanied by a significant increase of the pre-exponential factor σ_0 in $\sigma_{\text{DC}} T = \sigma_0 \exp(-E_a/(k_B T))$, see also [50]. While $\log(\sigma_0/(\text{S cm}^{-1}\text{K}))$ of SrF_2 amounts to 4.1, it increases to 5.3 for $\text{Sr}_{0.9}\text{Y}_{0.1}\text{F}_{2.1}$. Thus, the new defect structure, most likely involving F clustering as seen by ^{89}Y NMR [36], also influences the attempt frequencies (and/or the number of effective charge carriers) of the underlying jump processes. Presumably, substitution of Sr^{2+} with Y^{3+} will also influence the activation entropy for ionic migration. For $x > 0.1$ no further increase of σ_0 is seen; the additional increase in σ_{DC} is mainly governed by the reduction in activation energy. As the defect concentration is already high in this regime, we expect that predominantly lower migration energies facilitate ion transport further.

4. Conclusions

The mixed system $\text{Sr}_{1-x}\text{Y}_x\text{F}_{2+x}$ represents an attractive system to control ionic conductivities via the concept of cation mismatch. High-energy ball milling is able to force the distinctly sized cations to form a mixed phase with structural disorder at atomic scale. Treating SrF_2 with YF_3 in a high-energy planetary mill causes the original conductivity to increase by some orders of magnitude. Simultaneously, the corresponding activation energy decreases from 0.88 eV to 0.67 eV clearly showing a lowering of the migration barrier the ions have to surmount to take part in long-range transport. Besides this decrease in E_a we also observed the influence of the Arrhenius pre-factor to decisively initiate a further increase in ionic transport at $x \leq 0.1$, i.e., in the compositional range where F clustering starts.

Impedance spectroscopy shows that no grain boundary regions hinder the ions from moving over long distances. Most likely, the cation-mixed interfacial regions also provide fast diffusion pathways

similar to those in the bulk structure. As we deal with nm-sized crystallites, space charge regions are expected to also contribute to overall F anion dynamics.

Acknowledgments: We thank M. Gabriel for his help with sample preparation. Moreover, we thank the Deutsche Forschungsgemeinschaft (DFG) for financial support (SPP 1415).

Author Contributions: Stefan Breuer, Bernhard Stanje and Martin Wilkening conceived and designed the experiments; Stefan Breuer, Veronika Pregartner and Sarah Lunghammer performed the experiments; all authors were involved in analyzing and interpreting the data. Stefan Breuer and Martin Wilkening wrote the paper.

Conflicts of Interest: The authors declare no conflict of interest. The founding sponsors had no role in the design of the study; in the collection, analyses, or interpretation of data; in the writing of the manuscript, and in the decision to publish the results.

References

1. Vollath, D. *Nanomaterials—An Introduction to Synthesis, Properties and Applications*; Wiley-VCH: Weinheim, Germany, 2008; pp. 21–22.
2. Tuller, H.L. Ionic conduction in nanocrystalline materials. *Solid State Ion.* **2000**, *131*, 143–157.
3. Knauth, P. Inorganic solid Li ion conductors: An overview. *Solid State Ion.* **2009**, *180*, 911–916.
4. Kobayashi, S.; Tsurekawa, S.; Watanabe, T. A new approach to grain boundary engineering for nanocrystalline materials. *Beilstein J. Nanotechnol.* **2016**, *7*, 1829.
5. Uitz, M.; Epp, V.; Bottke, P.; Wilkening, M. Ion dynamics in solid electrolytes for lithium batteries. *J. Electroceram.* **2017**, *38*, 142–156.
6. Heitjans, P.; Indris, S. Diffusion and ionic conduction in nanocrystalline ceramics. *J. Phys. Condens. Matter* **2003**, *15*, R1257.
7. Prutsch, D.; Breuer, S.; Uitz, M.; Bottke, P.; Langer, J.; Lunghammer, S.; Philipp, M.; Posch, P.; Pregartner, V.; Stanje, B.; et al. Nanostructured Ceramics: Ionic Transport and Electrochemical Activity. *Z. Phys. Chem.* **2017**, *231*, 1361–1405.
8. Heitjans, P.; Masoud, M.; Feldhoff, A.; Wilkening, M. NMR and impedance studies of nanocrystalline and amorphous ion conductors: Lithium niobate as a model system. *Faraday Discuss.* **2007**, *134*, 67–82.
9. Epp, V.; Wilkening, M. Motion of Li⁺ in nanoengineered LiBH₄ and LiBH₄:Al₂O₃ comparison with the microcrystalline form. *ChemPhysChem* **2013**, *14*, 3706–3713.
10. Wilkening, M.; Epp, V.; Feldhoff, A.; Heitjans, P. Tuning the Li diffusivity of poor ionic conductors by mechanical treatment: High Li conductivity of strongly defective LiTaO₃ nanoparticles. *J. Phys. Chem. C* **2008**, *112*, 9291–9300.
11. Düvel, A.; Ruprecht, B.; Heitjans, P.; Wilkening, M. Mixed Alkaline-Earth Effect in the Metastable Anion Conductor Ba_{1-x}Ca_xF₂ (0 ≤ x ≤ 1): Correlating Long-Range Ion Transport with Local Structures Revealed by Ultrafast ¹⁹F MAS NMR. *J. Phys. Chem. C* **2011**, *115*, 23784–23789.
12. Ruprecht, B.; Wilkening, M.; Steuernagel, S.; Heitjans, P. Anion diffusivity in highly conductive nanocrystalline BaF₂:CaF₂ composites prepared by high-energy ball milling. *J. Mater. Chem.* **2008**, *18*, 5412–5416.
13. Sorokin, N.I.; Buchinskaya, I.I.; Fedorov, P.P.; Sobolev, B.P. Electrical conductivity of a CaF₂-BaF₂ nanocomposite. *Inorg. Mater.* **2008**, *44*, 189–192.
14. Maier, J. Ionic conduction in space charge regions. *Prog. Solid State Chem.* **1995**, *23*, 171–263.
15. Maier, J. Nanoionics: Ion transport and electrochemical storage in confined systems. *Nat. Mater.* **2005**, *4*, 805–815.
16. Maier, J. Nano-Ionics: Trivial and Non-Trivial Size Effects on Ion Conduction in Solids. *Zeitschrift für Physikalische Chemie* **2003**, *217*, 415–436.
17. Maier, J. Nanoionics: Ionic charge carriers in small systems. *Phys. Chem. Chem. Phys.* **2009**, *11*, 3011–3022.
18. Puin, W.; Rodewald, S.; Ramlau, R.; Heitjans, P.; Maier, J. Local and overall ionic conductivity in nanocrystalline CaF₂. *Solid State Ion.* **2000**, *131*, 159–164.
19. Blanchard, D.; Nale, A.; Sveinbjörnsson, D.; Eggenhuisen, T.M.; Verkuijlen, M.H.W.; Vegge, T.; Kentgens, A.P.; de Jongh, P.E. Nanoconfined LiBH₄ as a fast lithium ion conductor. *Adv. Funct. Mater.* **2015**, *25*, 184–192.

20. Sata, N.; Eberman, K.; Eberl, K.; Maier, J. Mesoscopic fast ion conduction in nanometre-scale planar heterostructures. *Nature* **2000**, *408*, 946–949.
21. Jin-Phillipp, N.Y.; Sata, N.; Maier, J.; Scheu, C.; Hahn, K.; Kelsch, M.; Rühle, M. Structures of BaF₂-CaF₂ heterolayers and their influences on ionic conductivity. *J. Chem. Phys.* **2004**, *120*, 2375–2381.
22. Vergentev, T.; Banshchikov, A.; Filimonov, A.; Koroleva, E.; Sokolov, N.; Wurz, M.C. Longitudinal conductivity of LaF₃/SrF₂ multilayer heterostructures. *Sci. Technol. Adv. Mater.* **2016**, *17*, 799–806.
23. Šepelak, V.; Düvel, A.; Wilkening, M.; Becker, K.D.; Heitjans, P. Mechanochemical reactions and syntheses of oxides. *Chem. Soc. Rev.* **2013**, *42*, 7507–7520.
24. Wilkening, M.; Bork, D.; Indris, S.; Heitjans, P. Diffusion in amorphous LiNbO₃ studied by ⁷Li NMR—Comparison with the nano-and microcrystalline material. *Phys. Chem. Chem. Phys.* **2002**, *4*, 3246–3251.
25. Wilkening, M.; Indris, S.; Heitjans, P. Heterogeneous lithium diffusion in nanocrystalline Li₂O: Al₂O₃ composites. *Phys. Chem. Chem. Phys.* **2003**, *5*, 2225–2231.
26. Gleiter, H. Nanoglasses: A new kind of noncrystalline materials. *Beilstein J. Nanotechnol.* **2013**, *4*, 517–533.
27. Chadwick, A.V.; Düvel, A.; Heitjans, P.; Pickup, D.M.; Ramos, S.; Sayle, D.C.; Sayle, T.X.T. X-ray absorption spectroscopy and computer modelling study of nanocrystalline binary alkaline earth fluorides. In *IOP Conference Series: Materials Science and Engineering*; IOP Publishing: Bristol, UK, 2015; Volume 80, p. 012005.
28. Preishuber-Pflügl, F.; Wilkening, M. Mechanochemically synthesized fluorides: Local structures and ion transport. *Dalton Trans.* **2016**, *45*, 8675–8687.
29. Preishuber-Pflügl, F.; Bottke, P.; Pregartner, V.; Bitschnau, B.; Wilkening, M. Correlated fluorine diffusion and ionic conduction in the nanocrystalline F[−] solid electrolyte Ba_{0.6}La_{0.4}F_{2.4}—¹⁹F T_{1(ρ)} NMR relaxation vs. conductivity measurements. *Phys. Chem. Chem. Phys.* **2014**, *16*, 9580–9590.
30. Ruprecht, B.; Wilkening, M.; Feldhoff, A.; Steuernagel, S.; Heitjans, P. High anion conductivity in a ternary non-equilibrium phase of BaF₂ and CaF₂ with mixed cations. *Phys. Chem. Chem. Phys.* **2009**, *11*, 3071–3081.
31. Rongeat, C.; Reddy, M.A.; Witter, R.; Fichtner, M. Nanostructured fluorite-type fluorides as electrolytes for fluoride ion batteries. *J. Phys. Chem. C* **2013**, *117*, 4943–4950.
32. Anji Reddy, M.; Fichtner, M. Batteries based on fluoride shuttle. *J. Mater. Chem.* **2011**, *21*, 17059–17062.
33. Nowroozi, M.A.; Wissel, K.; Rohrer, J.; Munnangi, A.R.; Clemens, O. LaSrMnO₄: Reversible Electrochemical Intercalation of Fluoride Ions in the Context of Fluoride Ion Batteries. *Chem. Mater.* **2017**, *29*, 3441–3453.
34. Grenier, A.; Porras-Gutierrez, A.G.; Groult, H.; Beyer, K.A.; Borkiewicz, O.J.; Chapman, K.W.; Dambournet, D. Electrochemical reactions in fluoride-ion batteries: Mechanistic insights from pair distribution function analysis. *J. Mater. Chem. A* **2017**, *5*, 15700–15705.
35. Grenier, A.; Porras-Gutierrez, A.G.; Body, M.; Legein, C.; Chrétien, F.; Raymundo-Piñero, E.; Dollé, M.; Groult, H.; Dambournet, D. Solid Fluoride Electrolytes and Their Composite with Carbon: Issues and Challenges for Rechargeable Solid State Fluoride-Ion Batteries. *J. Phys. Chem. C* **2017**, *121*, 24962–24970.
36. Ritter, B.; Krahl, T.; Scholz, G.; Kemnitz, E. Local Structures of Solid Solutions Sr_{1-x}Y_xF_{2+x} ($x = 0 \dots 0.5$) with Fluorite Structure Prepared by Sol-Gel and Mechanochemical Syntheses. *J. Phys. Chem. C* **2016**, *120*, 8992–8999.
37. Scherrer, P. Bestimmung der Größe und der inneren Struktur von Kolloidteilchen mittels Röntgenstrahlen. *Nachrichten Ges. Wiss. Göttingen* **1918**, *2*, 98.
38. Düvel, A.; Wegner, S.; Efimov, K.; Feldhoff, A.; Heitjans, P.; Wilkening, M. Access to metastable complex ion conductors via mechanosynthesis: Preparation, microstructure and conductivity of (Ba, Sr) LiF₃ with inverse perovskite structure. *J. Mater. Chem.* **2011**, *21*, 6238–6250.
39. Indris, S.; Bork, D.; Heitjans, P. Nanocrystalline oxide ceramics prepared by high-energy ball milling. *J. Mater. Synth. Proc.* **2000**, *8*, 245–250.
40. Sadoc, A.; Body, M.; Legein, C.; Biswal, M.; Fayon, F.; Rocquefelte, X.; Boucher, F. NMR parameters in alkali, alkaline earth and rare earth fluorides from first principle calculations. *Phys. Chem. Chem. Phys.* **2011**, *13*, 18539–18550.
41. Williamson, G.; Hall, W. X-ray line broadening from filed aluminium and wolfram. *Acta Metall.* **1953**, *1*, 22–31.
42. Düvel, A.; Wilkening, M.; Uecker, R.; Wegner, S.; Šepelak, V.; Heitjans, P. Mechanothesized nanocrystalline BaLiF₃: The impact of grain boundaries and structural disorder on ionic transport. *Phys. Chem. Chem. Phys.* **2010**, *12*, 11251–11262.

43. Breuer, S.; Prutsch, D.; Ma, Q.; Epp, V.; Preishuber-Pflügl, F.; Tietz, F.; Wilkening, M. Separating bulk from grain boundary Li ion conductivity in the sol-gel prepared solid electrolyte $\text{Li}_{1.5}\text{Al}_{0.5}(\text{PO}_4)_3$. *J. Mater. Chem. A* **2015**, *3*, 21343–21350.
44. Dyre, J.C.; Maass, P.; Roling, B.; Sidebottom, D.L. Fundamental questions relating to ion conduction in disordered solids. *Rep. Prog. Phys.* **2009**, *72*, 046501.
45. Sakellis, I. On the origin of time-temperature superposition in disordered solids. *Appl. Phys. Lett.* **2011**, *98*, 072904.
46. Jonscher, A. The ‘universal’ dielectric response. *Nature* **1977**, *267*, 673–679.
47. Funke, K.; Cramer, C.; Wilmer, D. *Diffusion in Condensed Matter*, 2nd ed.; Heijmans, P., Kärger, J., Eds.; Springer: Berlin, Germany, 2005; Chapter 21, pp. 857–893.
48. Bollmann, W.; Görlich, P.; Hauk, W.; Mothes, H. Ionic conduction of pure and doped CaF_2 and SrF_2 crystals. *Phys. Status Solidi (A)* **1970**, *2*, 157–170.
49. Sorokin, N.I.; Sobolev, B.P.; Krivandina, E.A.; Zhmurova, Z.I. Optimization of single crystals of solid electrolytes with tysonite-type structure (LaF_3) for conductivity at 293 K: 2. Nonstoichiometric phases $R_{1-y}M_y\text{F}_{3-y}$ ($R = \text{La-Lu}$, Y ; $M = \text{Sr, Ba}$). *Cryst. Rep.* **2015**, *60*, 123.
50. Breuer, S.; Wilkening, M. Mismatch in cation size causes rapid anion dynamics in solid electrolytes: The role of the Arrhenius pre-factor. *Dalton Trans.* **2018**, in press, doi:10.1039/C7DT04487A.



© 2018 by the authors. Licensee MDPI, Basel, Switzerland. This article is an open access article distributed under the terms and conditions of the Creative Commons Attribution (CC BY) license (<http://creativecommons.org/licenses/by/4.0/>).

3.2.3 F anion dynamics in cation-mixed nanocrystalline LaF₃:SrF₂

Auch dieser Artikel beschäftigt sich mit der Synthese und Charakterisierung neuer Fluor-Ionenleiter für verschiedenste bereits genannte Anwendungen. Wiederum wurden hierbei heterovalente Substitutionsstrategien verwendet, um mechanochemisch Mischprodukte zu synthetisieren, die stark verbesserte Transporteigenschaften im Vergleich zu ihren binären Ausgangsstoffen aufweisen.

Im speziellen wurden mit Hilfe einer Planetenmühle unterschiedliche LaF₃:SrF₂ *solid solutions* durch den Einbau von kubischem Strontiumfluorid in die komplexere und mobilere Tysonit-Struktur des Lanthanfluorids hergestellt. Die Phasenreinheit der Proben wurde abermals durch Pulverdiffraktometrie sowie MAS NMR überprüft. Zusätzlich wurden NMR Hahn-Echo Messungen durchgeführt, um die lokalen magnetischen Umgebungen der F Spins zu untersuchen. Anhand von Impedanzmessungen konnten für die Mischungen hohe Fluor-Anionen-Leitfähigkeiten von bis zu 10^{-5} S cm⁻¹ (373 K) gefunden werden, also um einige Größenordnungen erhöhte Leitfähigkeiten, im Vergleich zu reinem LaF₃. Die Ursache dafür sind entstehende strukturelle Fehlordnungen sowie Gitterverspannungen in den Festkörperionenleitern. Übereinstimmend damit sind mit zunehmendem Substituierungsgrad die Aktivierungsenergien stark abgefallen.

Insgesamt konnte somit gezeigt werden, wie eine ursprünglich schlecht leitende Fluoridverbindung (LaF₃) durch Substitution mit einem eigentlich schlechten Ionenleiter (SrF₂) durch die *one-pot* mechanochemische Synthese bei milden Temperaturen in einen schnellen Ionenleiter umgewandelt werden kann.

F anion dynamics in cation-mixed nanocrystalline LaF₃:SrF₂

S. Breuer, S. Lunghammer, A. Kiesl, and M. Wilkening, *J Mater Sci*, 2018.

<https://doi.org/10.1007/s10853-018-2361-x>, *in press*

F anion dynamics in cation-mixed nanocrystalline LaF_3 : SrF_2

S. Breuer¹, S. Lunghammer¹, A. Kiesl¹, and M. Wilkening^{1,*} 

¹Christian Doppler Laboratory for Lithium Batteries, and Institute for Chemistry and Technology of Materials, Graz University of Technology (NAWI Graz), Stremayrgasse 9, 8010 Graz, Austria

Received: 16 February 2018

Accepted: 21 April 2018

© The Author(s) 2018

ABSTRACT

Ion dynamics in nanocrystalline materials can be quite different compared to that in materials with μm -sized crystallites. In particular, the substitution of iso- or aliovalent ions opens pathways to systematically control ion transport properties. Here we studied the incorporation of SrF_2 into the tysonite structure of LaF_3 and its effect on F^- transport. High-energy ball milling directly transforms the binary fluorides in a structurally disordered, phase pure nanocrystalline ceramic. Compared to Sr-free LaF_3 , ionic conductivity could be increased by several orders of magnitude. We attribute this enhancement to the generation of lattice strain and the formation of F defect sites. In agreement with this increase, the activation energy E_a of long-range ionic transport in the solid solution $\text{La}_{1-x}\text{Sr}_x\text{F}_{3-x}$ significantly decreases from 0.75 eV ($x = 0$) to 0.49 eV ($x = 0.1$).

Introduction

Ionic conductors take on an essential rôle in materials science [1, 2]. They constitute an important part in many devices such as sensors [3] and those constructed for electrochemical energy storage [4, 5]. Apart from Li and Na ion conductors, also materials with high F anion conductivity have increasingly attracted attention [6], because there is renewed interest in the realization of batteries with fluorine anions as main charge carriers [7–9]. Apart from that, binary earth alkaline fluorides, especially CaF_2 and BaF_2 , easily accept rare-earth-elements and, thus, allow the preparation of luminescent solid solutions with improved optical properties. Considering lanthanum, the ionic radius of

La^{3+} (103 pm) is very similar to that of Ca^{2+} in CaF_2 (100 pm); it is, however, somewhat smaller than the cation radius of Sr^{2+} (118 pm) in cubic SrF_2 (Fig. 1). Recently, $\text{La}_{1-x}\text{Ba}_x\text{F}_{3-x}$ solid solutions with $x = 0.1$ have been introduced as promising ion conductor for F-ion battery systems [8, 10]. Ba^{2+} has a larger ionic radius (135 pm) than La^{3+} . Starting with undoped LaF_3 it is expected that also the ionic conductivity of nanocrystalline $\text{La}_{1-x}\text{Sr}_x\text{F}_{3-x}$ (with $x \leq 0.1$) significantly changes with SrF_2 incorporation [11]. As seen for other systems, see Ref. [12] for a brief review on fluorides, we expect lattice strain and distortions [13–15], caused by the difference in ionic radii, to promote ionic transport.

Address correspondence to E-mail: wilkening@tugraz.at

<https://doi.org/10.1007/s10853-018-2361-x>

Published online: 03 May 2018

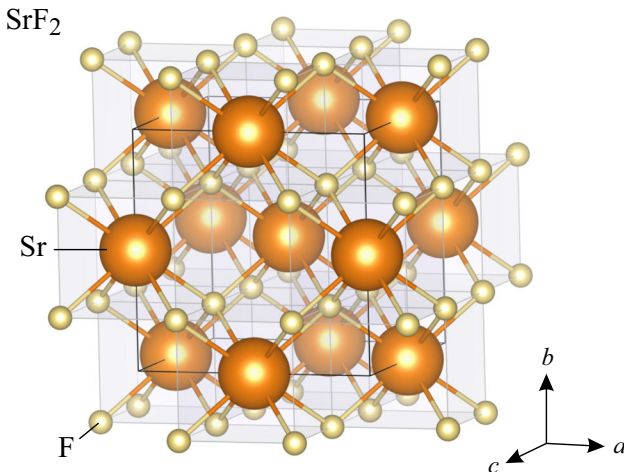


Figure 1 Crystal structure of SrF_2 . Strontium fluoride crystallizes with cubic symmetry ($Fd\bar{3}m$); F anions occupy the same crystallographic position ($8c$) which produces a single resonance in ^{19}F NMR spectroscopy.

Here, we used high-energy ball milling to prepare a series of nanocrystalline $\text{La}_{1-x}\text{Sr}_x\text{F}_{3-x}$ samples and studied (local) structures as well as long-range F anion transport. While Sr^{2+} crystallizes with cubic symmetry (Fig. 1), LaF_3 adopts the more complex tysonite structure, see Fig. 2. During ball milling the number density of defect sites usually increases which causes the bulk ionic conductivity also to increase as compared to the more ordered, single crystalline state. This effect has, in particular, been shown for oxides such as LiNbO_3 [16] and LiTaO_3 [17]. Recently, a quite similar enhancement has been reported for LiAlO_2 [18] and Li_2TiO_3 [19]. We expect that a measurable increase is also seen for ball milled SrF_2 and LaF_3 . Whereas in SrF_2 only one crystallographic F site exist, in LaF_3 three crystallographically distinct F sites can be found [20]. The F1 anions residing on $12g$ are located in the $\infty[\text{F}_{2-x}]^{-2+x}$ inter-slab. F3 and F2 anions are found in or near the La layers, see Fig. 2. In the pioneering work of Wang and Grey F anion exchange processes in LaF_3 were studied by high-resolution solid-state nuclear magnetic resonance (NMR) spectroscopy. It turned out that fast F1-F1 exchange processes markedly determine ionic conductivity in the tysonite structure, whereas the F1-(F2,F3) hopping processes are less frequent.

In general, ball milling is a versatile method not only to prepare single-phase nanostructured materials but also to induce and to carry out mechanochemical

reactions [12, 21]. The latter often lead to non-equilibrium (or metastable) compounds that cannot be prepared via conventional high-temperature synthesis routes [12]. Apart from that, high-energy ball milling is also useful to prepare phases, which are only stable at high pressures. As an example, mechanical treatment of $\gamma\text{-LiAlO}_2$ leads to the formation of several modifications which are usually observed at high pressures [18]. If cubic BaF_2 is ball milled for several hours in planetary mills one can follow the generation of orthorhombic BaF_2 by both X-ray diffraction and high-resolution ^{19}F nuclear magnetic resonance (NMR) [14]. In the present case we used mechanical treatment to force the cations to mix on atomic scale. The major component, which is, if not stated otherwise, LaF_3 , determines the final crystal structure, i.e., the smaller Sr^{2+} ions are incorporated into the tysonite structure. In many cases phase pure mixed compounds are available by ball milling under dry conditions [22, 23]. The effect of abraded material from vial sets and milling balls has only a negligible effect if other factors, such as cation mixing, governs ion dynamics [14]. As has been documented for other nanocrystalline systems, the main change in ionic conductivity is caused by structural disorder, lattice strain introduced and the mixed cation effect [15–17]. The mismatch in size of the cations sensitively changes the potential landscape the mobile F anions are exposed to. In our case, because of charge balance, the replacement of La^{3+} by Sr^{2+} also leads to the formation of F vacancies in the anion sublattice. Vacant F sites are anticipated to further boost ion conductivity in nanocrystalline LaF_3 , i.e., it is expected to control overall ionic conductivity for samples with $x > 0$. Of course, cation-mixed fluorides can also be prepared via alternative solid-state routes requiring, however, relatively high calcination temperatures. As an example, Chable et al. and Dieudonné et al. studied ion dynamics in $\text{La}_{1-x}\text{Ba}_x\text{F}_{3-x}$ ($x < 0.15$) and $\text{Sm}_{1-x}\text{Ca}_x\text{F}_{3-x}$ ($x < 0.17$) solid solutions, respectively [24–26].

Experimental

Nanocrystalline solid solutions of $\text{La}_{1-x}\text{Sr}_x\text{F}_{3-x}$ with $0.01 \leq x \leq 0.1$ were prepared via high-energy ball milling. We used a planetary mill (Fritsch P7, Premium line) and treated the various mixtures of LaF_3 and SrF_2 in cups made of ZrO_2 (45 mL, Fritsch). Milling was

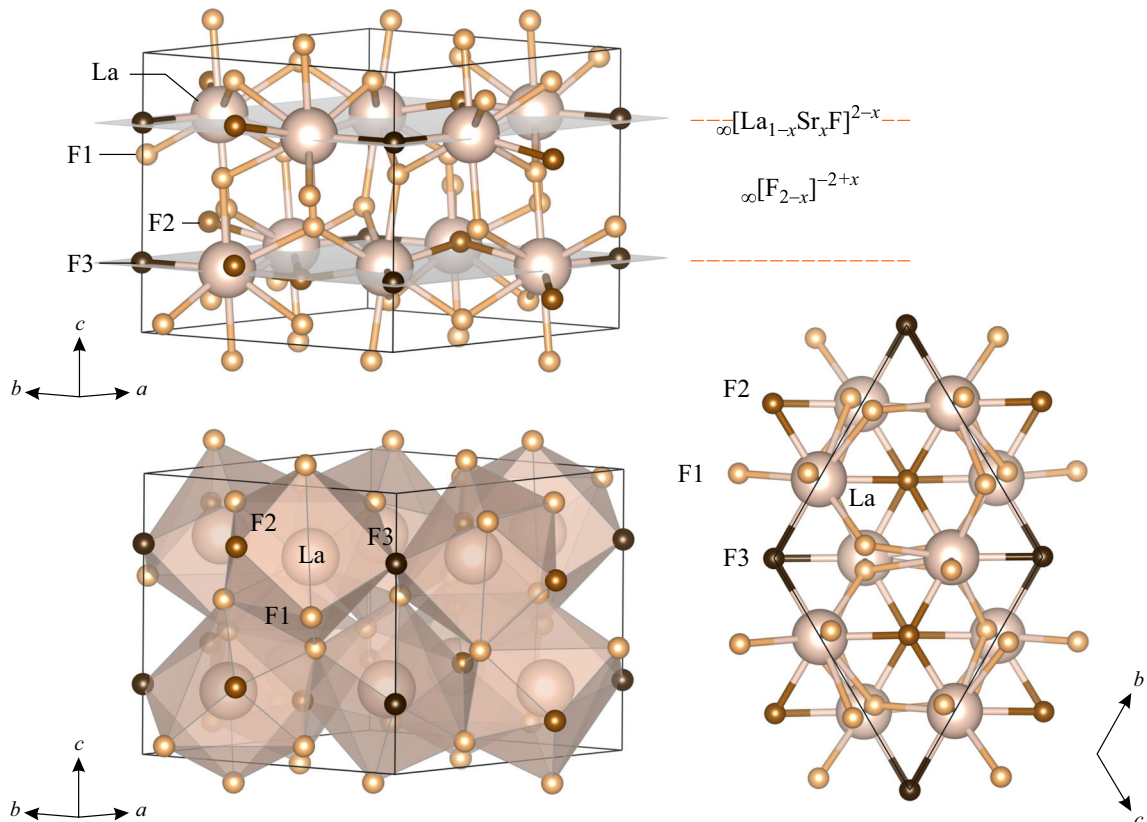


Figure 2 Crystal structure of LaF_3 ($P\bar{3}c1$, $Z = 6$). The tyanite structure provides 3 different F sites labeled F1 (12g, C_1 or distorted T_d point symmetry), F2 (4d, C_{3v} point symmetry), and F3

($2a$, D_{3h} point symmetry). Each site is fully occupied by fluorine anions. F1 anions reside in the $\infty[\text{F}_{2-x}]^{-2+x}$ interslab. These ions are located in distorted La_4 tetrahedra.

carried out with 180 zirconium oxide milling balls (5 mm in diameter). Prior to the milling process, the starting materials were dried at 200°C under vacuum. The subsequent preparation steps were carried out in inert gas atmosphere by taking advantage of Ar-filled gloveboxes ($\text{O}_2, \text{H}_2\text{O} < 0.1 \text{ ppm}$). A milling time of 10 h (600 rpm) leads to almost full incorporation of SrF_2 into LaF_3 . After each 30 min we interrupted the milling process for 15 min to let the vial cool down to room temperature. According to our experience, this way of milling ensures that the temperature of the vial during milling does not exceed values above 60 to 80°C .

The phase purity of the samples prepared was checked by both X-ray diffraction (Bruker D8 Advance, Bragg Brentano geometry, 40 kV) and ^{19}F magic angle spinning (MAS) NMR spectroscopy. Analyzing the reflections of the nanocrystalline materials with the Scherrer equation [27, 28] resulted in mean crystallite sizes in the order of 14 to 20 nm, see also Refs. [17, 22, 23] for similar analyses on

nanocrystalline oxides that partly also considered the effect of lattice strain on samples prepared mechanochemically.

To probe local magnetic environments of the F spins, we recorded rotor-synchronized NMR Hahn echoes by employing a Bruker 1.3-mm MAS probe placed in a 11.4 T cryomagnet (470.39 MHz). This probe allowed us to spin the rotor at frequencies as high as 60 kHz. Spectra were measured with a two pulse ($90^\circ - t_p - 180^\circ$) sequence using a Bruker Avance 500 spectrometer. The 90° pulse length was 1.5 μs at a power level of 50 W. Between each scan a recycle delay of 30 s was ensured to consider almost full longitudinal relaxation. Up to 64 transients were accumulated for a single spectrum, see Figs. 4 and 5. We took advantage of LiF powder as a secondary reference (-204.3 ppm) [29] to determine chemical shifts δ_{iso} ; CFCl_3 (0 ppm) served as the primary reference.

Ionic conductivities of the pressed powders were analyzed with a Novocontrol Concept 80 broadband spectrometer. To prepare pellets for the impedance measurements the powders were uniaxially cold-pressed at ca. 1 GPa. With the pressing tools available in our laboratory we prepared pellets with a diameter of 8 mm and thicknesses varying from 0.5 to 1 mm. Sputtering was used to apply electrically conducting Au electrodes (100 to 200 nm in thickness). The pellets were placed in a ZGS active cell (Novocontrol). The temperature in the sample chamber was controlled by a QUATRO cryo system (Novocontrol) that allows precise settings of temperature as well as a fully automatic execution of the measurements for a range of temperatures. A stream of freshly evaporated nitrogen gas, which passes a heater before entering the sample chamber, is used to ensure stable stability (± 2 K). For the conductivity (and impedance) measurements we used a voltage amplitude of 100 mV and varied the frequency ν from 0.1 Hz to 10 MHz. Specific conductivities were calculated by taking into account the cell constant, i.e., diameter and thicknesses of the individual pellets, which showed densities of ca. 90% of the theoretical one.

Results and discussion

X-ray diffraction and ^{19}F MAS NMR

In Fig. 3 the X-ray powder patterns of the starting materials as well as those of the mixtures, each milled for 10 h, are shown. For comparison, the patterns of nanocrystalline LaF_3 and SrF_2 are included as well. We clearly see that the reflections broaden when going from microcrystalline LaF_3 to the nanocrystalline sample. According to Scherrer's equation an average crystallite of ca. 18 nm is estimated for nano- LaF_3 prepared by ball milling. At first glance, substitution of La^{3+} ions by Sr^{2+} in the compositional range $0 < x \leq 0.1$ does not show a great effect on the lattice parameters of LaF_3 , careful inspection of the patterns reveals slight shifts, which will be discussed below. Importantly, no other phases than LaF_3 were detected by X-ray diffraction. Thus, no decomposition products or other phases than $\text{La}_{1-x}\text{Sr}_x\text{F}_{3-x}$ have been formed. This observation is confirmed by high-resolution ^{19}F MAS NMR spectroscopy, which solely

shows signals that can be attributed to F anions in $\text{La}_{1-x}\text{Sr}_x\text{F}_{3-x}$ (see below).

Careful inspection of the diffraction patterns shows that with increasing x the broadening of the reflections increases. Mixing two fluorides, which differ in Mohs hardness, might lead to smaller crystallites. In our case, however, Mohs' hardness of the fluorides is very similar (LaF_3 (4.5); SrF_2 (4)). Thus, the broadening is assumed to be also affected by lattice strain and disorder due to the mixed cation effect. Indeed lattice strain, when estimated using the method introduced by Williamson and Hall [30] increases from 0.0077 ($x = 0.01$) to 0.0107 ($x = 0.1$), see also Table 1. The estimated mean crystallite sizes $\langle d \rangle$ represent apparent values as they do not consider small distributions of lattice constants because of Sr^{2+} incorporation. As is exemplarily shown for the (2–11) reflection, see Fig. 3b, its position slightly shifts toward smaller diffraction angles 2θ . This shift is explained by lattice expansion due to successful heterovalent replacement of La^{3+} by the larger Sr^{2+} species. Refinement of the XRD patterns reveals that the lattice expands slightly along the c -axis (Table 1); note that all the values shown in Table 1 are to be regarded as rough estimates as we deal with broad reflections from nanocrystalline samples. A small distribution of lattice constants will contribute to the broadening effect. Thus, it is likely that the crystallite diameter of the samples does not change much with composition. ^{19}F MAS NMR, which locally probes the different magnetic environments seen by the F spins, also points to an increase in lattice distortions with increasing x , at least if we consider values larger than 0.01, see Table 1.

In Fig. 4 the ^{19}F MAS NMR spectra of microcrystalline and nanocrystalline LaF_3 are shown. The spectra have been deconvoluted with appropriate Voigt functions to analyze the areas under the three lines visible. The most intense one belongs to the F1 ions on the $12g$ position. The F ions F2 (4d) and F3 (2a) are attributed to the signals showing up at $\delta_{\text{iso}} = 28.9$ ppm and 20.9 ppm, respectively. NMR tells us that the (ideal) occupation ratio of 6:2:1 ($12g : 4d : 2a$) is almost fulfilled; experimentally we obtain 6:1.7:0.92 indicating vacant F sites in the La-rich regions of LaF_3 . Because of charge neutrality one may suspect that we have a La deficient binary fluoride at hand where F anions preferentially fill the F1 sites rather than the F2 and F3 sites. Ball milling drastically

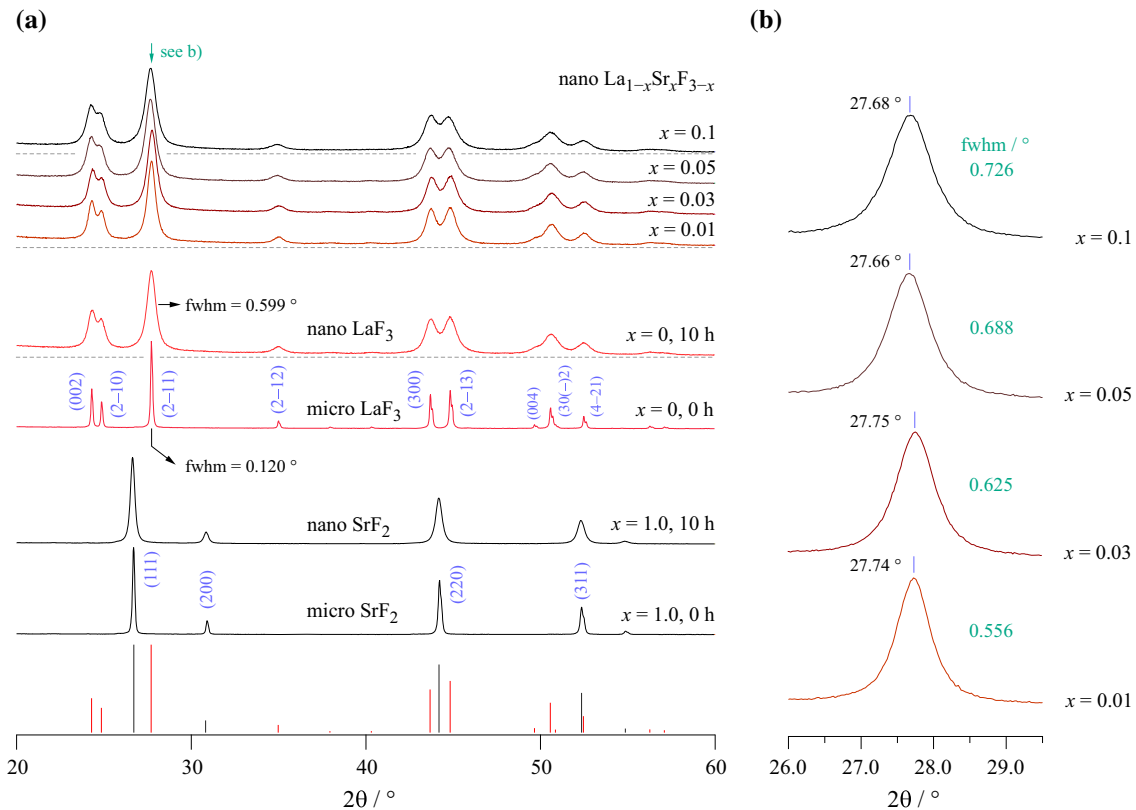


Figure 3 X-ray diffractograms of SrF_2 and LaF_3 as well as the mechanosynthesized cation-mixed ternary fluorides $\text{La}_{1-x}\text{Sr}_x\text{F}_{3-x}$. The nanocrystalline samples were obtained after 10 h of mechanical treatment in a planetary mill. Numbers in parentheses denote the hkl indices. The starting materials as well as the were phase pure; neither foreign phases nor abrasion from the vial sets used could be detected by X-ray diffraction. Broadening of the reflections is due to gain-size effects and strain introduced during

milling. The reflection at $2\theta = 27.7^\circ$ is shown in a magnified view in **b**. The slight shift toward lower diffraction angles shows the incorporation of larger Sr^{2+} ions into the tysonite structure of LaF_3 . Broadening with increasing Sr content indicates increasing strain or distortions because of the cation mixing effect. An increasing extent of structural disorder upon mixing the two cations is also seen through ^{19}F MAS NMR, see below.

Table 1 Crystallite sizes ($\langle d \rangle$) and strain (ϵ) as estimated via Scherrer's equation and the method introduced by Williamson and Hall; values refer to mechanosynthesized, nanocrystalline $\text{La}_{1-x}\text{Sr}_x\text{F}_{3-x}$ obtained after a milling period of 10 h. Lattice parameters a and c are also included; for unmilled LaF_3 we obtained $a = 7.1886 \text{ \AA}$ and $c = 7.3539 \text{ \AA}$

x	$\langle d \rangle/\text{nm}$	strain ϵ	$a / \text{\AA}$	$c / \text{\AA}$
0	18	0.0085	7.1882	7.3542
0.01	20	0.0077	7.1849	7.3533
0.03	17	0.0089	7.1876	7.3557
0.05	15	0.0101	7.1849	7.3536
0.10	14	0.0107	7.1833	7.3586

broadens the lines and reveals a large distribution of chemical shifts revolving around the original isotropic values. Importantly, it is no longer possible to

reproduce the whole signal with only three lines. Instead, an additional broad line centered at $\delta_{\text{iso}} = -11 \text{ ppm}$ has to be considered to parameterize the overall NMR response. Most likely, this line represents F1 ions in distorted environments between the La-rich layers in lanthanum fluoride.

As an representative of the cation-mixed samples, the ^{19}F high-resolution MAS NMR spectrum of $\text{La}_{1-x}\text{Sr}_x\text{F}_{3-x}$ with $x = 0.1$ is presented in Fig. 5. Obviously, the mixed cation effect causes additional broadening of the NMR lines. Still, we are able to resolve the F1 and F2/F3 sites via MAS NMR. The line attributed to the F1 anions shifts toward lower ppm values as it has also been documented by Chable et al. in the literature before [24]. The signal at -85 ppm reveals a very tiny amount of residual SrF_2 . Such small amount is difficult to be detected by X-ray

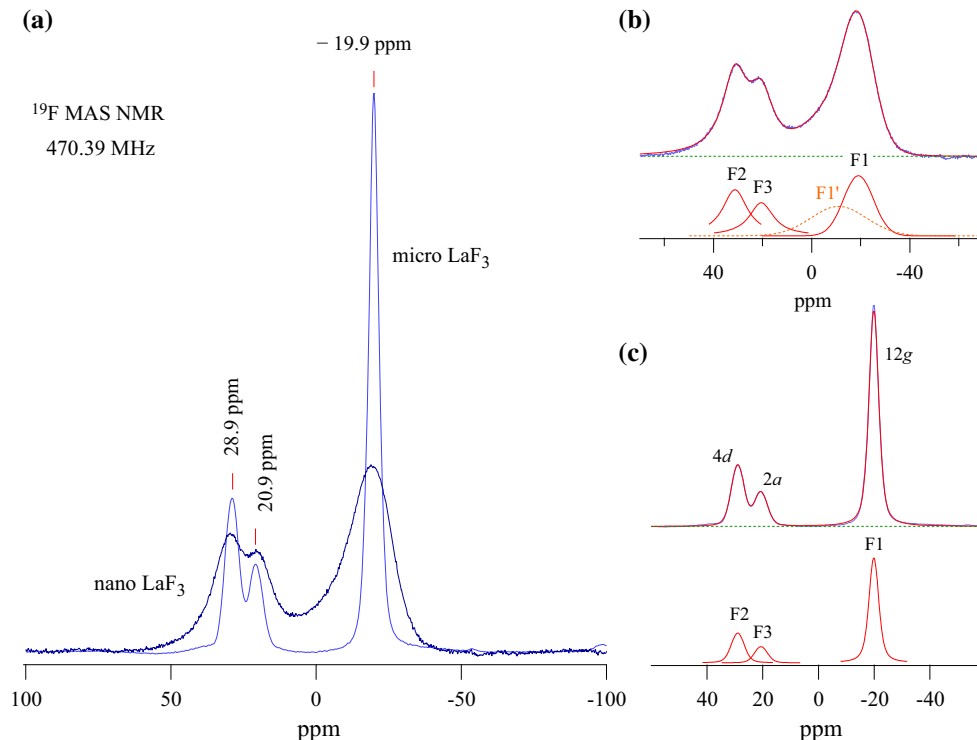


Figure 4 ^{19}F MAS NMR spectra recorded at 60 kHz rotation speed and 470.39 MHz: **a** spectra of microcrystalline and nanocrystalline LaF_3 . The nanocrystalline sample was obtained after ball milling the microcrystalline material for 10 h in a planetary mill. **b** deconvolution of the spectra shown in **a** with appropriate Lorentzian functions. For nano LaF_3 the

diffraction because of signal overlapping and its possible non-crystallinity.

In Fig. 5b we tried to reproduce the spectrum of nanocrystalline $\text{La}_{0.9}\text{Sr}_{0.1}\text{F}_{2.9}$ with appropriate Lorentzian-shaped functions that simply represent the F1 part and F2/F3 region of the spectrum, respectively. These lines have no further meaning as it is no longer possible to reproduce the original F sites with just one NMR line, either Gaussian, Lorentzian or a combination of both. The lines depicted are just used to highlight that the whole spectrum can only be parameterized if a broad line near 0 ppm is considered, see the dashed line in the lower graph of Fig. 5. As these additional NMR intensities needed to describe the spectrum are located near the center of the whole NMR response we suppose that besides the F1 sites also the F2 and F3 sites, to a minor extent, also contribute to overall F anion exchange, as has already assumed earlier for pure LaF_3 [20].

Worth noting, at ambient bearing gas temperature the MAS NMR lines can be well resolved. A single

deconvolution is only possible after considering a fourth line centered at -11 ppm. Presumably, this line reflects F anion in the $\infty[\text{F}_{2-x}]^{-2+x}$ interslab as its chemical shift is comparable to that of the original F1 ions. F jumps via vacancies along the $\text{F}_{12g}-\text{V}_{12g}-\text{F}'_{12g}$ pathway seems to be likely.

sharp single, which would be the result of a fast exchange processes leading to full coalescence of some or all of the signals, is not seen. Therefore, MAS NMR suggests, if we consider the spectral range the lines cover, F anion jump rates involving all of the available sites to be much lower than 10^5 s^{-1} . This estimation, which is valid for temperatures around ambient, is in good agreement with earlier NMR results [20] and the ionic conductivities probed here (see below). It points out the poor F anion mobility in LaF_3 , even for nanostructured LaF_3 ionic conductivities are low compared to other ionic conductors, see Fig. 6 (and the next section) where the corresponding conductivity and permittivity isotherms of the sample with $x = 0.1$ are shown. According to Grey and co-workers the line representing the F1 anions starts to narrow at elevated temperatures before two distinct coalescence effects take place representing the F1–F3 exchange and F1–(F2,F3) exchange; for a microcrystalline sample with $x = 0.01$ full coalescence of all signals is only observed at $T \geq 266^\circ\text{C}$.

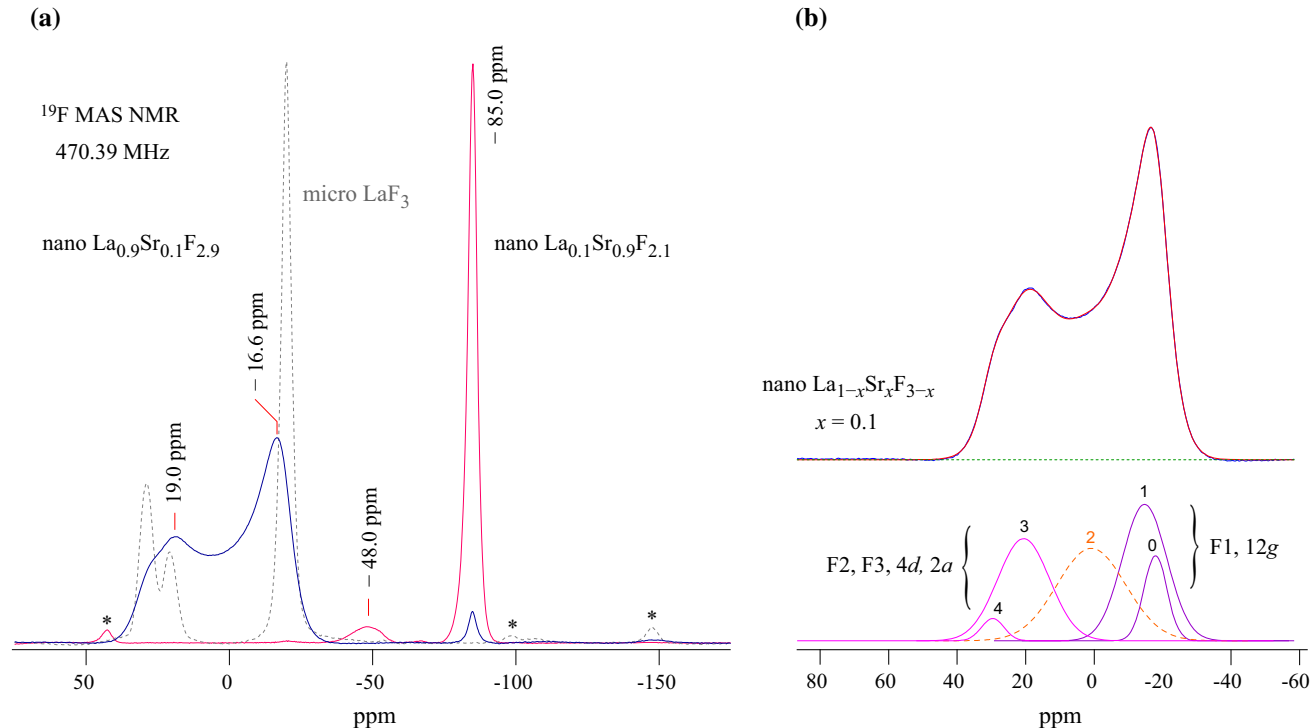


Figure 5 ^{19}F MAS NMR spectra of nanocrystalline $\text{La}_{1-x}\text{Sr}_x\text{F}_{3-x}$ with $x = 0.1$ as the nominal composition. In addition, the spectra of nano LaF_3 and $\text{La}_{1-x}\text{Sr}_x\text{F}_{3-x}$ with $x = 0.9$ are shown. Asterisks (*) mark spinning side bands. In the Sr-rich sample crystallizing with $Fd\bar{3}m$ symmetry a new signal at -48 ppm is seen; most likely this line represents F anions near La centers. For $\text{La}_{0.9}\text{Sr}_{0.1}\text{F}_{2.9}$ broadened lines are seen slightly shifted to new positions as

For comparison, in Fig. 5 the NMR spectrum of a Sr-rich compound, $\text{La}_{0.1}\text{Sr}_{0.9}\text{F}_{2.1}$ is shown that has been prepared in the same way as the other samples. $\text{La}_{0.1}\text{Sr}_{0.9}\text{F}_{2.1}$ crystallizes with SrF_2 structure. Apart from the prominent F NMR signal of SrF_2 a new line shows up at -48 ppm. It reflects the F anions near La ions in the mixed compound. The Sr-rich compounds are characterized by ionic conductivities that are lower than those of the La-rich fluorides. Therefore, here we focus on the samples that crystallize with the more complex tysonite structure. In the following section the change in ionic conductivity when going from pure LaF_3 to cation-mixed $\text{La}_{1-x}\text{Sr}_x\text{F}_{3-x}$ is presented.

Conductivity measurements

To probe ionic conductivities of both the microcrystalline and nanocrystalline samples, including the mixed ones, we recorded conductivity isotherms

compared to those in microcrystalline Sr-free LaF_3 . In b a formal deconvolution of the spectrum of $\text{La}_{0.9}\text{Sr}_{0.1}\text{F}_{2.9}$ is shown. As already seen for nano LaF_3 , NMR intensities around 0 ppm show up which reveal F anions in mixed environments with distorted polyhedra, see the line drawn with a dashed line. See text for further explanations.

covering both a broad frequency range and a large temperature region. Exemplarily, in Fig. 6 the real part σ' of the complex conductivity (as well as the real part ϵ' of the complex permittivity) of mechanosynthesized $\text{La}_{0.9}\text{Sr}_{0.1}\text{F}_{2.9}$ is shown as a function of the frequency ν covering a dynamic range of 9 orders of magnitude.

At high temperatures and low frequencies electrode polarization is seen as the F ions cannot pass the Au blocking electrodes used to measure the total electrical response. This response causes a significant, in many cases multistep, decrease of σ' in the low frequency limit. Here it is characterized by capacitances in the μF regime, values being typically expected for the piling up of ions near blocking electrodes. Most importantly, the conductivity isotherms reveal distinct frequency independent plateaus, denoted as P1 in Fig. 6b), from which we read off the so-called direct current values σ_{DC} . σ_{DC} refers to long-range ion transport through the macroscopic

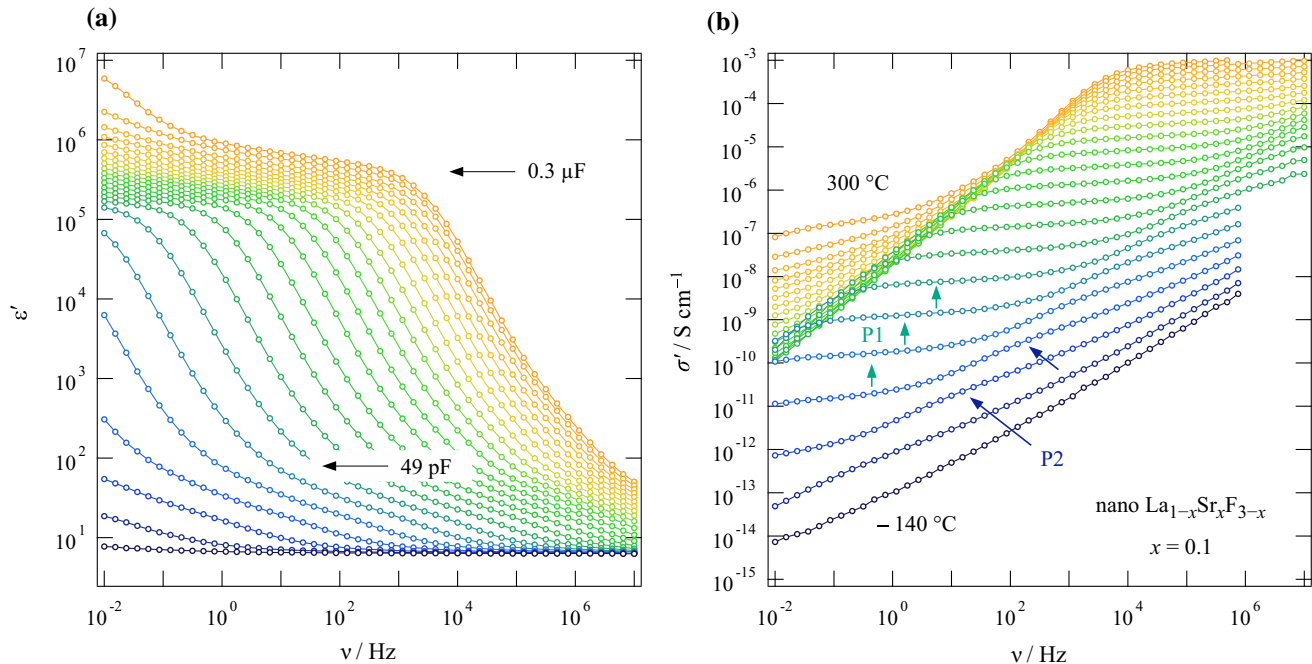


Figure 6 Permittivity spectra (a) and conductivity spectra (b) of nanocrystalline $\text{La}_{0.9}\text{Sr}_{0.1}\text{F}_{2.9}$. The isotherms were recorded at temperatures ranging from $-140\text{ }^\circ\text{C}$ to $300\text{ }^\circ\text{C}$ in steps of $20\text{ }^\circ\text{C}$. Besides electrode polarization, which is seen at the best at high

sample. Here, at ambient temperature the capacitance C associated with this main electrical process turned out to be in the order of 38 pF . This value was derived from analyzing the corresponding complex plane plots, that is, Nyquist diagrams, which were obtained by plotting the imaginary part of the complex impedance as a function of its real part. Capacitances of a few pF usually suggest σ_{DC} to be related to a bulk response. The relatively high value of ca. 38 pF indicates that the response causing P1 is partly affected by the surface-influenced areas of the nm-sized crystallites. A second plateau (P2), only poorly visible at higher T but recognizable in the isotherms measured at the lowest temperatures, also points to a bulk response. We attribute this shallow plateau to ion dynamics in the inner core of the nanocrystals (see the arrows in Fig. 6b).

From the corresponding Nyquist diagrams the faster relaxation processes, corresponding to P2, cannot be resolved properly. Instead, it is well seen if we plot the imaginary part M'' of the complex modulus vs. frequency, see Fig. 7a. At sufficiently low temperature two relaxation peaks, M1 and M2, are visible (see red arrows), which are separated by almost two orders of magnitude on the frequency

temperatures (see also a), the conductivity spectra measured at low T (see b) reveal two distinct electrical responses marked as P1 and P2.

scale. This separation agrees well with the ratio $\sigma_{DC,P2}/\sigma_{DC,P1}$. While the peak with the larger amplitude corresponds to P2 in $\sigma'(v)$, the weaker one represents an electrical process with a longer (characteristic) relaxation time (P1). As M'' is proportional to the inverse of the capacitance, $M'' \propto 1/C$, peak M2 is characterized by an even lower capacitance C (ca. 25 pF) than that estimated for response P1. This lower capacitance underpins our assumption that plateau P2 reflects ion dynamics in the crystalline bulk regions.

In Fig. 7b the DC conductivities, plotted as $\sigma_{DC}T$, of the plateaus P1 and P2 are shown as a function of the inverse temperature. While the values corresponding to P1 follow Arrhenius behavior, $\sigma_{DC}T = \sigma_0 \exp(-E_a/(k_B T))$, with an activation energy of $0.49(1)\text{ eV}$, those of P2 slightly deviate from the Arrhenius line governing ion dynamics above 220 K . At higher temperatures we found an activation energy E_a of $0.45(3)\text{ eV}$, which is slightly lower than that determining P1.

An overview of the change in ionic conductivity in nanocrystalline $\text{La}_{1-x}\text{Sr}_x\text{F}_{3-x}$ is finally given in Fig. 8. Table 2 compares the activation energies obtained with the pre-factors σ_0 . Microcrystalline SrF_2 shows

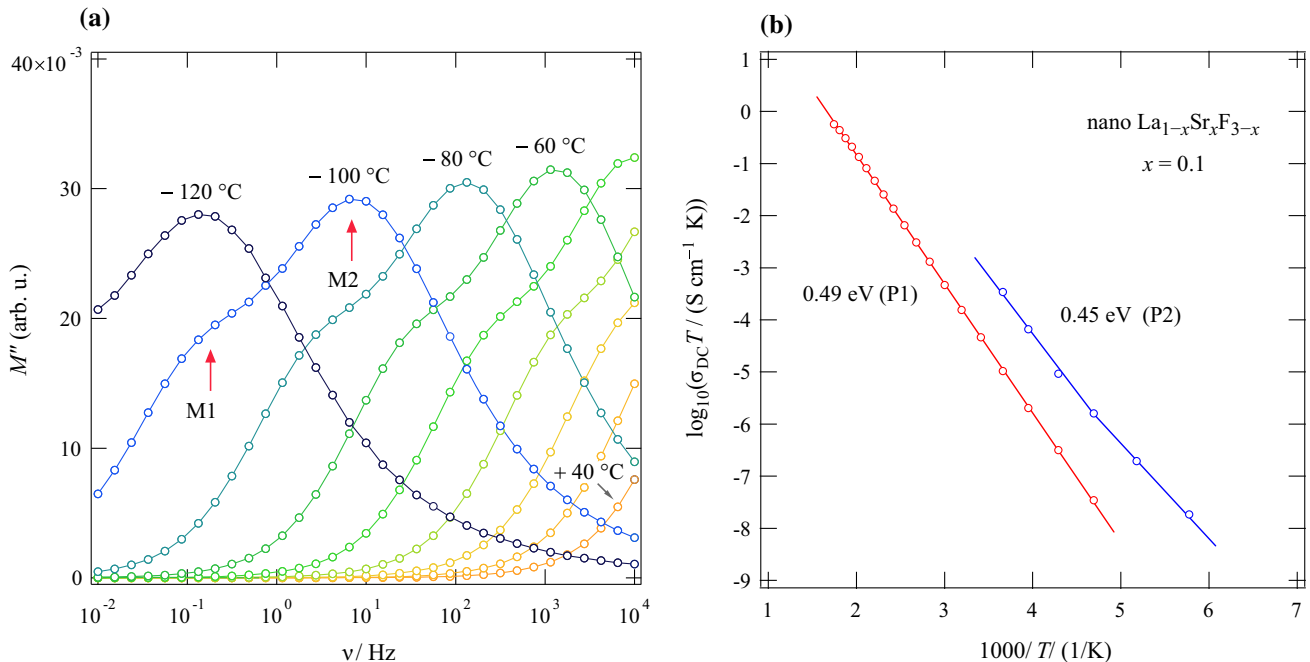


Figure 7 **a** Modulus representation of the data. As suggested by the conductivity isotherms two distinct peaks are visible denoted as M1 and M2. **b** Arrhenius representation of $\sigma_{\text{DC}} T(1/T)$; σ_{DC}

the lowest conductivities with an activation energy as high as 1.13 eV. Ball milling for 10 h leads to an increase of σ_{DC} by approximately one order of magnitude; accordingly, E_a slightly decreases to 1.04 eV. A very similar situation is found for LaF_3 although the original conductivity of coarse-grained lanthanum fluoride, if we consider values at $T = 440\text{ K}$, exceeds that of SrF_2 by 4 orders of magnitude. Through heterovalent replacement of the La cations the overall conductivity can be further increased reaching values that compete with those found for mechanosynthesized $\text{La}_{1-x}\text{Ba}_x\text{F}_{3-x}$ [10, 37], which takes advantage of an even larger size mismatch of the mixed cations [38]. Obviously, the mismatch in size in the Sr-compound is already large enough to reach the upper limit of σ_{DC} , at least if mechanosynthesized samples are considered. The activation energy of tysonite-type $\text{La}_{0.9}\text{Ba}_{0.1}\text{F}_{2.9}$, which has been studied in detail in [10, 37], is comparable to that of the Sr analogue. Just for comparison, ion transport in $\text{La}_{0.9}\text{Ba}_{0.1}\text{F}_{2.9}$ [31] turned out to be clearly higher than that in metastable and nanocrystalline $\text{Ba}_{0.5}\text{Ca}_{0.5}\text{F}_2$ [32], which crystallizes with cubic symmetry and which has been studied earlier by some of us [15, 32].

For the sake of clarity, for most of the samples only the values referring to P1 have been included in

was read off from the plateaus P1 and P2 (see Fig. 6b). The solid lines show fits with an Arrhenius law yielding activation energies for the P1 response slightly lower than 0.5 eV.

Fig. 7. For the sample with $x = 0.1$ we also inserted the conductivities corresponding to plateau P2. The latter values, if extrapolated to higher T , exceed those of a $\text{LaF}_3|\text{SrF}_2$ multilayer system, which has been prepared by molecular beam epitaxy (MBE) and discussed in literature quite recently [33]. The spacing of the heterolayer sample was 25 nm. In such a sample, besides any possible mixing effect directly at the interfaces, ion movements in space-charge zones [6, 39–42] are anticipated to govern ionic conductivity. Worth mentioning, the conductivity of the $\text{LaF}_3|\text{SrF}_2$ hetero-layers shown reflects the longitudinal one, i.e., the values represent ion transport perpendicular to the fluoride layers. In this ionic conductor overlapping space-charge zones are assumed to enable fast ion transport even perpendicular to the hetero-interfaces. The most prominent example for this kind of artificial ion conductor is epitaxially grown $\text{BaF}_2|\text{CaF}_2$ [6].

For comparison, a mixed $\text{La}_{1-x}\text{Sr}_x\text{F}_{3-x}$ sample, which has also been prepared by MBE [33], is shown in Fig. 8, too. Interestingly, the conductivities from plateau P2 of our mechanosynthesized nanocrystalline sample with $x = 0.1$ are at least comparable with these results. This finding indicates that $\text{La}_{1-x}\text{Sr}_x\text{F}_{3-x}$ powders with transport properties

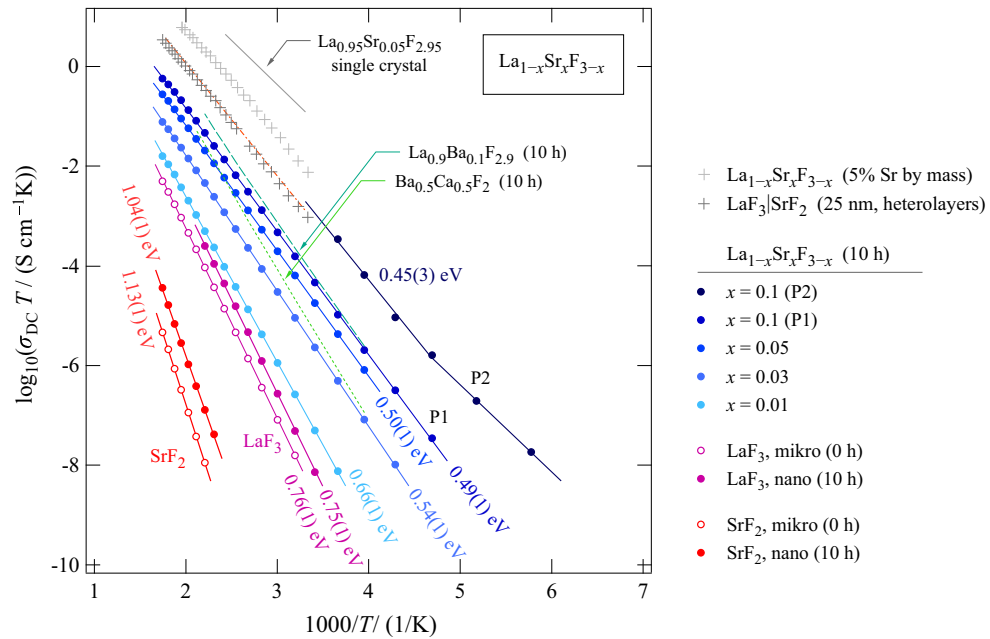


Figure 8 Arrhenius plot of the ion conductivities ($\sigma_{DC} T$ vs. $1000/T$) of cation-mixed nanocrystalline $\text{La}_{1-x}\text{Sr}_x\text{F}_{3-x}$. Solid lines represent fits with Arrhenius equations yielding the activation energies E_a indicated. For comparison, the coarse-grained starting materials as well as LaF_3 and SrF_2 milled for 10 h are also shown. The dashed lines represent values of $\sigma_{DC} T$ of two further ternary fluorides already presented and discussed in literature viz. $\text{La}_{1-x}\text{Ba}_x\text{F}_{3-x}$ ($x = 0.1$) [31] and $\text{Ba}_{1-x}\text{Ca}_x\text{F}_2$ ($x = 0.5$) [32]; here, we have prepared these two reference materials by milling the respective starting materials for 10 h. Crosses indicate conductivities taken from literature [33]: the data points show conductivities of

$\text{La}_{1-x}\text{Sr}_x\text{F}_{3-x}$ with 5 mass-% Sr and ion transport properties of multilayer $\text{LaF}_3|\text{SrF}_2$ heterostructures with an interfacial spacing of 25 nm. These samples were prepared by molecular beam epitaxy, see [33]. For the sake of completeness, also results from a $\text{La}_{0.95}\text{Sr}_{0.05}\text{F}_{2.95}$ single crystal and mechanosynthesized, but annealed, $\text{La}_{0.95}\text{Sr}_{0.05}\text{F}_{2.95}$ (dashed-dotted line, the values almost coincide with the $\text{LaF}_3|\text{SrF}_2$ multilayer system) are included [34, 35]. Space-charge and segregation effects might be used to explain the decrease in ionic conductivity when going from single crystals to nm-sized systems with high surface areas [36].

Table 2 Comparison of activation energies E_a and pre-factors σ_0 of the Arrhenius lines shown in Fig. 8. The values refer to the mechanosynthesized, nanocrystalline samples $\text{La}_{1-x}\text{Sr}_x\text{F}_{3-x}$. The uncertainty of E_a is in the last digit, for σ_0 it is roughly $\pm 0.1 \text{ S cm}^{-1}\text{K}$

x	E_a (eV)	$\log_{10}(\sigma_0 / (\text{S cm}^{-1}\text{K}))$	Remarks
0	0.75	4.79	
0.01	0.66	4.04	
0.03	0.54	3.65	
0.05	0.50	3.87	
0.10	0.49	4.13	P1
0.10	0.45	4.81	P2
0.05	0.45	4.55	Milled, annealed [34, 35]
0.05	0.35	4.95	Single crystal [34]

being similar to those of MBE grown films can be made available also by high-energy ball milling. Of course, ball milling is a much more feasible technique able to produce large quantities of powders [25].

If we consider $\text{La}_{1-x}\text{Sr}_x\text{F}_{3-x}$ samples prepared differently and with different morphologies and preparation histories than here, see, e.g., the systematic studies by Sorokin and Sobolev [34], we find that $\sigma_{DC} T$ of P2 is considerably lower than that what is usually found for a $\text{La}_{0.95}\text{Sr}_{0.05}\text{F}_{2.95}$ single crystal. σ of a mechanosynthesized, but annealed sample is slightly lower than $\sigma_{DC} T$ of P2, see Fig. 8 and Table 2, which also includes the corresponding activation energies and pre-factors (see below). To our knowledge and understanding, the origin of this decrease is not fully understood yet. At first glance, one might speculate that grain-boundary regions might block long-range ion transport. Here, we could not find strong evidence that the conductivities measured reflect ion transport across grain boundaries. They mainly refer, as far as electrical capacitances are considered, to bulk properties. This assignment is in agreement with ^{19}F NMR line shape measurements. Conductivities in the mS range at room temperature

would translate into very fast F exchange processes as reported for single crystals. Even if such processes were hidden in our samples as non-ascertainable electric bulk property, they should produce strongly motionally narrowed NMR lines. Such lines are absent in our case. The bulk ion dynamics in mechanosynthesized $\text{La}_{1-x}\text{Sr}_x\text{F}_{3-x}$ does not reach the conductivities reported for the single crystalline state. The situation resembles that of Durá et al. [36] who studied oxygen ion conductivity in nanostructured ZrO_2 . The authors presented indications of an extended space-charge layer because of oxygen vacancy segregation in the grain-boundary core region. This effect leads to charge carrier depletion in the grain leading to a decrease in oxygen ion conductivity. Such segregation and space-charge effects might be useful to also explain the discrepancy seen between nm-sized polycrystalline fluorides on the one hand and single crystals on the other.

Going back to the samples studied here, the increase in σ_{DC} for mechanosynthesized $\text{La}_{1-x}\text{Sr}_x\text{F}_{3-x}$ powder samples (Fig. 8, Table 2) seems to be mainly driven by the decrease in migration barrier. Indeed, E_a sharply decreases from 0.75 eV ($x = 0$) to 0.54 eV ($x = 0.03$) if only a tiny amount of Sr^{2+} ions were incorporated into the tyanite structure, see also Table 2. The lowering of the activation energy is, however, accompanied by a decrease of the Arrhenius pre-factor σ_0 , which partly compensates for the enhancement in ionic conductivity. In particular, a low σ_0 has an impact on conductivities at high temperatures rather than at lower T .

The trend shown in Table 2 is in fair agreement with this so-called Meyer-Neldel rule [43], an enthalpy-entropy compensation effect. This compensation effect is based on a linear dependence of the pre-factor on the activation enthalpy (or energy). The higher the activation enthalpy, the higher the pre-factor σ_0 , which is affected by entropy contributions, attempt frequencies and, in the case of ionic conductivity, also by the effective number of charge carriers. Careful inspection of σ_0 reveals that, for values of x larger than 0.03, the pre-factor increases again. This increase tells us that, while E_a remains almost constant for compositions above $x = 0.03$, the further enhancement of σ_{DC} is driven by σ_0 rather than by E_a . A similar observation has been quite recently reported for mechanosynthesized samples of $\text{Ba}_{1-x}\text{Ca}_x\text{F}_2$ [32].

In the low-concentration limit ($x \leq 0.1$), which we focused on here, we do not expect large changes in attempt frequencies. Instead, in this compositional regime contributions of both the migration and configurational entropy as well as the effective number of charge carriers are expected to govern σ_0 . After E_a has reached its limiting value of ca. 0.5 eV these effects take over and allow the ions to move quickly in a disordered potential landscape generated by size mismatch.

Conclusions

Mechanosynthesis is a versatile tool to prepare cation-mixed fluorides that exhibit ion transport properties greatly exceeding those of their nanocrystalline but binary fluorides. By taking advantage of high-energy planetary mills we showed how poorly conducting LaF_3 can be turned into a highly conducting material via heterovalent replacement strategies. Already at low substitution levels of $x = 0.1$ the ionic conductivity of $\text{La}_{1-x}\text{Sr}_x\text{F}_{3-x}$ can be significantly improved when referenced to that of pure, nanocrystalline LaF_3 . After 10 h of mechanical treatment under dry conditions, a phase pure powder is obtained that is characterized by high F anion conductivities ($1 \times 10^{-5} \text{ S cm}^{-1}$ (373 K)) and relatively low activation energies of 0.49 eV. Structural disorder and lattice strain, being a result of mixing cations differing in ionic radii, is assumed to cause the increase in ionic conductivity observed. ^{19}F MAS NMR clearly supports this idea as the lines reveal a broadened lines pointing to a distribution of chemical shifts. This distribution is caused by point defects, particularly vacant F sites, and polyhedra distortions in the mechanically treated samples. These features facilitate rapid anion exchange that boosts ionic conductivity. For $x > 0.03$ the Arrhenius pre-factor rather than the activation energy is responsible for the increase in σ_{DC} with increasing Sr content.

Acknowledgements

Open access funding provided by Graz University of Technology. We thank V. Pregartner for her help with sample preparation and the impedance measurements. Furthermore, we thank the Deutsche Forschungsgemeinschaft (DFG) for financial support

in the frame of the priority program *crystalline non-equilibrium phases* (SPP 1415). Further support by the FFG K-project *safe battery* is highly appreciated.

Open Access This article is distributed under the terms of the Creative Commons Attribution 4.0 International License (<http://creativecommons.org/licenses/by/4.0/>), which permits unrestricted use, distribution, and reproduction in any medium, provided you give appropriate credit to the original author(s) and the source, provide a link to the Creative Commons license, and indicate if changes were made.

References

- [1] Knauth P (2009) Inorganic solid Li ion conductors: an overview. *Solid State Ion* 180(14–16):911
- [2] Tuller HL (2000) Ionic conduction in nanocrystalline materials. *Solid State Ion* 131(1):143
- [3] Fergus JW (1997) The application of solid fluoride electrolytes in chemical sensors. *Sens Act B: Chem* 42(2):119–130
- [4] Whittingham MS (2004) Lithium batteries and cathode materials. *Chem Rev* 104:4271
- [5] Bachman JC, Muy S, Grimaud A, Chang H-H, Pour N, Lux SF, Paschos O, Maglia F, Lupart S, Lamp P, Giordano L, Shao-Horn Y (2016) Inorganic solid-state electrolytes for lithium batteries: mechanisms and properties governing ion conduction. *Chem Rev* 116(1):140–162
- [6] Sata N, Eberman K, Eberl K, Maier J (2000) Mesoscopic fast ion conduction in nanometre-scale planar heterostructures. *Nature* 408:946
- [7] Reddy MA, Fichtner M (2011) Batteries based on fluoride shuttle. *J Mater Chem* 21:17059–17062
- [8] Ronge C, Reddy MA, Witter R, Fichtner M (2013) Nanostructured fluorite-type fluorides as electrolytes for fluoride ion batteries. *J Phys Chem C* 117(10):4943
- [9] Ronge C, Anji Reddy M, Witter R, Fichtner M (2014) Solid electrolytes for fluoride ion batteries: ionic conductivity in polycrystalline tyanite-type fluorides. *ACS Appl Mater Interf* 6(3):2103–2110
- [10] Preishuber-Pflügl F, Bottke P, Pregartner V, Bitschnau B, Wilkening M (2014) Correlated fluorine diffusion and ionic conduction in the nanocrystalline F^- solid electrolyte $Ba_{0.6}La_{0.4}F_{2.4}$ - $^{19}FT_{1(\rho)}$ NMR relaxation vs. conductivity measurements. *Phys Chem Chem Phys* 16:9580
- [11] Sorokin NI, Sobolev BP (2007) Nonstoichiometric fluorides—solid electrolytes for electrochemical devices: a review. *Cryst Rep* 52(5):842–863
- [12] Preishuber-Pflügl F, Wilkening M (2016) Mechanochemically synthesized fluorides: local structures and ion transport. *Dalton Trans* 45:8675
- [13] Ruprecht B, Wilkening M, Steuernagel S, Heitjans P (2008) Anion diffusivity in highly conductive nanocrystalline $BaF_2 : CaF_2$ composites prepared by high-energy ball milling. *J Mater Chem* 18:5412
- [14] Ruprecht B, Wilkening M, Feldhoff A, Steuernagel S, Heitjans P (2009) High anion conductivity in a ternary non-equilibrium phase of BaF_2 and CaF_2 with mixed cations. *Phys Chem Chem Phys* 11:3071
- [15] Düvel A, Ruprecht B, Heitjans P, Wilkening M (2011) Mixed alkaline-earth effect in the metastable anion conductor $Ba_{1-x}Ca_xF_2$ ($0 \leq x \leq 1$): correlating long-range ion transport with local structures revealed by ultrafast ^{19}F MAS NMR. *J Phys Chem C* 115(48):23784
- [16] Heitjans P, Masoud M, Feldhoff A, Wilkening M (2007) NMR and impedance studies of nanocrystalline and amorphous ion conductors: lithium niobate as a model system. *Faraday Discuss* 134:67
- [17] Wilkening M, Epp V, Feldhoff A, Heitjans P (2008) Tuning the Li diffusivity of poor ionic conductors by mechanical treatment: high Li conductivity of strongly defective $LiTaO_3$ nanoparticles. *J Phys Chem C* 112(25):9291
- [18] Wohlmuth D, Epp V, Bottke P, Hanzu I, Bitschnau B, Letofsky-Papst I, Kriechbaum M, Amenitsch H, Hofer F, Wilkening M (2014) Order vs. disorder—a huge increase in ionic conductivity of nanocrystalline $LiAlO_2$ embedded in an amorphous-like matrix of lithium aluminate. *J Mater Chem A* 2:20295–20306
- [19] Prutsch D, Breuer S, Uitz M, Bottke P, Langer J, Lunghammer S, Philipp M, Posch P, Pregartner V, Stanje B, Dunst A, Wohlmuth D, Brandstätter H, Schmidt W, Epp V, Chadwick A, Hanzu I, Wilkening M (2017) Nanostructured ceramics: ionic transport and electrochemical activity. *Z Phys Chem* 231:1361
- [20] Wang F, Grey CP (1997) Probing the mechanism of fluoride-ion conduction in LaF_3 and strontium-doped LaF_3 with high-resolution ^{19}F MAS NMR. *Chem Mater* 9(5):1068–1070
- [21] Šepelak V, Düvel A, Wilkening M, Becker K-D, Heitjans P (2013) Mechanochemical reactions and syntheses of oxides. *Chem Soc Rev* 42:7507
- [22] Düvel A, Wegner S, Efimov K, Feldhoff A, Heitjans P, Wilkening M (2011) Access to metastable complex ion conductors via mechanosynthesis: preparation, microstructure and conductivity of $(Ba,Sr)LiF_3$ with inverse perovskite structure. *J Mater Chem* 21:6238
- [23] Breuer S, Stanje B, Pregartner V, Lunghammer S, Hanzu I, Wilkening M (2018) Fluorine translational anion dynamics

- in nanocrystalline ceramics: $\text{SrF}_2\text{-YF}_3$ solid solutions. *Crystals* 8(3):122
- [24] Chable J, Dieudonne B, Body M, Legein C, Crosnier-Lopez M-P, Galven C, Mauvy F, Durand E, Fourcade S, Sheptyakov D, Leblanc M, Maisonneuve V, Demourgues A (2015) Fluoride solid electrolytes: investigation of the tysonite-type solid solutions $\text{La}_{1-x}\text{Ba}_x\text{F}_{3-x}$ ($x < 0.15$). *Dalton Trans* 44:19625–19635
- [25] Chable J, Martin A, Bourdin A, Body M, Legein C, Jouanneaux A, Crosnier-Lopez M-P, Galven C, Dieudonne B, Leblanc M, Demourgues A, Maisonneuve V (2017) Fluoride solid electrolytes: from microcrystalline to nanosstructured tysonite-type $\text{La}_{0.95}\text{Ba}_{0.05}\text{F}_{2.95}$. *J Alloys Comp* 692:980–988
- [26] Dieudonné B, Chable J, Mauvy F, Fourcade S, Durand E, Lebraud E, Leblanc M, Legein C, Body M, Maisonneuve V, Demourgues A (2015) Exploring the $\text{Sm}_{1-x}\text{Ca}_x\text{F}_{3+x}$ tysonite solid solution as a solid-state electrolyte: relationships between structural features and F^- ionic conductivity. *J Phys Chem C* 119(45):25170–25179
- [27] Scherrer P (1918) Bestimmung der Größe und der inneren Struktur von Kolloidteilchen mittels Röntgenstrahlen. *Nachr Ges Wiss Göttingen* 2:98
- [28] Patterson AL (1939) The scherrer formula for x-ray particle size determination. *Phys Rev* 56:978–982
- [29] Sadoc A, Body M, Legein C, Biswal M, Fayon F, Rocquefelte X, Boucher F (2011) NMR parameters in alkali, alkaline earth and rare earth fluorides from first principle calculations. *Phys Chem Chem Phys* 13:18539–18550
- [30] Williamson G, Hall W (1953) X-ray line broadening from filed aluminium and wolfram. *Acta Metall* 1(1):22
- [31] Breuer S, Wilkening M (To be published; manuscript under preparation)
- [32] Breuer S, Wilkening M (2018) Mismatch in cation size causes rapid anion dynamics in solid electrolytes: the role of the arrhenius pre-factor. *Dalton Trans* 47:4105–4117
- [33] Vergentev T, Banshchikov A, Filimonov A, Koroleva E, Sokolov N, Wurz MC (2016) Longitudinal conductivity of $\text{LaF}_3/\text{SrF}_2$ multilayer heterostructures. *Sci Tech Adv Mater* 17(1):799–806
- [34] Sorokin NI, Sobolev BP (2016) Fluorine-ion conductivity of different technological forms of solid electrolytes $R_{1-y}\text{M}_y\text{F}_{3-y}$ (LaF_3 type) ($R = \text{Ca}, \text{Sr}, \text{Ba}; \text{M} = \text{Ca}, \text{Sr}, \text{Ba}$ are rare earth elements). *Cryst Rep* 61(3):499–505
- [35] Sorokin NI, Ivanovskaya NA, Sobolev BP (2014) Ionic conductivity of cold-pressed ceramics from grinding of $R_{0.95}\text{M}_{0.05}\text{F}_{2.95}$ solid electrolytes ($R = \text{La}, \text{Nd}; \text{M} = \text{Ca}, \text{Sr}, \text{Ba}$) synthesized by reaction in melt. *Cryst Rep* 59(2):248–251
- [36] Durá OJ, López de la Torre MA, Vázquez L, Chaboy J, Boada R, Rivera-Calzada A, Santamaría J, Leon C (2010) Ionic conductivity of nanocrystalline yttria-stabilized zirconia: grain boundary and size effects. *Phys Rev B* 81:184301
- [37] Düvel A, Bednarcik J, Šepelák V, Heitjans P (2014) Mechanosynthesis of the fast fluoride ion conductor $\text{Ba}_{1-x}\text{La}_x\text{F}_{2+x}$: from the fluorite to the tysonite structure. *J Phys Chem C* 118(13):7117–7129
- [38] Cazorla C, Sagotra AK, King M, Errandonea D (2018) High-pressure phase diagram and superionicity of alkaline earth metal difluorides. *J Phys Chem C* 122(2):1267–1279
- [39] Maier J (2005) Nanoionics: ion transport and electrochemical storage in confined systems. *Nature Mater* 4(11):805
- [40] Maier J (2003) Nano-ionics: trivial and non-trivial size effects on ion conduction in solids. *Z Phys Chem Int Ed* 217(4):415
- [41] Maier J (1995) Ionic conduction in space charge regions. *Prog Solid State Chem* 23(3):171
- [42] Puin W, Rodewald S, Ramlau R, Heitjans P, Maier J (2000) Local and overall ionic conductivity in nanocrystalline CaF_2 . *Solid State Ion* 131(1):159
- [43] Meyer W, Neldel H (1937) Concerning the relationship between the energy constant epsilon and the quantum constant alpha in the conduction-temperature formula in oxydising semi-conductors. *Phys Z* 38:1014–1019

3.2.4 Heterogeneous F anion transport, local dynamics and electrochemical stability of nanocrystalline $\text{La}_{1-x}\text{Ba}_x\text{F}_{3-x}$

Das letzte Manuskript zum Thema Fluor-Ionenleiter, das bereits eingereicht wurde und sich im Review-Prozess befindet, hatte zum Ziel einen Festkörperelektrolyten mit hoher Ionenleitfähigkeit zu synthetisieren und anschließend seine elektrochemische Stabilität im Hinblick auf einen Einsatz in Fluorid-Ionen-Batterien zu untersuchen. Die hergestellten $\text{La}_{1-x}\text{Ba}_x\text{F}_{3-x}$ Verbindungen weisen, vor allem wenn sie in der Tysonit-Struktur kristallisieren, sehr gute Gesamtleitfähigkeiten auf und sind daher ein vielversprechendes Elektrolytmaterial. Im Rahmen dieser Arbeit wurden die Proben zuerst mechanochemisch hergestellt und via XRD strukturell charakterisiert. Von großer Bedeutung war es anschließend herauszufinden, ob sich die elementaren Ionensprünge im Ångström-Bereich stark von der langreichweiten Ionendynamik unterscheiden. Dafür wurden verschiedenste Impedanz- sowie NMR-Messungen durchgeführt. Es konnte so gezeigt werden, dass vor allem die Morphologie der Grenzflächen großen Einfluss auf den durchgängigen Ionentransport durch die Materialien besitzt. Mit Hilfe von Polarisationsmessungen und Cyclovoltammetrie wurde zudem noch der Potentialbereich bestimmt, in dem die Probe elektrochemisch stabil ist.

Die hohe Ionenleitfähigkeit, in Verbindung mit der vernachlässigbaren Elektronenleitfähigkeit und dem breiten elektrochemischen Stabilitätsfenster, machen $\text{La}_{1-x}\text{Ba}_x\text{F}_{3-x}$ in der Tat zu einem äußerst vielversprechenden Fluor-Elektrolyten.

Heterogeneous F anion transport, local dynamics and electrochemical stability of nanocrystalline $\text{La}_{1-x}\text{Ba}_x\text{F}_{3-x}$

S. Breuer, M. Gombotz, V. Pregartner, I. Hanzu, and M. Wilkening.

under review

Heterogeneous F anion transport, local dynamics and electrochemical stability of nanocrystalline $\text{La}_{1-x}\text{Ba}_x\text{F}_{3-x}$

Stefan Breuer,^{1,*} Maria Gombotz,¹ Veronika Pregartner¹, I. Hanzu^{1,2} and Martin Wilkening^{1,2}

¹ Institute for Chemistry and Technology of Materials, and Christian Doppler Laboratory for Lithium Batteries, Graz University of Technology (NAWI Graz), Stremayrgasse 9, 8010 Graz, Austria

² ALISTORE - European Research Institute, CNRS FR3104, Hub de l'Energie, Rue Baudelocque, 80039 Amiens, France

*corresponding author, breuer@tugraz.at

Abstract. Solid state ion conductors exhibiting fast ion dynamics are of utmost importance for the development of modern energy storage systems or sensors. For the realization of fluoride ion batteries (FIBs), that is, batteries relying on F^- ions as charge carriers, materials with fast fluorine anion dynamics are needed. Here we used high-energy ball milling to incorporate BaF_2 into the tysonite structure of LaF_3 and studied ion dynamics by both broadband impedance and ¹⁹F nuclear magnetic resonance (NMR) spectroscopy. The nanocrystalline solid solution formed revealed increased ion conductivity compared to pure LaF_3 . Apart from the formation of F vacancies through aliovalent substitution, the increase in conductivity is also stimulated by the introduction of lattice strain and the high degree of local disorder produced. While long-range ion dynamics has been studied recently, less information is known about local ion hopping processes to which ¹⁹F NMR spin-lattice relaxation is sensitive. In this work, we tried to correlate short-range ion diffusion with long-range transport properties measured by conductivity spectroscopy. Additionally, we used electrochemical polarization and cyclic voltammetry to judge whether the ternary fluoride shows a sufficiently high electrochemical stability to work in FIBs.

Keywords: Fluorides, electrolytes, NMR, conductivity, nanocrystalline ceramics, diffusion

Introduction

Understanding ionic diffusion in crystalline and amorphous solids is a vital topic in material science [1-9]. In hardly any other field than energy storage fast ion conductors play an overall role [10-15]. As the highly advanced and already matured technology of Li-ion batteries [16-20] is expected to crest in the future new concepts need to be envisaged. Game changing breakthroughs are, however, difficult to reach with concepts being very similar to those studied in the past [21]. Thus, much effort is put into finding suitable materials that meet the needs to develop new leading-edge energy storage devices, which presumably are being based on solid electrolytes [11]. One of these technologies, which attracted attention over the last couple of years is the all-solid-state fluoride ion battery (FIB) that relies on an anionic charge carrier [22, 23].

As fluorine is the most electronegative element in the periodic table, it is very stable and has a wide electrochemical stability window making it a suitable ion for charge transfer processes in such a battery. In general, the increase in safety, the higher cycle stability as well as the theoretically high energy density are major advantages of all-solid-state systems over those relying on liquid electrolytes [10-13, 24-27]. The

investigation of novel electrode and electrolyte materials useful for FIBs [22, 23, 28-35] has, therefore, pushed our interest in this field of materials research lately. Besides studies driven directly by applications, fundamentally oriented investigations are required to shine further light on the structure-property relationships determining fast ion transport being necessary for these types of batteries [29, 36-43].

The solid electrolyte, which should provide fast F anion transport and negligible electronic conductivity, is a fundamental component to realize FIBs. In 2014, Rongeat *et al.* [29] introduced solid solutions of $\text{La}_{1-x}\text{Ba}_x\text{F}_{3-x}$ to act as promising solid F^- electrolytes. Depending on the composition x the material shows either a fluorite-type or a highly conductive tysonite-type structure. In Fig. 1 the crystal structure of lanthanum fluoride LaF_3 crystallizing with tysonite-type structure is illustrated. The fluoride anions are distributed among three crystallographically and magnetically inequivalent sites. Anions located on F2 (4d) and F3 (2a) positions form sublattices together with La. F1 (12g) anions reside in the interspace between these La(F2/F3) layers and feature the highest multiplicity with 12 compared to 4 and 2 for F1 and F2, respectively [43]. As Privalov and co-workers already reported in 1997, the fluorine anions in the interspace are the most mobile ones being primarily responsible for the overall ionic conductivity [44], see also the NMR study of Grey and Wang [45]. Among tysonite-type fluorides, the highest conductivities yet reported are in the range of $10^{-3} \text{ S cm}^{-1}$ for single crystals of LaF_3 -based solid solutions, see, *e.g.*, $\text{La}_{0.95}\text{Sr}_{0.05}\text{F}_{2.95}$ [46]. Ion blocking grain boundaries have been assumed to be responsible for the large difference seen between single crystals and powder samples [28, 29].

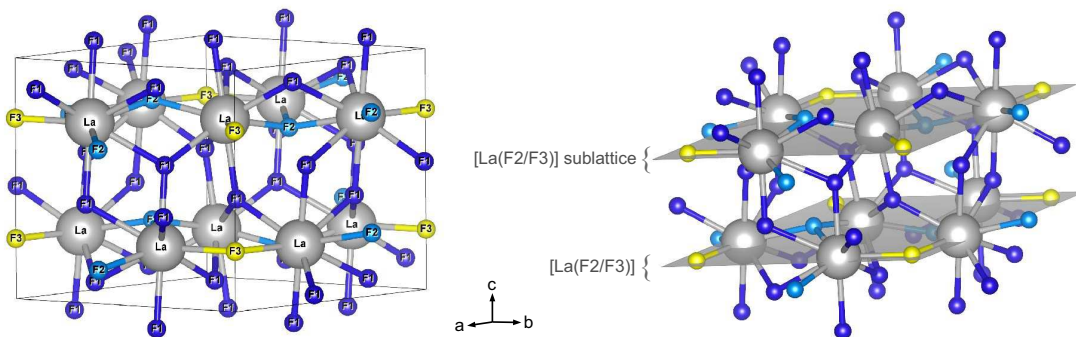


Fig. 1 Crystal structure of LaF_3 . The tysonite structure provides three different F sites labelled F1 (12g), F2 (4d) and F3 (2a). Each site is fully occupied by fluorine anions. F2 and F3 ions are located in the $\text{La}(\text{F2/F3})$ sublattice, F1 ions reside in the interspace between these layers.

To shed further light on ion dynamics in this ternary system we used high-energy ball milling to prepare a series of solid solutions of nanocrystalline $\text{La}_{1-x}\text{Ba}_x\text{F}_{3-x}$ and studied local structures as well as short-range and long-range F anion dynamics by means of conductivity [47] as well as NMR spectroscopy [48]. At sufficiently low x , the major component, LaF_3 , determines the final tysonite-type structure and accepts the Ba^{2+} ions to form a solid solution rich in F anion vacancies [49]. Anion vacancies, local structural disorder and lattice strain, generated through the intimate mixing of cations differing in ionic radii cation are expected to influence the overall ionic conductivity. The combination of impedance and conductivity spectroscopy

with various solid-state NMR techniques [39-41, 50] might help providing a better understanding of the relevant conduction mechanisms. In particular, the present study also aims at finding out whether short-range ion hopping on the angstrom length scale is considerably different to long-range ion dynamics [39]. If so, such heterogenous ion dynamics would, depending on the method applied, result in length-scale dependent motional correlation times and activation energies. Finally, we used polarization measurements and cyclic voltammetry to answer the question in which potential range the sample is electrochemically stable.

Experimental

Mechanochemical preparation and characterization of the samples

Nanocrystalline samples of $\text{La}_{1-x}\text{Ba}_x\text{F}_{3-x}$ ($0 \leq x \leq 0.2$) were prepared by high-energy ball milling of LaF_3 (99.99%, Alfa Aesar) along with BaF_2 (99.99%, Sigma-Aldrich) in a Fritsch Pulverisette 7 Premium line planetary mill. For the synthesis, two 45 mL grinding beakers, filled with the educts (total mass of about 3 g) and 180 ZrO_2 milling balls (5 mm in diameter) in each case, were employed. The mixtures were treated under Ar atmosphere for 10 hours at a rotational speed of 600 rpm. Additionally, nanocrystalline samples of $\text{La}_{0.9}\text{Ba}_{0.1}\text{F}_{2.9}$ have been annealed at various temperatures for 5 h in a tube furnace under a constant flow of argon gas. Structural analysis of the powders obtained was carried out at room temperature using X-ray powder diffraction (XRPD). The pattern were recorded on a Bruker D8 Advance diffractometer with Bragg Brentano geometry operating with $\text{Cu K}\alpha$ radiation.

Impedance spectroscopy

For the conductivity measurements cylindrical pellets with a diameter of 5 mm and approximately 1.5 mm in thickness were prepared via compacting the powders by applying a pressure of *ca.* 0.5 GPa. Au blocking electrodes of 100 nm were applied using a sputter coater (Leica). The measurements were carried out with a Novocontrol Concept 80 broadband dielectric spectrometer being able to record complex impedances over a frequency from 0.01 Hz to 10 MHz. We measured impedance data at temperatures from 173 K to 453 K. In our setup the temperature is automatically controlled by means of a QUATRO cryosystem (Novocontrol), which uses a heating element to build up a specific pressure in a liquid nitrogen Dewar to create a constant N_2 gas flow. This constant flow in the cryostat also helps to avoid contamination with water or carbon dioxide as best as possible.

NMR measurements

To sharpen our view on ion dynamics on short as well as long time scales, the nanocrystalline sample featuring the highest ionic conductivity was investigated with various time-domain ^{19}F NMR techniques. For these measurements, the $\text{La}_{0.9}\text{Ba}_{0.1}\text{F}_{2.9}$ nanocrystalline powder was fire-sealed in a Duran glass ampoule (about 3 cm in length and 5 mm in diameter) under vacuum to protect the sample from any contamination via humidity. NMR data were recorded using a Bruker Avance III spectrometer operating at 7 T; this field

corresponds to a ^{19}F Larmor frequency of $\omega_0/2\pi = 282$ MHz. We used a home-built NMR probe, suitable to record NMR signals under static conditions up to temperatures as high as 533 K. The 90° pulse lengths ranged from 1.15 to 1.92 μs at 200 W. For the temperature controlling and monitoring, a Eurotherm temperature controller together with a type T thermocouple was utilized.

Longitudinal spin-lattice relaxation (SLR) rates ($1/T_1$) were measured by using the saturation recovery pulse sequence $10 \times \pi/2 - t_d - \pi/2 - \text{acquisition (acq.)}$. Transversal ^{19}F SLR ρ rates $1/T_{1\rho}$ in the rotating frame, were recorded with the spin-lock sequence, $\pi/2 p(t_{\text{lock}}) - \text{acq.}$ [51], where $p(t_{\text{lock}})$ denotes the variable spin-lock pulse directly sent after the $\pi/2$ pulse to prepare the spin system. The spin-locking frequency was set to approximately 100 kHz and the duration of the locking pulse p was varied from $t_{\text{lock}} = 10 \mu\text{s}$ to $t_{\text{lock}} = 730$ ms. A sufficiently long recycle delay of at least $6 \times T_1$ ensured full longitudinal relaxation between each scan. All transients were parameterized with stretched exponentials to extract the $1/T_1$ and $1/T_{1\rho}$ rates, respectively [14, 39, 52-54].

Static ^{19}F NMR spectra were recorded using a single 90° pulse experiment via Fourier transformation of the free induction decay. High-resolution ^{19}F NMR spectra under magic angle spinning (MAS) were recorded using a 500 MHz Avance spectrometer (Bruker) operating at 11 T, which corresponds to a ^{19}F Larmor frequency of 470.4 MHz. The MAS NMR measurements were performed at 303 K and a spinning speed of 60 kHz using 1.3-mm rotors and at a spinning speed of 25 kHz using 2.5-mm rotors, respectively. NMR spectra were referenced to LiF as a secondary reference, which shows a chemical shift δ_{iso} of -204.3 ppm. CFCl_3 (0 ppm) served as the primary reference.

Polarization measurements and cyclic voltammetry

For our polarization experiments we also used cylindrical pellets which were cold-pressed at a pressure of 0.5 GPa. The pellets prepared had a diameter of 8 mm and a thickness of approximately 1 mm. To guarantee electrical contact, Au blocking electrodes of 100 nm were applied using a sputter coater (Leica), see above. The samples were mounted in a sample cell, which was continuously purged with N_2 and connected to a Parstat MC potentiostat (Princeton Applied Research) equipped with a low-current option. Measurements were carried out at 473 K and a constant potential of 1.5 V. For cyclic voltammetry (CV) measurements we used another pellet (8 mm in diameter) with one side completely sputtered with Au (100 nm in thickness) and the other side equipped with a sputtered Au electrode with a diameter of 2 mm. CV measurements were carried out at 473 K. The initial potential was set to the corresponding open circuit voltage (OCV), the vertex potential to -3 V and the final potential again to OCV. The scan rate ranged from 0.1 V/s to 1 V/s.

Results and discussion

X-ray diffraction

The purity of the nanocrystalline samples was examined by X-ray powder diffraction (XRPD). Diffraction patterns were collected at room temperature and under air atmosphere. Fig. 2 a) shows patterns of all nanocrystalline samples prepared as well as those of the nanocrystalline binaries BaF_2 and LaF_3 . The milling

time was 10 h. Starting from non-substituted LaF_3 the patterns reveal the successful incorporation of BaF_2 up to a composition of $x = 0.15$ [49]. XRPD shows that solid solutions are obtained that crystallize with trigonal tyanite-type LaF_3 structure. As expected if La^{3+} (ionic radius of 1.22) [55] is successfully replaced by Ba^{2+} (ionic radius of 1.42) [55], the reflections slightly shift toward smaller diffraction angles showing lattice expansion. The higher the BaF_2 content, the more pronounced the shift.

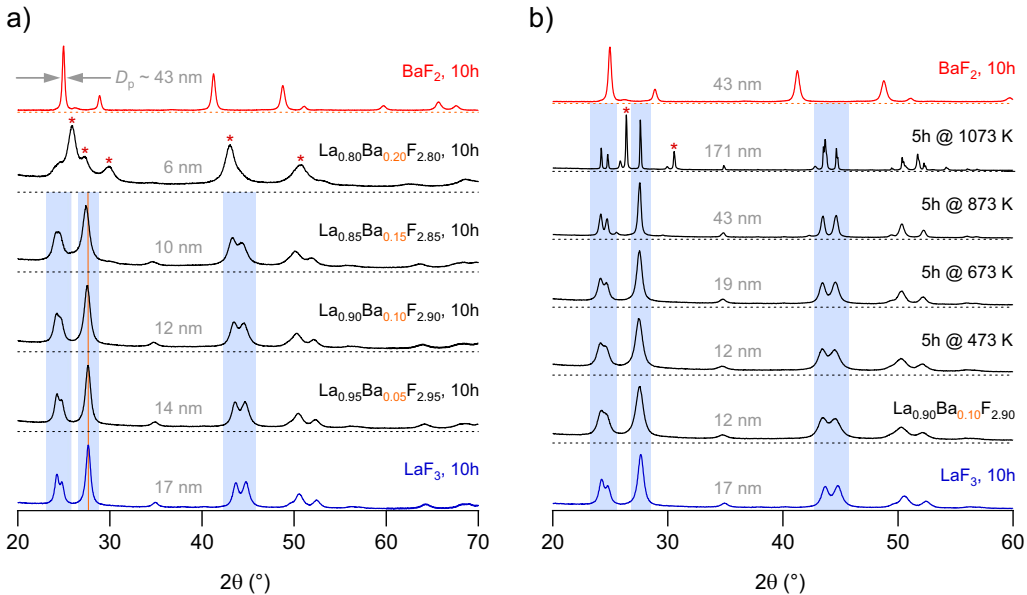


Fig. 2 a) X-ray powder diffraction pattern of mechanochemically prepared nanocrystalline BaF_2 , LaF_3 and solid solutions of $\text{La}_{1-x}\text{Ba}_x\text{F}_{3-x}$ with $0 \leq x \leq 0.2$. All samples were synthesized using a ZrO_2 vial set at a rotational speed of 600 rpm and a milling time of 10 h. The values in nm refer to mean crystallite sizes D_p . b) Effect of annealing on the XRPD of $\text{La}_{0.9}\text{Ba}_{0.1}\text{F}_{2.9}$ (see a); the patterns reveal changes of $\text{La}_{0.9}\text{Ba}_{0.1}\text{F}_{2.9}$ upon heat treatment at the temperatures and durations indicated. For comparison, the patterns of LaF_3 (10 h) and BaF_2 (10 h) are shown. See text for further discussion.

Considering the pattern of $\text{La}_{1-x}\text{Ba}_x\text{F}_{3-x}$ with $x = 0.2$ new reflections other than those assigned to LaF_3 show up. At too high x the reverse process takes place and La^{3+} ions are incorporated into BaF_2 . The original reflections of cubic BaF_2 shift toward smaller angles and reveal lattice contraction. Hence, for $x = 0.2$ a mixture of tyanite-type and cubic $\text{La}_{1-x}\text{Ba}_x\text{F}_{3-x}$ is formed rather than a structurally homogenous solid solution. Besides the fact that the larger BaF_2 lattice integrates a significant amount of the smaller La^{3+} ions, we also observe a relatively broad background signal which indicates the presence of some amount of amorphous material. In particular, it is likely that amorphous $\text{La}_{1-x}\text{Ba}_x\text{F}_{3-x}$ is present in the sample characterized by $x = 0.2$. Mean crystallite sizes, D_p , were estimated using the relationship introduced by Scherrer. Values range from 8 nm to 43 nm. While the samples with tyanite structure show comparable grain sizes, the reflections belonging to $\text{La}_{0.8}\text{Ba}_{0.2}\text{F}_{2.8}$ point to rather small crystallites. Of course, overlapping of intensities for $x = 0.2$ and lattice strain affect the quality of the estimation of D_p in this case.

Fig. 2 b) illustrates the effect of heat treatment on the XRD patterns of nanocrystalline $\text{La}_{0.9}\text{Ba}_{0.1}\text{F}_{2.9}$. The sample has been annealed for 5 h at the temperatures indicated. Up to 873 K annealing only causes an

increase in mean crystallite size reaching values of up to 43 nm. Above 1073 K not only grain growth is seen but also decomposition of the sample reflecting the metastable nature of nanocrystalline $\text{La}_{0.9}\text{Ba}_{0.1}\text{F}_{2.9}$. A significant amount of tysonite-type LaF_3 , most likely doped with Ba^{2+} , shows up. Furthermore, XRD reveals the presence of La-rich, fluorite-type $\text{La}_{1-x}\text{Ba}_x\text{F}_{3-x}$, see the reflections marked with asterisks. For this sample the diameter D_p turned out to be in the order of 171 nm. Sharp reflections and the absence of any broad humps show that a highly crystalline sample is obtained after heat treatment at 1073 K.

Impedance spectroscopy

To study how F anion transport changes with both x and heat treatment we measured complex impedances and conductivities over a large temperature and frequency range, including frequencies with values of up to 3 GHz [39]. Exemplarily, in Fig. 3 a) the real part, σ' , of the complex conductivity of $\text{La}_{0.9}\text{Ba}_{0.1}\text{F}_{2.9}$ is plotted vs. the frequency ν .

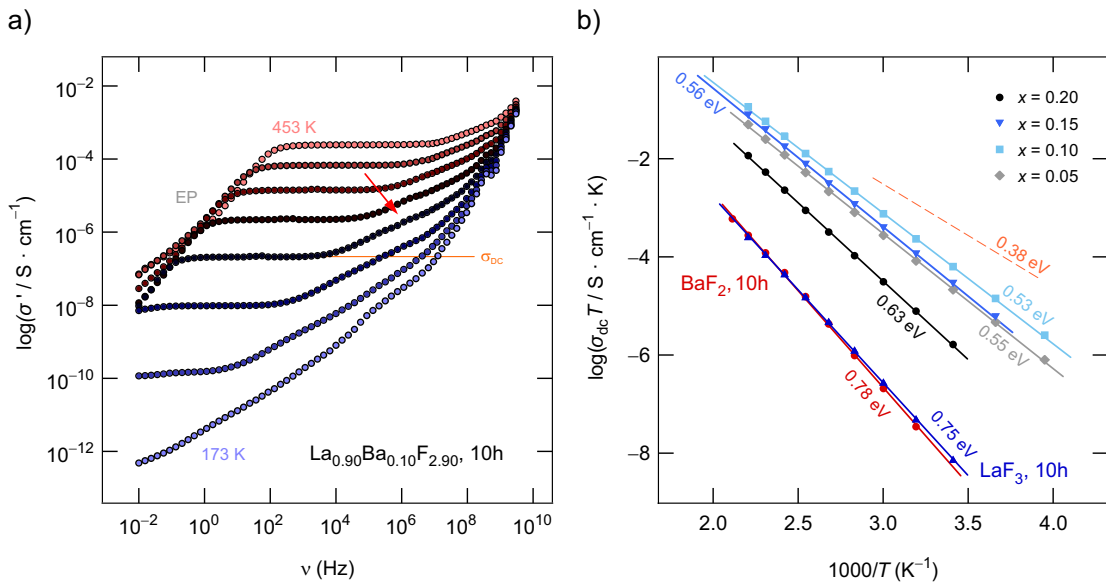


Fig. 3 a) Conductivity isotherms of nanocrystalline $\text{La}_{0.9}\text{Ba}_{0.1}\text{F}_{2.9}$ recorded at temperatures ranging from 173 K to 453 K; altogether we covered a frequency range of eleven decades. b) Arrhenius plot illustrating the change of the DC conductivity of the $\text{La}_{1-x}\text{Ba}_x\text{F}_{3-x}$ samples mechanochemically synthesized by high-energy ball milling the starting materials for 10 h. The highest conductivity is found for the sample with $x = 0.1$. Solid lines represent linear fits to extract activation energies and Arrhenius pre-factors. The dashed line corresponds to conductivities read off from the second shallow σ_{dc} plateau marked in a) with an arrow. The activation energy of 0.38 eV corresponds to that probed for F anion transport in single crystals.

The isotherms show regions that correspond to specific dielectric phenomena such as electrode polarization (EP) or electrical bulk response. At elevated T and low ν electrode polarization shows up which originates from the piling up of the ions in front of the surface of the ion blocking electrodes [41]. Going to higher frequencies distinct direct current (dc) plateaus are visible from which we directly read off conductivities being responsible for long-range ion transport. For $\text{La}_{0.9}\text{Ba}_{0.1}\text{F}_{2.9}$ σ_{dc} yields an activation energy of 0.53 eV,

see Figure 3 a). Subsequently, with increasing ν for each isotherm a Jonscher-type [56] dispersive region is observable, which can usually be approximated with a power law according to $\sigma' = \sigma_{dc} + A_0\omega^n$. Here A_0 is the so-called dispersion parameter and n represents the power law exponent [56]. In the present case, the dispersive region for some of the isotherms show a shallow curvature at sufficiently high frequencies. Most likely, medium to short-range motions are responsible for this feature indicating that several length-scale dependent motional processes contribute to the overall electric response. The dashed line in Fig. 3 b) illustrates the corresponding conductivities. They reveal a highly conductive bulk F ion transport process, which is characterized by 0.38 eV, see also Fig. 4 a). Interestingly, for single crystalline $\text{La}_{0.9}\text{Ba}_{0.1}\text{F}_{2.9}$ similar values (0.36 to 0.37 eV) have been reported. The corresponding ionic conductivities of single crystals are, however, still much higher than those found for this second relaxation process. Since the activation energies are quite similar, the difference is given by the pre-factors σ_0 of the Arrhenius lines, see below [57]. For comparison, the electric modulus representation of our impedance data yields an activation energy of 0.44 eV, see below and Fig. S1.

At frequencies above 100 MHz (and at high T) the isotherms start to pass into a high-frequency region for which the conductivity turned out to be almost independent of T . Strictly localized ions motions or caged-type forward-backward jumps have frequently been used to explain this feature [58-61].

To compare the change in ionic dc conductivity of the samples, $\sigma_{dc}T$ has been plotted vs. the inverse temperature ($1000/T$) in an Arrhenius representation (see Fig. 3 b)). Solid lines show fits according to $\sigma_{dc}T = \sigma_0 \cdot \exp(E_A/(k_B T))$. σ_0 represents the pre-exponential factor, E_A the activation energy and k_B denotes Boltzmann's constant. Nanocrystalline non-substituted LaF_3 and BaF_2 clearly exhibit the poorest ion conductivities with values as low as $10^{-11} \text{ S cm}^{-1}$ at room temperature. The activation energy of 0.78 eV for BaF_2 points to F vacancies controlling ion transport for which 0.75 eV is assumed [62].

Joint milling of the binaries significantly increases σ_{dc} . Among the series of samples prepared, $\text{La}_{0.9}\text{Ba}_{0.1}\text{F}_{2.9}$ provides the best conductivities, roughly four orders of magnitude higher compared to those of the binary fluorides. This finding is in very good agreement with results presented by Rongeat *et al* [29]. The sample with $x = 0.2$, which is a mixture of cubic and tysonite-type $\text{La}_{1-x}\text{Ba}_x\text{F}_{3-x}$ (see above, Fig. 2 a)) features a considerably lower ion conductivity. Obviously, tysonite $\text{La}_{1-x}\text{Ba}_x\text{F}_{3-x}$ is a much better ionic conductor than Ba-rich $\text{La}_{1-x}\text{Ba}_x\text{F}_{3-x}$ crystallizing with cubic symmetry. The increase in conductivity when going from $x = 0$ to $x = 0.1$ is accompanied by a reduction in activation energy, which decreases by more than 0.2 eV from 0.78 eV to 0.53 eV. This value and σ_{dc} of $\text{La}_{0.9}\text{Ba}_{0.1}\text{F}_{2.9}$ is very similar to the behavior of mechanosynthesized $\text{La}_{0.9}\text{Sr}_{0.1}\text{F}_{2.9}$ investigated quite recently [63].

To underpin our assumption that the prominent dc plateaus seen in Fig. 2 a) are caused by bulk ion dynamics in $\text{La}_{1-x}\text{Ba}_x\text{F}_{3-x}$ we used the Nyquist representation to calculate the associated electrical capacities C . At 293 K the corresponding Nyquist plot is dominated by a depressed semicircle (see Fig. 4 a)) combined with an electrode spike in the low frequency region. C can be estimated via the maximum condition $\omega_{el} = 1/(RC)$, where R is the resistance and $\omega_{el} = 2\pi\nu$ the electric relaxation frequency [64]. Here we obtain $C = 9.1 \text{ pF}$ which clearly points to bulk ion dynamics. The same holds for the other nanocrystalline samples. The capacity estimated perfectly agrees with that which can be calculated from the real part of the complex permittivity (10.4 pF) when plotted vs. ν , see Fig. 4 b). We used the equation for a parallel-plate capacitor,

$C = \epsilon' \epsilon_0 (A/l)$, to estimate C . ϵ_0 represents the permittivity of free space (8.854×10^{-14}), A the area and l the thickness of our sample [64]. Of course, we cannot exclude that also interfacial effects influence this main transport process seen in the limit $v \rightarrow 0$.

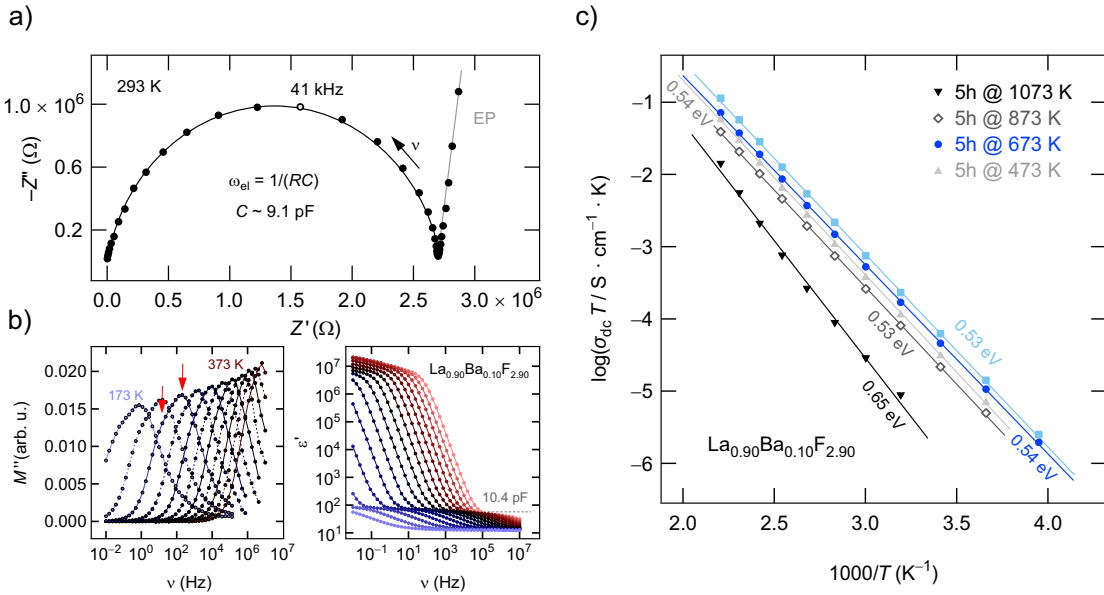


Fig. 4 a) Complex plane plot of the conductivity isotherm of nanocrystalline $\text{La}_{0.9}\text{Ba}_{0.1}\text{F}_{2.9}$ (293 K). The curve consists of an electrode polarization spike at low v and a semicircle, which is characterized by a capacity of approximately 9 pF. b) Change of the modulus spectra and the real part of the complex permittivity with frequency and temperature. c) Arrhenius diagram showing the temperature dependence of $\sigma_{dc}T$ of $\text{La}_{0.9}\text{Ba}_{0.1}\text{F}_{2.9}$. The non-annealed sample shows the highest conductivity. Annealing causes grain growth and a continuous decrease in overall conductivity, at least for powder samples. Most likely, heat treatment also affects the structure of interfacial regions of the nm-sized grains.

In Fig. 4 b) the electrical modulus is shown *vs.* frequency. The broad peaks are composed of at least two sub-peaks with comparable amplitude. The sub-peaks are separated by 1 to 2 orders of magnitude on the frequency scale. They are in agreement with the above-mentioned slight curvature in the dispersive region of the conductivity isotherms, see Fig. 3 a) and b). Plotting the electrical relaxation frequencies of the modulus peaks $M''(v)$ as a function of the inverse temperature yields activation energies, for both processes, of approximately 0.44 eV (see Fig. S1). As this value is lower than that probed by σ_{dc} in the limit $v \rightarrow 0$, we assume that the number density of mobile charge carriers, to which σ_{dc} is directly proportional, increases with temperature. This behavior is clearly supported by ^{19}F NMR line shapes, which visualize the heterogeneous nature of ion dynamics in $\text{La}_{0.9}\text{Ba}_{0.1}\text{F}_{2.9}$ by bringing the temperature-dependent number fraction of mobile F anions to light that mainly contribute to σ_{dc} , see below.

The effect of heat treatment on ionic conductivity in nanocrystalline $\text{La}_{0.9}\text{Ba}_{0.1}\text{F}_{2.9}$ is shown in Fig. 4 c). While the non-annealed sample shows the highest conductivity, annealing the powder samples reduces $\sigma_{DC}T$. Grain growth as well as re-crystallization of the originally disordered interfacial regions could explain the decrease in transport properties observed. Obviously, the formation of structurally ordered grain boundaries and the associated reduction of the volume fraction of these regions as a result of grain growth has no

positive effect on ion dynamics. As expected, the sample treated for 5 h at 1073 K, which shows a considerable amount of La-rich BaF₂ crystallizing with cubic symmetry, has to be characterized by the lowest conductivity and highest activation energy. Sintering of pressed pellets, as has been shown by Chable *et al.* [34], results boosts conductivity leading to values comparable to those seen for single crystals. The combination of sintering and pressure forms g.b. regions being non-blocking for the F anions.

¹⁹F NMR spectroscopy

Spin-lattice relaxation. Fig. 5 a) uses an Arrhenius presentation to give an overview of the variable-temperature ¹⁹F SLR and spin-lock NMR relaxation rates measured. In Fig. 5 b) only the rates of nanocrystalline La_{0.9}Ba_{0.1}F_{2.9} are shown.

Below 285 K spin-lattice relaxation of nanocrystalline LaF₃ and BaF₂ is caused by non-diffusive effects. The rate 1/T₁ reveals a so-called weaker-than-activated SLR background, they barely depend on temperature at temperatures below 250 K. The same holds for nanocrystalline La_{0.9}Ba_{0.1}F_{2.9}. In contrast to the binaries the ¹⁹F SLR NMR rates start to increase just slightly above room temperature passing into the low-temperature flank of a 1/T₁(1/T) peak. The same increase is seen for LaF₃ and BaF₂ but shifted towards much higher *T*. This finding clearly supports our results from conductivity measurements and shows a significant increase in F anion self-diffusivity for the solid solution.

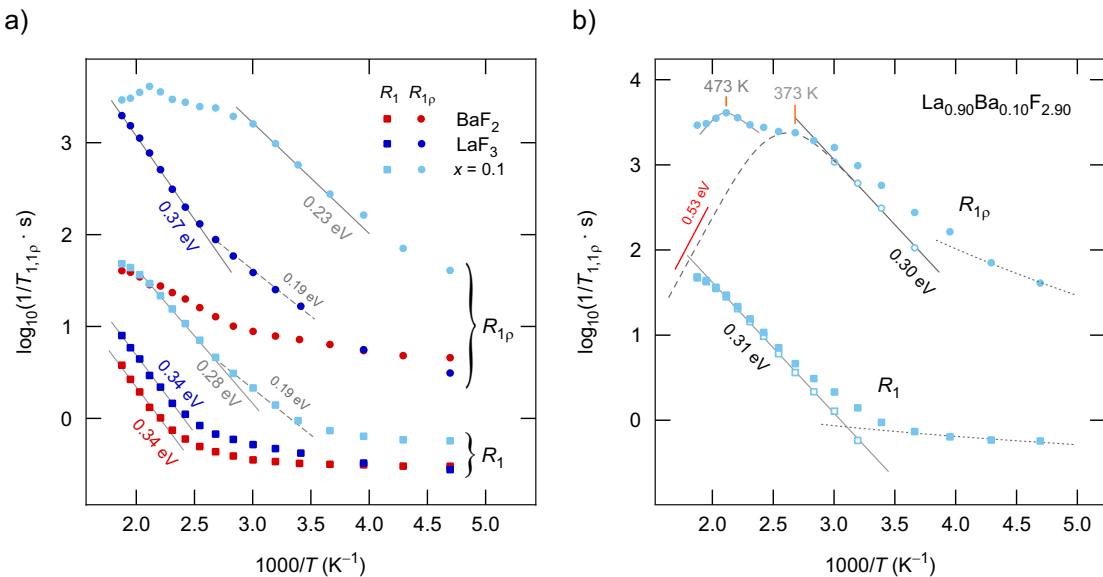


Fig. 5 a) Temperature dependence of the ¹⁹F NMR SLR rates 1/T₁ (282.0 MHz) and 1/T_{1p} (100 kHz) of nanocrystalline LaF₃, BaF₂ and La_{0.9}Ba_{0.1}F_{2.9}. The nanocrystalline samples were prepared by high-energy ball milling; the milling time was 10 h. b) Analysis of the ¹⁹F SLR NMR rates of La_{0.9}Ba_{0.1}F_{2.9} shown in a). The dashed lines show fits with a power law to extrapolate non-diffusive background rates to higher *T* and to calculate 1/T_{1(p)diff}. Solid lines represent Arrhenius fits to extract activation energies from the rates 1/T_{1(p)diff} rates. For both techniques, rather similar activation energies are obtained *viz.* 0.3 eV and 0.31 eV, respectively.

In order to separate non-diffusive background relaxation from purely diffusion-induced contributions, we approximated the low- T background rates with a suitable power law, $1/T_{1,\text{bgr}} \propto T^\beta$, and extrapolated the rates to higher temperatures [65, 66]. For $\text{La}_{0.9}\text{Ba}_{0.1}\text{F}_{2.9}$ this procedure is exemplarily shown in Fig. 5 b) where the dashed line represents the approximation with a power law. Afterwards we subtracted the background rates from the overall ones to obtain purely diffusion-induced SLR rates $1/T_{1,\text{diff}}$ (unfilled symbols in Fig. 5 b)). $1/T_{1,\text{diff}}$ of $\text{La}_{0.9}\text{Ba}_{0.1}\text{F}_{2.9}$ follows Arrhenius behavior which is characterized by an activation energy of 0.31 eV. This activation energy reflects short-ranged F anion dynamics and is expected to be influenced by correlation effects. The value obtained without background correction is 0.28 eV, see Fig. 5a). For comparison, for both nanocrystalline LaF_3 and nanocrystalline BaF_2 the activation energy turned out to be 0.34 eV. This value is in close agreement to that reported by Heitjans and Indris (0.32 eV) [66]; they investigated nanocrystalline BaF_2 which was prepared by a shaker mill. For coarse-grained BaF_2 the activation energy extracted from diffusion-induced R_1 ^{19}F NMR rates turned out to be much higher viz. 1.02 eV [66] illustrating the effect of interfacial regions in nanomaterials on ion dynamics [9].

Worth noting, LaF_3 shows slightly higher absolute NMR SLR rates (see Fig. 5 a). This behavior is even more pronounced for $1/T_{1,\text{diff}}$ of nanocrystalline $\text{La}_{0.9}\text{Ba}_{0.1}\text{F}_{2.9}$ as the rate peak is significantly shifted toward lower T . As can be seen at the highest temperatures, $1/T_{1,\text{diff}}$ already reaches the beginning of the diffusion-induced rate peak. We expect the maximum in $1/T_{1,\text{diff}}(1/T)$ at approximately 575 K. Due to the heat sensitivity of the nanocrystalline samples we restricted the measurements to temperatures below 550 K. The difference in activation energy of 0.02 eV when going from $x = 0$ to $x = 0.1$ is relatively small. As we have recently pointed out for nanocrystalline $(\text{Ba},\text{Ca})\text{F}_2$ the shift of the $1/T_{1,\text{diff}}$ -flank toward lower T is, most likely, also associated with an increase in the pre-factor $1/\tau_0$ of the underlying Arrhenius relation $1/\tau = 1/\tau_0 \exp(-E_a/(k_B T))$ where $1/\tau$ represents the F anion jump rate. Presumably, in $\text{La}_{0.9}\text{Ba}_{0.1}\text{F}_{2.9}$, being rich in F vacancies, entropy effects are responsible for the increase in $1/\tau_0$ and thus the number of F jumps per time unit.

Besides $1/T_1$ measurements we used spin-lock NMR to collect information about F motions on a longer time scale. ^{19}F T_{1p} NMR SLR rates in the rotating frame were carried out at locking frequencies much smaller than the Larmor frequency used to acquire the R_1 rates. As expected, the low- T flank of the $R_{1p}(1/T)$ peaks of nanocrystalline LaF_3 and $\text{La}_{0.9}\text{Ba}_{0.1}\text{F}_{2.9}$ are shifted toward much lower T , see Fig. 5 a) [5, 39, 67]. When comparing $R_1(1/T)$ and $R_{1p}(1/T)$ of nanocrystalline LaF_3 we see that above 400 K both techniques yields very similar activation energies of 0.34 and 0.37 eV, respectively.

Without having applied any correction procedure as described above, it is evident that below 330 K the rates R_{1p} of nanocrystalline $\text{La}_{0.9}\text{Ba}_{0.1}\text{F}_{2.9}$ reveal a weaker temperature dependence (0.23 eV) than R_1 . In this T range the spin-lock rates seem to be largely influenced by rather strong background effects. Correcting the rates for interfering effects at low T , see Fig. 5 b), yields $E_a = 0.30$ eV, being comparable with the corrected value obtained for $R_{1,\text{diff}}$. It is evident from Fig. 5 that the increase in F self-diffusivity, when going from LaF_3 to $\text{La}_{0.9}\text{Ba}_{0.1}\text{F}_{2.9}$ is mainly reflected by an increase in absolute NMR SLR rates, *i.e.*, the shifts of the corresponding flanks of the $R_{1(p)}(1/T)$ peaks toward lower T rather than a significant decrease in E_a characterizing short-ranged motions. Hence, also on the local length scale the pre-factor of the Arrhenius equation plays a prominent role to explain the boost in diffusivity seen.

R_{1p} of nanocrystalline BaF₂ plays a special role. The absolute increase of R_{1p} above 350 K turned out to be rather small. Therefore, the overall rates in this temperature regime are still dominated by the rather strong non-diffusive background effects. Background correction roughly yields $E_a = 0.2$ eV. This value is in agreement with those seen for $R_{1(p)}$ at intermediate temperatures.

Most importantly, E_a extracted from $R_{1(p)}$ of LaF₃ and La_{0.9}Ba_{0.1}F_{2.9} reflects local barriers seen by the F anions including correlated jump processes between neighboring sites. Thus, E_a from NMR in this temperature range should be comparable to results from AC impedance spectroscopy carried out at sufficiently high frequencies being in the range of the Larmor frequency of 282 MHz. Indeed, if we read off conductivities measured at 274 MHz, we obtain $E_a \approx 0.3$ eV (see Fig. S1) being in line with the value from nuclear spin relaxation measurements. Taken together, while F anion transport in La_{0.9}Ba_{0.1}F_{2.9} is characterized by 0.53 eV on a long-range length scale, short-range motions are governed by an activation energy of 0.31 eV if we use E_a extracted from $R_{1,\text{diff}}$ for this comparison. As a consequence, we would expect a highly asymmetric $R_{1,\text{diff}}(1/T)$ peak with the flank on the high- T side being characterized by 0.53 eV. This expectation is illustrated in Fig. 5 b); the maximum of the peak is located at 373 K. The ratio $\alpha - 1 = 0.31/0.53 \approx 0.58$ would correspond to $\alpha \approx 1.58$, which is the frequency dependence of the R_1 rate in the low- T limit, *i.e.*, in the regime where $\omega_0\tau_c \gg 1$. $\alpha = 2$ would correspond to uncorrelated (3D) motion, as predicted by BPP theory [68, 69]. Values $\alpha < 2$ are expected for structurally disordered materials with correlation effects influencing the motional processes taking place [6, 67]. Ignoring background relaxation does not change $\alpha - 1$ much, we obtain 0.28/0.53 ≈ 0.53. The R_1 rates following the Arrhenius line characterized by 0.19 eV (see the rates just above room temperature in Fig. 5 a)) might correspond to the ionic conductivities thermally activated by 0.38 eV (see Fig. 3 b)); for α we obtain $1 + (0.19/0.38) = 1.5$. In general, α also determines the shape of the underlying motional correlation function characterizing 3D diffusion in nanocrystalline La_{0.9}Ba_{0.1}F_{2.9}. $\alpha - 1 = 0.5$ points to non-exponential correlation functions, which in many cases are approximated by stretched exponentials.

At the rate maximum the condition $\omega_0\tau_c \approx 0.5$ holds, which can be used to estimate the mean motional correlation time τ_c that is expected to be within a factor of 2 identical with the residence time τ , see above. With $\omega_0 = 100$ kHz we obtain a mean jump rate of 1.3×10^6 s⁻¹. This value can be translated into a self-diffusion coefficient D_{NMR} of 1.9×10^{-14} m²s⁻¹ via the Einstein-Smoluchowski equation $D = a^2/(6\tau_c)$, where a denotes the average jump distance of approximately 3 Å. By means of the Nernst-Einstein relation, $D_\sigma = \sigma_D c k_B T / (q^2 N)$, where q is the charge of the F anions and N the number density of charge carriers, we estimated that the solid-state diffusion coefficient of D_σ (373 K) is in the order of 0.8×10^{-14} m²s⁻¹, which agrees very well with D_{NMR} . Hence, the maximum of the $R_{1p}(1/T)$ peak reflects long-range ion transport in the solid solution. The remaining difference between D_σ and D_{NMR} can be explained by the correlation factor f ($0 < f \leq 1$) and the Haven ratio H_R connecting the two diffusion coefficients according to the relation $D_{\text{NMR}} = (H_R/f)D_\sigma$ [48].

NMR spectra. Static ¹⁹F NMR lines, shown in Fig. 6 a) to c), reveal how homonuclear magnetic ¹⁹F-¹⁹F dipole-dipole interactions are averaged through sufficiently rapid ionic movements. The faster the F anion

the more effective dipolar interactions get eliminated. In formidable cases one is also able to exclusively study the fast ions separated from the slow spin reservoir.

As has been described earlier for nanocrystalline CaF_2 [6], which was prepared by inert gas condensation, the static ^{19}F NMR spectra are composed of a broad Gaussian and a sharp Lorentzian-shaped line. The same feature is found for nanocrystalline BaF_2 if we regard the spectra at high temperatures, see Fig. 6 a). The small tip on top of the broad line has been assigned to those ions residing in the interfacial regions of the nm-sized crystallites. Diffusion in these regions turned out to be much faster than that in the bulk regions. At 373 K, these ions are, however, still too slow to affect the line shape. In contrast, in $\text{La}_{0.9}\text{Ba}_{0.1}\text{F}_{2.9}$ most of the ions in the bulk regions are sufficiently mobile to eliminate dipole-dipole broadening already at 473 K. Heating the sample up to 473 K reveals that a ^{19}F NMR line is obtained which is almost identically equal to that seen in the extreme regime of narrowing (573 K), *i.e.*, the overall line is dominated by those F anions being mobile with respect to the NMR time scale. Roughly speaking, and comparing nanocrystalline $\text{La}_{0.9}\text{Ba}_{0.1}\text{F}_{2.9}$ with LaF_3 (see Figure 6 b) and c)), for the vacancy-rich solid solution the onset of motional averaging is shifted by at least 100 K toward lower T . Careful inspection of the ^{19}F NMR lines of $\text{La}_{0.9}\text{Ba}_{0.1}\text{F}_{2.9}$ shows that line narrowing already starts at temperatures as low as 293 K. The considerably larger number fraction of mobile anions in the cation-mixed solid solution, as compared to the educts, causes the overall ion conductivity (see Fig. 3 b)) to increase by several orders of magnitude. Thus, fast ion dynamics on the angstrom length scale, as seen by SLR NMR, triggers long-range ion transport that is characterized by 0.53 eV.

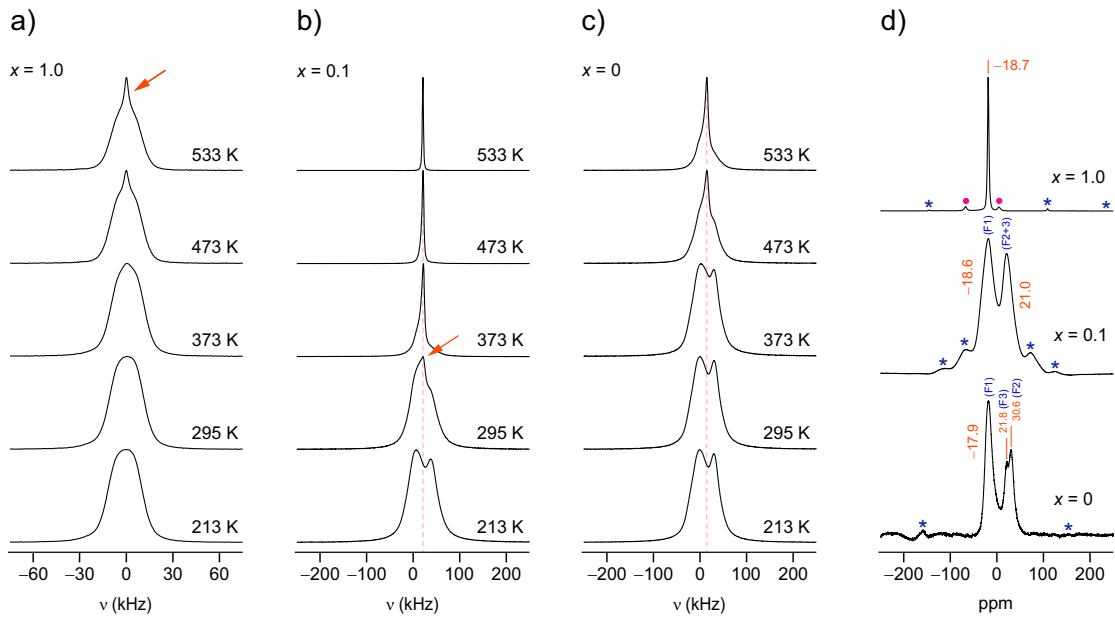


Fig. 6 a) to c) Variable-temperature ^{19}F NMR spectra of $\text{La}_{1-x}\text{B}_{\text{x}}\text{F}_{3-x}$, recorded at $T = 282$ MHz under static conditions, *i.e.*, non-MAS conditions. For $x = 0.1$, motional narrowing already starts at 295 K corroborating fast ionic conduction as seen by impedance spectroscopy. A narrow line emerges at the centre of the NMR signal; the line recorded at 373 K definitely reveals heterogeneous ion dynamics with slow and fast F anions. With increasing T the number fraction of mobile F anions continuously increases. The rigid-lattice line (231 K) of $\text{La}_{0.9}\text{Ba}_{0.1}\text{F}_{2.9}$ reveals two signals that reflect

the magnetically inequivalent F sites (F1 and F2, F3), see d). d) ^{19}F MAS NMR spectra of nanocrystalline LaF_3 , $\text{La}_{0.9}\text{Ba}_{0.1}\text{F}_{2.9}$ and BaF_2 . Spectra were recorded at 303 K and at spinning speeds of 60 kHz ($x = 0$ and $x = 1.0$) respectively 25 kHz ($x = 0.1$). Asterisks indicate the various spinning sidebands. The spectra were referenced to LiF (-204.3 ppm). Dots mark orthorhombic BaF_2 , which is formed when cubic BaF_2 is mechanically treated in ball mills.

High-resolution ^{19}F NMR spectra of nanocrystalline LaF_3 and BaF_2 , prepared by milling for 10 h, are shown in Figure 6 d). The corresponding spectrum of nanocrystalline $\text{La}_{0.9}\text{Ba}_{0.1}\text{F}_{2.9}$ is also shown. ^{19}F MAS NMR of nanocrystalline BaF_2 reveals a line at $\delta_{\text{iso}} = -18.7$ ppm, which belongs to cubic BaF_2 , and two lines with low intensity which indicate the formation of a small amount of orthorhombic BaF_2 . Compared to coarse-grained BaF_2 the line of cubic- BaF_2 is lightly broader because of structural disorder and strain introduced during ball milling. The isotropic chemical shift δ_{iso} is, however, almost unchanged. In principle, the same is true for nanocrystalline LaF_3 whose spectrum is composed of three lines reflecting the magnetically inequivalent positions F1, F2 and F3, respectively.

The line with the highest intensity, which shows up at -17.9 ppm, represents the anions residing on the F1 positions located between the Ba-La sub-lattices. The lines at 21.8 and 30.6 ppm reflect anions on the F2 and F3 positions in the sublattices (see Fig. 1). Turning to the NMR spectrum of nanocrystalline $\text{La}_{0.9}\text{Ba}_{0.1}\text{F}_{2.9}$ we see two broader lines. The lines belonging to F2 and F3 cannot be distinguished from each other because of the La-Ba disorder introduced that leads to distributions of chemical shifts. The changes in intensity of the lines assigned to F1 and F2/F3, as compared to the initial situation with $x = 0$, as well as the slight shift of δ_{iso} can be explained by the interplay of both the aliovalent replacement of La by Ba and the onset of coalescence effects on the NMR lines. Note that the ^{19}F MAS NMR spectra have been recorded near room temperature. For comparison, at 295 K the static line already starts to change with respect to that observed in the rigid lattice regime. The decrease in intensity of the F1 line might also be affected by the generation of F vacancies on the F1 positions.

As has been pointed out by Grey and co-workers by using variable-temperature MAS ^{19}F NMR, in LaF_3 the F1-F1 exchange is, from an energetic point of view, slightly preferred against possible F1-F2/3 exchange processes [45]. The motionally narrowed line seen in our static NMR lines, whose position agrees with the center of the total NMR signal, reveals that all three sites participate in overall anion exchange in nano- $\text{La}_{0.9}\text{Ba}_{0.1}\text{F}_{2.9}$. This finding is at least valid for temperatures higher than 473 K.

Electrochemical measurements

Battery applications of solid electrolytes require materials with negligible electronic conductivity and a sufficiently high electrochemical stability. Here we used polarization measurements to estimate the electronic conductivity of nanocrystalline $\text{La}_{0.9}\text{Ba}_{0.1}\text{F}_{2.9}$; cyclic voltammetry was employed to shed light on possible redox processes taking place between -3 V and 2 V. In Fig. 7 a) the result of a DC polarization experiment, carried out at a potential of 1.5 V at 473 K, is shown.

At the beginning of electrical polarization, both ions and electrons contribute to the overall conductivity of the sample. The ion-blocking electrodes applied generate an F anion concentration gradient. With increasing time the contribution of ionic species to the total conductivity continuously decreases until a

constant current plateau I_{final} is reached which solely corresponds to electronic conduction. This final electronic conductivity can be calculated via $\sigma_{\text{el}} = I_{\text{final}}/V \cdot d/(r^2\pi)$, where d denotes the thickness of the tablet and r its radius. In our case a steady-state current is reached within a short time period of less than 2 h (see Fig. 7 a)), which results in $\sigma_{\text{el}} = 1.6 \times 10^{-7} \text{ S cm}^{-1}$. Since the overall conductivity σ_{dc} of $\text{La}_{0.9}\text{Ba}_{0.1}\text{F}_{2.9}$ determined by impedance spectroscopy in the dc limit is $\sigma_{\text{dc}} = 3.8 \times 10^{-4} \text{ S cm}^{-1}$ the ionic conductivity the ternary fluoride is by three orders of magnitude higher and σ_{el} has a negligible effect on σ_{dc} , *i.e.*, the transference number t_{ion} of nanocrystalline $\text{La}_{0.9}\text{Ba}_{0.1}\text{F}_{2.9}$ is close to 1.

On the right-hand side of Fig. 7 b) the cyclic voltammograms of the sample characterized by $x = 0.1$ are shown that have been recorded at 473 K and at scanning rates ranging from 0.1 to 1 V/s. The CVs reveal relatively low currents; nevertheless, as no sharp peaks show up it is difficult to ultimately state whether redox reactions occurs or not. Fortunately, the changes of the overall shape noticeable turn out to be marginal indicating reversible processes taking place. This fact, along with the negligible electrical conductivity, makes $\text{La}_{0.9}\text{Ba}_{0.1}\text{F}_{2.9}$ indeed a highly suitable solid electrolyte being able to function in a high-temperature fluorine battery.

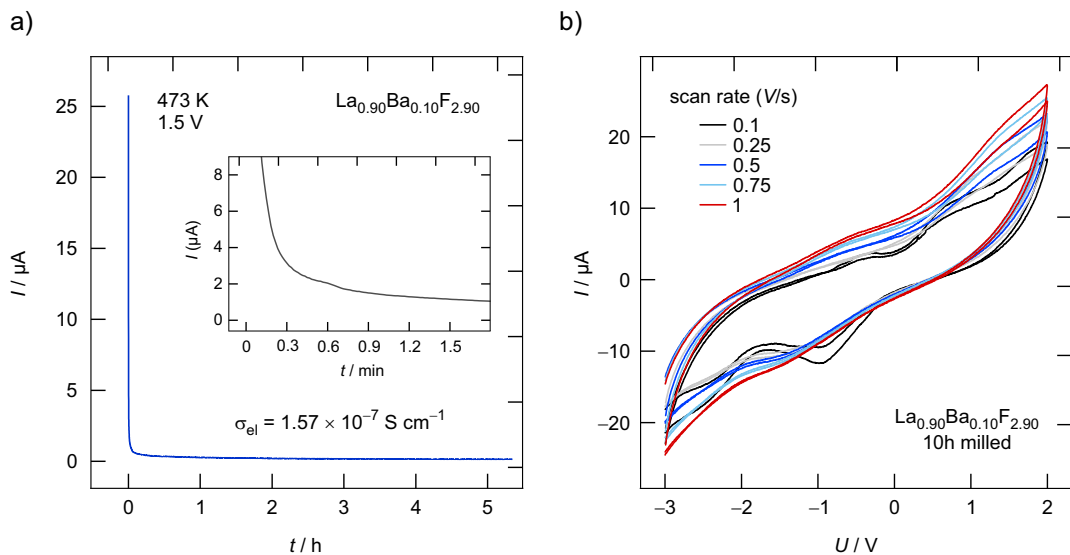


Fig. 7 a) Potentiostatic polarization curve recorded for nanocrystalline $\text{La}_{0.9}\text{Ba}_{0.1}\text{F}_{2.9}$. The current response was measured at 473 K with a symmetrical cell configuration. A steady-state current is reached within two hours leading to a very small electrical conductivity in the order of $10^{-7} \text{ S cm}^{-1}$. b) Electrochemical stability of the sample characterized by $x = 0.1$ as tested via cyclic voltammetry in the potential range from -3 V to 2 V. The scan rate varied from 0.1 to 1.0 V/s. Inset: Change of I during the first minutes.

Summary and conclusion

We used broadband conductivity measurements and ^{19}F solid-state NMR spectroscopy to shed light on the dynamic processes in nanocrystalline $\text{La}_{0.9}\text{Ba}_{0.1}\text{F}_{2.9}$, which has directly been prepared by a mechanochemical approach. In agreement with literature, we see that F anion transport significantly increases with increasing

Ba content reaching approximately 10^{-6} S cm $^{-1}$ at 330 K, which is an increase by 4 orders of magnitude compared to nanocrystalline LaF₃. Conductivity spectroscopy revealed two electrical relaxation processes with activation energies of 0.53 eV and 0.38 eV, respectively. While the associated capacities point to bulk responses, we think that the main transport process (0.53 eV) is influenced by the structurally disordered interfacial regions of the nanocrystalline sample. Importantly, the study provides one step further to understand the significant differences seen between nanostructured samples and single crystals. As we discovered a highly conductive transport process with an activation energy being very similar to that known for single crystals, a greatly decreased pre-factor seems to explain the astonishing difference rather than distinctly lower activation energies.

Through laboratory-frame ¹⁹F NMR spin-lattice relaxation we were able to look at ion dynamics on the angstrom length scale. For La_{0.9}Ba_{0.1}F_{2.9} activation energies, characterizing ion dynamics, turned out to be 0.31 eV. AC conductivities recorded at 270 MHz, that is, at the same frequency used to sample the NMR rates, point to a very similar activation energy of 0.3 eV. Hence, ion transport in nanocrystalline La_{0.9}Ba_{0.1}F_{2.9} turned out to be clearly length-scale dependent. For comparison, values of 0.3 eV are comparable to sintered, grain-boundary optimized La_{0.9}Ba_{0.1}F_{2.9} as studied by Chable *et al.* [34].

Interestingly, although single crystalline La_{0.9}Ba_{0.1}F_{2.9} shows much higher conductivities, sintering of our powder samples always lead to a decrease in ionic conductivity. The behaviour is different when pressed pellets were sintered [34]. At least if annealing at 1000 K is regarded, grain growth and the associated reduction of the volume fraction of grain boundaries blocks long-range ion transport in powder samples. Obviously, through-going ionic transport in polycrystalline, cold-pressed La_{0.9}Ba_{0.1}F_{2.9} is chiefly influenced by the morphology of the interfacial regions. Interfacial regions when characterized by structural disorder, as introduced during mechanical treatment, seem to be beneficial for ion transport in nanocrystalline La_{0.9}Ba_{0.1}F_{2.9}.

Acknowledgements. Financial support by the Austrian Federal Ministry for Digital and Economic Affairs and the National Foundation for Research, Technology and Development is gratefully acknowledged. We also thank the Deutsche Forschungsgemeinschaft (FOR1277, WI 3600 2-1, 4-1; SPP 1415 WI 3600 5-2) and the FFG (project safe battery) for financial support.

References

- [1] K. Funke, Sci. Technol. Adv. Mat., 14 (2013) 043502.
- [2] P. Knauth, Solid State Ion., 180 (2009) 911-916.
- [3] P. Heitjans, S. Indris, J. Phys.: Condens. Matter, 15 (2003) R1257-R1289.
- [4] J. Maier, Chem. Mater., 26 (2014) 348-360.
- [5] H. Mehrer, Diffusion in Solids, Springer Berlin, 2006.

- [6] P. Heitjans, A. Schirmer, S. Indris, in: P. Heitjans, J. Kärger (Eds.) *Diffusion in Condensed Matter – Methods, Materials, Models*, Springer, Berlin, 2005, pp. 367-415.
- [7] M. Wilkening, A. Kuhn, P. Heitjans, *Phys. Rev. B*, 78 (2008).
- [8] B. Stanje, D. Rettenwander, S. Breuer, M. Uitz, S. Berendts, M. Lerch, R. Uecker, G. Redhammer, I. Hanzu, M. Wilkening, *Ann. Phys.*, 529 (2017) 1700140.
- [9] D. Prutsch, S. Breuer, M. Uitz, P. Bottke, J. Langer, S. Lunghammer, M. Philipp, P. Posch, V. Pregartner, B. Stanje, A. Dunst, D. Wohlmuth, H. Brandstatter, W. Schmidt, V. Epp, A. Chadwick, I. Hanzu, M. Wilkening, *Z. Phys. Chem.*, 231 (2017) 1361-1405.
- [10] M. Guin, F. Tietz, *J. Power Sources*, 273 (2015) 1056-1064.
- [11] Z. Zhang, Y. Shao, B. Lotsch, Y.-S. Hu, H. Li, J. Janek, L.F. Nazar, C.-W. Nan, J. Maier, M. Armand, L. Chen, *Energy. Environ. Sci.*, (2018) doi: 10.1039/C1038EE01053F, in press.
- [12] J. Janek, W.G. Zeier, *Nat. Energy*, 1 (2016) 16141.
- [13] B. Zhang, R. Tan, L. Yang, J. Zheng, K. Zhang, S. Mo, Z. Lin, F. Pan, *Energy Storage Mater.*, 10 (2018) 139-159.
- [14] W. Schmidt, P. Bottke, M. Sternad, P. Gollob, V. Hennige, M. Wilkening, *Chem. Mater.*, 27 (2015) 1740-1750.
- [15] P. Bottke, D. Rettenwander, W. Schmidt, G. Amthauer, M. Wilkening, *Chem. Mater.*, 27 (2015) 6571-6582.
- [16] M.S. Whittingham, *Chem. Rev.*, 104 (2004) 4271-4301.
- [17] J.B. Goodenough, Y. Kim, *Chem. Mater.*, 22 (2010) 587-603.
- [18] J.B. Goodenough, *Acc. Chem. Res.*, 46 (2013) 1053-1061.
- [19] J.B. Goodenough, K.-S. Park, *J. Am. Chem. Soc.*, 135 (2013) 1167-1176.
- [20] L.W. Ji, Z. Lin, M. Alcoutlabi, X.W. Zhang, *Energy. Environ. Sci.*, 4 (2011) 2682-2699.
- [21] M.S. Whittingham, *Chem. Rev.*, 114 (2014) 11414-11443.
- [22] M. Anji Reddy, M. Fichtner, *J. Mater. Chem.*, 21 (2011) 17059-17062.
- [23] A. Grenier, A.G. Porras-Gutierrez, M. Body, C. Legein, F. Chrétien, E. Raymundo-Piñero, M. Dollé, H. Grout, D. Dambourret, *J. Phys. Chem. C*, 121 (2017) 24962-24970.
- [24] J.C. Bachman, S. Muy, A. Grimaud, H.H. Chang, N. Pour, S.F. Lux, O. Paschos, F. Maglia, S. Lupart, P. Lamp, L. Giordano, Y. Shao-Horn, *Chem. Rev.*, 116 (2016) 140-162.
- [25] V. Thangadurai, S. Narayanan, D. Pinzaru, *Chem. Soc. Rev.*, 43 (2014) 4714-4727.
- [26] S. Chen, D. Xie, G. Liu, J.P. Mwizerwa, Q. Zhang, Y. Zhao, X. Xu, X. Yao, *Energy Storage Mater.*, 14 (2018) 58-74.

- [27] Y. Wang, W.D. Richards, S.P. Ong, L.J. Miara, J.C. Kim, Y.F. Mo, G. Ceder, *Nat. Mater.*, 14 (2015) 1026-1031.
- [28] C. Rongeat, M.A. Reddy, R. Witter, M. Fichtner, *J. Phys. Chem. C*, 117 (2013) 4943-4950.
- [29] C. Rongeat, M.A. Reddy, R. Witter, M. Fichtner, *ACS Appl. Mater. Interfaces*, 6 (2014) 2103-2110.
- [30] F. Gschwind, G. Rodriguez-Garcia, D.J.S. Sandbeck, A. Gross, M. Weil, M. Fichtner, N. Hörmann, *J. Fluorine Chem.*, 182 (2016) 76-90.
- [31] L.N. Patro, K. Hariharan, *Solid State Ion.*, 239 (2013) 41-49.
- [32] L.N. Patro, K. Hariharan, *Mater. Lett.*, 80 (2012) 26-28.
- [33] L.N. Patro, K. Hariharan, *Mater. Res. Bull.*, 46 (2011) 732-737.
- [34] J. Chable, B. Dieudonne, M. Body, C. Legein, M.-P. Crosnier-Lopez, C. Galven, F. Mauvy, E. Durand, S. Fourcade, D. Sheptyakov, M. Leblanc, V. Maisonneuve, A. Demourgues, *Dalton. Trans.*, 44 (2015) 19625-19635.
- [35] B. Dieudonné, J. Chable, F. Mauvy, S. Fourcade, E. Durand, E. Lebraud, M. Leblanc, C. Legein, M. Body, V. Maisonneuve, A. Demourgues, *J. Phys. Chem. C*, 119 (2015) 25170-25179.
- [36] A. Düvel, B. Ruprecht, P. Heitjans, M. Wilkening, *J. Phys. Chem. C*, 115 (2011) 23784-23789.
- [37] A. Düvel, S. Wegner, K. Efimov, A. Feldhoff, P. Heitjans, M. Wilkening, *J. Mater. Chem.*, 21 (2011) 6238-6250.
- [38] F. Preishuber-Pflügl, M. Wilkening, *Dalton. Trans.*, 43 (2014) 9901-9908.
- [39] F. Preishuber-Pflügl, P. Bottke, V. Pregartner, B. Bitschnau, M. Wilkening, *Phys. Chem. Chem. Phys.*, 16 (2014) 9580-9590.
- [40] F. Preishuber-Pflügl, V. Epp, S. Nakhal, M. Lerch, M. Wilkening, *Phys. Status Sol. C*, 12 (2015) 10-14.
- [41] F. Preishuber-Pflügl, M. Wilkening, *Dalton. Trans.*, 45 (2016) 8675-8687.
- [42] M. Wilkening, A. Düvel, F. Preishuber-Pflügl, K. da Silva, S. Breuer, V. Šepelák, P. Heitjans, Z. Krist.-Cryst. Mater., 232 (2016) 107-127.
- [43] S. Breuer, B. Stanje, V. Pregartner, S. Lunghammer, I. Hanzu, M. Wilkening, *Crystals*, 8 (2018) 122.
- [44] A.F. Privalov, A. Cenian, F. Fujara, H. Gabriel, I.V. Murin, H.M. Vieth, *J. Phys.: Condens. Matter*, 9 (1997) 9275.
- [45] F. Wang, C.P. Grey, *Chem. Mater.*, 9 (1997) 1068-1070.
- [46] N.I. Sorokin, B.P. Sobolev, *Phys. Solid State*, 50 (2008) 416-421.
- [47] S. Lunghammer, Q. Ma, D. Rettenwander, I. Hanzu, F. Tietz, H.M.R. Wilkening, *Chem. Phys. Lett.*, 701 (2018) 147-150.

- [48] M. Uitz, V. Epp, P. Bottke, M. Wilkening, *J. Electroceram.*, 38 (2017) 142-156.
- [49] A. Düvel, J. Bednarcik, V. Šepelák, P. Heitjans, *J. Phys. Chem. C*, 118 (2014) 7117-7129.
- [50] M. Wilkening, P. Heitjans, *ChemPhysChem*, 13 (2012) 53-65.
- [51] E. Fukushima, S. B. W. Roeder, *Experimental Pulse NMR*, Addison-Wesley, Reading, 1981.
- [52] D. Ailion, C.P. Slichter, *Physical Review Letters*, 12 (1964) 168-171.
- [53] C.P. Slichter, D. Ailion, *Physical Review*, 135 (1964) A1099-A1110.
- [54] D.C. Look, I.J. Lowe, *Journal of Chemical Physics*, 44 (1966) 2995-3000.
- [55] R.D. Shannon, *Acta Crystallographica Section A*, 32 (1976) 751-767.
- [56] A.K. Jonscher, *Nature*, 267 (1977) 673-679.
- [57] S. Breuer, M. Wilkening, *Dalton. Trans.*, 47 (2018) 4105-4117.
- [58] K.L. Ngai, *Relaxation and diffusion in complex systems*, Springer, New York, 2011.
- [59] J. Habasaki, K.L. Ngai, *J. Phys. Chem. C*, 121 (2017) 13729-13737.
- [60] K. Funke, R.D. Banhatti, C. Cramer, *Phys. Chem. Chem. Phys.*, 7 (2005) 157-165.
- [61] K. Funke, I. Ross, R.D. Banhatti, *Solid State Ion.*, 175 (2004) 819-822.
- [62] B. W., *Phys. Status Sol. A*, 18 (1973) 313-321.
- [63] S. Breuer, S. Lunghammer, A. Kiesl, M. Wilkening, *J. Mater. Sci.*, (2018) doi: 10.1007/s10853-10018-12361-x, in press.
- [64] J.T.S. Irvine, D.C. Sinclair, A.R. West, *Adv. Mater.*, 2 (1990) 132-138.
- [65] M. Wilkening, S. Indris, P. Heitjans, *Phys. Chem. Chem. Phys.*, 5 (2003) 2225-2231.
- [66] P. Heitjans, S. Indris, *Journal of Materials Science*, 39 (2004) 5091-5096.
- [67] M. Wilkening, P. Heitjans, *ChemPhysChem*, 13 (2012) 53-65.
- [68] N. Bloembergen, E.M. Purcell, R.V. Pound, *Nature*, 160 (1947) 475-476.
- [69] N. Bloembergen, E.M. Purcell, R.V. Pound, *Phys. Rev.*, 73 (1948) 679-712.

3.3 Nanokomposite mit zwei mobilen Ladungsträger-Spezies

Neben der anwendungsorientierten Forschung, die sich intensiv mit der Suche nach einsetzbaren Materialien für Sensoren oder Energiespeichersysteme beschäftigt, ist auch die grundlagenorientierte Forschung von großer Bedeutung. Dabei kann unter anderem ein genauer Blick auf die Beziehungen der Struktureigenschaften einzelner Komponenten in *mehrphasigen* Festkörpersystemen geworfen werden.

Materialien die zwei Arten von beweglichen Ladungsträgern enthalten, also zum Beispiel sowohl Li als auch F Ionen besitzen, sind perfekt als Modellsysteme für derartige Fragestellungen geeignet. Durch getrennte Analyse der einzelnen Spezies und anschließender Gegenüberstellung der Ergebnisse soll der Frage nachgegangen werden, ob die ionische Bewegung der beiden mobilen Spezies gekoppelt ist.³² und in welcher Weise Isolator-Ionenleiter-Grenzflächen die makroskopischen, dynamischen Eigenschaften bestimmen. Der disperse Ionenleiter LiF:Al₂O₃ dient als Modellsystem für Impedanz- und NMR-Untersuchungen.

3.3.1 Interfacial Li ion dynamics in nanostructured LiF and LiF:Al₂O₃ composites

Das folgende, noch nicht veröffentlichte Manuskript, präsentiert eine grundlagenorientierte Arbeit, bei der ein Modellsystem mit zwei unterschiedlichen Ladungsträger-Spezies, in diesem Fall LiF beziehungsweise LiF:Al₂O₃, untersucht wurde, um grundlegende Informationen zu den Sprungprozessen in den Kristalliten und an den Korngrenzen zu erhalten. LiF ist ein sehr attraktives Material im Bereich der Materialwissenschaften, da es ein wichtiger Bestandteil des *Solid Electrolyte Interface (SEI)* in Lithium-Ionen-Batterien sowie eine Komponente von Hochleistungselektroden ist.

Nanokristalline LiF und (1-x_v)LiF:x_vAl₂O₃ (0 ≤ x_v ≤ 0.5 vol-%) Proben wurden mechanochemisch in einer Kugelmühle hergestellt und anschließend mittels Röntgendiffraktometrie strukturell untersucht. Zur Ermittlung der Gesamtleitfähigkeiten der hergestellten Verbindungen wurde die Methode der Leitfähigkeitsspektroskopie verwendet, bei der eine signifikante Erhöhung der Gesamtionenleitfähigkeit durch gemeinsame Nanostrukturierung des LiF mit einem Isolatormaterial (Al₂O₃) deutlich wurde. Die Ursache dafür liegt in der Ausbildung heterogener Grenzflächen, entlang derer sich schnelle Diffusionspfade für die mobilen Ionen ausbilden. Um die Ionendynamik beider mobiler Ladungsträger getrennt voneinander zu analysieren, wurden ionenselektive ⁷Li- und ¹⁹F-Festkörper-NMR-Messungen durchgeführt. Dabei wurden sowohl statische Spektren aufgenommen, als auch dynamische Messungen zur Bestimmung der Relaxationszeiten durchgeführt. Mit Hilfe der statischen Spektren ist es so gelungen, die dynamische Heterogenität der Proben deutlich sichtbar zu machen. Die schnelleren Ionen konnten von einem Reservoir an langsameren Ionen gut unterschieden werden. Es wurde außerdem deutlich, dass für den Anstieg der Gesamtleitfähigkeit hauptsächlich die Lithium-Ionen verantwortlich sind, die sich entlang energetisch günstiger Diffusionspfade mit niedrigen Aktivierungsenergien bewegen dürfen.

Interfacial Li ion dynamics in nanostructured LiF and LiF:Al₂O₃ composites

S. Breuer, V. Pregartner, and M. Wilkening.

in preparation

Interfacial Li ion dynamics in nanostructured LiF and LiF:Al₂O₃ composites

Stefan Breuer, Veronika Pregartner and Martin Wilkening

Institute for Chemistry and Technology of Materials, and Christian Doppler Laboratory for Lithium Batteries, Graz University of Technology (NAWI Graz), Stremayrgasse 9, 8010 Graz, Austria

Abstract. Lithium fluoride plays an important role in materials science as it is present in a range of applications, *e.g.*, as a component for high capacity electrode materials or as part of the solid electrolyte interface (SEI) in lithium ion batteries (LIBs). It also serves as a model system to study Li and F hopping processes in a material solely composed of mobile ions with opposite charge. LiF, when present in its microcrystalline form, is known to be a very poor ionic conductor. In this work we studied the effect of nanostructuring LiF on ionic conductivity and diffusivity. It is known for other materials that structural disorder and size effects are able to drastically increase overall ionic conductivity. Moreover, we prepared a so-called nanocrystalline two-phase ionic conductor by adding an insulator such as alkaline Al₂O₃. In such dispersed ionic conductors percolating pathways, generated through the conductor:insulator (LiF:Al₂O₃) contacts are formed enabling the ions to move over long distances. The study is aimed at the two following questions: i) is this insulator effect present for LiF:Al₂O₃ prepared by high-energy ball milling, and ii) is it possible to find out which of the two mobile ions benefits from this effect mostly. Indeed, we found an increase in ionic conductivity for nanocrystalline LiF. A further increase of up to three orders of magnitude is seen for 0.7LiF:0.3Al₂O₃ (vol-%). Variable-temperature NMR line shapes showed that Li diffusivity is considerably faster than F ion dynamics. For both nanocrystalline LiF and the composite our ⁷Li NMR measurements revealed heterogeneous dynamics with a fast and a slow spin reservoir indicating fast ions near the interfacial regions and slow ions in the bulk areas of the crystallites. This heterogenous dynamics manifested in so-called two-component line shapes. By comparing results from NMR relaxometry with those from conductivity measurements it comes apparent that highly correlated motions govern overall ion dynamics. Moreover, the increase in the number of highly mobile Li ions, as inferred from NMR line shapes, excellently agrees with the increase in macroscopic ionic conductivity.

Introduction

Studying the ion dynamics in highly conducting solids is a very vital topic in materials science, as these solids play an important role in numerous modern energy storage systems or sensors. Besides application-driven research, also fundamentally orientated studies are essential for a better understanding of diffusion processes in crystalline frameworks.[1-3] Currently two approaches are common to find materials featuring high ionic conductivity. One is to synthesize new compounds with enhanced conductivities and low energy barriers due to i) favorable polyhedra connections and/or ii) the introduction of frustration concerning available sites, bonds or rotational dynamics of anions surrounding the mobile cations. The other possibility is to modify the microstructure of already known materials via nanostructuring to take advantage of size effects, structural disorder or strain. In such materials ions located in or near the interfacial regions dominate dynamic properties.[4-6] In many cases the properties of nanocrystalline materials, with their large surface areas and, thus, high volume fractions of interfacial regions, considerably differ from those of their coarse-

grained counterparts. Therefore, it has early been recognized that a reduction of the grain size may open new ways to tune mechanical, electrical, optical or magnetic properties of solids.[7, 8]

Lithium fluoride turned out to be suitable model system to study the effect of structural disorder in interfacial regions on ion transport and diffusivity. Studying dynamics in nanocrystalline LiF might also be of interest for application-oriented research. LiF has been used as a component for high capacity electrode materials in lithium ion batteries[9]. Furthermore, it is a fundamental component of the solid electrolyte interface (SEI).[10] Diffusion properties of SEI components directly affect the rate performance of a battery as well as other phenomena such as capacity fading or power loss.[11]

Here, nanostructuring of LiF was achieved via high-energy ball milling of the starting material in a planetary mill for several hours. Mechanical impact and grinding reduces the crystallite size down to the nanometer range. Milling also introduces structural disorder, which is expected to result in a strong increase of the ionic conductivity. This increase has been found for several originally poor ionic conductors such as LiXO_3 ($\text{X} = \text{Nb}, \text{Ta}$) and LiAlO_2 , for example.

Besides structural disorder, mostly generated in the interfacial regions of ball milled materials, also size effects govern transport properties. Space charges zones [12, 13] represent regions offering enhanced hopping rates and low energy barriers for the ions. In so-called dispersed ion conductors, that is, mixing an ionic conductor with an insulating phase, such as alkaline Al_2O_3 , B_2O_3 or acidic SiO_2 , the conductor:insulator interface is reported to offer even faster diffusion pathways for the mobile ions.[14] In ideal cases in these materials an extended interfacial network of homo-contacts (conductor:conductor) and hetero-contacts (conductor : isolator) is present. In a pioneering work Liang reported enhanced dynamics in mesoporous $\text{LiI:Al}_2\text{O}_3$ composites[15], later similar effects have been studied on nanocrystalline ceramics by Heijmans and co-workers.[16]

Here, we extend these studies to a systems with two mobile species viz. Li^+ and F^- . NMR as well as conductivity spectroscopy are sued to study short- as well as long-range ion dynamics in mechano-synthesized, nanocrystalline LiF. The results are compared with those on $\text{LiF:Al}_2\text{O}_3$ composites. Via ^7Li and ^{19}F NMR line shape measurements we managed to identify the species which is mostly responsible for ionic conductivity in the composites.

Experimental

Nanocrystalline $(1-x_v)\text{LiF}:x_v\text{Al}_2\text{O}_3$ ($0 \leq x_v \leq 0.5$ vol-%) composites were synthesized via high-energy ball milling of the original microcrystalline materials LiF (Sigma-Aldrich, 99.98 %) and Al_2O_3 (Sigma-Aldrich, 99.99 %). We used a planetary mill (Fritsch Pulverisette 7, Premium line) and treated the mixtures for 15 h in 45 mL ZrO_2 beakers filled with 180 zirconium oxide milling balls (5 mm in diameter) and the materials. Milling was carried out at a rotational speed of 600 rpm under dry conditions. To exclude contamination with moisture or oxygen during the synthesis, the cups were filled and emptied in a glovebox with dry argon atmosphere. Phase purity of the prepared composites was checked via X-ray powder diffraction (XRPD) using a Bruker D8 Advance diffractometer that operates with Bragg Brentano geometry and Cu K_α radiation at 40 kV.

Ionic conductivities of the pressed powders were analyzed with a Novocontrol Concept 80 broadband dielectric spectrometer. We used cylindrical pellets with a diameter of 5 mm and a thickness of about 1 mm for the measurements. Pellets were uniaxially cold-pressed at a pressure of approximately 0.5 GPa. Blocking electrodes with a layer thickness of 100 nm were applied with a Leica EM SCD 050 evaporator. Conductivity spectra at frequencies ranging from 10 mHz to 10 MHz were recorded with an Alpha A frequency analyzer in connection with a ZGS active sample cell. The temperature was varied between 173 K and 453 K in the sample chamber and was controlled by a QUATRO cryo system (Novocontrol). To avoid any contamination with water or oxygen during the measurements, the pellets were dried inside the impedance cell, which was permanently flushed with freshly evaporated nitrogen gas. Specific conductivities were calculated by taking into account the cell constant, *i.e.*, the diameter and thickness of the individual pellets.

Nuclear magnetic resonance data were recorded using a Bruker Avance 300 spectrometer that was connected to a shimmed cryomagnet with a nominal magnetic field of 7 T. This field corresponds to a ${}^7\text{Li}$ Larmor frequency of $\omega_0/2\pi = 116$ MHz, and a ${}^{19}\text{F}$ Larmor frequency of 282 MHz. To study Li and F ion dynamics, line shape studies as well as spin-lattice relaxation (SLR) rate ($1/T_1$) measurements in the laboratory frame were carried out. For all NMR measurements the dry powders were fire-sealed in Duran glass tubes (ca. 4 mm in length and 3 mm in diameter) under vacuum to protect them from any impact of humidity. A home-built NMR probe, suitable to record NMR signals under static conditions in a temperature range from 193 K to 533 K, was used to record the SLR rates and the ${}^7\text{Li}$ respectively ${}^{19}\text{F}$ spectra. Temperature controlling and monitoring was realized by a Eurotherm temperature controller in combination with a type-T thermocouple. At 200 W the $\pi/2$ pulse length was approximately 2 μs for ${}^7\text{Li}$ and ca. 1 μs for ${}^{19}\text{F}$.

Static ${}^7\text{Li}$ and ${}^{19}\text{F}$ NMR spectra were obtained with a single 90° pulse experiment via Fourier transformation of the free induction decay (FID). The saturation recovery pulse sequence, used for the determination of the ($1/T_1$) rates, consisted of ten succeeding pulses that destroy any longitudinal magnetization M_z . After a delay time t_d , the reading pulse was sent to detect the recovery of M_z as a FID: $10 \times \pi/2 - t_d - \pi/2$ -acquisition (acq.)[17]. Afterwards we plotted the area under the FIDs *vs.* t_d in order to gain the magnetization transients $M_z(t_d)$. To guarantee full longitudinal relaxation between each scan the recycle delay was set to at least $5 \times T_1$. The $1/T_1$ rates were obtained by parameterizing the resulting transients $M_z(t_d)$ with stretched exponentials of the form $M_z(t_d) \propto 1 - \exp(-(t_w/T_1)^\beta)$.

Results

X-ray diffraction

The phase purity of nanocrystalline LiF and the composites with Al_2O_3 was checked via XRPD. In Fig. 1 a) X-ray powder patterns of the starting material, cubic LiF, as well as those of the composites, each milled for 15 h, are shown. For comparison, the reference pattern of trigonal Al_2O_3 was inserted as well (see bottom

of Fig. 1 a)). Nanocrystalline LiF turned out to be highly crystalline sample without any significant amorphous material as no humps in the XRD patterns are visible. Joint milling with the isolator Al_2O_3 lead to composites consisting of LiF with retained cubic symmetry and, interestingly, amorphous Al_2O_3 most likely surrounding the LiF crystallites or cluster-assembled particles. We clearly see, when regarding the background signal of the pattern, that the amount of amorphous material in the samples increases with an increasing amount of isolator. Hence, we conclude that Al_2O_3 is almost exclusively responsible for the formation of amorphous fractions in the composites. Samples in a compositional range of $0 < x_v \leq 0.3$ reveal for the most part well-defined cubic LiF crystallites in contact with the amorphous isolator. It is evident that the presence of Al_2O_3 crystallites also helps in reducing the crystallite size of LiF. The reflections of LiF continuously broaden with increasing Al_2O_3 content. $0.5\text{LiF}:0.5\text{Al}_2\text{O}_3$ turned out to be mixture of amorphous Al_2O_3 with very small crystallites of LiF. Note that at $67^\circ 2\theta$ a reflection with low intensity appears that likely originates from a so far unknown contamination.

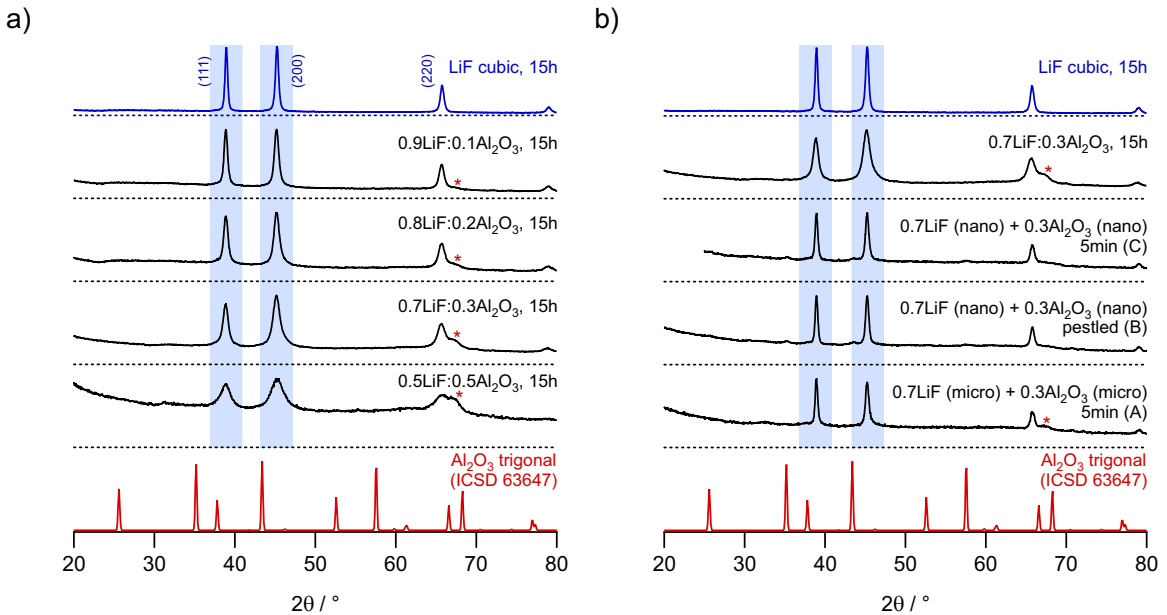


Fig. 1 a) X-ray powder patterns of high-energy ball milled LiF and two phase composites with composition of $(1-x_v)\text{LiF}:x_v\text{Al}_2\text{O}_3$ ($0 \leq x_v \leq 0.5$ vol-%). All samples were prepared using a ZrO_2 vial set at a rotational speed of 600 rpm and a milling time of 15 h. As a reference, the pattern of trigonal Al_2O_3 is integrated in red. The reflections in all composites refer to a cubic phase and include varying amounts of amorphous material. b) XRPD pattern of samples with $x_v = 0.3$ prepared according o the conditions listed. Again, the reflections refer to a cubic phase and are narrowed, which indicates larger crystallite sizes. See text for further explanation.

On the right hand side of Fig. 1 b) the X-ray pattern of $0.7\text{LiF}:0.3\text{Al}_2\text{O}_3$ synthesized according to different milling conditions are presented. These composites have been prepared by milling the coarse grained precursors for only 5 minutes or by mixing nanocrystalline LiF ($t_{\text{mill}} = 1$ h) and Al_2O_3 ($t_{\text{mill}} = 1$ h) either by hand with mortar and pestle or again by high-energy ball milling for 5 minutes (see samples A – C in Fig. 1 b)). Again, a composite of nanocrystalline cubic LiF with nanocrystalline amorphous Al_2O_3 is formed. However, these samples feature narrowed reflections compared to the one milled for 15 h, caused by larger

crystallite sizes and less lattice strain. In Table 1 the particle sizes as well as microstrains of all synthesized composites can be found. Keep in mind that all sizes and strains are average values of the three values calculated for the most prominent LiF reflections at 38, 45 and 65° 2θ, respectively. Crystallite sizes were determined by evaluating the width of the reflections with the equation introduced by Scherrer[18]. Microstrains were estimated using the method proposed by Williamson and Hall[19]. High-energy ball milling in a planetary mill leads to nm-sized materials. As mentioned above, the particle size decreases with an increasing amount of insulator added; simultaneously, lattice strain enhances. As long treatments promote the reduction in mean crystallite size and the enhancement of strain, samples A to C, which were only mixed for short times, exhibit larger crystallites and less microstrain, as expected.

Table 1: Mean crystallite sizes and microstrains as derived from XRPD measurements for all samples prepared. Note that D_p steadily decreases from $x_v = 0$ to $x_v = 0.5$ while ε increases. Samples A to C feature higher crystallite sizes as is also indicated by the narrowed reflections seen in Fig. 1 b)

x	0	0.1	0.2	0.3	0.5	0.3 (A)	0.3 (B)	0.3 (C)
D_p (nm)	38	24	18	14	7	45	45	42
ε	0.0027	0.0044	0.0058	0.0076	0.0148	0.0024	0.0024	0.0049

Conductivity Measurements

In order to investigate ionic conductivities of the nanocrystalline ceramics we recorded conductivity isotherms covering both a broad frequency range and a large temperature region. In Fig. 2 a) the real part σ' of the complex conductivity as well as the real part ε' of the complex permittivity of mechanosynthesized 0.7LiF:0.3Al₂O₃ is shown as a function of frequency ν . At high temperatures and low frequencies electrode polarization is apparent because of the piling up of ions on the surface of the Au blocking electrodes. At the highest frequencies dispersive regions dominate the spectra. In between these two regimes the isotherms reveal distinct frequency independent plateaus, from which we read off direct current (DC) values σ_{DC} . These values refer to long-range ion transport through the macroscopic sample and can be used to determine specific ionic conductivities as a function of temperature.

In Figure 2 b) $\sigma_{DC}T$ is plotted vs. the inverse temperature $1000/T$ in order to calculate the activation energies E_a as well as to illustrate the change in ionic conductivity upon mixing of LiF with various insulator amounts. Activation energies were determined via $\sigma_{DC} \cdot T = \sigma_0 \cdot \exp(E_a / (k_B T))$. σ_0 represents the pre-exponential factor, E_a the activation energy and k_B the Boltzmann constant.[20] For comparison, we included microcrystalline lithium fluoride, which clearly shows the lowest conductivities. Ball-milling of this sample for 15 h enhanced the ionic conductivity by approximately two orders of magnitude; accordingly, E_a slightly decreases from 1.04 eV to 0.98 eV. Most likely ions in disordered interfacial regions provide fast diffusion pathways for the mobile ions.

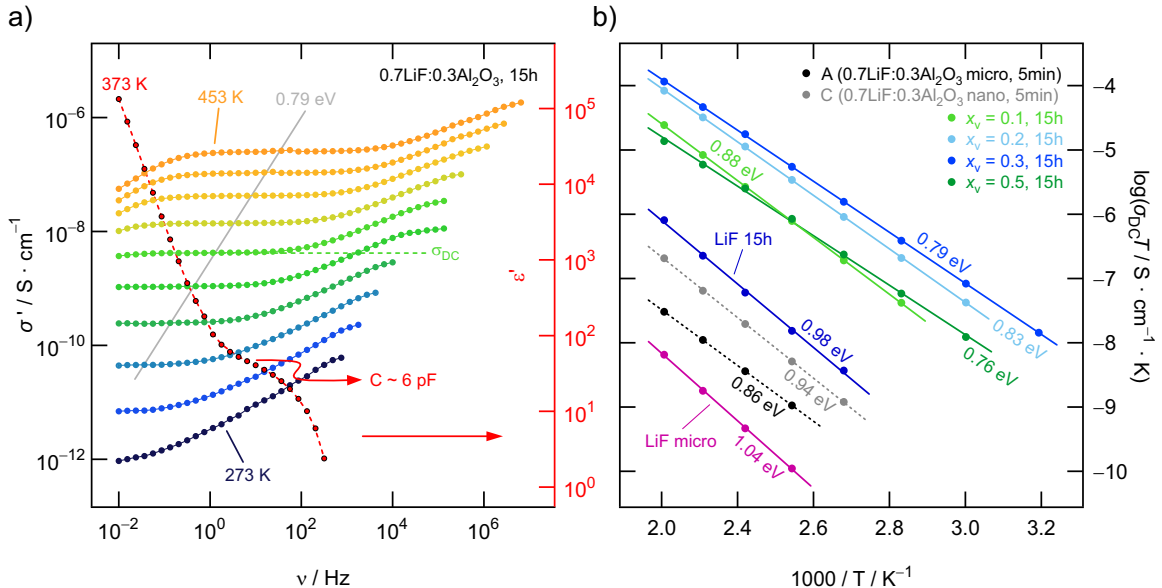


Fig. 2 a) Conductivity isotherms of milled 0.7LiF:0.3Al₂O₃. While at low T dispersive regions dominate the spectra, these portions get smaller with increasing temperature. DC conductivities were read off from the frequency independent plateau regions. Additionally the frequency dependence of the real part of the permittivity is presented as well showing a plateau which corresponds to a diffusion process exhibiting a capacity of 6 pF. b) Change of the DC conductivity of LiF and $(1-x_v)\text{LiF}:x_v\text{Al}_2\text{O}_3$ ($0 \leq x_v \leq 0.5$ vol-%) as a function of inverse temperature. The highest conductivities are found for $x_v = 0.3$. While the solid lines show linear fits to extract activation energies for samples prepared by milling for $t_{\text{mill}} = 15$ h, dashed lines refer to samples milled for only 5 min.

Non-trivial size effects, which are based on the formation of space charge zones[12], may influence the dynamic properties of the nanomaterial as well.

Even short milling times of only 5 min cause a significant increase of σ_{DC} compared to the coarse grained starting material, as can be seen by samples A and C in Fig. 2 b). Most likely, joint milling with Al₂O₃ leads to an interfacial network of homo-contacts (LiF:LiF) and hetero-contacts (LiF:Al₂O₃), see similar studies on composites with Li₂O [14] and LiBH₄ and[3]. These two-component interfacial regions further facilitate ionic diffusivity for the mobile ions and, thus, lead to a significant enhancement in ionic conductivity. The sample with $x_v = 0.3$ features the highest values, compared to microcrystalline LiF ($\sigma_{DC, 393\text{K}} = 2.8 \times 10^{-13} \text{ S cm}^{-1}$) the conductivity could be enhanced by approximately five orders of magnitude reaching $1.4 \times 10^{-8} \text{ S cm}^{-1}$ at 393 K. Simultaneously, E_a decreased from 1.04 eV to 0.79 eV. As mentioned before, in Fig. 2 a) a permittivity spectrum of 0.7LiF:0.3Al₂O₃ at 373 K is integrated as well displaying revealing the bulk electrical process above 10 Hz; the associated electrical capacity of 6 pF reveals that the whole response is characterized by values being typical for a bulk response.

NMR measurements

Before discussing the NMR SLR rates of nanostructured LiF and 0.7LiF:0.3Al₂O₃ we take a closer look at their variable-temperature ⁷Li and ¹⁹F NMR line-shapes, which were recorded under static, *i.e.*, non-rotating conditions. In Fig. 3 a) and b) the ⁷Li NMR spectra of $x_v = 0$ and $x_v = 0.3$ are presented. For nanocrystalline [6]

lithium fluoride at 473 K heterogeneous motional narrowing sets in, which is marked by the circles in Fig. 3 a).

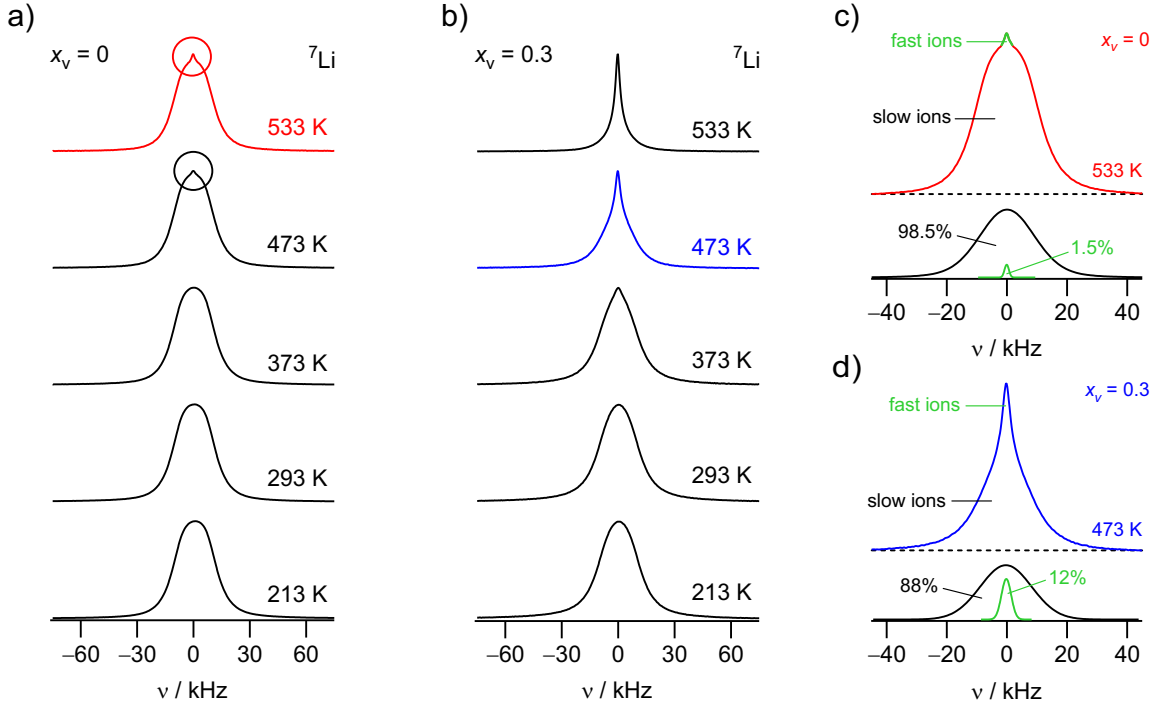


Fig. 3 a) and b) Variable-temperature ${}^7\text{Li}$ NMR spectra of $x_v = 0$ and $x_v = 0.3$ (116 MHz, static conditions). At low T broad NMR lines are seen. Spectra are shown such that the centre of the NMR signal is located at 0 kHz. As T increases heterogeneous motional narrowing sets in. The narrowed line, which emerges with increasing temperature at the centre of the NMR signal, reflects the number fraction of mobile Li cations with respect to the NMR time scale. c) and d) In order to estimate the area fraction of the narrow component several Gaussian and Lorentzian curves were used to deconvolute the spectra. Exemplary, spectra of $x_v = 0$ (533 K) and $x_v = 0.3$ (473 K) are displayed. The narrowed lines at the centre of the NMR signals reflect the number fraction of mobile Li cations. For $x_v = 0.3$ (473 K) approximately 12 % of the Li ions participate in fast ion dynamics. Most likely, they have access to percolating pathways constructed by heterointerfaces due to conductor:insulator regions.

Starting from this temperature the line consists of two contributions, namely, a motionally narrowed line atop a broad one which does not show any narrowing effect. This small superimposed line represents highly mobile Li ions moving along the fast diffusion pathways in the interfacial regions indicating. The component is absent for microcrystalline LiF being characterized by much lower conductivities. The motionally narrowed line makes visible the ions that cause enhanced ionic transport in nano-LiF.

In Fig. 3 b) the ${}^7\text{Li}$ NMR spectra for the two-phase composite with $x_v = 0.3$ are displayed. For this sample motional narrowing can already be seen at 373 K and dominates the spectrum recorded at 533 K. Again the narrowed component reflects fast ions in the interfacial regions. It can be clearly seen that the hetero-contacts introduced drastically promote Li^+ diffusivity for the composite with $x_v = 0.3$. Pronounced motional narrowing is consistent with an increase of σ_{DC} by three orders of magnitude when going from $x_v = 0$ to $x_v = 0.3$.

In order to estimate the area fractions of the narrow component a combination of Gaussian and Lorentzian curves was used to deconvolute the spectra (see Fig. 3 c) and d)). In both cases, *i.e.*, for $x_v = 0$ at 533 K (Fig. 3 c)) and for $x_v = 0.3$ at 473 K (Fig. 3 d)), the green lines at the centre of the NMR signals reflect the number fraction of mobile Li ions. While in nano-LiF even at a temperature as high as 533 K only 1.5 % of the total number of Li ions participate in fast ion dynamics, a huge increase in percentage is seen for the composite 0.7LiF:0.3Al₂O₃. At 473 K approximately 12 % and at 533 K ca. 44 % of the ions take advantage of the insulator effect.

Lithium fluoride is a material where not only Li cations but also F anions can act as mobile charge carriers. Hence, to take a closer look at the fluorine anion dynamics, variable-temperature ¹⁹F NMR spectra were recorded, which are illustrated in Fig. 4. The spectra of nano-LiF are presumably composed of two different F regimes which are superimposed by one very broad line and exhibit no observable narrowing in the investigated

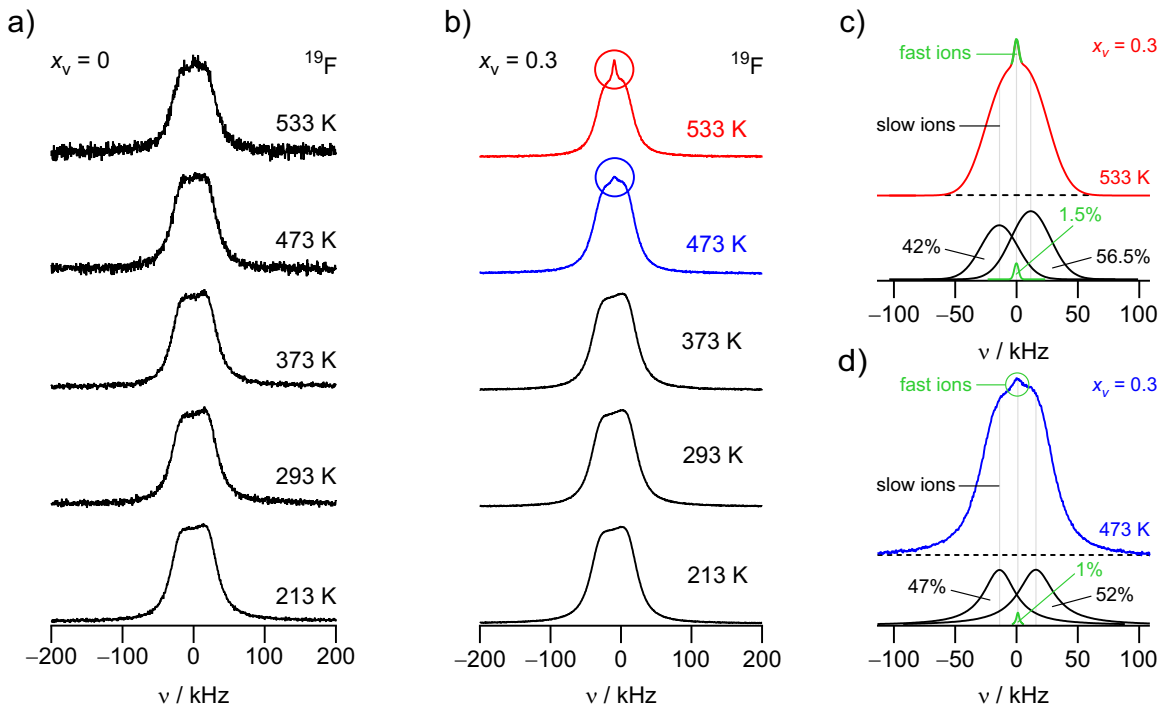


Fig. 4 a) and b) Variable-temperature ¹⁹F NMR spectra of $x_v = 0$ and $x_v = 0.3$ (282 MHz, static conditions). Spectra are again shown such that the centre of the NMR signal is located at 0 kHz. For LiF very broad NMR lines with no sign of motional narrowing are visible. Looking at 0.7LiF:0.3Al₂O₃, at high temperatures again heterogeneous narrowing sets in. Here the narrowed line reflects the number fraction of mobile F anions with respect to the NMR time scale. c) and d) Via deconvolution of the spectra with Gaussian and Lorentzian lines, three different superimposed contributions to the overall signal were determined. The small, sharp lines at the centre of the NMR signals reflect the marginal number fraction of mobile F anions in the composite. At 533 K only ca. 1 % participate in fast ion dynamics.

temperature range (see Fig. 4 a)). For the sample with $x_v = 0.3$ again a narrowed second component, representing fast F ions with respect to the NMR time scale, becomes apparent at elevated temperatures

(Fig. 4 b)). The deconvolution of the $0.7\text{LiF}:0.3\text{Al}_2\text{O}_3$ NMR lines at 473 K and 533 K, visible in Fig. 4 c) and d), revealed that the area fraction does only slightly increase with temperature (1.5 % at 533 K and ca. 1 % at 473 K). The area fraction turned out to be much smaller than that seen for the Li spectra, which indicates that mainly Li ions are responsible for the large enhancement of the overall conductivity in the composites.

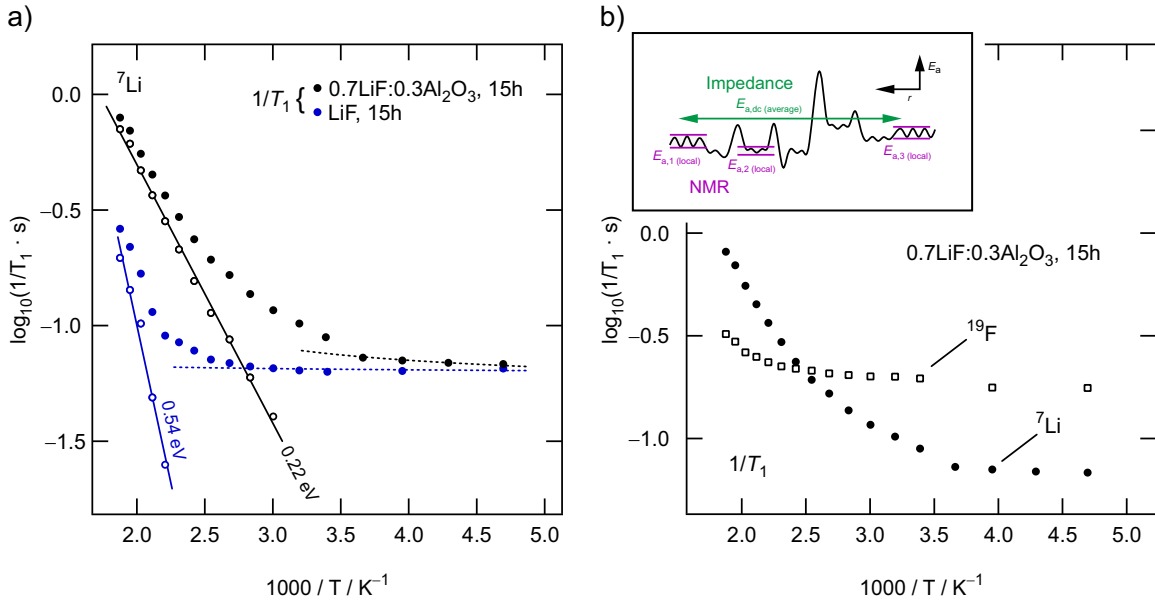


Fig. 5 a) Temperature dependence of the ^7Li NMR SLR rates $1/T_1$ (116 MHz) for nanocrystalline samples LiF and $0.7\text{LiF}:0.3\text{Al}_2\text{O}_3$ prepared via high-energy ball milling. A power law was used to extrapolate the background rates to higher T to obtain purely diffusion-induced relaxation rates $1/T_{1,\text{diff}}$. The unfilled symbols display rates after the correction procedure. Solid lines show linear fits to extract NMR activation energies. b) Arrhenius representation of the not corrected ^7Li NMR rates $1/T_1$ (116 MHz) and ^{19}F NMR rates $1/T_1$ (282 MHz) for sample $x_v = 0.3$. The inset of b) is a schematic illustration of a heterogenous potential landscape. Depending on the length scale, the method chosen to study ion dynamics is either sensitive to long-range ion dynamics or to local ionic jump processes being governed by correlation effects.

To estimate activation energies from NMR measurements, we recorded spin-lattice relaxation rates. In Fig. 5 an overview of all variable-temperature ^7Li and ^{19}F spin-lattice NMR relaxation rates is presented. Rates were plotted in an Arrhenius representation in order to identify the thermally activated regions, from which hopping activation energies can be extracted. Stretched exponential functions served to parameterize the magnetization transients $M_z(t_d)$. As can be clearly seen in Fig. 5 a), all ^7Li rates show a non-diffusive regime at lower temperatures; in this T range the rates do only marginally depend on T . Going to higher temperatures they start to increase and to reach the so-called low- T flank of the corresponding diffusion-induced rate peak.

To analyze purely diffusion-induced rates, we approximated the background rates with a power law, $1/T_{1,\text{bgr}} \propto T^\beta$, after extrapolation to higher temperatures (see the dashed lines in Fig. 5 a)) subsequent subtraction from the overall rates lead to background-free, corrected rates: $1/T_{1,\text{diff}} = 1/T_1 - 1/T_{1,\text{bgr}}$ [21]. These

rates are represented by unfilled symbols. $1/T_{\text{1diff}}$ follows an Arrhenius behavior characterized by an activation energy E_a of 0.54 eV for nanocrystalline LiF. For the 0.7LiF:0.3Al₂O₃ composite, E_a turned out to be significantly smaller, viz. 0.22 eV. The beginning of the corresponding diffusion-induced flank of the composite is clearly shifted to much lower temperatures. This behaviour shows increased Li diffusion in the mixed phase. For comparison, the corresponding ¹⁹F NMR rates of the composite reveal the beginning of a diffusion-induced rate peak at much higher temperatures than observed for ⁷Li NMR. The low- T flank of the sample with $x = 0.3$ cannot be reached completely with our measurement setup. This observation once again supports the idea that Li diffuses much faster in the composite than F does.

As expected for highly correlated motion, both activation energies are far below the values determined via impedance spectroscopy (0.98 eV and 0.79 eV, respectively; see Fig. 2). In contrast to DC conductivity measurements, NMR spin-lattice relaxation rates, particularly if low- T flanks of NMR rate peaks ($1/T_1(1/T)$) are considered, probe short-range Li motions on the angstrom length scale. The difference has frequently explained by correlated motions and heterogenous, disordered potential landscapes the ions are exposed to.

Conclusion

Mechanical treatment of LiF together with Al₂O₃, acting as an insulating second phase, in a high-energy ball mill lead to composite materials that feature ion transport properties greatly exceeding those of single phase nanocrystalline LiF. We used broadband conductivity measurements as well as ⁷Li and ¹⁹F solid-state NMR spectroscopy to study the ion dynamics of the two mobile charge carriers in detail. The introduction of a large volume fraction of hetero-interfaces in the two-phase composite LiF:Al₂O₃ is mainly responsible for the increase of the diffusivity, because of the formation of fast diffusion pathways along this interfacial regions. Impedance studies showed the highest overall conductivity for the mixture with the volume fraction 0.7LiF:0.3Al₂O₃, which exhibits, compared to nanocrystalline LiF, an increase in ionic conductivity by approximately five orders of magnitude. Simultaneously, the activation energy decreased from ca. 1 eV to 0.79 eV.

At elevated temperatures, static ⁷Li NMR experiments revealed a two-component line shape for the composite with $x_v = 0.3$; the spectra consist of a broad and a motionally narrowed component reflecting heterogeneous dynamics of slow- and fast-diffusing Li spins. We attribute the two spin ensembles to the highly mobile ions located in the hetero-interfaces and to much slower charge carriers in the bulk regions. NMR line-shape measurements as well as spin-lattice relaxation experiments clearly identify Li as the dominant charge carrier that controls ionic conductivity. Diffusion of F anions turned out to be much slower.

Acknowledgements. We thank the Deutsche Forschungsgemeinschaft (DFG) for financial support in the frame of the priority program crystalline non-equilibrium phases (SPP 1415). Further support by the FFG K-project safe battery is highly appreciated.

References

- [1] J. B. Goodenough, Y. Kim, *Chemistry of Materials*, 22 (2010) 587-603.
- [2] P. Knauth, *Solid State Ionics*, 180 (2009) 911-6.
- [3] V. Epp, M. Wilkening, *ChemPhysChem*, 14 (2013) 3706-13.
- [4] J. Maier, *Journal of Electroceramics*, 13 (2004) 593-8.
- [5] J. Maier, *Nature Materials*, 4 (2005) 805.
- [6] A. Duvel, M. Wilkening, R. Uecker, S. Wegner, V. Sepelak, P. Heitjans, *Physical Chemistry Chemical Physics*, 12 (2010) 11251-62.
- [7] H. Gleiter, *Acta Materialia*, 48 (2000) 1-29.
- [8] M. Wilkening, S. Indris, P. Heitjans, *Physical Chemistry Chemical Physics*, 5 (2003) 2225-31.
- [9] H. Li, G. Richter, J. Maier, *Advanced Materials*, 15 (2003) 736-9.
- [10] C. Wall, A. Pohl, M. Knapp, H. Hahn, M. Fichtner, *Powder Technology*, 264 (2014) 409-17.
- [11] H. Yildirim, A. Kinaci, M. K. Y. Chan, J. P. Greeley, *ACS Applied Materials & Interfaces*, 7 (2015) 18985-96.
- [12] J. Maier, *Progress in Solid State Chemistry*, 23 (1995) 171-263.
- [13] J. Maier. Nanoionics. In: Sattler KD, editor. *Handbook of Nanophysics - Principles and Methods*. Boca Raton, Florida Taylor & Francis Group; 2011.
- [14] P. Heitjans, S. Indris, *Journal of Physics-Condensed Matter*, 15 (2003) R1257-R89.
- [15] C. C. Liang, *Journal of the Electrochemical Society*, 120 (1973) 1289-92.
- [16] P. Heitjans, M. Wilkening, *MRS Bulletin*, 34 (2011) 915-22.
- [17] E. Fukushima, S. B. W. Roeder. *Experimental Pulse NMR. A Nuts and Bolts Approach*. Reading: Addison-Wesley Publ. Comp.; 1981.
- [18] A. L. Patterson, *Physical Review*, 56 (1939) 978-82.
- [19] G. K. Williamson, W. H. Hall, *Acta Metallurgica*, 1 (1953) 22-31.
- [20] L. N. Patro, K. Hariharan, *Materials Research Bulletin*, 46 (2011) 732-7.
- [21] M. Wilkening, D. Bork, S. Indris, P. Heitjans, *Physical Chemistry Chemical Physics*, 4 (2002) 3246-51.

4. Zusammenfassung und Ausblick

Im Rahmen dieser Dissertation wurden verschiedene Lithium- und Fluor-Festkörper-Ionenleiter hergestellt und detailliert im Hinblick auf ihre Diffusionseigenschaften untersucht. Die Synthesen wurden mechanochemisch mit Hilfe von Hochenergie-Kugelmühlen durchgeführt. Diese Technik erlaubt sowohl die Präparation von Verbindungen über neue Syntheserouten als auch die Verbesserung der Transporteigenschaften bestehender Materialien durch Zerkleinerung der Kristallite und das Einbringen struktureller Unordnung. Impedanzspektroskopie und NMR-Spektroskopie waren die Methoden der Wahl für die anschließende Analyse der Transport- und Diffusionsparameter. Die Kombination dieser beiden Spektroskopiearten ermöglicht die Charakterisierung der Ladungsträgerbewegung in einem breiten dynamischen Bereich, das heißt auf einer breiten Längenskala. Zusätzlich trägt die Kombination beziehungsweise der Vergleich der Ergebnisse zu einem besseren Verständnis der Li- bzw. F-Diffusion bei, wenn es darum geht korrelierte, längenskalenabhängige Ionenbewegungen zu studieren.

Li-Ionenleiter. LATP war das erste, im Rahmen dieser Dissertation untersuchte, Material. Eine bereits via Sol-Gel Verfahren hergestellte Probe aus der Gruppe von Frank Tietz (FZ Jülich), wurde dabei impedanzspektroskopisch in einem großen Temperaturbereich vermessen. Dadurch ist es gelungen, bulk- und Korngrenzenprozesse in der Verbindung zu separieren und getrennt voneinander zu analysieren. Die Korngrenzenleitfähigkeit wurde dabei, mit einer um drei Größenordnungen niedrigeren ionischen Leitfähigkeit als der limitierende Prozess identifiziert. Insgesamt kann gesagt werden, dass LATP mit seiner

relativen hohen Bulk-Leitfähigkeit von circa $3 \times 10^{-3} \text{ S cm}^{-1}$ und der geringen Aktivierungsenergie ein vielversprechendes Elektrolytmaterial für den Einsatz in Festkörper-Lithium-Ionen-Batterien darstellt. Weitere Studien müssen zeigen, inwiefern man es gegenüber Li-Metall durch z.B. Schutzschichten elektrochemisch stabilisieren kann.

Ein weiterer Li-Festelektrolyt, der im Umfang dieser Arbeit studiert wurde, ist Lithiumborhydrid. Im Gegensatz zu mikrokristallinem LiBH_4 zeigt nanostrukturiertes LiBH_4 deutlich zwei dynamisch unterschiedliche Ionenspezies. NMR-Linienformmessungen und Spin-Gitter-Relaxationsratenmessungen offenbaren deutlich zwei verschiedene Li-Reservoirs. Die schnellere Spezies (0.18 eV) wird den Ionen in oder in der Nähe der Grenzflächenregionen in nano- LiBH_4 zugeordnet. Die Separation der Li-Spins gelingt sowohl bei Analyse der freien Induktionszerfälle als auch bei der Untersuchung der Magnetisierungstransienten eines T_1 -Experiments.

F-Ionenleiter. Zur Forschung an Materialien für neue, alternative chemische Energiespeichermethoden, wie zum Beispiel die Fluorid-Ionen-Batterie, wurden für diese Dissertation eine Reihe unterschiedlicher Systeme von Fluor-Ionenleitern untersucht. Allesamt wurden mechanochemisch durch Mahlen in einer Hochenergie-Kugelmühle hergestellt und strukturell via Röntgenkristallstrukturanalysen charakterisiert. Die mechanische Behandlung resultierte jeweils in signifikanten Erhöhungen der Fluor-Ionenleitfähigkeiten, die aufgrund von unterschiedlichen Ursachen zustande gekommen sind, und die mit Hilfe von Impedanz- sowie NMR-Messungen aufgezeichnet und interpretiert wurden. Die verschiedenen Substitutionsstrategien können zu einer erhöhten Anzahl an Defekten, einer höheren Ladungsträgerdichte, Gitterverspannungen oder Änderungen des Volumenanteils an Grenzflächen führen. Allesamt Phänomene, die Auswirkungen auf die Ionendiffusion in Festkörpern haben und dementsprechend die Leitfähigkeit der Fluor-Ionen beeinflussen.

Im Falle der metastabilen $(\text{Ba,Ca})\text{F}_2$ Verbindungen mit struktureller Frustration wurde außerdem noch deutlich, dass der präexponentielle Faktor, der den T_1 -NMR-Messungen zugrunde liegt, hauptsächlich für die erhöhte Diffusion auf kurzreichweiter Längenskala verantwortlich ist. Die Aktivierungsenergien aus NMR-Messungen bleiben für diesen Fall nahezu unabhängig von der Zusammensetzung, dies ist anders für den langreichweiten Fall, der eine signifikante Abnahme der Aktivierungsenergie aus Leitfähigkeitsmessungen zeigt,

wenn die ionische Leitfähigkeit ihr Maximum bei äquimolarer Zusammensetzung durchläuft. Ob ähnliche Ergebnisse für andere isovalente Mischsysteme zu erwarten sind, muss noch geklärt werden.

Sowohl bei den synthetisierten $\text{Sr}_{1-x}\text{Y}_x\text{F}_{2+x}$ Systemen als auch bei den präparierten $\text{LaF}_3:\text{SrF}_2$ *solid solutions* ging aus den Leitfähigkeitsmessungen, ganz analog zu $(\text{Ba},\text{Ca})\text{F}_2$, mit der Zunahme der Leitfähigkeit auch eine Abnahme der Aktivierungsenergie und damit eine Verringerung der Barrieren, die für einen erfolgreichen Ionensprung überwunden werden müssen, einher. Interessanterweise sind, im Gegensatz zum System $(\text{Ba},\text{Ca})\text{F}_2$, neben Aktivierungsenergien auch die Vorfaktoren aus Leitfähigkeitsmessungen (in Anlehnung an die Meyer-Neldel-Regel) abhängig von der Zusammensetzung und durchlaufen ein Minimum, wenn die Aktivierungsenergie ebenfalls minimal wird.

Die $\text{La}_{1-x}\text{Ba}_x\text{F}_{3-x}$ Proben zeigten eine starke Abhängigkeit des Ladungsträgertransportes von der Morphologie der Grenzflächen. Zusätzlich wurde in diesem System mit Hilfe von Polarisationsmessungen und Cyclovoltammetrie die elektrochemische Stabilität untersucht. Es gibt deutliche Unterschiede zwischen Ergebnissen aus Leitfähigkeits- und NMR-Messungen, die auf eine zeitskalenabhängige, heterogene Dynamik schließen lassen.

Zusammenfassend kann gesagt werden, dass an mehreren Beispielen gezeigt werden konnte, wie ein langsamer Ionenleiter durch mechanische Behandlung in einer Kugelmühle zu einem schnellen, stark verbesserten Festkörperionenleiter modifiziert werden kann. Die analysierten Materialien sind nach diesem „tuning“-Prozess allesamt potentiell in Fluorid-Ionen-Batterien einsetzbar.

Für die Realisierung eines neuen, modernen chemischen Energiespeichersystems, das nur aus Feststoffen zusammengesetzt ist, sind selbstverständlich noch viele weitere Studien nötig. Speziell im Hinblick auf Fluorid-Ionen-Batterien werden, für ein besseres Verständnis der elementaren Sprungprozesse in den Materialien, noch grundlagenorientierte Forschungen an Modellsystemen durchgeführt werden müssen (siehe Kap. 3.3.1). Diese dienen dem Verständnis der zugrundeliegenden Diffusionsbewegungen auf atomarer Ebene. Zum anderen wird die anwendungsorientierte Forschung nach neuen, einsetzbaren Verbindungen für moderne Energiespeichersysteme intensiv weiter gehen.

Ein letzter wichtiger Punkt betrifft das anschließende *Upscaling* der Technologien vom Labormaßstab in einen großtechnischen Maßstab. Dieser Prozess umfasst sowohl die

Verarbeitbarkeit der Komponenten, als auch die mechanischen Eigenschaften, sämtliche andere Materialeigenschaften oder die maschinelle Herstellung. Auch hier werden die Materialwissenschaften in den nächsten Jahren noch vor große Probleme gestellt werden.

Trotz alledem werden Jahr für Jahr, auch aufgrund der Aktualität des Problems der effizienten Energiespeicherung, enorme Fortschritte in der Forschung und Entwicklung neuer Festkörperperionenleiter für Sekundärbatterien erzielt. Ausgewählte Festkörper-Lithium-Ionen-Batterien sind bereits kommerziell erhältlich, was ein erstes vielversprechendes Zeichen für einen möglichen, zukünftigen Durchbruch dieser Technologien sein sollte. Man denke dabei nur an die Erfolgsgeschichte der Lithium-Ionen-Batterie nach der ersten Kommerzialisierung von Sony im Jahre 1991, die heute nicht mehr aus unserem täglichen Alltag wegzudenken wäre.⁷¹

A. Anhang

A.1 Verwendete Geräte

Gloveboxen: MBRAUN Model LabStar und Model LabMaster Pro SP (O_2 und $H_2O < 1 \text{ ppm}$);

Analysenwaagen: METTLER TOLEDO Model XA 303S und Model XA 105;

Hochenergie-Kugelmühle: FRITSCH Model Pulverisette Premium line 7 mit gasdichten, verschließbaren 45 mL Mahlbechern und ZrO_2 Mahlkugeln;

Pulverpressen: P/O/WEBER Model PW30 und SPECAC;

Sputteranlage: LEICA Model EM SCD 050 mit EM QSG 100 Filmdickemonitor;

Öfen: REETZ Model LOBA 1200-45-400-1-OW Rohrofen mit OMRON E5CK-T Temperaturregler;
BÜCHI Glasofen B-585 Drying;

Röntgendiffraktometer: BRUKER D8 Advance Diffraktometer mit Bragg-Brentano Geometrie und $Cu K\alpha$ Strahlung;

Impedanzspektrometer: NOVOCONTROL Model Concept 80 Breitband-Dielektrikums-Spektrometer in Kombination mit einer aktiven ZGS Zelle (Frequenzbereich 10 mHz – 10 MHz);

AGILENT E4991 Hochfrequenz-Analyser verbunden mit einer Hochfrequenzmesszelle (Frequenzbereich 1 MHz – 3 GHz);

Temperaturkontrolle mit Hilfe eines QUATRO Kryosystems (NOVOCONTROL);

NMR-Spektrometer: BRUKER Model Avance III 300 WB mit 7 T Magnet;

BRUKER Model Avance III Ultrashield 500 WB Plus mit 11 T Magnet;

NMR-Probenköpfe: BRUKER Keramikprobenkopf Model HP BBHT 500WB Sol5 Ceramics für ^7Li Messungen;

BRUKER MAS Probenkopf Model HP WB73 MAS 1,3;

BRUKER MAS Probenkopf Model HP WB73 A MAS BL 2,5;

NMR SERVICE statischer Probenkopf für ^{19}F Messungen;

Rasterelektronenmikroskop: TESCAN Model VEGA3;

A.2 Verwendete Software

WinDETA 5.73 (NOVOCONTROL): Programm zur Durchführung aller Impedanzexperimente und zum Export der erhaltenen Daten.

TopSpin 3.1 (BRUKER): Software zur Bedienung der NMR Spektrometer und Durchführung aller Messungen. Ebenso diente es der Bearbeitung und dem Export der aufgezeichneten Daten.

IGOR Pro 6.37: Auswertesoftware zur Verarbeitung, Analyse und Darstellung der gesammelten Daten.

CorelDraw X7: Grafikprogramm zur Bearbeitung von Abbildungen und der Erstellung von Postern beziehungsweise Präsentationen.

Diamond 3.2: Programm zur Darstellung von Kristallstrukturen.

Vesta 3.4.3: Alternative Software zur Visualisierung von Kristallstrukturen.

Microsoft Word 2013: Programm zur Erstellung von Texten wie dieser Dissertation oder sämtlichen Publikationen.

EndNote X7.3.1: Software zum Management der Referenzen und zur Erstellung von Literaturverzeichnissen.

B. Literaturverzeichnis

- [1] J.-M. Tarascon, *ChemSusChem*, **1** (2008), 777-779.
- [2] M. Armand und J.M. Tarascon, *Nature*, **451** (2008), 652.
- [3] J.B. Goodenough und Y. Kim, *Chemistry of Materials*, **22** (2010), 587-603.
- [4] V. Thangadurai, S. Narayanan, und D. Pinzaru, *Chemical Society Reviews*, **43** (2014), 4714-4727.
- [5] P. Knauth, *Solid State Ionics*, **180** (2009), 911-916.
- [6] F. Gschwind, G. Rodriguez-Garcia, D.J.S. Sandbeck, A. Gross, M. Weil, M. Fichtner, und N. Hörmann, *Journal of Fluorine Chemistry*, **182** (2016), 76-90.
- [7] M. Uitz, V. Epp, P. Bottke, und M. Wilkening, *Journal of Electroceramics*, **38** (2017), 142-156.
- [8] J. Falbe und M. Regitz, *RÖMPP Lexikon Chemie Cm – G*, Georg Thieme Verlag, Stuttgart, 2014.
- [9] H. Mehrer, *Diffusion in Solids*, Springer-Verlag Berlin Heidelberg, Berlin, 2007.
- [10] P. Heitjans und J. Kärger, *Diffusion in Condensed Matter*, Springer-Verlag Berlin Heidelberg, Berlin, 2005.
- [11] L.E. Smart und E.A. Moore, *Solid State Chemistry: An Introduction*, Taylor & Francis Group, Boca Raton, 2012.
- [12] W. Borchardt-Ott, *Kristallographie - Eine Einführung für Naturwissenschaftler*, Springer-Verlag Berlin Heidelberg, Berlin, 2009.
- [13] J. Pelleg, *Diffusion in Ceramics*, Springer International Publishing, Cham, 2016.

- [14] G.E. Murch, *Diffusion Kinetics in Solids*, WILEY-VCH Verlag GmbH, Weinheim, 2001.
- [15] F. Preishuber-Pflügl und M. Wilkening, *Dalton Transactions*, **45** (2016), 8675-8687.
- [16] V. Sepelak, A. Düvel, M. Wilkening, K.-D. Becker, und P. Heitjans, *Chemical Society Reviews*, **42** (2013), 7507-7520.
- [17] P. Baláž, *Mechanochemistry in Nanoscience and Minerals Engineering*, Springer-Verlag Berlin Heidelberg, Berlin, 2008.
- [18] G. Heinicke, *Tribochemistry*, Akademie-Verlag, Berlin, 1984.
- [19] S. Kipp, V. Šepelák, und K.D. Becker, *Chemie in unserer Zeit*, **39** (2005), 384-392.
- [20] D. Wohlmuth, *et al.*, *Journal of Materials Chemistry A*, **2** (2014), 20295-20306.
- [21] A. Düvel, S. Wegner, K. Efimov, A. Feldhoff, P. Heitjans, und M. Wilkening, *Journal of Materials Chemistry*, **21** (2011), 6238-6250.
- [22] Y. Yamane, K. Yamada, und K. Inoue, *Solid State Ionics*, **179** (2008), 605-610.
- [23] A.V. Chadwick und S.L.P. Savin, *Solid State Ionics*, **177** (2006), 3001-3008.
- [24] A. Düvel, J. Bednarcik, V. Šepelák, und P. Heitjans, *The Journal of Physical Chemistry C*, **118** (2014), 7117-7129.
- [25] C. Suryanarayana, *Progress in Materials Science*, **46** (2001), 1-184.
- [26] F. Preishuber-Pflügl, *Dissertation*, Technische Universität Graz, 2016.
- [27] P. Heitjans und S. Indris, *Journal of Physics: Condensed Matter*, **15** (2003), R1257.
- [28] H. Gleiter, *Makromolekulare Chemie. Macromolecular Symposia*, **50** (1991), 171-182.
- [29] G. Cao, *Nanostructures & Nanomaterials*, Imperial College Press, London, 2004.
- [30] R. Malik, D. Burch, M. Bazant, und G. Ceder, *Nano Letters*, **10** (2010), 4123-4127.
- [31] M. Wilkening, S. Indris, und P. Heitjans, *Physical Chemistry Chemical Physics*, **5** (2003), 2225-2231.
- [32] V. Epp und M. Wilkening, *ChemPhysChem*, **14** (2013), 3706-3713.
- [33] J. Maier, *Progress in Solid State Chemistry*, **23** (1995), 171-263.
- [34] W. Schatt und H. Worch, *Werkstoffwissenschaft*, Deutscher Verlag für Grundstoffindustrie, Stuttgart, 1996.
- [35] F. Preishuber-Pflügl und M. Wilkening, *Dalton Transactions*, **43** (2014), 9901-9908.
- [36] R. Feidenhans'l, *Surface Science Reports*, **10** (1989), 105-188.
- [37] R. Guinebretière, *X-ray Diffraction by Polycrystalline Materials*, ISTE Ltd, London, 2007.

- [38] D. Schwarzenbach, *Kristallographie*, Springer-Verlag Berlin Heidelberg, Berlin, 2001.
- [39] P. Scherrer, *Göttinger Nachrichten*, **2** (1918), 98.
- [40] Y. Waseda, E. Matsubara, und K. Shinoda, *X-Ray Diffraction Crystallography*, Springer-Verlag Berlin Heidelberg, Berlin, 2011.
- [41] A. Düvel, *Dissertation*, Leibniz Universität Hannover, 2014.
- [42] A. Düvel, M. Wilkening, R. Uecker, S. Wegner, V. Sepelak, und P. Heitjans, *Physical Chemistry Chemical Physics*, **12** (2010), 11251-11262.
- [43] M. Imafuku, H. Suzuki, K. Sueyoshi, K. Akita, und S.-i. Ohya, *Applied Physics Letters*, **92** (2008), 231903.
- [44] G.K. Williamson und W.H. Hall, *Acta Metallurgica*, **1** (1953), 22-31.
- [45] E. Barsoukov und J.R. Macdonald, *Impedance Spectroscopy*, John Wiley & Sons, Hoboken, 2005.
- [46] V.F. Lvovich, *Impedance Spectroscopy*, John Wiley & Sons, Hoboken, 2012.
- [47] F. Kremer und A. Schönhals, *Broadband Dielectric Spectroscopy*, Springer-Verlag Berlin Heidelberg, Berlin, 2003.
- [48] M.A. Alim, *Immittance Spectroscopy*, John Wiley & Sons, Hoboken, 2017.
- [49] J.C. Dyre, P. Maass, B. Roling, und D.L. Sidebottom, *Reports on Progress in Physics*, **72** (2009), 046501.
- [50] D.L. Sidebottom, *Reviews of Modern Physics*, **81** (2009), 999-1014.
- [51] A.K. Jonscher, *Nature*, **267** (1977), 673.
- [52] D.L. Sidebottom, B. Roling, und K. Funke, *Physical Review B*, **63** (2000), 024301.
- [53] B. Roling, M. Meyer, A. Bunde, und K. Funke, *Journal of Non-Crystalline Solids*, **226** (1998), 138-144.
- [54] J.T.S. Irvine, D.C. Sinclair, und A.R. West, *Advanced Materials*, **2** (1990), 132-138.
- [55] A. Abragam, *Principles of Nuclear Magnetism*, Oxford University Press, New York, 1961.
- [56] H. Friebolin, *Basic One- and Two-Dimensional NMR Spectroscopy*, Wiley-VCH Verlag, Weinheim, 2011.
- [57] J. Keeler, *Understanding NMR Spectroscopy*, John Wiley & Sons Ltd, Chichester, 2010.
- [58] A.-R. Grimmer und B. Blümich, *Introduction to Solid-State NMR*, Springer-Verlag Berlin Heidelberg, Berlin, 1994.
- [59] M. Wilkening und P. Heitjans, *ChemPhysChem*, **13** (2012), 53-65.

- [60] N. Bloembergen, E.M. Purcell, und R.V. Pound, *Physical Review*, **73** (1948), 679-712.
- [61] M. Meyer, P. Maass, und A. Bunde, *Physical Review Letters*, **71** (1993), 573-576.
- [62] P. Knauth und J. Schoonman, *Nanocomposites - Ionic Conducting Materials and Structural Spectroscopies*, Springer Science + Business Media, Boston, 2008.
- [63] S. Breuer und M. Wilkening, *Dalton Transactions*, **47** (2018), 4105-4117.
- [64] T. Polenova, R. Gupta, und A. Goldbourt, *Analytical chemistry*, **87** (2015), 5458-5469.
- [65] A. Alia, S. Ganapathy, und H.J.M. de Groot, *Photosynthesis Research*, **102** (2009), 415-425.
- [66] J. Sakamoto, *Super-ionic Conducting Oxide Electrolytes*, in *Handbook of Solid State Batteries*. 2015, World Scientific Publishing Co. Pte. Ltd.: Singapur. p. 391-414.
- [67] N. Kamaya, *et al.*, *Nature Materials*, **10** (2011), 682.
- [68] S. Breuer, D. Prutsch, Q. Ma, V. Epp, F. Preishuber-Pflügl, F. Tietz, und M. Wilkening, *Journal of Materials Chemistry A*, **3** (2015), 21343-21350.
- [69] J.B. Goodenough, H.Y.P. Hong, und J.A. Kafalas, *Materials Research Bulletin*, **11** (1976), 203-220.
- [70] M. Anji Reddy und M. Fichtner, *Journal of Materials Chemistry*, **21** (2011), 17059-17062.
- [71] R. Korthauer, *Handbuch Lithium-Ionen-Batterien*, Springer Verlag Berlin Heidelberg, Berlin, 2013.

C. Publikationen

C.1 Artikel in referierten Fachzeitschriften

Separating bulk from grain boundary Li ion conductivity in the sol-gel prepared solid electrolyte LATP

S. Breuer, Q. Ma, D. Prutsch, V. Epp, F. Preishuber-Pflügl, F. Tietz, and M. Wilkening, *J. Mater. Chem. A*, **3** (2015), 21343-21350.

Structure and ion dynamics of mechanosynthesized oxides and fluorides

M. Wilkening, A. Düvel, F. Preishuber-Pflügl, K. da Silva, S. Breuer, V. Sepelak, and P. Heitjans, *Z. Krist.-Cryst. Mater.*, **232** (2017), 107.

An X-Ray Absorption Spectroscopy Study of Ball-Milled Lithium Tantalate and Lithium Titanate Nanocrystals

A. V. Chadwick, D. M. Pickup, S. Ramos, G. Cibin, N. Tapia-Ruiz, S. Breuer, D. Wohlmuth, and M. Wilkening, *IOP Conf. Series: Mater. Sci. Engin.*, **169** (2017), 012015.

Nanostructured Ceramics: Ionic Transport and Electrochemical Activity – A short journey across various families of materials

D. Prutsch, S. Breuer, M. Uitz, B. Stanje, J. Langer, P. Bottke, S. Lunghammer, P. Posch, V. Pregartner, M. Phillip, A. Dunst, D. Wohlmuth, H. Brandstätter, W. Schmidt, V. Epp, A. Chadwick, I. Hanzu, and M. Wilkening, *Z. Phys. Chem.*, **231** (2017), 1361.

Solid Electrolytes: Extremely Fast Charge Carriers in Garnet-Type $\text{Li}_6\text{La}_3\text{ZrTaO}_{12}$ Single Crystals

B. Stanje, D. Rettenwander, S. Breuer, M. Uitz, S. Berendts, M. Lerch, R. Uecker, G. Redhammer, I. Hanzu, and M. Wilkening, *Ann. Phys.*, **529** (2017), 1700140.

Ageing of Tesla Model S 18650 Lithium-Ion Cells: Correlating Solid Electrolyte Interphase Evolution with Fading in Capacity and Power

M. Uitz, M. Sternad, S. Breuer, C. Täubert, T. Traußnig, V. Hennige, I. Hanzu, and M. Wilkening, *J. Electrochem. Soc.*, **164** (2017), A3503-A3510.

Rapid Li ion dynamics in the interfacial regions of nanocrystalline solids

S. Breuer, M. Uitz, and M. Wilkening, *J. Phys. Chem. Lett.*, **9** (2018), 2093-2097.

Mismatch in cation size causes rapid anion dynamics in solid electrolytes: the role of the Arrhenius pre-factor

S. Breuer and M. Wilkening, *Dalton Trans.*, **47** (2018), 4105-4117.

Solutions Fluorine Translational Anion Dynamics in Nanocrystalline Ceramics: $\text{SrF}_2\text{-YF}_3$ Solid

S. Breuer, B. Stanje, V. Pregartner, S. Lunghammer, I. Hanzu, and M. Wilkening, *Crystals*, **8** (2018), 122.

F anion dynamics in cation-mixed nanocrystalline $\text{LaF}_3\text{:SrF}_2$

S. Breuer, S. Lunghammer, A. Kiesl, and M. Wilkening, *J Mater Sci*, 2018.

<https://doi.org/10.1007/s10853-018-2361-x>, *in press*

Ion Dynamics in a New Class of Materials: Nanoglassy Lithium Alumosilicates

B. Stanje, P. Bottke, S. Breuer, I. Hanzu, P. Heijmans, and M. Wilkening, *Mat. Res. Express*, **5** (2018), 035202.

C.2 Manuskripte

Heterogeneous F anion transport, local dynamics and electrochemical stability of nanocrystalline $\text{La}_{1-x}\text{Ba}_x\text{F}_{3-x}$

S. Breuer, M. Gombotz, V. Pregartner, I. Hanzu, and M. Wilkening, *under review*

Interfacial Li ion dynamics in nanostructured LiF and LiF: Al_2O_3 composites

S. Breuer, V. Pregartner, and M. Wilkening, *in preparation*

Fast Na ion transport triggered by rapid ion exchange on local length scales: ^{23}Na NMR spin-lattice relaxation reveals ultrafast Na ion dynamics in the solid electrolyte $\text{Na}_{3.4}\text{Sc}_{0.4}\text{Zr}_{1.6}(\text{SiO}_4)_2\text{PO}_4$

S. Lunghammer, D. Prutsch, S. Breuer, D. Rettenwander, I. Hanzu, Q. Ma, F. Tietz, and M. Wilkening, *Sci. Rep.* 2018, under review

C.3 Posterbeiträge auf internationalen Konferenzen

Mechanochemical synthesis and characterization of the metastable, nanocrystalline F ion conductor $(\text{Ba}_x\text{Ca}_y)\text{La}_{(1-x-y)}\text{F}_{(3-x-y)}$

S. Breuer, F. Preishuber-Pflügl, and M. Wilkening, *15th European Conference on Solid State Chemistry*, 23-26.08.2015, Vienna, Austria.

Separating bulk from grain boundary Li ion conductivity in the sol-gel prepared solid electrolyte $\text{Li}_{1.5}\text{Al}_{0.5}\text{Ti}_{1.5}(\text{PO}_4)_3$

S. Breuer, D. Prutsch, Q. Ma, V. Epp, F. Preishuber-Pflügl, F. Tietz, and M. Wilkening, *IBA2016 – International Battery Association*, 20-25.03.2016, Nantes, France.

Bulk and Grain Boundary Li Ion Conductivity of $\text{Li}_{1.5}\text{Al}_{0.5}\text{Ti}_{1.5}(\text{PO}_4)_3$

S. Breuer, D. Prutsch, Q. Ma, V. Epp, F. Preishuber-Pflügl, F. Tietz, and M. Wilkening, *18th International Meeting on Lithium Batteries*, 19-24.06.2016, Chicago, IL, USA.

All-Solid-State Batteries Based on Nanocrystalline LiBH₄

M. Uitz, S. Breuer, C. Täubert, V. Hennige, and M. Wilkening, *2017 MRS Spring Meeting & Exhibit*, 17-21.04.2017, Phoenix, AZ, USA.

Rapid Li Spin Dynamics in the Interfacial Regions of the Nanocrystalline Solid Electrolyte LiBH₄

S. Breuer, M. Uitz, D. Prutsch, and M. Wilkening, *19th International Meeting on Lithium Batteries*, 17-22.06.2018, Kyoto, Japan.

Fast Interfacial Li⁺ Diffusion in Nanostructured LiF and LiF-Al₂O₃ composites as Seen by NMR Spectroscopy

V. Pregartner, S. Breuer, and M. Wilkening, *19th International Meeting on Lithium Batteries*, 17-22.06.2018, Kyoto, Japan.

C.4 Vorträge

Investigation of bulk and grain boundary Li ion conductivity via impedance spectroscopy in the solid electrolyte Li_{1.5}Al_{0.5}Ti_{1.5}(PO₄)₃

S. Breuer, D. Prutsch, Q. Ma, V. Epp, F. Preishuber-Pflügl, F. Tietz, and M. Wilkening, DocDays 2016, 05-06.04.2016, Graz, Austria.

D. Danksagung

Mein größter Dank gilt Prof. Dr. Martin Wilkening, sowohl dafür mir die Möglichkeit gegeben zu haben meine Dissertation am Institut für Chemische Technologie von Materialien an der TU Graz zu verfassen, als auch für die großartige Betreuung im Rahmen dieser. Ich danke ihm für die viele Zeit, die er sich stets für wissenschaftliche Diskussionen und sämtliche andere Fragestellungen genommen hat. Er ist nicht nur in wissenschaftlicher Hinsicht, sondern ebenso auf menschlicher Ebene ein toller Lehrer. Auch für die Möglichkeit meine wissenschaftlichen Arbeiten auf vielen internationalen Konferenzen auf der ganzen Welt präsentieren zu dürfen, möchte ich mich herzlich bedanken.

Des Weiteren gilt mein großer Dank zwei Personen: Dr. Florian Preishuber-Pflügl für die enorme Hilfe beim Erlernen diverser Methoden bzw. Messtechniken und die vielen interessanten Gespräche mit ihm, die mir den Einstieg in die Materie sehr erleichtert haben. Meiner Bürokollegin Veronika Pregartner für die riesige Unterstützung bei den präparativen Arbeiten, ohne die das Verfassen von einigen der gezeigten Publikationen nicht möglich gewesen wäre. Ebenso möchte ich mich bei ihr für die unzähligen schönen und lustigen gemeinsamen Stunden sowohl im Büro als auch in der Freizeit bedanken, die stets eine willkommene Abwechslung zum Arbeitsalltag waren.

Ein besonderer Dank geht auch an alle ehemaligen und aktuellen Kollegen der Arbeitsgruppe Wilkening für die gute Zusammenarbeit. Im speziellen möchte ich mich bei meinen „Konferenzkollegen“ Denise Prutsch, Marlena Uitz, Isabel Hanghofer und Bernhard Gadermaier bedanken, mit denen ich gemeinsam viele wertvolle Erfahrungen sammeln konnte und mit denen ich zahlreiche Länder bzw. Städte rund um den Globus zu sehen bekam. Es freut

mich, euch nicht nur zu meinen Arbeitskollegen, sondern auch zu meinen Freunden zählen zu dürfen.

Weiters danke ich Dr. Brigitte Bitschnau und Prof. Dr. Franz Mautner für die XRD Messungen sowie Liane Hochgatterer und Christina Albering für ihre Hilfe bei organisatorischen Fragen oder Bestellungen.

Auch abseits der Universität sind einige Menschen entscheidend am Gelingen dieser Dissertation beteiligt gewesen. Allen voran meine Freunde in der Steiermark und in Salzburg, die mir immer mit Rat und Tat zur Seite gestanden sind und mit denen ich sehr viele angenehme, aber vor allem auch lustige, gemeinsame Zeiten abseits dieser Arbeit verbringen durfte.

Abschließend möchte ich noch meiner Familie, im speziellen meinen Eltern einen ganz großen Dank aussprechen, die mich immer in allem unterstützt haben und so diese Arbeit überhaupt erst möglich gemacht haben.